Inaugural dissertation

for

obtaining the doctoral degree

of the

Combined Faculty of Mathematics, Engineering and Natural Sciences

of the

Ruprecht - Karls - University

Heidelberg

Presented by

M.Sc. Sankeert Satheesan

born in: Kannur, Kerala, India

Oral examination: 03.07.2025

Design and implementation of workflow tools for multiplexed time-lapse imaging experiments in zebrafish screening

Referees: Prof. Dr. Joachim Wittbrodt

Prof. Dr. Stephen A Renshaw

Abstract

Recent high-throughput microscopy advancements have made it possible to perform multiplexed time-lapse imaging in a single experimental run. However, despite these technological improvements, a major gap remains in the practical application and optimization of multiplexed time-lapse imaging for studying dynamic biological processes in vivo. This is particularly evident when quantifying complex dynamic phenotypes, such as regeneration and cell migration, in small model organisms like zebrafish. Challenges in sample preparation, spatiotemporal sampling, and the lack of dedicated imaging protocols and bioimage analysis tools aggravate this problem. Zebrafish, with their genetic accessibility and optical transparency, provide an excellent model for live imaging and high-content screening. However, it lacks dedicated protocols and solutions to multiplexed time-lapse imaging screening experiments, hindering it from fully exploiting its potential.

To address these challenges and bridge this gap, I established a benchmark high-throughput screening platform for quantifying kidney regeneration in zebrafish embryos post-laser-induced injury. This platform integrates multiple components, optimized sample mounting strategies to ensure optimal imaging conditions over extended periods, a high-throughput laser-induced injury workflow, and a smart imaging framework that seamlessly integrates lasering and imaging to capture regenerating renal tubules efficiently. This followed a dedicated image processing pipeline that allows the detection and tracking of regenerating tissues. Utilizing open-source tools such as Fiji, Python, and KNIME, I built analysis workflows capable of stabilizing images, segmenting key regions of interest, and quantitatively assessing regeneration dynamics across hundreds of embryos. Finally, the platform was validated through experiments under different environmental conditions to verify the platform's ability to assess regeneration efficiency and variability at an unprecedented scale.

In conclusion, using the established high-throughput platform, I set a new benchmark for multiplexed time-lapse imaging in zebrafish-based screening. The platform's protocol components and flexible analysis workflows can be applied to other dynamic phenotypes. Ultimately, through this thesis, I present a comprehensive methodology and versatile tools for long-term imaging and set a precedent for investigating dynamic phenomena across biology.

Zusammenfassung

Jüngste Fortschritte in der Hochdurchsatz-Mikroskopie ermöglichen die Durchführung multipler mehrdimensionaler Zeitrafferexperimente in einem einzigen Durchlauf. Trotz dieser technologischen Entwicklungen bleibt die praktische Anwendung und Optimierung dieser Methoden eine Herausforderung, insbesondere für die Untersuchung dynamischer biologischer Prozesse in vivo. Die Quantifizierung komplexer Phänotypen wie Regeneration und Zellmigration gestaltet sich besonders schwierig in kleinen Modellorganismen wie dem Zebrafisch. Herausforderungen in der Probenvorbereitung, räumlich-zeitlichen Abtastung sowie das Fehlen spezialisierter Bildgebungsprotokolle und Bioimage-Analysewerkzeuge begrenzen die effiziente Nutzung dieser Technologie. Obwohl der Zebrafisch durch seine genetische Zugänglichkeit und optische Transparenz ein ideales Modell für Live-Bildgebung und Hochdurchsatz-Screening darstellt, fehlen standardisierte Protokolle und Lösungen für multiplexe Zeitrafferbildgebung, was sein Potenzial für Hochdurchsatzstudien eingeschränkt.

Um diese Lücke zu schließen, habe ich eine hochdurchsatzfähige Screening-Plattform entwickelt, die als neuer Benchmark für die Quantifizierung der Nierenregeneration in Zebrafisch-Embryonen nach laserinduzierter Schädigung dient. Diese Plattform kombiniert eine optimierte Probenvorbereitung, eine Hochdurchsatz-Laserschädigungsstrategie sowie ein intelligentes Imaging-Framework, das Lasern und Bildaufnahme nahtlos integriert, um regenerierende Nierentubuli effizient zu erfassen. Es folgte eine spezielle Bildverarbeitungspipeline, die die Erkennung und Verfolgung von regenerierendem Gewebe ermöglicht. Mithilfe von Open-Source-Tools wie Fiji, Python und KNIME habe ich Analyse-Workflows entwickelt, die Bildstabilisierung, Segmentierung relevanter Regionen und die quantitative Bewertung der Regenerationsdynamik über Hunderte von Embryonen ermöglichen. Die Plattform wurde unter verschiedenen Umweltbedingungen validiert und ihre Zuverlässigkeit für die Analyse der Regenerationseffizienz und -variabilität bestätigt.

Zusammenfassend stellt diese Hochdurchsatz-Plattform einen neuen Standard für multiplexe Zeitrafferbildgebung in Zebrafisch-Screenings dar. Die modularen Protokollkomponenten und flexiblen Analyse-Workflows sind auch auf andere dynamische Phänotypen übertragbar. Diese Arbeit liefert eine umfassende Methodologie und vielseitige Werkzeuge für die Langzeitbildgebung und setzt einen neuen Maßstab für die Untersuchung dynamischer biologischer Prozesse.

Table of Contents

Abbreviations

GPU:	Graphical Processing Unit
GUI:	Graphical User-Interface
PCA:	Principal Component Analysis
ROI:	Region Of Interest
CSV:	Comma Separated Values
TPR:	True Positive Rate
TNR:	True Negative Rate
API:	Application Programming Interface
CCD:	Charge-Coupled Device
SCMOS:	Scientific Complementary Metal-Oxide-Semiconductor
AF:	Auto Focus
TLM:	Time-Lapse Microscopy
FRET:	Förster Resonance Energy Transfer
LSFM:	Light-Sheet Fluorescence Microscopy
DSLM:	Digital Scanned Light-Sheet Microscope
STED:	Stimulated Emission Depletion Microscopy
STORM:	Stochastic Optical Reconstruction Microscopy
PALM:	Photoactivated Localization Microscopy
DMSO:	Dimethyl Sulfoxide
PTU:	Phenylthiourea
AKI:	Acute Kidney Injury
ZF:	Zebrafish
GFP:	Green Fluorescent Protein

CRISPR:	Clustered Regularly Interspaced Short Palindromic Repeats
ZFNs:	Zinc-Finger Nucleases
TALENs:	Transcription Activator-Like Effector Nucleases
HPF	Hours Post Fertilization
DPF	Days Post Fertilization
AA	Aristolochic Acid

Contributions

In this thesis, I conducted most of the work presented. However, certain validation experiments in the kidney regeneration screening assay and the collaborative projects (mentioned in the appendix) involved contributions from colleagues, which I acknowledge as follows:

Leon Rapp helped me prepare 96-well plates and orient embryos for the kidney regeneration screening assay validation experiments under my supervision.

The study titled "Developing a medium-throughput time-lapse workflow for quantitatively analyzing the neutrophil swarming response in zebrafish embryos" (See Appendix Section 7.1) was conducted in collaboration with **Nils Olijhoek.**

The study titled "Developing a high-throughput workflow to assess otic vesicle neutrophil recruitment following substrate injection in zebrafish embryos" (See Appendix Section 7.2) was a collaborative effort with **Liz Hernández**

1

Introduction

1.1. Microscopy in biomedical sciences

From the molecular level within cells to the complex interactions within ecosystems, biology is surrounded by constant change and adaptation across various scales and timescales. Constant visualization of these processes helps us as researchers to deepen our understanding of nature and biology. Microscopy is a powerful tool in this venture, enabling the study of biological phenomena at various scales—from single cells to whole organisms. Since the discovery of the first microscopes in the 1600s, which led to the discovery of cells and the development of cell theory (Hooke et al., 1665), microscopy has evolved dramatically.

The techniques in microscopy can be broadly divided into two categories light and electron microscopy. Light microscopy uses visible light to image, while electron microscopy employs accelerated electron beams, revealing molecular-level structural details and offering much higher resolution. Light microscopy is particularly popular in life science research due to its flexibility and accessibility (Reigoto et al., 2021). Light microscopy includes a range of techniques, from bright-field microscopy to advanced super-resolution microscopy. Advances in light microscopy, along with the development and constant evolution of fluorophores and fluorescent proteins, have enabled the labeling and detection of multiple endogenous molecules within the sample (Hmeljak & Agullo-Pascual, 2021). Intravital microscopy opened the avenues to image within the living specimens, although those techniques were initially invasive (physically disrupting, damaging, or altering the observed sample, potentially

affecting its viability). Continuous efforts and innovations to reduce the invasiveness of intravital microscopy techniques have led to the ability to image the samples at the most optimal physiological conditions for the sample (Scherf & Huisken, 2015).

These developments have opened up new directions in biomedical research. It enables capturing dynamic processes with 2D or 3D imaging and observing living cells, tissues, or whole organisms at various scales. In recent decades, microscopy has transformed from a primarily qualitative tool to a high-throughput, quantitative discipline (Mattiazzi Usaj et al., 2016). For instance, the development of an automated screening platform by Opris¸oreanu et al., 2021, using advanced microscopy techniques, identified synapse-stabilizing compounds in juvenile zebrafish models. This combination of high-throughput analysis and automated imaging improves our knowledge of complex biological systems and helps us find possible treatment approaches.

1.1.1. Capturing dynamic processes

A detailed exploration of complex biological systems was possible due to the improved spatial resolution of microscopy methods. But as biology is naturally dynamic, one must consider temporal elements to understand these systems fully. This led to the development of time-lapse microscopy (TLM), a powerful and constantly evolving microscopy technique enabling researchers to capture the dynamics of biological events. For instance C. C. Wong et al., 2010 showed how TLM distinguished two morphologically identical embryos. Although both embryos appeared identical morphologically, TLM revealed that one followed a typical developmental pattern, while the other showed abnormal cell division and fragmentation. This critical information is undetectable in an endpoint/fixed-timepoint imaging assay, underscoring the value of temporal aspects in studying biological processes (C. Wong et al., 2013).

The first basic TLM was pioneered in the twentieth century, starting with basic glass tissue chambers and manual image capture. Over the years, TLM gradually evolved and became a potent tool for the quantitative and qualitative assessment of diverse biological events, including embryonic development, physiology, and immune cell dynamics (Collins et al., 2018). Recent developments concentrate on further enhancing TLM's spatial and temporal resolution to investigate dynamic biological processes in greater detail. The integration of TLM with cutting-edge imaging

technologies, including confocal, multiphoton, and light-sheet microscopy, has paved the way for significant innovations, including Förster Resonance Energy Transfer (FRET), multiplexed/multifield TLM, and in-toto imaging. The study by Keller et al., 2008 marks a good example, they pioneered an advanced form of Light-Sheet Fluorescence Microscope (LSFM), Digital Scanned Light-Sheet Microscope (DSLM). Which enabled them to record long-term and high-resolution images of zebrafish embryonic development with little phototoxicity. This made the visualization of cellular dynamics possible over a long time, illuminating important new directions on morphogenesis, cell lineage specification, and developmental robustness.

While TLM offers invaluable insights into biological processes, there are still pressing challenges, such as the integration of advanced sub-diffraction techniques such as STED, STORM, and PALM to improve the spatial resolution in TLM, have significant drawbacks (Culley et al., 2018). They require very high-power illumination that potentially damages the sample with long-term exposure. Rapid movements during live imaging often pose the issue of samples losing focus while imaging, making it hard to track and analyze their dynamics (Samereier et al., 2010). This shows the need to optimize and develop new techniques to capture these ultra-fast rapid movements. Finally, maintaining the physiological conditions, although recent improvements have reduced the invasiveness of TLM, still poses some disruption to the samples (Nagy et al., 2012).

Despite the advancing technology, one key consideration in microscopy is often a necessary trade-off in choosing the optimal technique. Usually, this trade-off consists of balancing spatial and temporal characteristics, signal sensitivity, and phototoxicity and prioritizing one aspect inevitably compromises others (Scherf & Huisken, 2015). Recent attempts have adopted a more systematic strategy by using computational solutions, such as adaptive optics and deep learning-based image restoration, which are actively working toward reducing these trade-offs and stretching the limits of live-cell imaging. We are steadily progressing towards unraveling complex biological processes by pushing the limits, which makes the future of live imaging exciting and challenging (Balasubramanian et al., 2023).

1.2. Microscopy-based screening in biomedical sciences

Microscopy is a continuously evolving field that advances analytical power, imaging speed, and resolution. Early advances concentrated mostly on enhancing image quality and technical precision, providing valuable biological insights, but they remained limited in their scalability. This challenge was recognized by researchers from systems biology, drug discovery, and functional genomics, often dealing with large-scale studies. This motivated the development of high-throughput imaging techniques (Oheim, 2007; Pepperkok & Ellenberg, 2006; Zanella et al., 2010). Two main technical developments, automation, and parallel acquisition, made high-throughput imaging a reality. Developments in automation streamlined multiple steps of the microscopy workflow, including sample handling, image acquisition, and data analysis.

High throughput imaging screens were first utilized for cell-based assays in the 1980s (Deindoerfer et al., 1982), primarily for drug detection, which was further expanded to phenotypic screening with further advances in automated microscopes (Vaisberg et al., 2006). Microscopy-based screening allows researchers to explore heterogeneity in complex biological systems that might be missed in smaller-scale imaging experiments. This broader dataset provides a robust statistical foundation that helps researchers manage biological variability. It also enables the detection of rare events that are too infrequent to appear in lower-throughput assays. Automated and standardized procedures helped to lower biases and assure experimental consistency (Oheim, 2007, 2011; Way et al., 2023).

Widefield and confocal microscopy are the primary methods for high-throughput imaging of biological specimens among diverse microscopy techniques. Classical screens span from chemical to genetic screens. While genetic screens identify genes involved in particular biological processes such embryogenesis (Driever et al., 1996; Sönnichsen et al., 2005), chemical screens consist of libraries of small molecules to identify therapeutic compounds, toxic molecules, or modulators of signaling pathways (Rennekamp & Peterson, 2015; Richter et al., 2017). Within the last couple of decades beyond cell systems, microscopy-based screening emerged in small organisms screens such as in zebrafish larvae (Pandey et al., 2019; Rennekamp & Peterson, 2015; Richter et al., 2017) and organoid screens (Lukonin et al., 2020). In addition to the broad use of microscopy-based screening in imaging fluorescently labeled biological specimens (Esner et al., 2018; Futamura et al., 2012), it is also widely applied in histology and digital pathology with whole-slide imaging (Pantanowitz et al., 2011).

The current generation of screening-based microscopy has significantly enhanced high-throughput imaging and quantitative biological analysis. Advanced automated microscopy systems offer precise control over stage movement, focusing, illumination, and magnification, allowing simultaneous acquisition of multiple channels, improved autofocusing, and shorter acquisition times. Using sCMOS cameras in current-generation microscope chips over earlier CCDs increased pixel density, enabling the capture of larger areas with fewer fields (Hale & Nojima, 2016). These advances have enabled the imaging of small organisms/cells over relatively long periods (hours, days). Such time-lapse imaging enables the visualization of complex dynamic biological processes on larger sample sizes, providing a step change in increased robustness to unravel spatiotemporal aspects of the system (Čapek et al., 2023).

1.2.1. Challenges with microscopy-based screening in small organisms

Microscopy-based screening was introduced to address the complexity of biological systems in the throughput context, and since its outset, it has evolved significantly. Beginning with cells, we can now screen small organisms such as zebrafish embryos, but this evolution also presents new challenges. Three main areas define the challenges: sample/specimen handling, optics, and acquired data management and analysis (Bullen, 2008; Way et al., 2023). Specimen handling deals with the processes from specimen collection to imaging preparation. For instance, zebrafish embryo screening includes animal husbandry, embryo culture, micromanipulation, and treatment (e.g., drugs and anesthetics). Even for experienced researchers, handling thousands of embryos offers major logistical difficulties (Gehrig et al., 2018), making these procedures time-consuming. Recent advancements in automation have introduced systems for embryo sorting and culturing (Breitwieser et al., 2018), and automated robots are used to treat and load the embryos in the imaging plate (Letamendia et al., 2012; Pardo-Martin et al., 2010), significantly reducing manual labor. These systems are typically expensive and complex, in most laboratories majority of these steps are still performed manually.

Consistent specimen orientation demands dedicated mounting strategies. There are existing tools developed for zebrafish embryos that create agarose cavities within microtiter plate wells, therefore enabling consistent embryo positioning (Wittbrodt et al., 2014; Gehrig et al., 2018). However, these techniques have limited flexibility in

orientation, which often causes a bottleneck for experiments requiring specific specimen alignment. Additionally, the use of agarose can compromise image resolution during acquisition. Automated technologies enabling automated detection and rotational orientation in glass capillaries, followed by whole-specimen imaging, was a great substitute for these limitations (Pulak, 2016; Guo et al., 2017). While these techniques are adequate, these setups are complex, and the possibility of time-lapse acquisition is often challenging, which is crucial for studies looking at the dynamic aspects of morphological and developmental processes (Gehrig et al., 2018). Tissue pigmentation typically limits imaging deeper features even with optimized mounting. Pigment-mutant transgenic lines (Harrold et al., 2016), genetic modification (Lischik et al., 2019), or pharmacological therapies (such as PTU) can help to control pigment-related problems. While screening for dynamic aspects, maintaining a stable specimen orientation throughout imaging is a key challenge, which demands optimal immobilization strategies. Commonly used immobilization strategies include anesthetic agents (Tricaine) and genetic manipulation techniques (Lischik et al., 2019) offer an optimal solution, but they also pose risks. Over time, anesthetics can lose effectiveness and become lethal, and genetic manipulation techniques can interfere with normal development. Thus, maintaining specimen stability while minimizing possible health effects depends on carefully optimizing the immobilization strategies.

Compared to flat cell cultures small organisms are large three-dimensional objects, posing challenges to microscopy-based screens. While these techniques are currently developing in the framework of microscope-based screening, recent developments in microscopy technology seek to raise depth resolution and capture more complex 3D structures (Way et al., 2023). In the current scenario, multiphoton and light-sheet microscopy are widely used for imaging 3D objects, but these methods are still slow and lack throughput in the context of screening (Kumar et al., 2007; Stelzer, 2015). Ongoing advances seek to improve the throughput aspect of these widely used techniques (Way et al., 2023).

Despite the technological developments in microscopy for capturing dynamics in small organisms, considerable challenges persist in applying high-throughput screening to study these dynamics at scale. The challenges inherent to time-lapse microscopy and screening small organisms are further compounded. These challenges include the variability in orientation, size, morphology, and expression patterns across specimens and within image sequences (See Figure 1), which limits the capture of consistent, high-quality images over time. This also hinders the tracking and

identifying of subregions within dynamic targets, making automated analysis difficult due to inconsistent feature detection. These issues limit building a robust and precise imaging workflow for screening different dynamical biological processes. Another interesting domain that screening lacks and is gradually growing is integrating different subsystems to perturb specimens. For instance, laser ablation induces injury or photoactivation to the specimen. Integrating these technologies will allow us to utilize them to study complex dynamic processes like regeneration and cell migration at a large scale. While these techniques are well-established in classical microscopy, bridging them with high-throughput screening demands optimized methodology and protocols to envision it (Muzzey & van Oudenaarden, 2009).

With the advancement of microscopy techniques, small-organism screening can now generate large, multidimensional datasets (3D, channels, time), often spanning several gigabytes to terabytes, depending on the scale of the study (M. Chen, 2021). However, alongside improvements in acquisition, there is a growing need for advanced analytical tools and workflows to handle these vast datasets. Classically, in screening, most software tools are designed for analyzing cell-based systems and are not widely applicable to alternative biological models. In whole-organism screening, data analysis presents distinct challenges, requiring specialized solutions for storage, data handling, visualization, and interpretation (discussed in Section 1.3.2). Unlike cell-based assays, whole-organism imaging demands customized computational pipelines that manage specimen morphology, movement, and spatial complexity. Given the importance of optimizing the acquisition, it is essential to integrate analysis optimization into experimental planning from the beginning, rather than treating it as a post-processing step (Gehrig et al., 2018).

So far, acquiring multiplexed time-lapse screens in a single run is feasible. However, there remains a gap in this technology's practical application and optimization. To improve this situation, as part of my thesis, I developed innovative tools, protocols, and software to harness the full potential of these imaging technologies. This included creating novel protocols and versatile analysis workflows for long-term screening of

dynamic processes, specifically focusing on regeneration and immune responses in zebrafish embryos.

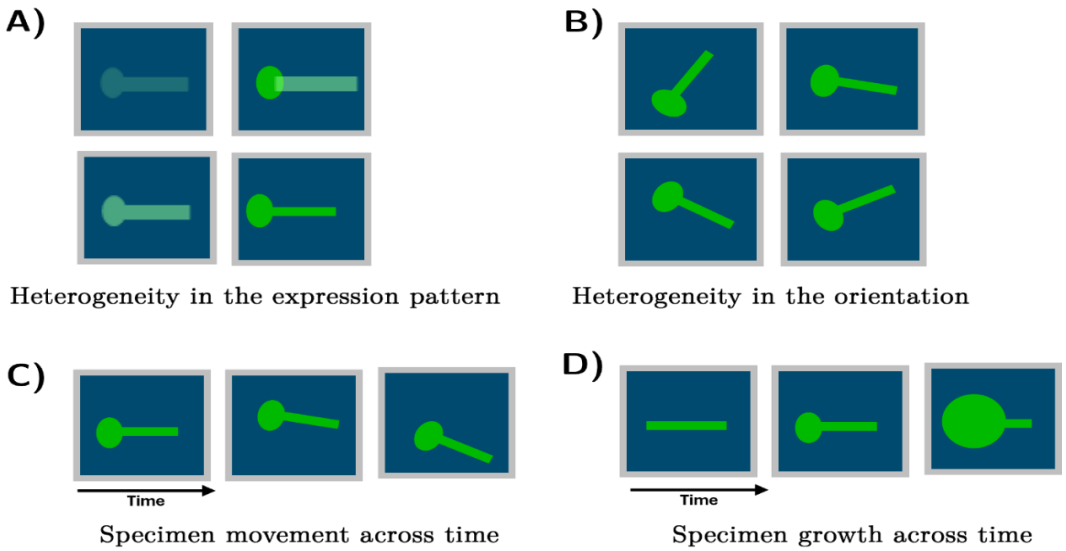

Figure 1:Schematic representing heterogeneity and dynamic changes in biological specimens Heterogeneous behaviors and dynamic properties of biological specimens are illustrated across multiple dimensions. A) Heterogeneity in expression patterns: Specimens display variation in the intensity and distribution of marker expression. B) Heterogeneity in orientation: Individual specimens exhibit diverse orientations in spatial arrangements. C) Specimen movement over time: Temporal imaging captures the dynamic relocation of specimens within a defined field. D) Specimen growth over time: Temporal progression shows the morphological expansion of specimens. Created with BioRender.com.

1.3. Bioimage analysis: Image analysis for microscopy

Traditional photographic cameras used films to acquire images, resulting in analog images. However, by the 1980s charge coupled cameras (CCD) were developed, enabling digital image capture (McNamara et al., 2005). In digital images, typically, a sensor collects the photons from the light signal, and a detector within the sensor detects and stores this information as a discrete 2-dimensional array of values known as pixels, arranged following a grid, forming the image matrix. For many applications including microscopy, the sensor is generally a camera, and the resulting acquired images are digital images with similar characteristics. The age-old idiom *"Seeing is believing"* marks the importance of images in multiple facets of life. Given the fact that nearly half of the human brain is involved in processing vision, our reliance on images is natural (Frisby & Stone, 2010). However, just a subjective interpretation of what one sees in an image can deter scientific reproducibility and reasoning (North, 2006). The past few decades saw a surge in the development and use of a wide array of imaging modalities, but this was not achievable without rapid advances in

computing technology. From sophisticated signal reconstruction to large data management, computers are indispensable in contemporary microscopy. A branch of artificial intelligence, computer vision lets machines independently and statistically evaluate visual data. From daily life situations like image processing in cellphones to image-based medical diagnostics, digital image analysis has been applied in many different disciplines.

Image analysis is done by building workflows or pipelines with successive simple or complex operations (Berthold et al., 2009). There is no single-shot solution or approach while dealing with image analysis, it is much like how human vision processes information (Meijering et al., 2016). The general mechanisms by which we perceive and analyze image features have been extensively studied in computer vision (Marr, 2010). The perceived information can be qualitative, such as reporting the absence or presence of an object, or quantitative, such as the count or spatial information about the object. Within the realm of biology, response to the growing need for powerful automated solutions in image processing and analysis gave rise to the field of bioimage informatics/bioimage analysis (Meijering et al., 2016; Peng et al., 2016). Bioimage analysis is a multidisciplinary field where computer vision meets biology (Danuser, 2011) involving collaborations among a diverse group of experts, including biologists, microscopists, engineers, clinicians, and physicists (Schlaeppi et al., 2022). Bioimage analysis research and techniques are beyond the automation of image interpretation. It enhances the objectivity, reproducibility, and sensitivity of the interpretations, which, at a human level with pre-conceived ideas, we tend to fail to depend on prior experiences (Meijering et al., 2016).

The first step in analyzing image data is to reduce imaging artifacts and noise by preprocessing the image. Background subtraction is a widely used preprocessing technique that removes noisy background elements to enhance the foreground elements. Another prominent example is deconvolution, which tries to undo the signal blurring by any microscope to make the image sharper (Sarder & Nehorai, 2006). The following common step is to detect the object of interest or various types of objects in the preprocessed image. There is a broad range of object detection techniques; for instance, template matching is a technique where a template containing the object of interest is provided, and the object is searched for within the image (Thomas & Gehrig, 2020a). With the detected object of interest, the following step is segmentation, which aims to classify and group pixels as either the object of interest or the background. Segmentation is often the most challenging aspect of bioimage analysis (Meijering, 2012). Upon successful segmentation, the forthcoming

step is to compute a host of quantifications, analytics, and visualizations. This forms a generalized scheme for most bioimage analysis workflows, where each step is interrelated and contributes to a positive feedback loop, enhancing the overall workflow (See Figure 2)(Meijering et al., 2016; Pincus & Theriot, 2007). Recently, machine learning and deep learning-based techniques have been increasingly applied to microscopy, refining bioimage analysis pipelines and solving more complex problems (Jan et al., 2024; Ma et al., 2024; von Chamier et al., 2021).

1.3.1. Bioimage analysis: When image analysis meets dynamics

Early microscopes using computers had a single experiment that resulted in 200x200 pixels of images and accounted for 40 kilobytes of memory (Prewitt & Mendelsohn, 1966). In the current scenario, the advances in spatial, temporal, multiplexing, and throughput imaging result in terabytes of data. Analyzing this manually is labor-intensive and nearly impossible, highlighting the need for automated analysis tools and solutions (Meijering et al., 2016).

The imaging data for a dynamic process consists of a series of images (with or without a z-dimension) at different timepoints; the first step is to convert this raw data to biologically meaningful information. For instance, after imaging fluorescently labeled cells (e.g., nuclei) over time, the raw images are stitched sequentially according to respective timepoints to create a consolidated movie that captures the process (Yao et al., 2017). These general image analysis functions involve visualization, colocalization, and basic quantification using commercial microscope software like ZEN (Zeiss) or Imaris (Bitplane). Open-source tools like FIJI/ImageJ (Schindelin et al., 2012) and, more recently, Napari (Sofroniew et al., 2024) have also been widely used for these purposes (Coutu & Schroeder, 2013). Object tracking is crucial for analyzing dynamic processes starting from the image preprocessing step. Apart from the basic preprocessing techniques applied in static image analysis, an additional step of image registration is used to adjust for jitter and motion artifacts during imaging, guaranteeing accurate and strong quantification downstream. With the additional complication of tracking changes over time, quantitative image analysis of dynamic processes follows the same ideas as stationary image analysis (See Figure 2) (Coutu & Schroeder, 2013; Meijering, n.d.; Meijering et al., 2016). Recent advances in integrating machine learning and deep learning techniques in the image analysis of dynamic processes have significantly enhanced the field, particularly in the

segmentation and tracking of dynamically active objects of interest (Hallou et al., 2021).

1.3.2. Bioimage analysis: Challenges and considerations

Bioimage analysis is crucial in the current life sciences context, especially with the advances in microscopy, both need to be in tandem for complex biological insights. In the current scenario, extracting meaningful information from the unfathomable amounts of acquired image data from multiple imaging experiments proves to be a bottleneck rather than the technology to acquire the image (Levet et al., 2021). Traditional bioimage analysis approaches failed to analyze this sheer amount of data resulting from these experiments, creating critical challenges in data accessibility and demanding adaptive data analysis approaches (Peng et al., 2016). Although bioimage analysis is steadily progressing, limitations persist, particularly for instance, while analyzing intricate biological systems where factors like overlapping structures or low signal-to-noise ratios obscure critical details. (Lucas et al., 2021; Meijering et al., 2016).

While studying dynamic processes, the limitations persisting in the static image analysis are compounded with dynamic artifacts, including variability in orientation, size, morphology, and expression patterns across specimens and within image sequences (See Figure 1). This hinders the development of a robust segmentation and tracking pipeline for dynamically evolving samples. High throughput imaging is advantageous regarding the number of samples being imaged rapidly and the heterogeneous data produced, adding to the experimental robustness. However, these key features become significant bottlenecks during post-imaging analysis; the heterogeneous profiles and the frequent technical artifacts (variability in the size of objects, expression pattern, and movement artifacts) from numerous image samples cause hindrances to the automated analysis pipelines. Within the current frameworks, integrating interactive quality control for extensive multiplexed imaging data remains a significant challenge (Vierdag & Saka, 2024). Additionally, the recent advances in implementing machine learning and deep learning tools in bioimage analysis have improved sample tracking and segmentation (Gómez-de-Mariscal et al., 2021). However, creating generalizable models for tracking remains challenging due to lack of large, diverse annotated datasets of time-lapse cell movies, which demands large-scale expert-assisted annotations (Jan et al., 2024). Additionally, these tools often require coding expertise, which can be a barrier for life scientists, although significant research efforts are underway to make it code-free. Finally, these dynamic, high-

throughput imaging experiments generate massive datasets, which demand substantial computational power to store and process. This requirement often limits the feasibility of many experiments (Gómez-de-Mariscal et al., 2021; Jan et al., 2024).

Bioimage analysis encountered significant challenges during the early days due to the lack of a standardized direction. Efforts were primarily focused on creating isolated custom solutions and not sharing the source code (Levet et al., 2021). This led to a competitive environment where novelty was prioritized over reproducibility. The race toward achieving novelty undervalued building analysis workflows using existing tools, leading to a flood of redundant tools with overlapping functionalities (Levet et al., 2021; Schlaeppi et al., 2022). A 2018 study (Serghiou & Ioannidis, 2018) revealed that of 204 preprints analyzed, only 44% shared code or data, and just 26% were reproducible. Consequently, the multitude of computational solutions requiring substantial computational expertise and customization created a bottleneck for life scientists, the primary end users (Levet et al., 2021). This highlighted the need for improved organization, collaboration efforts, and resource accessibility. In recent years, initiatives have emerged to build "bridge scientists" who will better flourish in this field through their multidisciplinary skills. (Schlaeppi et al., 2022; Soda, 2014) Ultimately, resulting in better outcomes that fulfill the needs of end users. The field is currently focusing on enriching existing open-source software by building plugins and additional packages for tools like FIJI (Schindelin et al., 2012), CellProfiler, and Napari (Sofroniew et al., 2024) and reserving the creation of new software for situations where it is truly essential. Forums and communities like NEUBIAS (Cimini et al., 2020) promote open-source tool development, data-sharing standards, and FAIR (Findable, Accessible, Interoperable, and Reusable) principles However, there still exists a void, which requires further research to develop open-source tools and strengthen workflow pipelines, emphasizing the robustness and reproducibility of the methodologies (Meijering et al., 2016; Schlaeppi et al., 2022; Soda, 2014). As part of my thesis, I sought to address this gap by creating flexible image analysis workflows to study dynamic processes using open-source tools such as Fiji, Python, and KNIME. Specifically, I established a generally applicable set of protocols and tools for analyzing dynamic features like regeneration and immune responses, in zebrafish

embryos. Additionally, the tools I developed hold the potential to extend to feedback microscopy applications, thereby advancing smart imaging techniques.

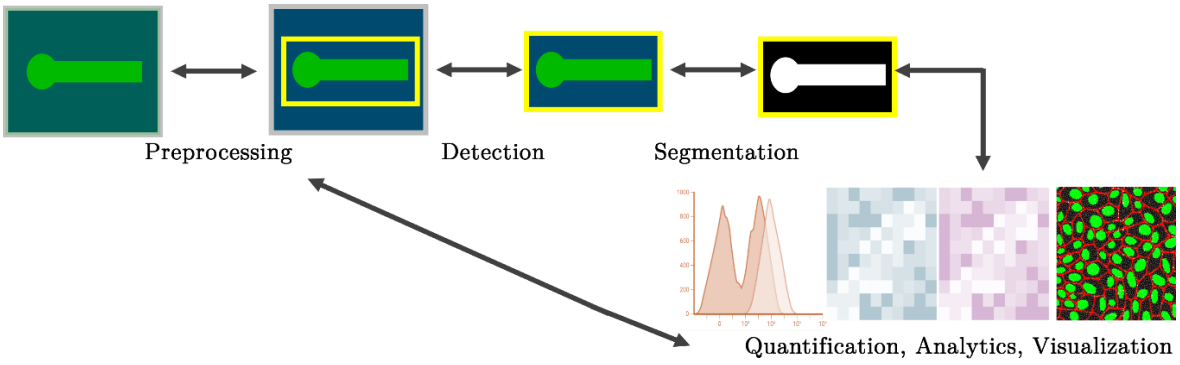

Figure 2: Schematic representing workflow for the image-based analysis of biological specimens. The figure demonstrates a typical workflow for analyzing biological images, from preprocessing to visualization. **Preprocessing**: Initial adjustments enhance image quality for subsequent analysis. **Detection**: Key features or regions of interest are identified within the image (yellow outlines highlight detected regions). **Segmentation**: Images are processed to separate distinct regions, such as cellular structures, creating binary or labeled outputs for analysis. **Quantification, Analytics, Visualization**: Extracted data is analyzed for distribution patterns, spatial relationships, or other metrics, and results are presented as histograms, heatmaps, or annotated images. Adapted from Meijering et al., 2016.

1.4. Zebrafish as a model system for microscopy-based screening

The zebrafish (*Danio rerio*) ,a tropical freshwater vertebrate that has emerged as a powerful model for studying vertebrate biology (Dooley & Zon, 2000). The model was found due to its tractability to large-scale forward genetic approaches, as its external development enables precise morphological observations of extensive populations of developing embryos (Garcia et al., 2016). From the early 1970s, zebrafish have been a model system for research on genetic disorders, development biology, and vertebrate evolution (Streisinger et al., 1981). Genomic studies that compare zebrafish genome to the human reference genome have demonstrated that 70% of the zebrafish genome contains orthologs to human genes, with 86% of known drug targets also preserved (Gunnarsson et al., 2008; Howe et al., 2013). Zebrafish embryos and larvae are preferred over adults due to their low maintenance cost, brief maturation time, easy breeding, small sizes, and transparency, making it an excellent model for microscopy and a go-to small organism model for high throughput screening. Furthermore, they have broader phylogenetic similarities with humans

than adults (Garcia et al., 2016). These attributes qualify them for the 3Rs principle (Replacement, Reduction, and Refinement), solidifying their status as a leading model organism in biomedical research (Rácz et al., 2021; Russell, 1995). The developments in molecular biology have helped to sequence and annotate the zebrafish genome (Silva Brito et al., 2022), enabling the analysis of the biochemical, genetic, and cellular levels to establish the observations made at the structural, functional, and behavioural levels (Garcia et al., 2016). The development of gene-editing techniques, such as transcription activator-like effector nucleases (TALENs), zinc-finger nucleases (ZFNs), and CRISPR-Cas9, has further revolutionized zebrafish research by enabling the creation of targeted genetic modifications. These advancements have produced numerous transgenic lines, mutants, and enabled researchers to study a wide range of biological processes and disease models. The first stable transgenic zebrafish line was successfully developed in 1988 (Stuart et al., 1988). Since then, a comprehensive and curated list of maintained mutant lines has been readily accessible from the Zebrafish International Resource Center.

1.4.1. Rise of zebrafish in biomedical research

Experimental innovations in whole organism screen, such as dedicated mounting systems for ideal positioning and orientation or sophisticated microfluidics, have significantly advanced the zebrafish screening research (Mohd Fuad et al., 2018; Pardo-Martin et al., 2010). The extensive availability of transgenic lines and disease models positions zebrafish embryos as an excellent model for investigating various organs, tissues, and associated pathologies. They have been extensively used to investigate cardiovascular development and disease mechanisms and their role in congenital heart defects and vascular disorders (Bakkers, 2011; Gierten et al., 2020; Nguyen et al., 2008; Pylatiuk et al., 2014). In oncology research, zebrafish models contribute to understanding tumorigenesis, metastasis, and drug screening for cancer therapeutics (Langenau et al., 2003; White, 2015). Zebrafish are also widely utilized in eye research, offering a powerful model for studying retinal development, degeneration, and vision-related disorders (Avanesov & Malicki, 2010; Bibliowicz et al., 2011; Fadool & Dowling, 2008). Furthermore, they contribute to intestine and digestive system research, providing insights into gut development, microbiota interactions, and digestive diseases (Flores et al., 2020; Kanther et al., 2011). Additionally, they provide insights into kidney development and renal disorders, aiding in the study of renal function and disease (Gehrig et al., 2018; Hostetter et

al., 2003; Pandey et al., 2019). Beyond organ-specific research, the remarkable regenerative capacity of zebrafish makes them an ideal system for regenerative medicine, particularly in exploring tissue regeneration and wound healing (Marques et al., 2019; Zhou et al., 2010). Possessing a complete immune system like humans makes the zebrafish ideal for investigating host-pathogen interactions (Li & Hu, 2012). In zebrafish, the innate immune system (macrophages and neutrophils) develops early in embryogenesis, followed by adaptive immunity (Bernut et al., 2015). This provides a unique opportunity to analyze specific immune responses without the added complexity of adaptive immune mechanisms. The flexibility to introduce various pathogens, including bacteria, viruses, and fungi, through multiple injection sites—such as the caudal vein, heart ventricle, or hindbrain—facilitates comprehensive investigations into both systemic and localized infections (Masud et al., 2017).

The zebrafish embryo demonstrates optical transparency during its early developmental stages, and its external development characteristics make it an ideal model organism for research in developmental biology (Kimmel et al., 1995; Nüsslein-Volhard, 2012). The close genetic relationship between zebrafish embryos and humans has enabled genetic screenings that have successfully identified genes involved in embryogenesis (Driever et al., 1996). The zebrafish embryo's resilience and ability to develop generally in agarose embedment aid in imaging dynamic cellular processes in early embryonic stages, which is virtually impossible in mammals (See overview Figure 3). These advantages, coupled with the accessibility of a diverse array of mutants and a continuously advancing molecular toolkit, render zebrafish embryos a powerful setting to study dynamic developmental events by time-lapse (Rieger et al., 2011).

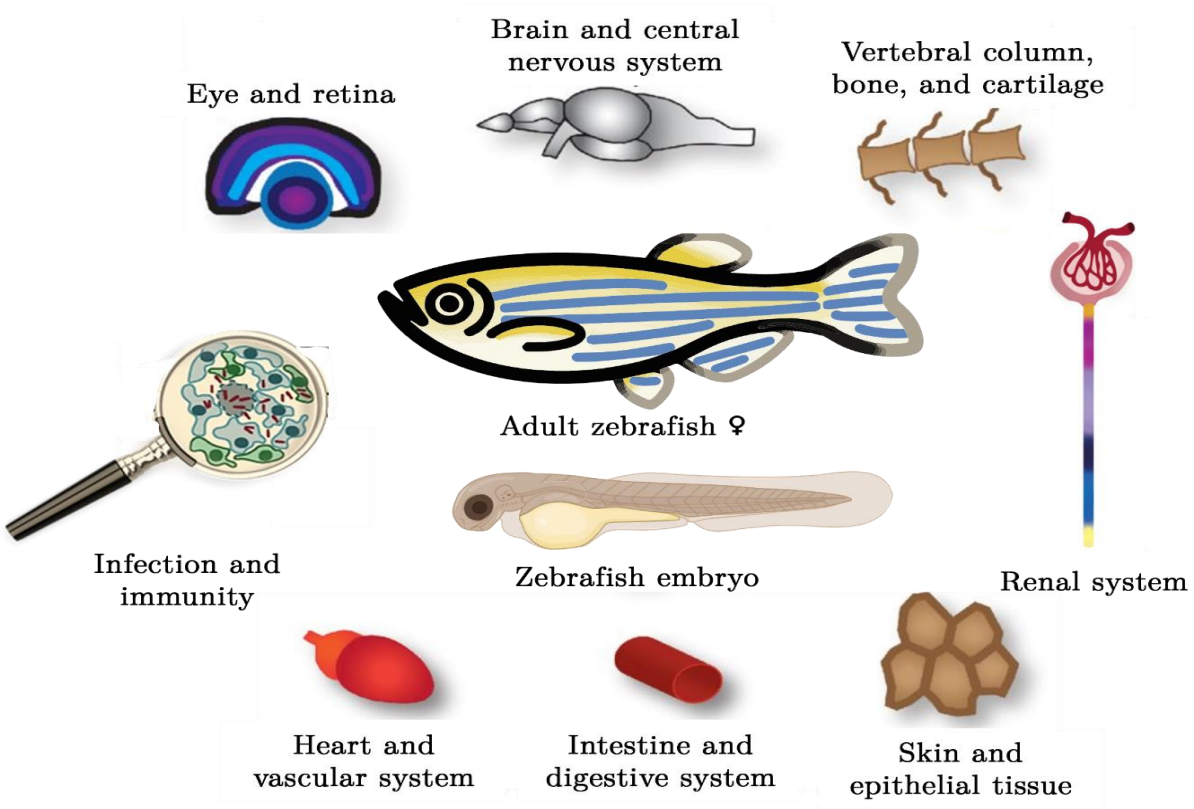

Figure 3: Zebrafish as a model organism for vertebrate biology. The figure outlines the wide use of the zebrafish model system encompassing development, immunity, oncology, cardiology, and other organs, tissues, and associated pathologies. Reproduced from (Koster and Sassen 2015) under Non Commercial (unported, v3.0) License, Wesselman & Wingert, 2023 under Non Commercial (unported, v4.0) License. Created with BioRender.com and biocoins.com

1.4.2. Zebrafish as a model system to study kidney regeneration

Over the past decades, zebrafish embryos have become a premier genetically tractable model organism for various human disease studies. Within the realm of renal biology, zebrafish is a well-established model for studying the development and physiology of nephrons, examining the pathophysiological aspects associated with renal diseases, and enhancing our understanding of nephron function and dysfunction (Ebarasi et al., 2011; Poureetezadi & Wingert, 2016). A series of forward genetic screens have pioneered kidney research in zebrafish, yielding a collection of mutations that influence nephron morphology and functionality. Which eventually aided in detailing the molecular characterization and revealed the overall conservation of the renal anatomy with human kidneys (Diep et al., 2011).

The renal system development in vertebrates has three stages: pronephric, mesonephric, and metanephric. The pronephric kidney represents the most basic form, which develops into the more mesonephric kidney, which functions as the primary excretory organ in aquatic vertebrates. In higher vertebrates, the

mesonephric kidneys are temporary and later develop into the more complex metanephric kidneys, which serve as the main excretory organs in reptiles, birds, and humans (P. Sharma et al., 2014).

The pronephric kidney is the excretory system in zebrafish for the first 30 days of larval development, consisting of two nephrons with fused glomeruli and pronephric tubules. Despite their anatomical simplicity, the tubular epithelium in the pronephric kidney of zebrafish imitates the mammalian kidney consisting of two proximal and distal tubular structures (see Figure 4). The genetic similarity discussed in (Section 1.4.) extends to kidney-related genes, making zebrafish a relevant model for studying human kidney diseases and potential treatments. The nephron repair mechanism is conserved across species, making larval zebrafish an excellent model for renal research. In adult zebrafish, the pronephros transitions into the mesonephros, which exhibits a unique process known as neo-nephrogenesis—the ability to generate new nephrons. This regenerative capability, which is absent in humans, is currently being investigated to understand its underlying mechanisms better and explore potential therapeutic applications for kidney repair and regeneration (Cirio et al., 2015; Poureetezadi & Wingert, 2016; P. Sharma et al., 2014).

1.4.3. Current approaches and techniques to study kidney regeneration in zebrafish

The conserved and distinctive renal features found in zebrafish and higher vertebrates present researchers with an excellent opportunity to explore fundamental disease pathologies and further discover ways to elicit regenerative responses. The extensive collection of zebrafish transgenic lines also encompasses well-established lines dedicated to the renal system that highlight distinct cell types and nephron regions. Among these, the most frequently utilized transgenic lines are *wt1b*, *cdh17*, and *lhx1a*. Although these lines are primarily employed to study the pronephric kidney, they can also be adapted for research on mesonephric kidneys (See Figure 4). Renal disease models have contributed majorly to the knowledge of cystic kidney diseases, glomerular disease, and acute kidney injury (AKI) (McCampbell & Wingert, 2014). Zebrafish benefit glomerular disease studies primarily because of their anatomical and functional similarity to mammalian podocytes. Zebrafish and humans preserve the expression of slit diaphragm-associated genes, which are necessary for filtration (McCampbell & Wingert, 2014). The development of podocyte-specific transgenic

lines, including *Tg(podocin:GFP)*, enabled real-time visualization of podocyte shape and function and helped to propel more developments in this field (He et al., 2011).

Besides glomerular illnesses, zebrafish have also given important new perspectives on cystic kidney disease pathophysiology. Zebrafish have several orthologous genes linked to human cystic kidney disease, and their renal system faithfully copies important disease features like cyst development and ciliary abnormalities. Moreover, the zebrafish model-based high-throughput screens help to enable large-scale research aiming at deciphering the genetic causes of cystic illness and assessing possible treatment approaches (Pandey et al., 2019; Poureetezadi & Wingert, 2016; Swanhart et al., 2011).

In zebrafish models, AKI is typically characterized by partial or complete loss of renal function, often resulting from ischemic injury due to sepsis or exposure to nephrotoxic agents that mimic human AKI. The morphological manifestations of AKI in zebrafish unfold in multiple overlapping phases. It starts with dedifferentiation of the neighboring cells surrounding the injury, followed by their detachment from the basement membrane and apoptosis in some instances (Cirio et al., 2015). The detached cells then often flow into the lumen of the tubule, causing tubular obstruction. The subsequent major phase involves tubular regeneration, wherein new epithelial cells are generated from the remaining cells within the nephron. Ongoing researches aim to unravel the true origin of new tubular epithelium (Bonventre, 2003; Verghese et al., 2008). Due to its simple two-nephron structure, the zebrafish pronephros is a well-established model for investigating AKI. Primarily, there are two approaches to induce AKI in zebrafish models, chemical induction and targeted cell ablation. Within chemical induction, gentamicin-induced injury is the most prevalent model, involving the injection of gentamicin into the circulation of zebrafish larvae at 48–72 hours post-fertilization (hpf), resulting in proximal tubular cell damage. The tubular injury results in tubular restriction, reduction of the pronephros ability to filter and eliminate fluid, and subsequent development of edema (Cirio et al., 2015; Lopez-Novoa et al., 2011). Aristolochic acid (AA) also constitutes a nephrotoxic agent that induces tubular and glomerular damage when embryos are exposed at 24 hpf (Arlt et al., 2002).

Nephrotoxic agents also often introduce limitations, particularly the occurrence of bilateral (complete) injury at undefined timepoints post-exposure, sometimes proving lethal. These limitations led to developing a laser-induced injury model for AKI, characterized by laser-induced cellular death within a localized region of the renal

field, exhibiting a low degree of larval lethality. Controlled laser ablation targeted to the distal tubule in larval zebrafish expressing green fluorescent protein (GFP) in the kidney tubule demonstrated that the repair process is driven by cell migration and is independent of cell proliferation. Although the physiological relevance of laser-induced damage to mammalian AKI is uncertain, the model remains valuable for addressing research questions requiring a highly controlled degree of injury (Cirio et al., 2015; C. S. Johnson et al., 2011a; Palmyre et al., 2014).

Given the relevance of larval zebrafish in high-throughput screening and the current absence of innovative methods for studying regeneration following controlled injury in these setups. I addressed this critical gap in my thesis by developing a high-throughput screening workflow for studying kidney regeneration post-controlled laser-induced injury, eventually aiding in discovering drugs that promote regeneration and offering more profound insights into the regeneration process to explore therapeutic strategies further.

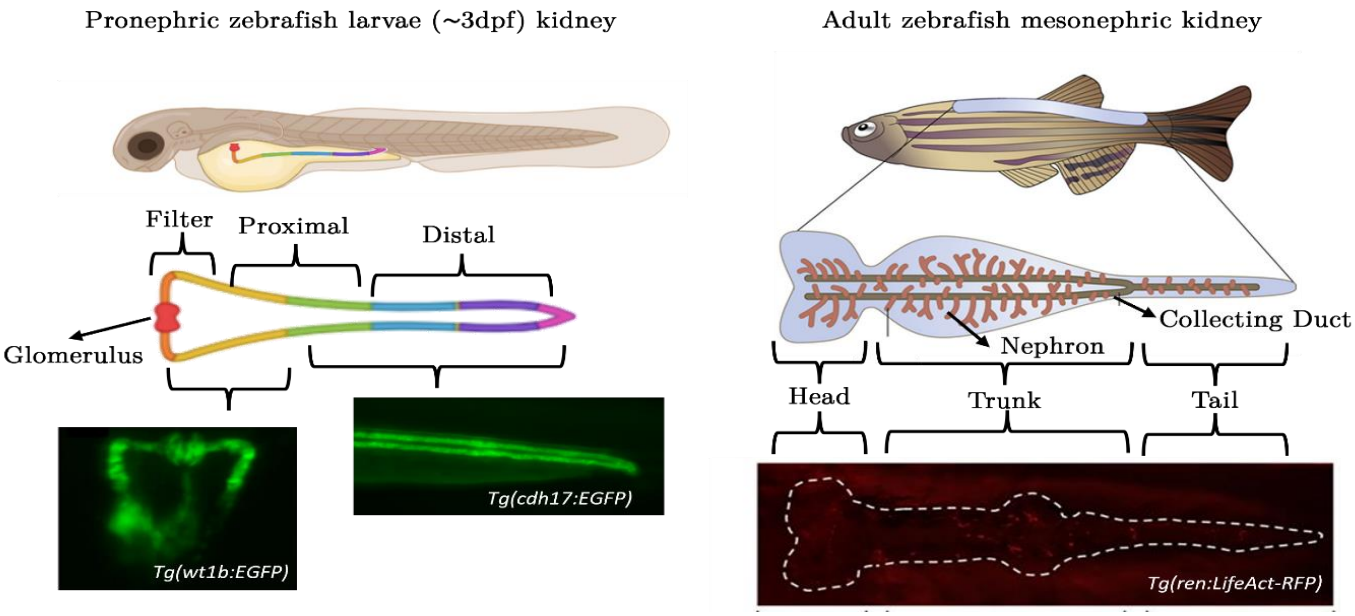

Figure 4: Structural and developmental comparison of zebrafish's larval and adult renal system. This figure depicts the anatomical and functional organization of the zebrafish kidney across two developmental stages, highlighting its utility as a model for renal research. Pronephric kidney (larval stage, ~3 days post-fertilization): The kidney comprises two nephrons with distinct functional segments, including the glomerulus, proximal tubule, and distal tubule. Fluorescent reporter lines illustrate specific features of the pronephros: Tg(wt1b) marks glomerular podocytes, visualizing the filtration structure. Tg(cdh17) labels epithelial cells of the pronephric tubule, highlighting the tubular architecture. Mesonephric kidney (adult stage): The adult zebrafish mesonephros comprises multiple nephrons organized longitudinally along the body axis, including regions corresponding to the head, trunk, and tail. Collecting ducts connect the nephrons for waste excretion. Tg(ren) fluorescently labels actin filaments within kidney structures, emphasizing the cytoskeletal framework of renal tissues. Reproduced from Ding et al., 2015 under Non Commercial (unported, v3.0) License, Hoffmann et al., 2018 under Non Commercial (unported, v4.0) License and Poureetezadi & Wingert, 2016 under Non Commercial (unported, v4.0). Created with BioRender.com

2

Aims and Approaches

The aim of my thesis was to develop solutions for multiplexed time-lapse imaging experiments in zebrafish screening. As a benchmark to address this aim, I established a high-throughput imaging platform to quantify kidney regeneration in zebrafish embryos post-laser-induced injury. To establish the platform, I pursued the following objectives:

1. Establishing a high throughput lasering and imaging workflow for injuring and imaging distal renal tubules in zebrafish embryos.
    - Designing and optimizing mounting strategies.
    - Developing a high throughput laser injury workflow.
    - Establishing an imaging workflow to image regenerating tubules.
    - Developing smart imaging approaches to integrate laser and imaging aspects.

2. Developing computational tools and workflows for image processing and regeneration analysis.
    - Establishing image processing strategies for standardizing, stabilizing, and segmenting the regenerating tubule time-lapses.
    - Developing a computational workflow to detect and track regenerating tubules in an automated manner.
    - Validating the established workflow with manual annotations to verify its robustness.

3. Validating the platform's ability to quantify kidney regeneration dynamics.
    - Investigating kidney regeneration dynamics at different temperatures.
    - Investigating kidney regeneration dynamics with varying DMSO levels.

3

Results

Studies utilizing laser-induced injury to explore kidney regeneration in zebrafish embryos were established recently (C. S. Johnson et al., 2011a). However, it lacked the efficiency and precision required for large-scale quantitative analyses, limiting their applicability in large-scale screens. I developed a novel high-throughput imaging platform to quantify kidney regeneration in zebrafish embryos post-laser-induced injury. While the platform was specific to regeneration studies, in a broader context, I aimed the platform to be a benchmark for multiplexed time-lapse screening solutions in zebrafish embryos. This platform employed laser-induced injury to the distal renal tubules of 3 dpf (days post fertilization) embryos of the *Tg(cdh17:eGFP)* zebrafish line, followed by tracking the regenerating tubule tip over time and determining the closure of the injury gap. While developing the platform, I used a benchmark dataset from an earlier proof-of-concept screening study by J. Heigwer at the University Children's Hospital, University of Heidelberg, Germany, to assess potential caveats and issues. The insights gained from this analysis were considered during the development of the current platform.

The development of the platform primarily centered on fulfilling two principal objectives, which were interdependent and informed by ongoing feedback throughout the process (See the overview Figure 5):

- Establishing a high-throughput workflow for time-lapse imaging of regenerating distal renal tubules post-laser-induced injury.
- Developing an analysis workflow to track and quantify tubule regeneration, offering a reliable approach to evaluate kidney regeneration.

Following the development of the platform, it was validated to evaluate its capacity to identify significant biological changes.

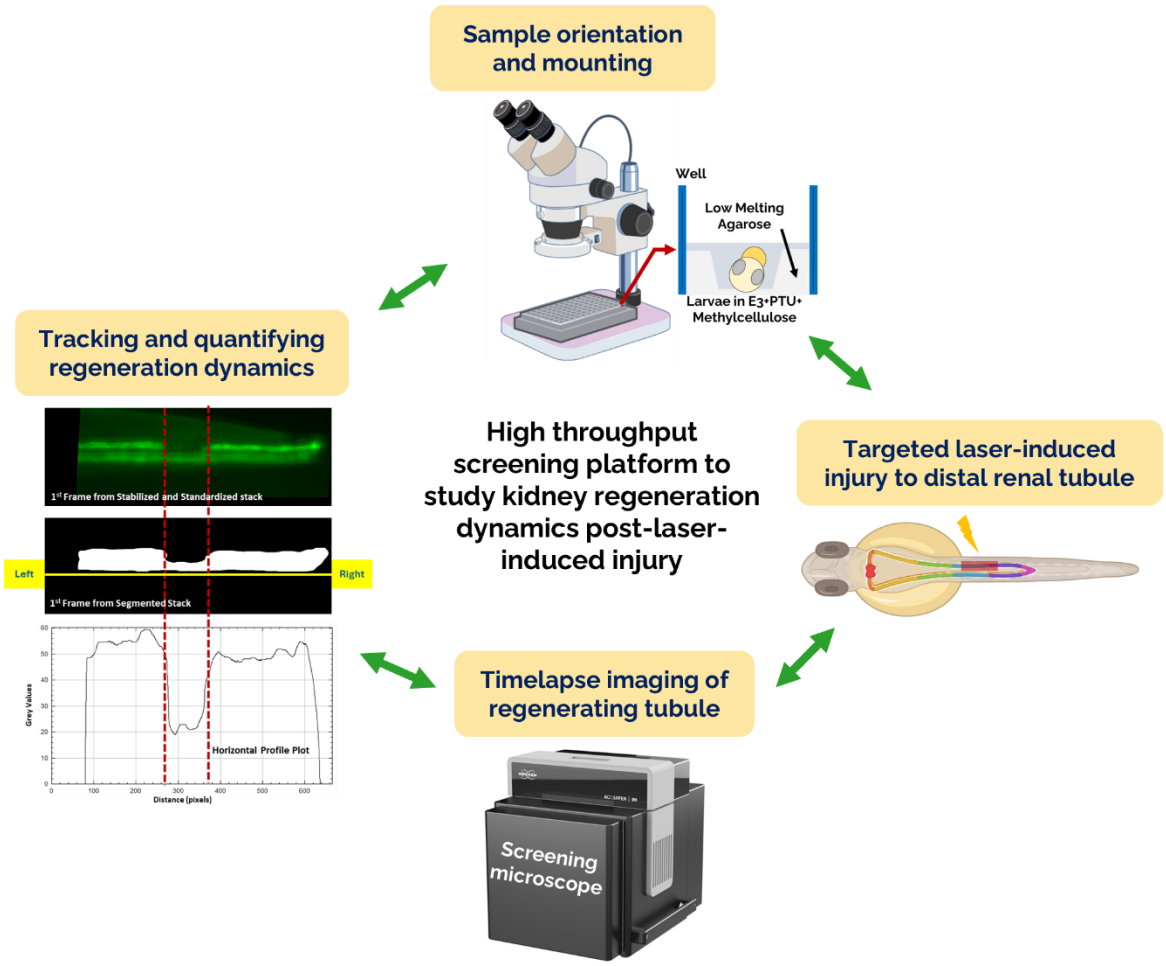

Figure 5: Overview of a high-throughput screening platform for studying kidney regeneration in zebrafish post-laser-induced injury. The schematic represents the key steps in creating the screening platform, from establishing sample orientation and mounting, targeted laser-induced injury to the distal renal tubules, timelapse imaging of regenerating tubules, and finally, tracking and quantifying the regenerating tubule. Each step is connected with a double-headed arrow representing the mutual feedback needed to develop the protocol. Created with BioRender.com

3.1. Developing a high throughput time-lapse imaging workflow to study regenerating distal renal tubules post-laser-induced injury

3.1.1. Evaluating optimal embryo orientation and sample mounting approach

Laser-induced injury to the distal renal tubule, followed by capturing the injured tubule's regeneration dynamics, depends on effective visualization of both distal renal tubules. The efficacy of the induced injury and the resulting acquired images can be severely compromised with suboptimal orientation or instability in sample positioning during imaging. Thus, establishing an optimal orientation and sample mounting approach for the embryos was critical before pursuing more complex experimental developments. I evaluated the ideal orientation of the embryo and sample mounting approach for visualizing GFP-expressing distal renal tubules in zebrafish embryos over long imaging periods.

3.1.1.1. Exploring optimal embryo orientation for visualization of distal renal tubules

Determining the optimal orientation of embryos to achieve clear visualization of the two distal renal tubules for effective laser targeting, followed by subsequent time-lapse imaging, constituted the initial and fundamental step in this investigation. Ensuring reliable and uniform imaging for subsequent steps (laser-induced injury and regeneration time-lapse) is unattainable without optimal orientation. I conducted experiments to assess the most effective and optimal orientation. I prepared imaging plates, as detailed in Section 6.5.1.1., using orientation tools (Wittbrodt et al., 2014) with lateral and dorsal mounts to position the embryos in lateral, dorsal, and tilted dorsal orientations. After that, I captured low-magnification (2x) and high-magnification (20x) images (see Figure 6A).

Upon reviewing the orientations, I determined the lateral orientation (see Figure 6A) was not ideal, as it provided visibility for only one of the two tubules. This limitation compromised the embryo's survival, as it increased the possibility of inadvertently damaging both tubules during the lasering procedure. On the other hand, whilst the dorsal orientation (see Figure 6A) allowed for clear visibility of both tubules, the autofluorescence from the yolk sac extension lowered the contrast and resolution of

the tubules. However, a tilted dorsal orientation (see Figure 6A) resulted in significantly sharper and clearer images of the tubules. Based on these results, I adopted a tilted dorsal orientation of the embryos as the optimal orientation for further workflow development.

3.1.1.2. Examining ideal sample mounting strategy for desired embryo orientation

Maintaining the tilted dorsal orientation was essential for extended imaging periods as it was determined as the ideal orientation for embryo imaging. It was essential to design a mounting strategy to prevent orientation shifts and imaging artifacts caused by poor sample mounting. To identify the ideal sample mounting approach for the long-term acquisition of the tilted dorsal orientation of embryos, I explored three different sample mounting approaches: ZF plate (Hashimoto - HDK-ZFA101-02a), cycloolefin film (Greiner - 655891), and plastic (Greiner - 655101) bottom well plates. In each approach, I oriented the embryos with the tilted dorsal orientation and captured high-magnification images (20x objective) hourly over 12 hours to observe the overall stability of the orientation and output image quality in different setups. In the case of ZF plates, embryos were directly pipetted into the wells and oriented for imaging (see Figure 6B), unlike in cycloolefin film and plastic bottom well plates where the embryos were loaded into wells containing low-melting agarose molds (see Materials and Method Section 6.5.1.2), before the orientation and imaging of the embryos (see Figure 6C).

After reviewing the time-lapses across each specific setup, in the ZF plate mounting approach, I observed that nearly 60% of the sample population deviated from the tilted dorsal orientation, transitioning to a lateral orientation during the time-lapse. While the absence of an agarose mold enabled acquiring sharper images of the tubules, this limitation became substantial, as the consistent, intact orientation of the tubules was not attainable over extended durations with this setup. Moreover, while orienting, I faced challenges due to the limited space within the slits of each well, resulting in damaging the embryos in several instances.

With just 10–15% of embryos experiencing lateral movements, I found that the embryo orientations were constant during the time-lapse in plastic and cycloolefin film bottom well plates. The acquired images on the plastic bottom well plates demonstrated reduced contrast and brightness compared to cycloolefin film bottom

well plates. These results led to choose the cycloolefin film bottom well plate with low-melting agarose molds as the optimum screening setup.

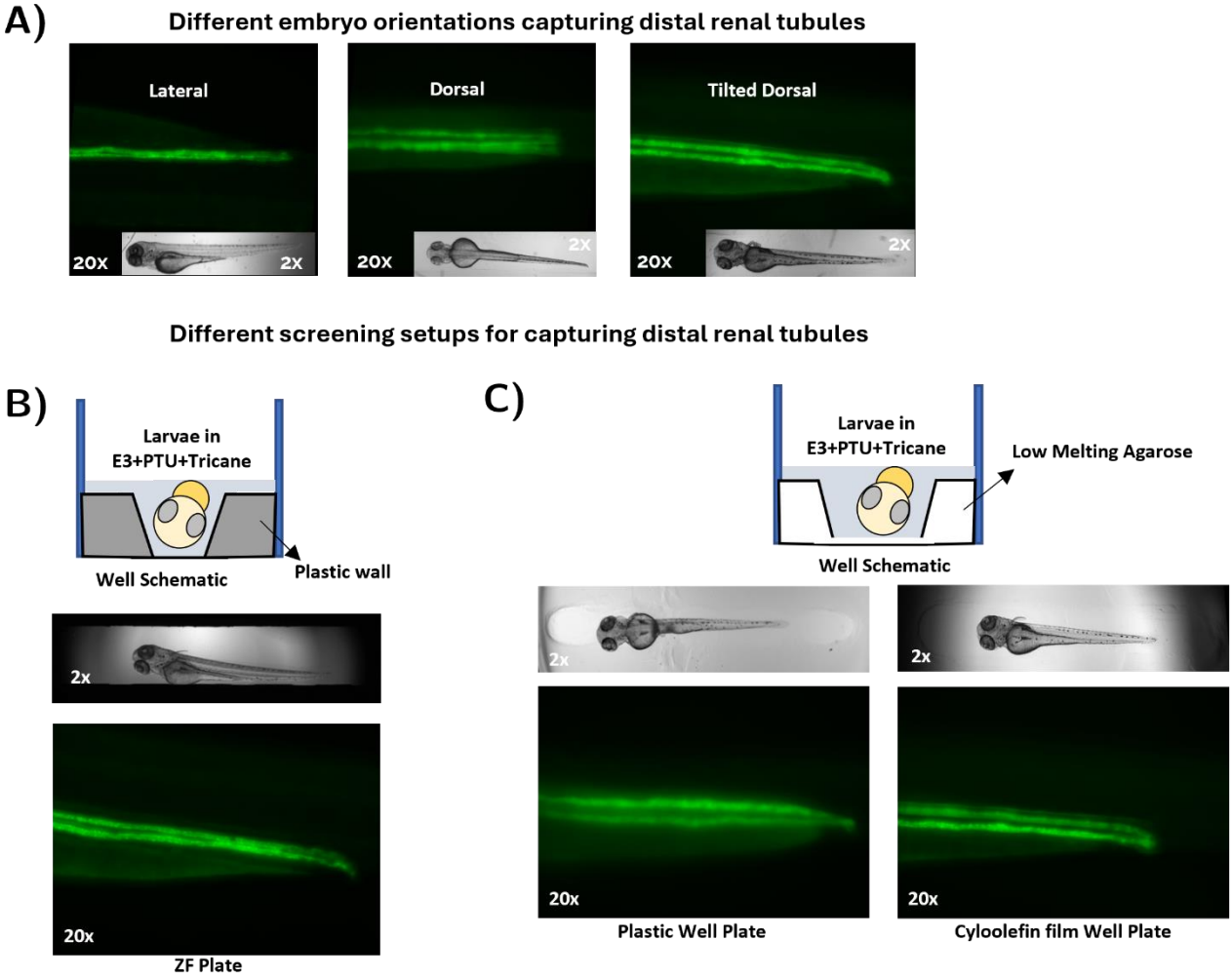

Figure 6: Exploring optimal embryo orientations and screening setups for visualizing distal renal tubules. A) Representative images of zebrafish embryos oriented in lateral, dorsal, and tilted dorsal orientation, captured at both low (2x, Brightfield) and high (20x, Green) magnifications. B) Schematic and imaging outputs of embryos mounted in a ZF plate. C) Schematic and imaging outputs of embryos mounted in plastic and cycloolefin film bottom well plates with low-melting agarose molds

3.1.2. Establishing pre-screen pre-laser workflow for laser-induced injury

After determining and establishing the optimal orientation and screening approach, developing a robust workflow for performing precise laser-induced injury was essential for studying the regeneration of distal renal tubules in zebrafish embryos. This required acquiring high-magnification images of the distal renal tubules to annotate the injury site precisely. I established a pre-screen pre-laser workflow, ensuring a systematic and reproducible approach for obtaining the high-magnification images marking the distal renal tubules.

The workflow began with pre-screen imaging, where embryos oriented on the imaging plate (see Materials and Method Section 6.5.1) were imaged at low magnification using a 2x objective. These prescreen images provided an overview of the embryos within their respective wells, allowing the distal renal tubules to be roughly located and annotated in the region of interest for high-magnification imaging (see Figure 12 A). Using these annotations, high-magnification images of the annotated regions marking the distal renal tubules were acquired using a 20x objective in the subsequent pre-laser step, providing detailed visualization of the tubules (see Figure 12 B). These high-magnification images were critical for precisely annotating the laser injury site and guiding the laser-induced injury process (see Materials and Method Section 6.5.2).

3.1.3. Developing strategies to enhance and optimize laser-induced injury

Precise laser-induced injuries to distal renal tubules are critical for studying regeneration dynamics, as inconsistent or inaccurate injury can compromise experimental reliability. After establishing the pre-screen pre-laser workflow and obtaining high-magnification images marking the distal renal tubules (see Results Section 3.1.2), I established a robust protocol for inducing precise injuries to distal renal tubules using the ACQUIFER IM microscope's photomanipulation module (see Materials and Method Section 6.5.3). The injury site was consistently positioned on the upper tubule at four somites to the left of the urogenital opening as shown in Figure 7A. The experiments involved varied laser power (ranging from 80–100%) with a single iteration (repeats for the laser), to determine the optimal parameters for

inducing injury. Following lasering, embryos were imaged at high magnification to evaluate the extent and accuracy of the induced injury.

Successful laser-induced injury of the tubules was achieved at 80% power, and increasing the power did not significantly improve the results. Additionally, a subset of samples exposed to various laser power settings were collected for histological analysis to verify the injury occurrence (in collaboration with Prof. Jens Westhoff's laboratory, Department of Pediatrics I, University Children's Hospital, Heidelberg, Germany). Histological examination corroborated that the tubules were indeed injured at the 80% power setting, prompting the selection of this parameter for subsequent experiments (see Figure 7B). Nonetheless, a comprehensive qualitative analysis of the post-laser images revealed a 40-45% failure rate in achieving the desired injury, primarily included injury to both tubules, incomplete injury to the targeted tubule, or entirely missing the targeted tubule (See Figure 8). After carefully examining the failed laser attempts, I found that the major cause of failed lasering attempts was due to the embryo movement during the laser process (about 1–2 tubule diameters). These results compelled me to explore techniques to reduce sample mobility and raise the success rate of laser-induced injuries.

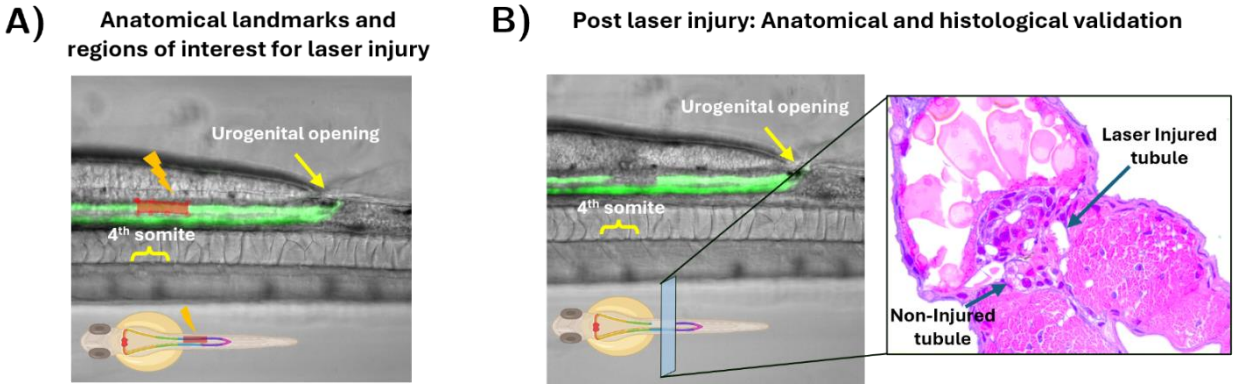

Figure 7: Anatomical landmarks, region of interest, and histological validation for laser-induced injury. A) The figure illustrates the region of interest for laser-induced injury and anatomical landmarks marking it. The ROI is annotated with a red box and is located four somites to the left of the urogenital opening, targeting the upper distal renal tubule. The schematic simplifies the visual depiction of the area of laser-induced injury. B) The left panel features fluorescence microscopy image showing the targeted laser-induced injury at the annotated region and a schematic highlighting the region of injury and transverse section for histological validation. The right panel shows the renal tissue's histological transverse section, confirming the laser injury. Stained sections distinctly show the structural disruption in the injured tubule, while the adjacent tubule remains intact, corroborating the laser-induced injury. The histological validation was done in collaboration with Westhoff Lab. Created with BioRender.com

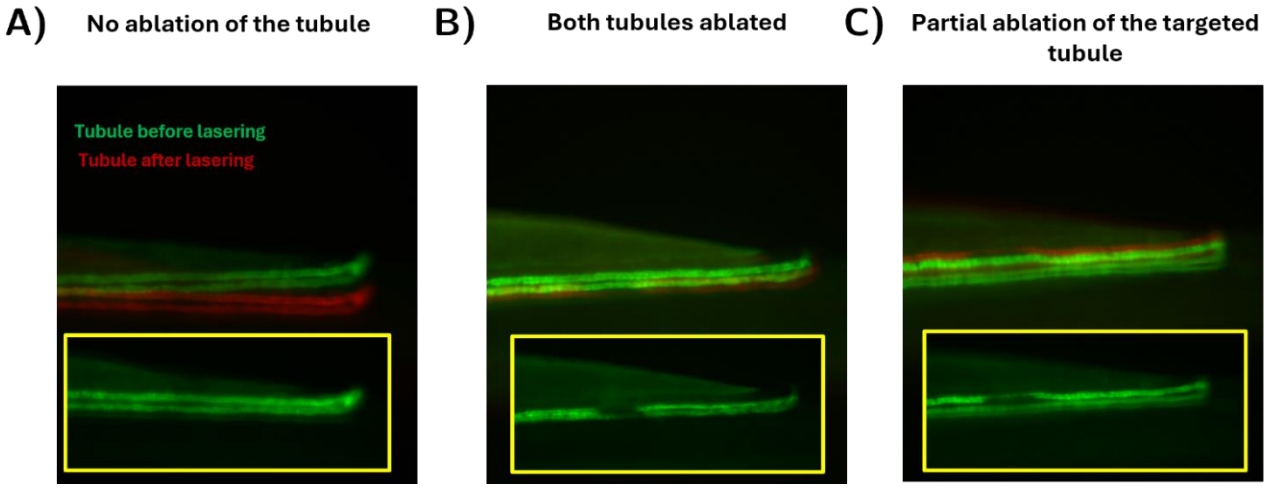

Figure 8: Inconsistencies in laser-induced injury. This figure presents examples of failed laser-induced injuries, characterized by three distinct outcomes: A) absence of ablation, B) injury affecting both tubules, and C) partial ablation of the targeted tubule. Each panel comprises merged images that depict the conditions of the sample before (green) and after (red) the laser application, alongside an inset that illustrates the morphology of the sample post-laser treatment.

3.1.3.1. Fine-tuning mounting media: Exploring anesthetic conditions and methylcellulose for improved sample stability

Accurate laser-induced injury requires precise sample stability during the lasering process. Observations from earlier experiments suggested that embryo movement during lasering (approximately 1–2 tubule diameters) contributed significantly to high failure rates. Within the established orientation and mounting setup, I began to consider how to enhance the stability of the sample. I hypothesized that the sample might be shifting due to inadequate anesthetic (tricaine) conditions—specifically, the sample could move while inflicting damage with the laser. To verify the effect of tricaine on embryo movement, I conducted an experiment using varying concentrations of tricaine, starting with the current concentration of 1.6X and exploring concentrations of 2X, 2.4X, and 3.2X while being careful not to increase them to levels that could harm the embryos.

Despite these modifications, the results showed no appreciable difference, and the incidence of laser injuries stayed high (See Figure 9A). Given these findings, I decided to use a new strategy to improve control over embryo mobility by raising the viscosity of the mounting media. To achieve this, I utilized methylcellulose, a chemically modified cellulose used for mounting (Weber et al., 2014). While standard protocols usually recommend a 3% concentration of methylcellulose for mounting, this level

was excessively viscous for the confined space within each well, which complicated the orientation process. I experimented with concentrations of 0.5%, 1%, and 1.5% methylcellulose per well. However, any concentration above 0.5% proved too viscous to handle and impacted the orientation process. Thus, I proceeded with a 0.5% methylcellulose concentration and experimented to determine if this adjustment would reduce the laser failure rate. The incorporation of methylcellulose reduced the number of samples with failed laser injury, but the overall yield of the assay was still not satisfactory (See Figure 9C).

3.1.3.2. Enhancing laser-induced injury outcomes through temperature modulation and a two-group approach

Embryo movement during laser-induced injury remained a persistent challenge, even after optimizing mounting media and anesthetic conditions. I hypothesized that the movement I observed might result from the embryo's development process and general metabolic activity, which could be beyond the control of anesthesia. I proposed to modify the incubation temperature to 20°C during the lasering process (previously 28°C, typical temperature for zebrafish development) from the moment the plate was positioned in the microscope. The lower temperature results in reduced metabolic activity, which in turn would reduce the movement. The plan involved maintaining the temperature at 20°C during the lasering procedure and restoring it to 28°C after the injury, ensuring that regeneration occurred at the normal temperature (typical temperature for zebrafish development). To assess the impact of this temperature modulation on the success rate of laser injury, I conducted an experiment in which I mounted and oriented the embryos within 0.5% methylcellulose while maintaining the incubation temperature at 20°C. After executing the lasering, I acquired post-laser images to evaluate the effectiveness of this approach. Looking at the post-laser images, I saw notable enhancements and, the failure rate of laser injury decreased from 33% to 13% (See Figure 9C). This demonstrated that temperature modulation effectively enhanced sample stability during lasering and substantially improved the accuracy of laser-induced injuries.

While temperature modulation reduced failure rates, the timespan between acquiring images for lasering, annotating the region for lasering, and performing the laser injury was an hour. This extended timeframe posed a risk of sample movement, as the lasering was based on images already an hour old. To refine the laser injury workflow and enhance the success rate of the laser injury treatment, I proposed a two-group

approach. This approach involved dividing the plate into two groups (as illustrated in Figure 9B), group A (first four rows) and group B (last four rows), and performing the laser treatment on one group at a time. This approach significantly reduced the time required for the entire process (20-25 min per group, from obtaining images for laser annotation to laser treatment) and minimized the chance of sample movement over a short time. By integrating this optimization into the laser injury workflow, I conducted an experiment and observed a notable reduction in laser injury failure rates, which decreased from 13% to 4% (See Figure 9C).

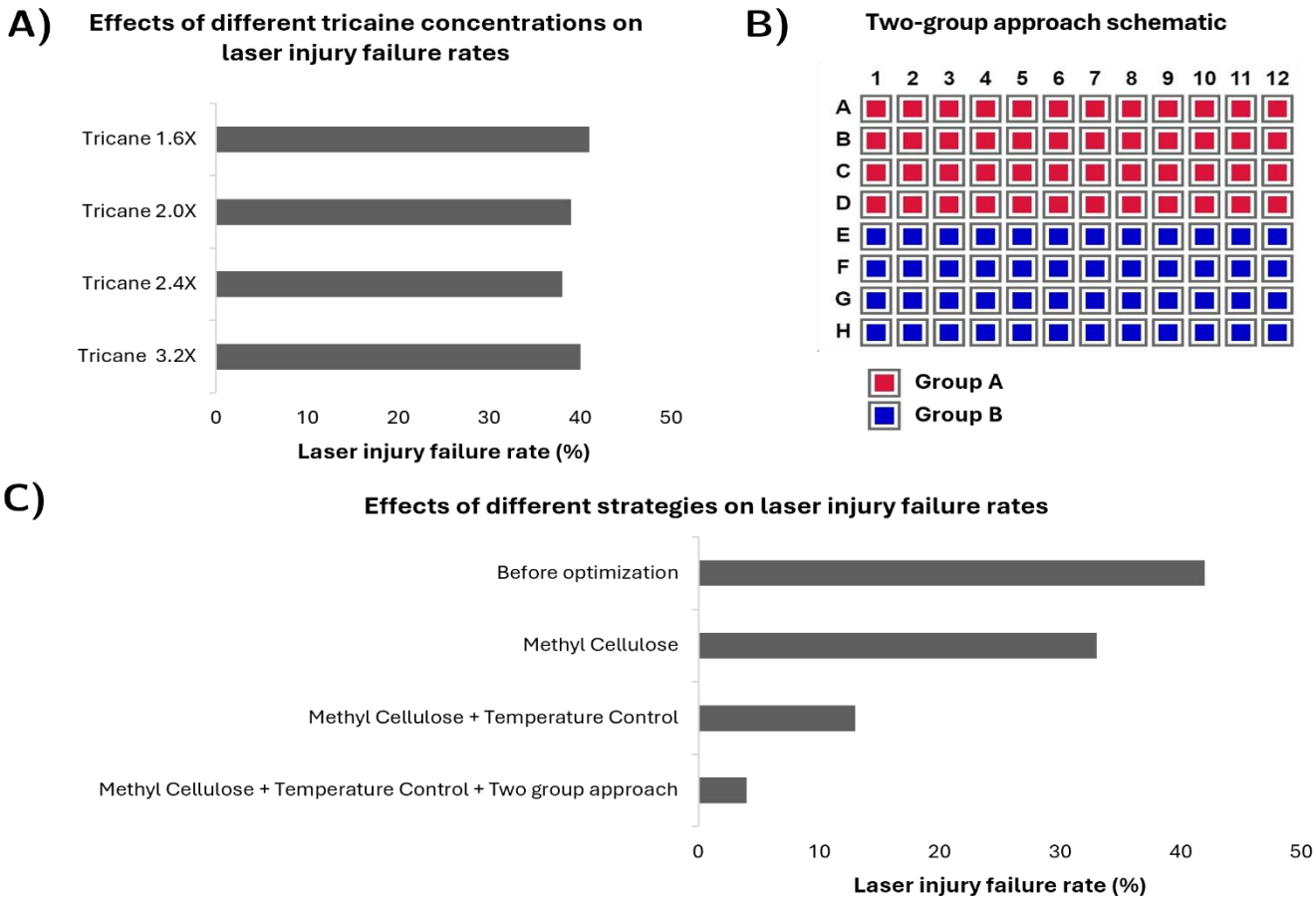

Figure 9: Optimizing laser-induced injury of distal renal tubules in zebrafish embryos. A) Effects of different tricaine concentrations on laser injury failure rates. A bar graph illustrates the failure rates of laser-induced injury at varying concentrations of tricaine from 1.6X- 3.2X; each condition had n=24 N=1. The failure rates for laser injuries in each tricaine concentration were assessed by counting the samples with inconsistencies in the laser-induced injuries and dividing this number by the total samples for each tricaine concentration. Adjustments to anesthetic concentrations showed no significant improvement in reducing laser injury failure rates. B) The schematic diagram visualizes the division of embryos in the screening plate into two groups (Group A: rows A–D; Group B: rows E–H) for sequential lasering (Schematic drawn using https://plateeditor.sourceforge.io/). This approach minimized the time between image acquisition, annotation, and laser treatment, reducing the risk of embryo movement. C) Effects of different strategies on laser injury failure rates. Under different conditions, a bar graph comparing the failure rates of laser-induced injuries; each condition had n=96 N=1. Counting the samples with inconsistent laser-induced injuries and dividing this number by the total samples for every experimental condition determined the failure rates for laser injuries in each of them. Before optimization: The initial protocol shows the highest failure rate (~40%). Methylcellulose: Adding 0.5% methylcellulose reduced failure rates by increasing sample stability. Methylcellulose + Temperature Control: Combining methylcellulose with temperature modulation (20°C during lasering) further reduced failure rates. Methylcellulose + Temperature Control + Two-group approach: The integration of all optimization strategies (methylcellulose, temperature control, and the two-group approach) resulted in the lowest failure rate (~4%), demonstrating the synergistic effect of these improvements on laser-induced injury workflow.

3.1.4.Optimizing long-term imaging of regenerating distal renal tubules

Developing a protocol that ensured reliable, high-quality time-lapse imaging over an extended period was essential to study the regeneration dynamics of distal renal tubules post-laser injury. Long-term imaging is crucial for capturing the progressive changes occurring during regeneration. I established a robust protocol for time-lapse imaging using the ACQUIFER IM microscope (see Materials and Method Section 6.5.2) following the successful induction of laser injury. Time-lapse imaging was initiated one-hour post-laser-induced injury, and for both groups, the entire laser injury process took approximately one hour to complete. The imaging began by setting the microscope temperature to 28°C to ensure regeneration occurred at the normal developmental temperature for zebrafish. Imaging of the regenerating distal renal tubules continued for 12 hours, with images captured every hour. To synchronize the start points of imaging between Group A and Group B, a 30-minute delay was introduced between the two groups. This accounted for the time required to complete the laser injury in Group A before starting with Group B, ensuring that both groups had a simultaneous imaging start while capturing regenerating tubule images.

Imaging a live sample for such an extended period using a single static focal plane was impractical, and adjusting the focal plane before each hourly capture was also not feasible. Thus, I employed a two-step autofocus approach to find the optimal focal plane at each timepoint. The distal renal tubules in the green channel were used as the target for the autofocus due to their well-defined structure and distinct texture. The procedure involved configuring two search ranges: a coarse search range and a fine search range (see Figure 10A). The coarse search range was set according to the sample thickness, while the fine focus range was tailored to the diameter of the tubule (as detailed in Table 8 of the Materials and Methods).

I observed that over 25% of the acquired time-lapses were losing focus (failing to focus on regenerating tubule) intermittently or throughout the time-lapse (see Figure 10D). Careful evaluation of the samples, which lost focus during time-lapse, revealed two primary issues. The autofocus occasionally locked onto agarose particles or dirt introduced during sample preparation, resulting in a loss of sample focus. Secondly, the autofocus failed to correctly identify the fluorescent tubules, focusing instead on non-fluorescent artifacts or other structures. These results prompted me to explore and develop strategies to optimize the autofocus further and mitigate focus loss.

3.1.4.1. Optimizing sample focus using a region of interest-based two-step autofocus approach

I could not maintain precise sample focus during the extended imaging periods using the two-step auto-focus approach. To improve the effectiveness of the current two-step, autofocus approach, I developed an area of interest-based two-step autofocus to enhance the efficacy of the established two-step autofocus approach. It involved defining a subregion of the camera's field of view, enclosing the distal renal tubules, and utilizing it for autofocus (see Figure 10B). The motivation behind this approach was to avoid detecting any other structures (dust, agarose) within the camera's field of view, which typically show a high contrast with the background and would bias the autofocus. Qualitative analysis of the acquired time-lapse data indicated that this refined approach effectively reduced the incidence of focus loss to 10% (see Figure 10D). Still, some samples lost focus across the time-lapse.

3.1.4.2. Enhancing autofocus efficiency by correcting back illumination issues

Despite the significant improvement in focus stability achieved by introducing the region of interest (ROI) for autofocus, a detailed analysis of failure cases revealed a recurring issue. I observed that instead of accurately targeting the renal tubules, the autofocus consistently selected non-fluorescent structures, particularly segments of the notochord, as demonstrated in the Figure 10C. This misidentification happened due to the back illumination from the autofluorescent yolk sac extension, which inadvertently highlighted non-fluorescent structures and led the autofocus to target these nonfluorescent structures.

To counter the back illumination of non-fluorescent structures, I aimed to reduce the overall light exposure on the sample during the autofocus process. This included reducing the exposure time and illumination power during the autofocus process from 20 ms and 20% to 5 ms and 5%, respectively (see Table 7). These adjustments successfully addressed the misidentification issue caused by back illumination. They effectively corrected the back illumination-induced misidentification problem, such that the autofocus always aimed at the fluorescent renal tubules instead of non-fluorescent objects. This optimization reduced the incidence of focus loss during time-lapse imaging from 10% to just 3% (see Figure 10D), hence improving the autofocus robustness.

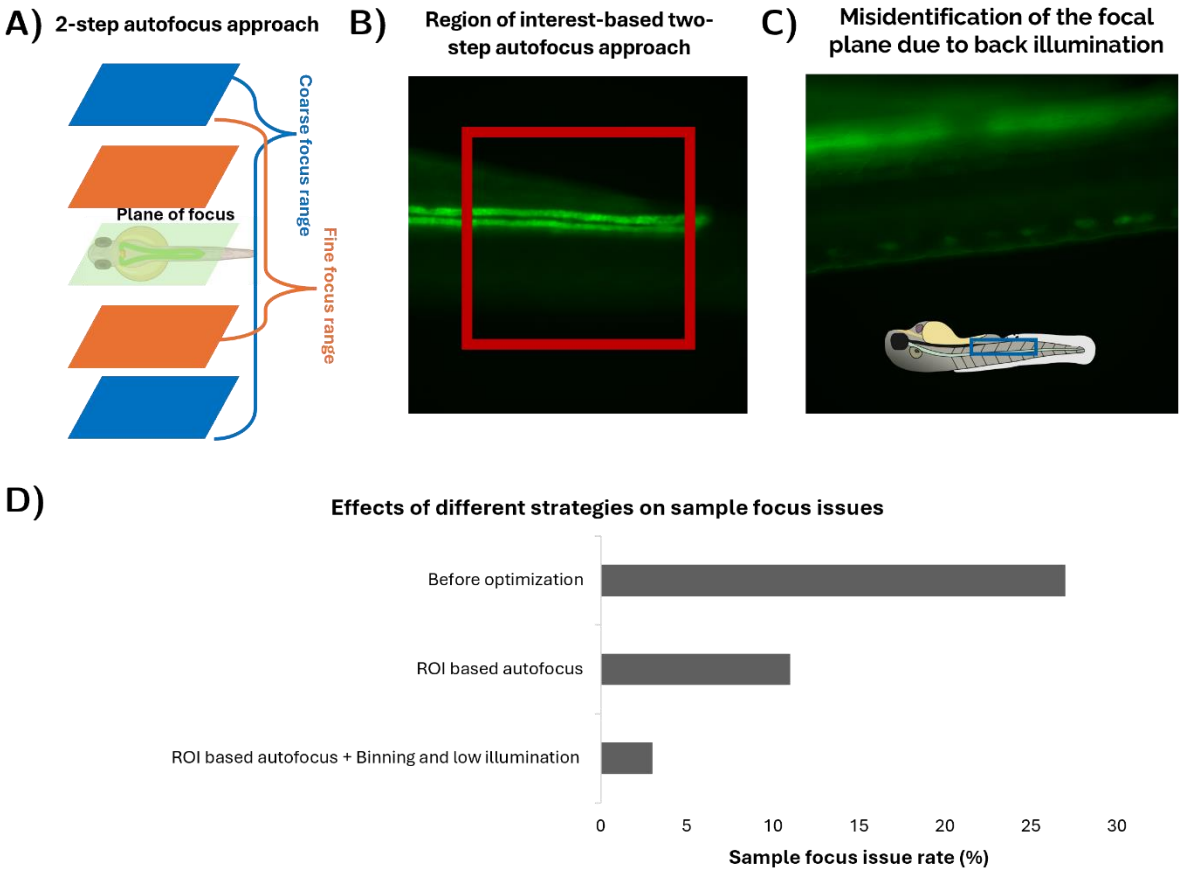

Figure 10: Strategies to optimize long-term imaging of regenerating distal renal tubules. A) Schematic of the two-step autofocus approach. The method involved optimizing two focus ranges a coarse focus range (blue), scanning the entire sample width to identify a broad focal plane, followed by a fine focus range (orange) tailored to the diameter of the distal renal tubule to identify the plane of focus (green). B) The figure illustrates Region of interest (ROI)-based two-step autofocus approach. To enhance autofocus precision, the ROI-based strategy restricted autofocus calculations to a subregion of the field of view (within the red box) containing the distal renal tubule, thereby reducing interference from other structures such as agarose debris or non-relevant areas in the imaging field. C) This figure presents an example of misidentification of the focal plane due to the back illumination of a non-fluorescent structure. The schematic consists of a blue box showing the structure misidentified by the autofocus due to back illumination. D) Effects of different strategies on minimizing focus loss during time-lapse imaging. A bar graph compares the sample focus issue rates under different conditions; each condition had n=96 N=1. The initial setup ("Before optimization") exhibited a high focus issue rate (~25%). Implementing the ROI-based autofocus approach reduced the rate to 10%, and further optimization of illumination settings, including image binning and reduced exposure, lowered the rate to just 3%.

3.1.5. Establishing a computer-guided imaging workflow

Temperature modulation, applying a two-group strategy, laser damage, and subsequent time-lapse imaging of regenerated distal renal tubules, the workflow for laser-induced injury, and subsequent time-lapse imaging of regenerating distal renal tubules comprised multiple complex steps. Although each step was critical for maintaining the quality and accuracy of the workflow, I realized that the overall process was labor-intensive and prone to human error due to its complexity. Given the high degree of intricacy and the repetitive nature of several tasks (especially between the groups), I identified a pressing need to streamline and automate the workflow. I utilized the scripting capabilities of the ACQUIFER IM microscope, which supports customizable smart imaging workflows, enabling the microscope to script each task. As shown in the workflow diagram (see Figure 11), I developed a template script for each task and an overarching Python script that integrated all these respective task scripts and guided users through manual interventions with clear, user-friendly instructions.

The developed script proceeded as follows:

- **Initialization and setup:** The script began by prompting the user to customize the project folder name for data organization.
- **Lower temperature incubation and pre-screen imaging:** The microscope temperature was set to 20°C (see Results Section 3.1.3.2), and the system waited until the target temperature was reached before acquiring pre-screen (2x) images for group A (see Figure 12A).
- **Annotation for high-magnification (20x) acquisition:** After prescreen imaging of group A, the script launched ACQUIFER's plate viewer software for the user to annotate regions of interest for high-magnification imaging in Group A. Based on the annotations, high-magnification images of the distal renal tubules were acquired (see Figure 12B).
- **Annotation for lasering and laser injury execution:** Following the high-magnification imaging of group A, the script launched the plate viewer software to annotate the region for lasering. After annotation, the script executed laser injury for group A (see Figure 12B).
- **Repeating the same steps for Group B.**
- **Normal temperature incubation and time-lapse imaging:** After completing laser injury for both groups, the script restored the microscope temperature to 28°C (normal zebrafish development temperature) for time-lapse imaging.

To synchronize the timeline of capturing the tubule regeneration events across both groups (see Results Section 3.1.3.2), the script also introduced a delay for the time-lapse imaging of the two groups (see Figure 12C).

- **Post-screen acquisition and max projection (across Z axis) of the time-lapses:** Upon completion of the time-lapse imaging, the script acquired post-screen images using 2x objective to validate the health of the embryos. After the acquisition processes, the script generated for each timepoint a maximum intensity projection (MIP) of the Z-stack . This allowed capturing tubules that spanned across z-planes due to their thickness and curvature, thereby enhancing the signal clarity of the tubules while reducing background noise. After max projecting the script efficiently transferred all the acquired data and MIP time-lapses from the imaging PC to the external hard drives.

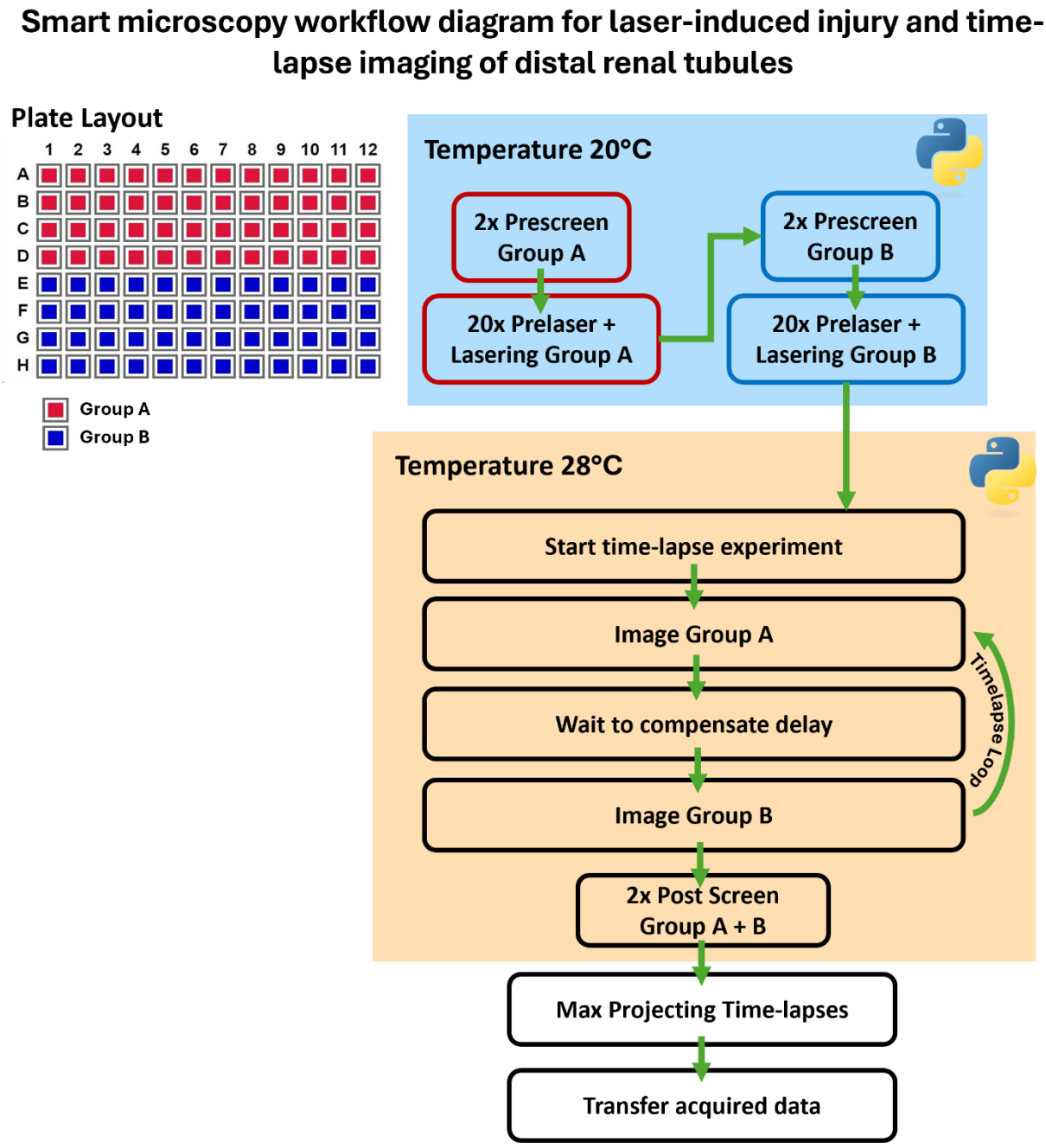

Figure 11: Computer-guided imaging workflow for laser-induced injury and time-lapse imaging of distal renal tubules. This schematic illustrates the step-by-step smart microscopy workflow developed to streamline the complex protocol of laser-induced injury and subsequent time-lapse imaging of regenerating distal renal tubules in zebrafish embryos.

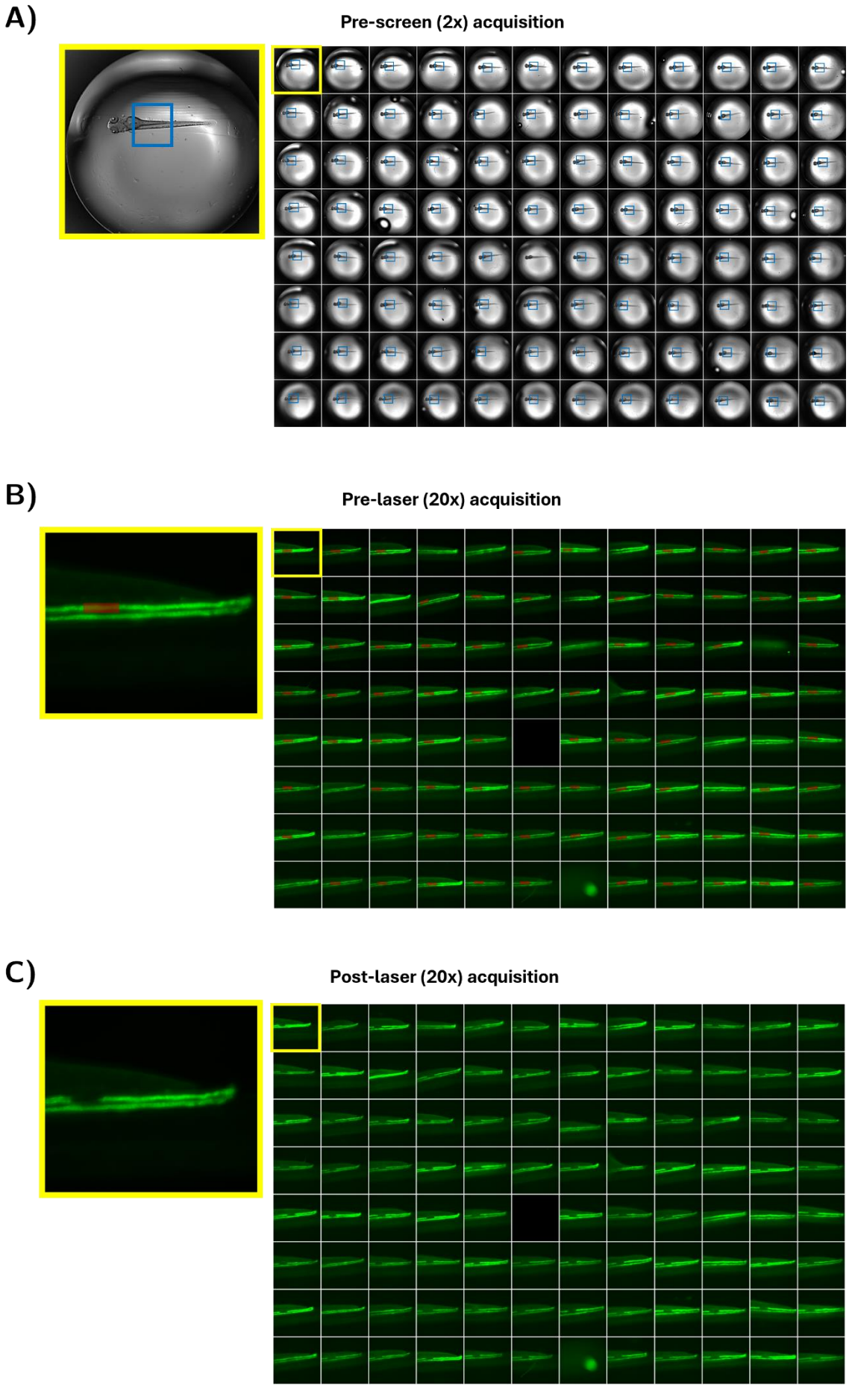
A)
Pre-screen (2x) acquisition
B)
Pre-laser (20x) acquisition
C)
Post-laser (20x) acquisition

Figure 12: High-throughput workflow for laser-induced injury and time-lapse imaging of distal renal tubules. A) This panel shows the low-magnification pre-screening images (merged groups A and B) from a 96-well plate, with images acquired at 2x magnification and annotated region of interest for subsequent high- magnification imaging steps. The left image highlights a representative embryo in its well, with the blue box denoting the annotated region of interest for higher- magnification imaging. B) This panel depicts a montage of pre-laser images (merged groups A and B) across the plate, demonstrating consistent high- magnification (20x objective) imaging of the renal tubules with annotated regions of injury for lasering. The left image shows a close-up of a selected distal renal tubule with a red box denoting the annotated region of injury for lasering. C) This panel presents a montage of time-lapse images first-time point (merged groups A and B) acquired hourly for a specific embryo, illustrating the regeneration progression over 12 hours at 20x magnification. The left image highlights a representative regenerating tubule

3.2. Virtual Orientation Tools (VOTj): Fiji plugins for object centering and alignment

Tilted dorsal orientation of zebrafish embryos was crucial for laser-induced injury and subsequent time-lapse imaging of regenerating distal renal tubules. This orientation ensured the visibility of both tubules within the kidney (see Results Section 3.1.1). The tubules have a longitudinal structure and having them aligned with the horizontal axis of the image would facilitate the subsequent quantification of regenerating tubules. However, the tilted positioning of the embryos led to a corresponding rotational deviation in the distal renal tubules observed in the acquired images (Figure 12B and C). The tilt caused an important constraint in measuring the regeneration of the distal renal tubules, as the extent of tilt differed among samples due to variations in embryo shape, resulting in a lack of uniformity among samples. Correcting this tilt during mounting was impractical, as the assay required a tilted orientation for proper imaging; images would thus need to be virtual/digitally realigned after the acquisition. Manually rotating the images for each sample would be labor-intensive and susceptible to inconsistency. Realizing the lack of solutions to resolve these challenges and to build automated solutions to streamline and standardize the post-acquisition alignment of distal renal tubules across datasets I developed the "Virtual Orientation Tools (VOTj)", a suite of plugins for the Fiji/ImageJ platform. VOTj facilitated the automated alignment and centering of an elongated object of interest in images along a vertical or horizontal orientation. I have detailed the development and application of VOTj in a peer-reviewed publication (Satheesan et al., 2024). I also established a dedicated GitHub repository that offers detailed instructions for obtaining and using the tool (https://github.com/sankeert1999/Virtual-Orientation-Tools-VOTj).

3.2.1.Virtual Orientation Tools (VOTj): Features, applications and workflow integration

The plugin employed Principal Component Analysis (PCA) to compute the necessary translation and rotation for aligning the object along a vertical or horizontal axis, utilizing the annotation/mask. The images were aligned based on the computed translation and rotation factors, leading to a uniform and standardized orientation across the dataset. To provide a user-friendly interface, I developed a VOTj GUI (see Figure 14D) to guide users through multiple configuration steps, including selecting the input image, providing the mask/annotation, and configuring the

alignment setting (see Figure 14A-D). As mentioned above, the tool accepted either mask or annotation. Accordingly, I included two different methods for the alignment:

- **Mask-assisted alignment:** prompted users to select the input image and its associated binary mask outlining the object (see Figure 14C).
- **Annotation-assisted alignment:** prompted the users to annotate the object of interest directly on the input image using the Fiji brush tool (see Figure 14B).

I integrated three operating modes in the plugins to ensure flexibility and adaptation for different alignments:

- **Centering:** Calculate the object's center of interest and translate it to the image center.
- **Alignment (Horizontal/Vertical):** Determining the center and base orientation of the object of interest and calculating the necessary rotation angle to align the object of interest.
- **Centering and Alignment:** Determining the center and base orientation of the object of interest and calculating the necessary translation and rotation angle to center and align the object of interest.

Naturally, the elongated objects mostly exhibit directionality (head/tail, top/bottom); this motivated me to include an additional option for specifying the intended alignment direction apart from the axis of alignment (horizontal/vertical). The plugin automatically orients the object in the closest direction if the alignment direction is not specified. To handle possible problems of losing the original image region departing the original image canvas during translation and rotation, I included a function to enlarge the output image canvas (see Figure 14F).

I implemented two operational modes for the VOTj plugins, single and batch, allowing users to align individual images or entire image folders. Figure 13A illustrates the application of VOTj's batch mode for the alignment of zebrafish embryos in a 96-well plate (subset), which resulted in uniform position and alignment of the embryos. Due to the inherent asymmetry of the zebrafish, which contributes to their natural directionality (head-tail), VOTj's directional alignment feature was employed to ensure that the heads of the embryos consistently faced left, as illustrated in Figure 13A. Although the plugin is primarily designed to align a single object within each image, the alignment also extends across multiple dimensions. For instance, in time-lapse imaging, each timepoint is aligned independently, whereas

channels and Z slices are typically aligned using the same transformation, as depicted in Figure 13B and C.

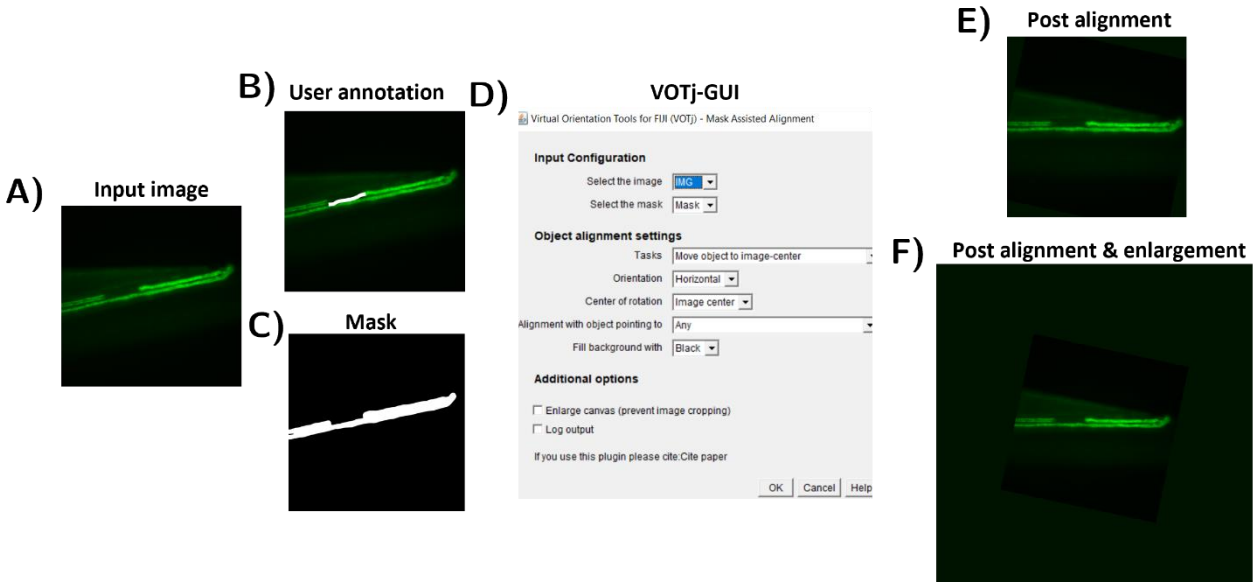

Figure 14: Virtual Orientation Tool (VOTj) workflow overview. A) Input image of distal renal tubule post-laser-induced injury. B) User annotation applied to highlight the object of interest (distal renal tubules) using the Fiji brush tool for annotation-assisted alignment. C) Binary mask outlining the object (distal renal tubules) for mask-assisted alignment. D) VOTj graphical user interface with configurable settings, users can choose the axis of alignment (horizontal or vertical), alignment method—centering, alignment, or both—operational mode, and enlarging the image canvas. E) Resulting image after applying alignment transformations to align the object along the desired axis. F) Resulting image post-alignment with an enlarged canvas to retain the original image regions, avoiding cropping during translation or rotation.

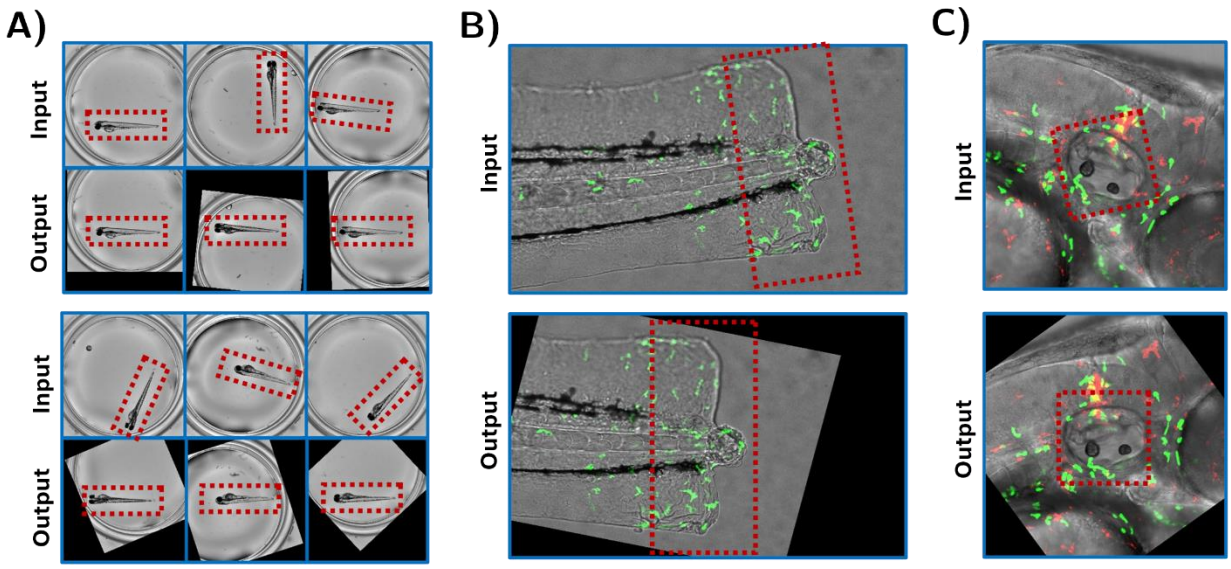

Figure 13: Virtual Orientation Tools (VOTj): Application overview. A) Illustrative subset of zebrafish embryos imaged in a 96-well plate. These embryos were oriented randomly without using any dedicated mounting methods. Images of the embryos were aligned using VOTj. (B-C) The tool can be used to align various samples and is compatible with multi-dimensional images such as Z-stacks and time-lapse images, as shown in (B, C) for the alignment of fluorescently labeled zebrafish embryos along their site of injury and otic vesicle, respectively.

3.3. Establishing an image processing workflow for stabilizing and segmenting regenerating tubules

Quantifying dynamic biological processes like the regeneration of distal renal tubules involves detecting and tracking the tubule growth over time (See Figure 5). This demands that the regenerating tubules within the acquired images are stable and aligned throughout the time-lapse across the sample space. However, imaging live specimens often introduces several challenges post-acquisition, including variability in embryo orientation, misalignment across frames in time-lapse sequences, and difficulties in localizing regions of interest for analysis. I also noted similar issues within the acquired regenerating tubule time-lapse. I established an integrated automated image processing workflow within FIJI to address these issues, which consisted of two individual pipelines (see materials and methods Section 6.5.4.1.) designed to stabilize and standardize time-lapses followed by segmenting the regenerating tubules from the stabilized time-lapses.

The pipelines prompted a GUI guiding users through multiple configuration steps, starting with selecting the max projected time-lapse folder as input and then processing each time-lapse. The pipeline dedicated to stabilizing and standardizing the time-lapse integrated three core image processing steps:

- Template matching-based stack alignment.
- Stack registration-based refinement of the alignment.
- VOTj-based injury centring and orientation of the injury along a uniform axis (Horizontal axis).

After stabilizing and standardizing the time-lapse, the pipeline dedicated to segmenting the tubules detected and segmented the tubules.

In the following subsections, I describe each pipeline component in detail, along with its implementation and impact on the quality of the imaging workflow.

3.3.1.Stack registration-based stack alignment

Initially, I aimed to stabilize the regenerating tubule time-lapse by resolving the movement artifacts and misalignment across the time-lapse. I used a stack registration-based approach using the Stackreg plugin created by (Thevenaz et al., 1998). The alignment process involved a pixel-by-pixel recursive registration of each frame to the upcoming frame. The accuracy of the alignment depended upon the optimal reference frame (the first frame being used for registration). I evaluated multiple choices using the time-lapse's mid-point, end, and beginning frame as the reference. Since the initial frame gave a constant basis for stabilizing the sequence from the beginning of the regeneration process, I chose it as the reference frame for alignment.

After stack alignment, I compared the standard deviation projections of the time-lapses before and after applying stack alignment (See Figure 15A-B). I observed that the approach reduced the movement and alignment artifacts, but misalignments persisted within the tubule regions. Additionally, as I applied stack registration (pixel-by-pixel alignment) on the raw image (2048x2048 pixels), the computation time for aligning each stack was significantly high. I explored other alternatives to enhance the stabilization and reduce the processing time.

3.3.2.Template matching based stack alignment and stack registration-based refinement

I observed that stack registration could not mitigate the issues completely, so I employed a template matching-based approach, utilizing a previously developed Fiji plugin (Thomas & Gehrig, 2020a). Template matching correlates an input template image with image regions to detect the desired region across the target images/stack. The critical aspect of the template matching-based approach was selecting the optimal template image for searching across the time-lapse. I initially attempted to create a generic set of template images derived from multiple time-lapses, to be used universally across experiments. However, the heterogeneity of the samples led to frequent misdetections. Thereby, I adopted a time-lapse-specific template selection approach, where a template was extracted individually for each time-lapse rather than applying a generalized template across datasets. I tested different template dimensions (to accommodate large drifts) and the optimum timeframe. Despite being relatively large, I determined that the first timeframe with a dimension of 1748x1748 pixels gave me the best results. After template matching-based stack alignment, I

compared the before and after standard deviation projections post-template matching and found that template matching also provided results similar to the stack registration-based approach (See Figure 15A-C). As an alternative approach, I considered combining these approaches: template matching-based stack alignment followed by stack registration-based refinement. This dual-step approach produced the most optimal results, where motion artifacts were limited only to the injury region, which was expected due to tubule regeneration dynamics (See Figure 15D). Additionally, I observed that stack registration's processing time for each time-lapse was lower as it was performed on smaller, localized images, further enhancing processing efficiency.

After establishing these methods, I developed a macro representing the stabilizing and standardization pipeline to implement these approaches. The macro started with a GUI prompt to upload the acquired max projected time-lapse data. To streamline the template generation process, I automated it by cropping a 1748 × 1748 pixel region centered on the field of view of the first timepoint of the acquired max projected time-lapse (See Figure 16A). The subsequent processing steps included template matching-based alignment followed by stack registration-based refinement, generating a 1748x1748 pixels sized stabilized time-lapse (See Figure 16B).

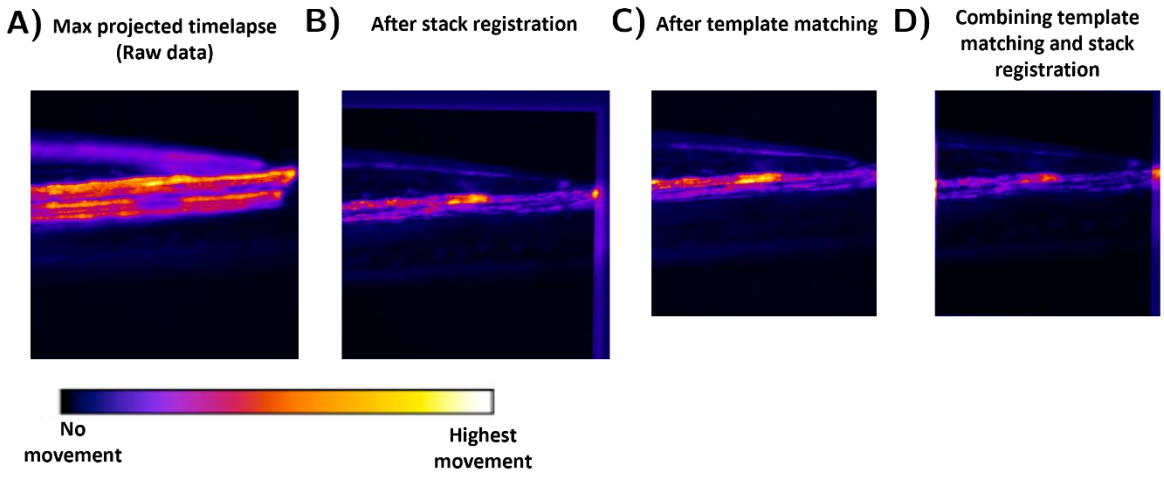

Figure 15: Representative standard deviation projection maps across the time-lapses after different stabilization approaches. A) Max projected timelapse, showing inherent alignment issues. B) The stack registration resolved it, but alignment issues were still near the tubule regions. C) Template matching also showed similar alignment results to stack registration. D) Combining both approaches gave optimum alignment.

3.3.3. Virtual Orientation Tool (VOTj)-based object alignment

The tilted dorsal orientation of the embryos, as discussed in the results of Section 3.1.1.1, led to a corresponding tilt in the acquired images of the regenerating tubules. Orienting the regenerating tubules to a uniform axis was necessary to ensure that regeneration of the injury was visualized along a consistent axis across the time-lapse and samples. The downstream quantifications, such as edge tracking and regeneration measurements, would be prone to errors caused by variability in the orientations. After successfully stabilizing the time-lapses, I aimed to center and orient the injury to a uniform axis as the next step within the stabilizing and standardizing pipeline.

I identified that orienting the tubules along a horizontal axis was a straightforward approach, as it allowed for analyzing the regeneration process as an injury gap being filled horizontally. To achieve this, I employed the Virtual Orientation Tool (See Results Section 3.2.) to center and orient the injury within the regenerating tubule. The virtual orientation tool was utilized in a two-step manner as a first step, the regenerating tubules were centered based on user annotations of the injury site in the initial frame of each time-lapse (See Figure 16C). Centering on the injury ensured consistency across the time-lapse and all samples, which also aided the downstream analysis (see Results Section 3.4.2). As the next step to orient the regenerating tubules, I developed an automated segmentation routine to compute masks (See Figure 16C) representing the regenerating tubule. Using the generated masks, VOTj oriented the regenerating tubules horizontally within the centered time-lapse stack. I implemented each step of the virtual orientation tool in the pipeline seamlessly, with clear prompts and annotations guiding the user. (See Figure 16C).

Following the centering and alignment of the regenerating tubule, the final step in the image-processing pipeline for stabilizing and standardizing the time-lapse involved cropping the time-lapse stacks to a fixed size (frames divided into three parts, with the middle section containing the regenerating tubules extracted). The Figure 17 illustrates the comparison of the time-lapse stacks before (See Figure 17A) and after (See Figure 17B) processing within a 96-well plate format, showcasing the pipeline's effectiveness in stabilizing and standardizing the datasets.

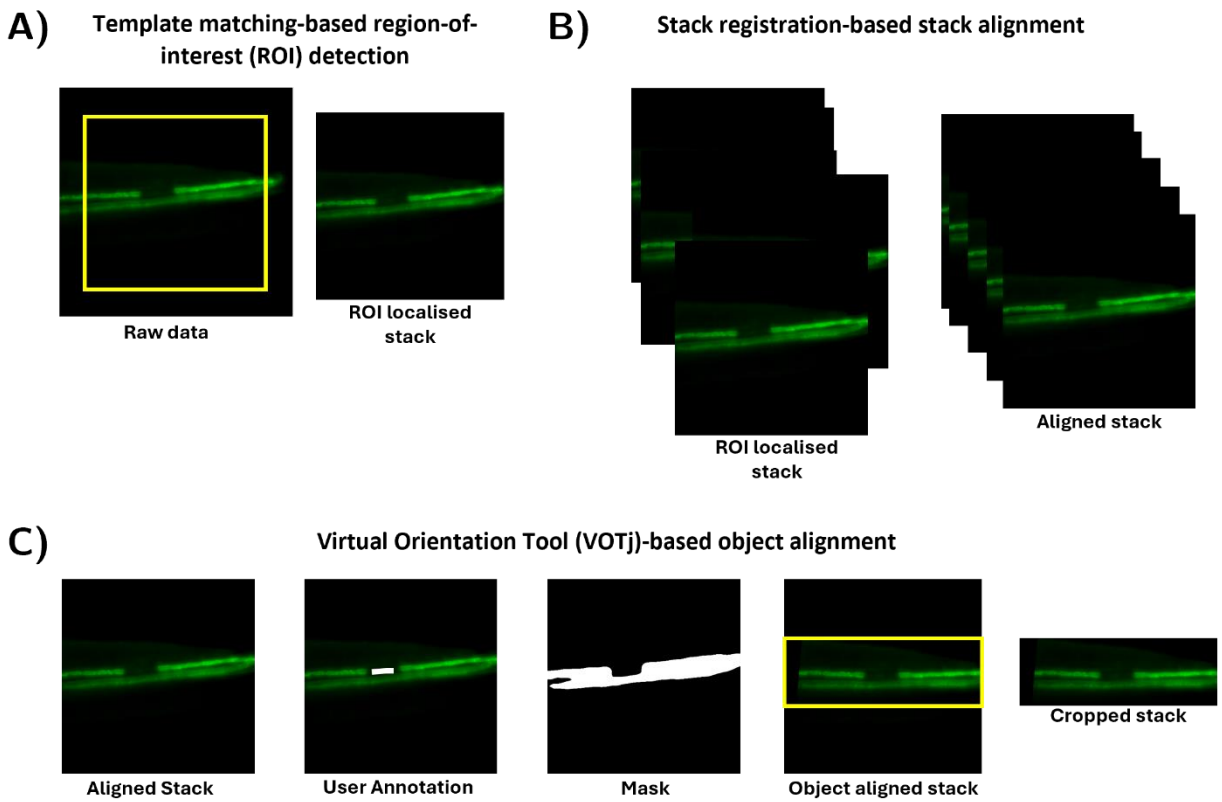

Figure 16: Overview of image processing pipeline for stabilizing and standardizing time-lapses. A) Template matching based stack alignment. This panel depicts the overview of the template matching-based stack alignment, where the yellow box represents the automatically generated template utilized for it. B) Stack registration-based refinement. After stabilizing the timelpases using template matching, the alignment was further refined using stack registration. C) Virtual orientation tool (VOTj) based injury cantering and orientation. After aligning the timelpases, VOTj was utilized in a two-step manner to standardize it. The injury was centered using a user annotation-based centering where the injury region in the first time frame of the timelapse was marked across the dataset, followed by mask-assisted orientation of the injury to a uniform axis. Finally, the stabilized and standardized stack was cropped to ensure that only the regenerating tubule region was retained for further analysis.

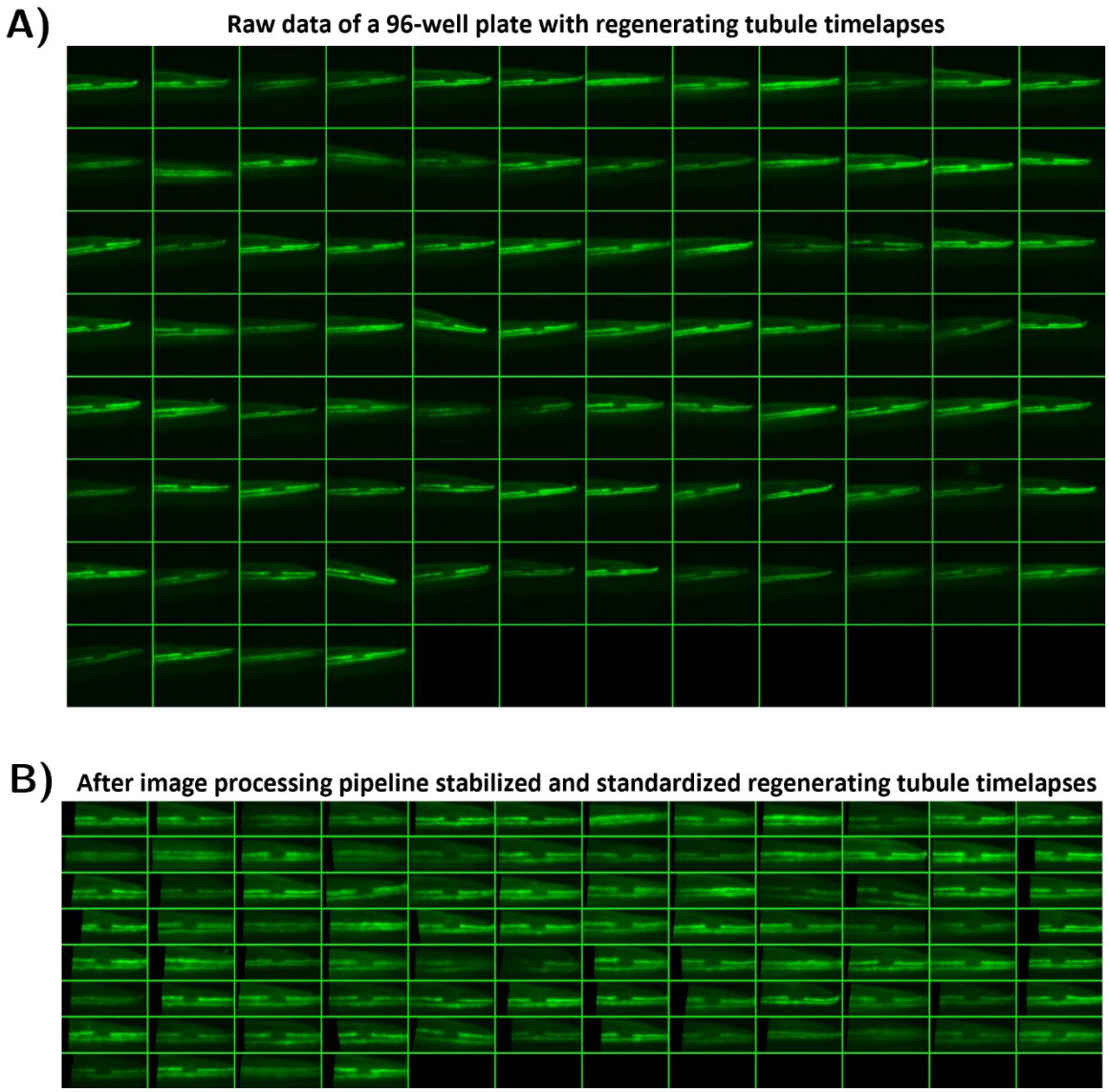

Figure 17: Overview of the effects of the image processing pipeline dedicated to stabilizing and standardizing the time-lapses. A) Raw Data of a 96-well Plate with Regenerating Tubule Time-lapses. This panel displays the initial raw data captured from a 96-well plate, each well containing time-lapse imaging of regenerating distal renal tubules. The images show the variability in positioning and alignment due to the inherent movements of the embryos during live imaging. B) After Image Processing Pipeline Stabilized and Standardized Regenerating Tubule Time-lapses. This panel showcases the same 96-well plate after applying the image processing pipeline. Including template matching for consistent region-of-interest detection, stack registration to correct for frame-to-frame drift, and the application of the Virtual Orientation Tool for uniform orientation of the tubules. The resulting images are aligned, centered, and standardized across all wells.

3.3.4. Establishing a segmentation pipeline to identify regenerating tubules

Following the stabilization and standardization of the regenerating tubule time-lapse, the critical next step was segmenting these structures. This step is crucial for delineating the injury and edges of the regenerating tubules across the time-lapse. Precise segmentation is essential for accurate quantification of tubule regeneration over time. To build a segmentation pipeline, I initially started with the dataset acquired previously by the collaborators. I employed a conventional intensity-based threshold segmentation method using FIJI. I developed a custom macro (see materials and methods Section 6.5.4.1.) that executed several preprocessing steps, including mean blurring and background subtraction, to enhance the visibility of the regenerating tubules, followed by applying a threshold to separate these tubules from the background. Due to the poor signal-to-noise ratio inherent in the earlier datasets, I noted over-segmentation. Accurate longitudinal analysis was challenging, as the segmentation errors led to disruptions in the continuity of the tubule structures across the time-lapse

I explored a machine learning-based image segmentation technique to resolve these potential issues. Utilizing Ilastik, an interactive machine-learning tool, I trained a pixel classifier (see materials and methods Section 6.5.4.2) on a set of manually annotated images (See Figure 18A). This method required creating user-defined classes for the foreground (regenerating tubules) and background regions and leveraged complex computed features from these annotations to achieve accurate segmentation. I found that the machine learning approach adapted more effectively to the variability and complexity of the image data and provided better segmentation results.

The improvements in imaging techniques and data standardization provided an opportunity to reevaluate the initial threshold-based segmentation approach. Given the enhanced image quality and consistency, I revisited the intensity-based threshold method and found that it was providing satisfactory results. The refined imaging conditions reduced the previous over-segmentation complications (See Figure 18C-D), which led me to favor this approach for segmenting regenerating tubules over the machine learning method, as it was simpler and less computationally intensive.

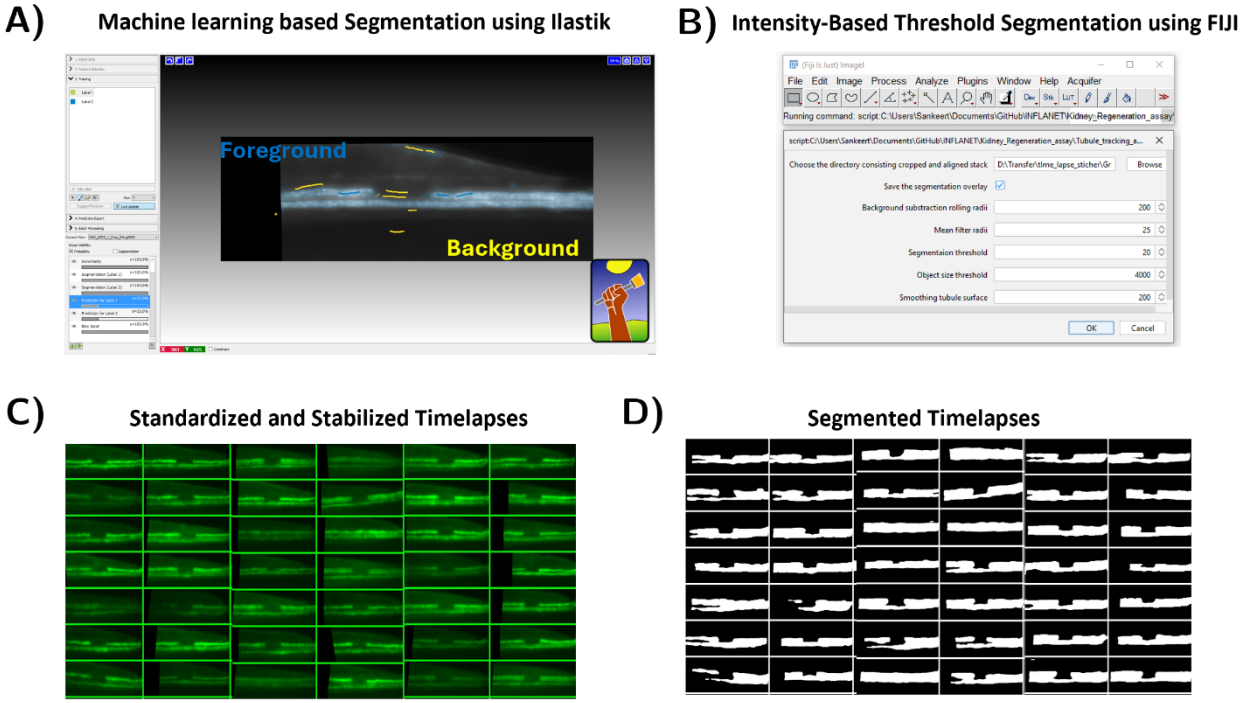

Figure 18: Establishing a segmentation pipeline for regenerating tubules. A) Machine Learning-based Segmentation using Ilastik. This panel shows applying a machine learning-based segmentation method using Ilastik, illustrating the interactive interface and segmentation preview. The method involves training a pixel classifier to distinguish between foreground (regenerating tubules) in blue and background in yellow based on manually annotated images. B) Intensity-Based Threshold Segmentation using FIJI. This panel depicts the Graphical User Interface for the intensity-based threshold segmentation method within the FIJI software interface, highlighting the settings used for thresholding. C) Standardized and Stabilized Time-lapses. This panel displays a subset of stabilized and standardized time-lapse images across the 96-well plate, ready for subsequent accurate segmentation. D) Segmented time-lapses. The final panel shows the outcome of the intensity-based threshold segmentation using FIJI of the stabilized and standardized images in panel C

As detailed above, the segmentation of regenerating tubules resulted in the segmentation masks of the regenerating tubules. I identified that the next critical step for analyzing the regenerating tubules was to engineer an approach to detect the injury over time within the segmented mask images. Ideally, it would mean detecting the regenerating tubule edges, which is essential for measuring the dynamics of tubule regeneration, including changes in the length of the injury gap over time.

To effectively identify the edges of the regenerating tubules, I designed a method using intensity profiles, also known as profile plots (See Figure 19C). These 2D graphs show pixel intensities along a designated line inside the image; the x-axis shows the position along the line, and the y-axis shows the intensity values. The profile plots can be vertical and horizontal, here I derived an average horizontal profile for the entire region of the segmented masks. Within these profiles, the injury site typically appears as a distinctive dip in intensity followed by a subsequent peak. This dip indicates the left edge, while the peak marks the right edge of the regenerating tubule (See Figure 19A, B, C).

After segmenting the stabilized and standardized time-lapse stacks, I obtained the horizontal profile plot for each frame within a stack and recorded it in a CSV file. Each column in the CSV file represented the profile data of each time point, which I exported for further processing, including the detection and tracking of the regenerating edges. I integrated the profile plot computation and exporting within the segmentation pipeline.

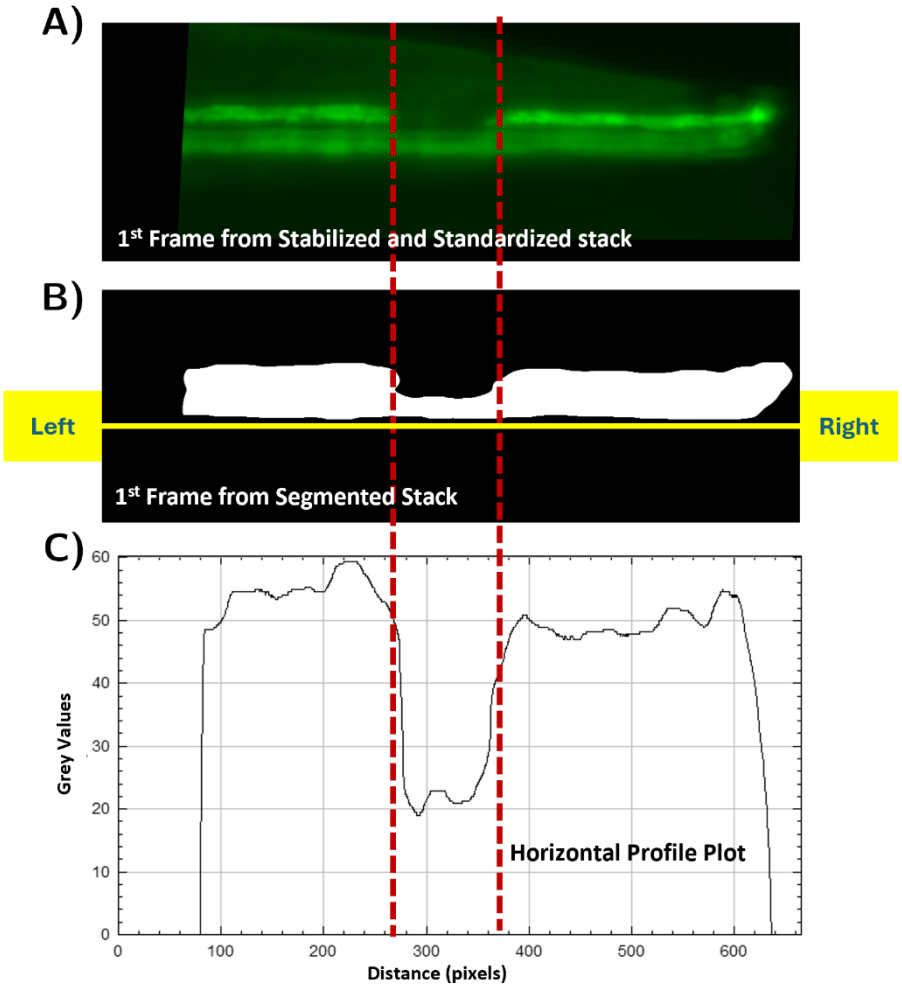

Figure 19: Analyzing regeneration dynamics through horizontal profile plots. A) Stabilized and Standardized First Frame from Time-lapse Stack. This panel displays the first frame from a stabilized and standardized stack of regenerating tubules. B) Segmented First Frame. This panel shows the corresponding segmented mask, emphasizing the regenerating tubule. C) Horizontal Profile Plot. The bottom panel depicts a horizontal profile plot derived from the segmented mask. This plot illustrates the intensity values across the tubule, with the x-axis representing the position along the tubule and the y-axis indicating the intensity at each position. Notably, the plot identifies significant features such as dips (left edge) and peaks (right edge), which correspond to the edges of the regenerating tubule.

3.4. Developing a KNIME-based regeneration tracking workflow

Accurate detection and tracking of regenerating tubule edges are critical for quantifying the dynamics of injury repair over time. Building on the horizontal profile plots approach discussed in the results Section 3.3.4, to streamline the process of detection and tracking of regenerating tubule edges, I developed a KNIME-based workflow that provides a semiautomated, reproducible, and efficient solution for analyzing tubule regeneration (See material and methods Section 6.5.4.3).

The workflow takes two inputs: the exported CSV file containing horizontal profile plots derived from segmented masks (one CSV file per time-lapse) and a folder containing the same experiment's cropped, stabilized, and standardized time-lapses images. Based on the input CSV file, the workflow automatically identifies the corresponding time-lapse and processes the data accordingly.

The developed KNIME workflow (See dashboard in Figure 20), followed a modular structure with four primary panels—three of which are user-configurable:

1. **Managing input** – Selection and organization of input files.
2. **Parameter configuration** – Configuring preprocessing and detection parameters.
3. **Visualizing tracking overlay and saving outputs** – Reviewing tracking results, saving processed data, and exporting tracking overlays.

Detection and tracking is the non-configurable fourth panel that holds the central nodes executing the edge detection and tracking computations. This section will discuss each panel, its application, and its usefulness.

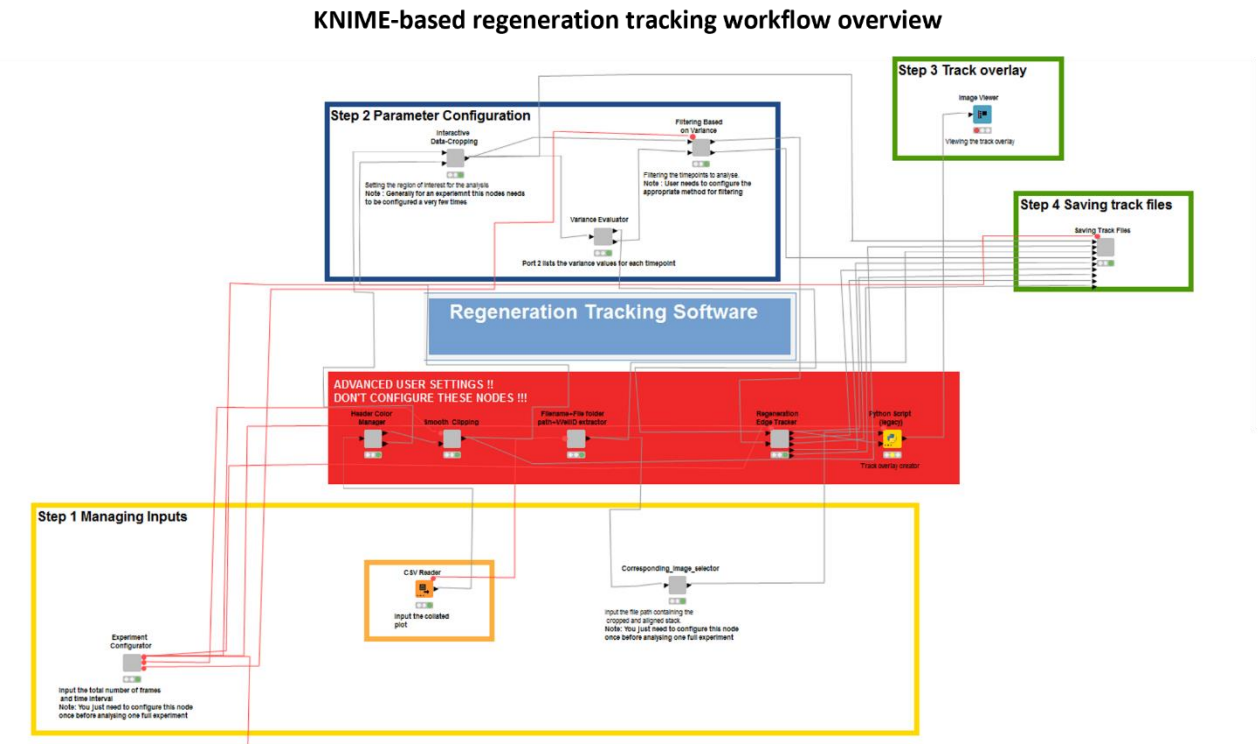

Figure 20: KNIME-based regeneration tracking workflow overview. This figure offers a complete picture of the KNIME-based approach created to monitor tubule regeneration throughout time-lapse images. Designed for simplicity of use and speed in processing complicated data, it shows the workflow's modular structure. It comprises modules for data input management, processing parameter setting, tracking and detection, displaying tracking overlays, and storing results. Powerful back-end processing features combine with an easy-to-use interface.

3.4.1. Managing inputs

The workflow's starting point was this panel (Figure 20, within the yellow box). I aimed to simplify the data input procedure using this panel and properly set the global settings. Within this panel, the user was prompted to:

- **Input a profile plot CSV file for each segmented time-lapse.**
- **Specify the folder containing the cropped and stabilized time-lapses** for an experiment. The panel then automatically identified the appropriate timelapse corresponding to the uploaded profile plot. This automation avoided manual file matching, which can sometimes result in mistakes, especially when handling huge datasets
- **Set global parameters,** the time interval and total number of timepoints in time-lapse.

.

3.4.2. Parameter configuration

This panel (Figure 21A) allowed the configuration of the parameters to detect and track the regenerating tubule edges. I designed it to ensure flexibility and adaptability in the workflow, allowing users to define key parameters for improved detection accuracy, particularly in cases where variability in datasets required fine-tuning. Specifically, this panel consists of two major components:

- **Defining the region of interest (ROI) within the horizontal profile plots:** To allow precise detection of regenerating tubule edges, I developed a collated plot (See Figure 21B), which combined all horizontal profile plots across the entire time-lapse into a single graph. I also developed an interactive ROI marker to interactively select the region of interest within the collated plot (See Figure 21B). This step allowed further analysis to focus specifically on the injury site across timepoints.
- **Tracking the closure of the injury gap based on variance in the profile plots:** In the second part of the panel, I implemented an approach to track the closure of the injury gap by analyzing the variance of the profile plot at each timepoint. Within the collated plots, I noticed that the profile variation was progressively approaching zero as the injury gap regenerated, lacking prominent dips in the later timepoints. Based on this observation, I designed an approach to estimate the closure timepoint. I computed the mean-variance of all timepoints and established it as the default threshold. Timepoints with variance above this threshold were selected for further detection analysis, while those below were filtered out. However, I observed that this approach was not robust. The threshold excluded the final timepoints where the tubule was still regenerating, the profile variance often fell below the threshold due to the low prominence of the dip in the injury gap. Consequently, these critical timepoints were ignored despite the ongoing regeneration process. Conversely, in other cases, regenerated timepoints with noisy profiles were wrongly included in the analysis because their high variance exceeded the threshold despite the injury having already closed. I implemented another option within the panel to allow users to set the threshold manually. This approach proved time-consuming and impractical. However, this approach proved time-consuming, as manually adjusting the threshold required multiple iterations. The manually set threshold was unique to one time-lapse, it was not transferable to others due to variability in noise levels and profile characteristics. To address these

challenges, I added an option (See Figure 21C) in the panel that allowed to manually include or exclude specific timepoints that the workflow might otherwise filter out. This feature provided more control over the filtering procedure in combination variance-based filtering, including or excluding timepoints missed or detected by variance-based filtering.

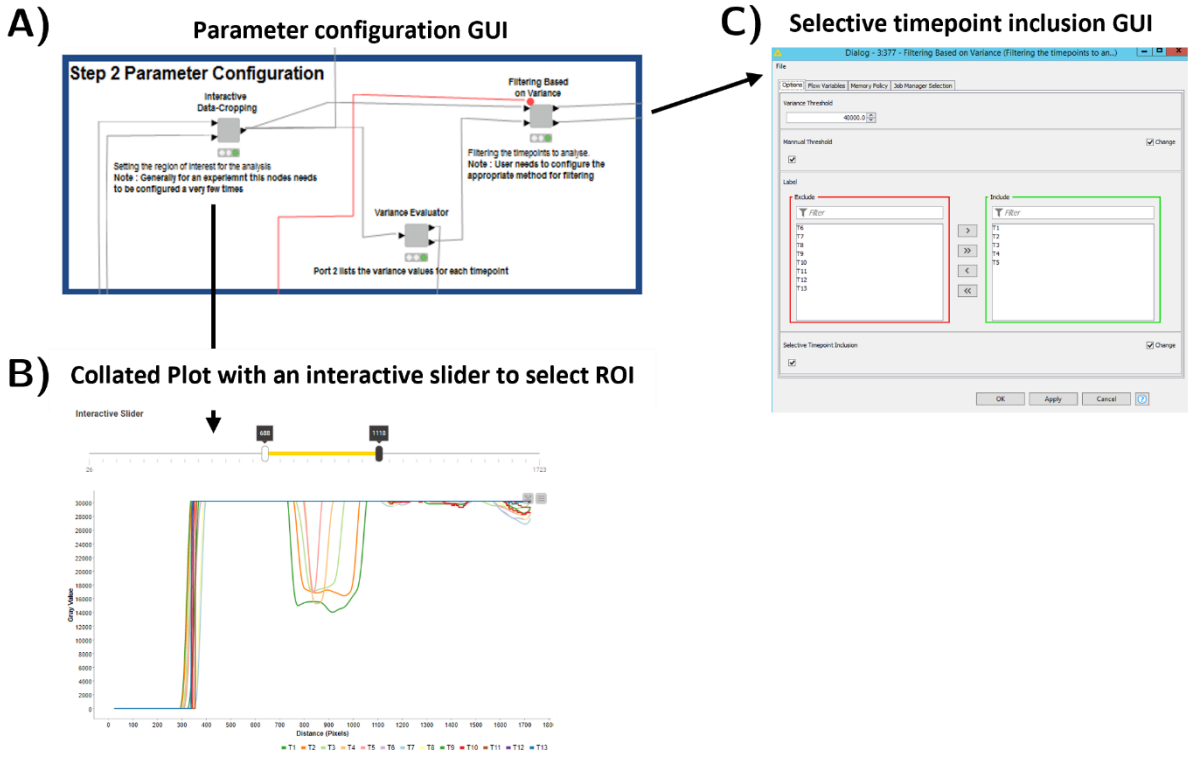

Figure 21: Overview of the KNIME-based regeneration tracking workflow-Parameter configuration. A) Parameter configuration GUI. Illustrates the graphical user interface of the parameter configuration panel, critical for the precise detection and analysis of regenerating tubule edges. B) Collated plot with interactive slider. Each horizontal profile plot from the time-lapse aggregated into a single graph shows a collected plot with timepoint colour-coded. This visualization helps users define the region of interest (ROI) for targeted study on the damage location, improving the edge detection over time. C) GUI for selective timepoint inclusion. It helps to either include or exclude particular time points selectively in the regeneration tracking study.

3.4.3. Detection and tracking

As shown in Figure 20, within the red box, serves as the central component of the workflow, responsible for detecting and tracking regenerating tubule edges. Using ruptures (Truong, 2018/2024), a Python library designed for change-point detection in time series data, I developed a Python script to track the edge of the regenerating tubules from the horizontal profile plots. Ruptures is appropriate for spotting sudden changes in signal behavior, something optimal to detect the prominent dips in the horizontal profiles. Handling the diversity and complexity of the regeneration data, its adaptability and processing efficiency made it the best fit. The detection and

tracking panel ensured a streamlined and automated analysis pipeline, applying the defined parameters to detect and track the regenerating tubule edges precisely.

3.4.4. Visualizing tracking overlay and saving outputs

This panel (See Figure 22A) is responsible for visualizing the results of the tracking analysis and managing the export of all outputs. I specifically designed tools to review and validate the accuracy of the tracked regenerating tubule edges, ensuring the results meet the required level of precision before proceeding to save the outputs.

- **Visualizing the Tracking Overlay.** I built this node within this panel to show the tracked results as an overlay on the original time-lapse (See Figure 22D). This visualization offered instantaneous feedback, verifying if the tracked edges match exactly the renewing tubules and helping to evaluate the detection quality. If the results are unsatisfactory, the tracking fails to capture the correct edges or includes irrelevant features, users can revisit earlier steps in the workflow, such as the Parameter configuration panel (See results Section 3.4.2), to fine-tune parameters like the ROI or variance thresholds.
- **Saving the Tracking Outputs.** I created an automatic node to save the outputs in the second half of the panel. This node arranges and outputs all tracking data, including:
    - The positional information of each detected edge over time (See Figure 22C).
    - Velocity computations of the regenerating edges.
    - Logging the workflow parameters, inputs, and outputs.

All the generated outputs were kept in a new directory called "Regeneration_Tracking", with subfolders for each different outputs (See Figure 22B).

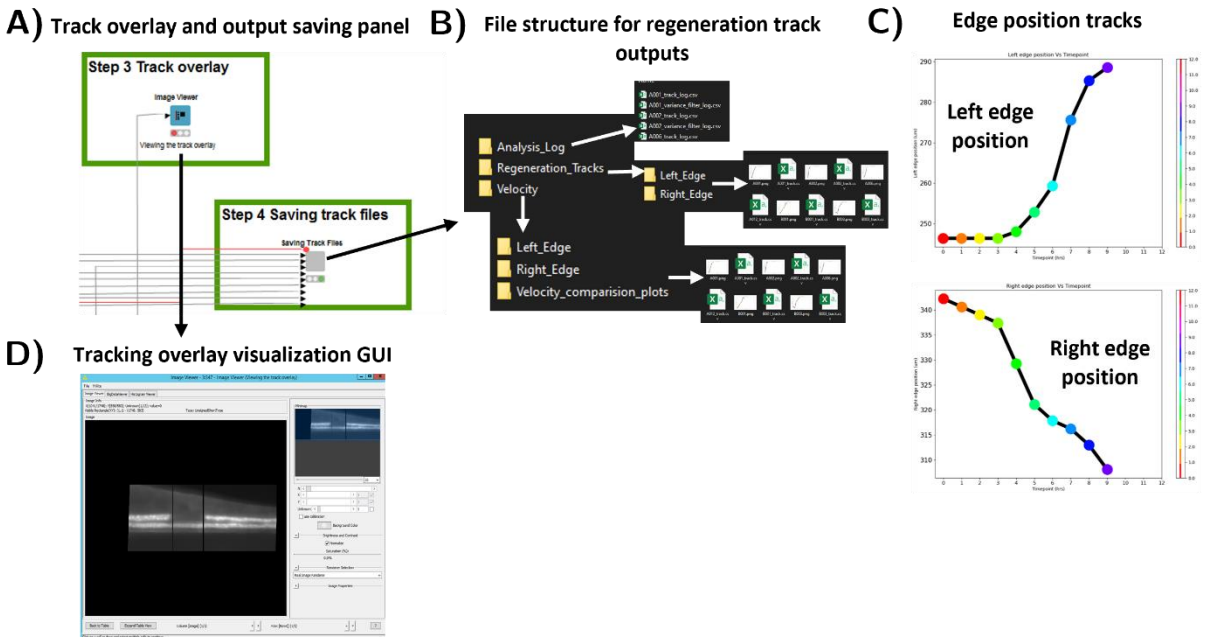

Figure 22: Overview of the KNIME-based regeneration tracking workflow- Visualizing tracking overlay and saving outputs. A) This section of the workflow shows the interface wherein users may examine the regenerated tracking results overlay on the original time-lapse photographs, therefore offering instantaneous visual validation of the tracking accuracy. The panel also includes the section for saving tracking results. B) File structure for outputs of regeneration tracks. Shows the ordered directory structure for storing the tracking outputs, folders for analysis logs, regeneration tracks, and edge velocities. C) Edge position tracks. Shows graphical representations of the left and right edge locations throughout time obtained from the tracking data. D) Tracking overlay visualization GUI. Shows the graphical user interface that allows users to visualize tracking overlays directly on the time-lapse images. This tool is crucial for confirming the accuracy of the tracked edges and making any necessary adjustments to the detection parameters or ROI settings.

3.4.5. Validation of the developed analysis workflow using manual ground truth annotation

An automated analysis workflow (See results Section 3.4) for detecting and tracking regenerating tubule edges was a major progress. However, to assess the robustness and accuracy of the workflow, it needed to be validated. To address this, I validated the outputs from the developed workflow against manual annotations. Using the developed analysis workflow, I analyzed one of the ninety-six well studies obtained using the established imaging assay. Out of the analyzed samples, I randomly selected 15 samples for manual annotations to track regeneration for validation. To ensure an unbiased assessment, I anonymized the file names before extracting the cropped and aligned time-lapse stacks for manual annotation. The manual annotation was performed using FIJI, where I acted as an expert annotator, and my colleague acted as a non-expert annotator. This approach enabled me to compare the workflow's outputs with expert annotations and those from a less experienced annotator. I then compared both the edge positions detected by the workflow to those annotated manually (See Figure 23A), calculating the positional differences for both the left and right edges (See Figure 23B-C).

For each edge positions, I quantified three metrics across each time-lapse: the positional differences between my annotations and the workflow's outputs, between the non-expert's annotations and the workflow's outputs, and between my annotations and those of the non-expert. For the right edge positions (See Figure 23B), the mean positional difference across the time-lapses was 2.28 µm for my annotations vs. the workflow, 4.47 µm for the non-expert's annotations vs. the workflow, and 2.87 µm for my annotations vs. the non-expert's. The mean differences for the left edge positions (See Figure 23C) were 4.90 µm, 2.54 µm, and 4.66 µm, respectively.

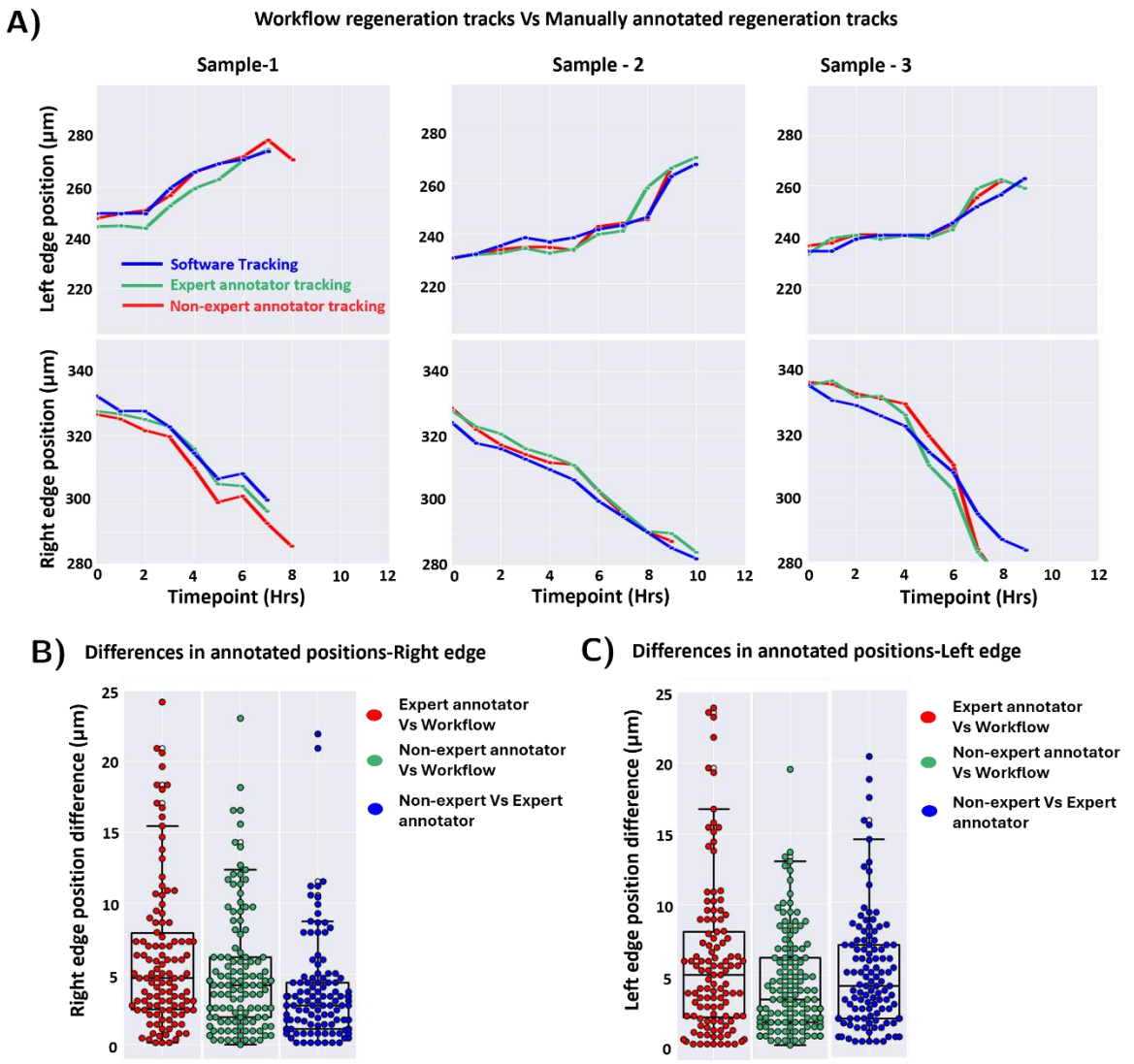

Figure 23: Validation of automated analysis workflow for tubule regeneration tracking. A) Workflow regeneration tracks vs. Manually annotated regeneration tracks. This panel displays a subset of comparative plots of regeneration tracks from the automated workflow and manual annotations across three sample datasets. Each plot consists of the respective regenerating tubule edges position of tracks, comparing the automated detection (workflow regeneration tracks) against the manual ground truth (manually annotated regeneration tracks) to validate the accuracy and consistency of the automated workflow. B)-C) Differences in annotated positions for the right and left edges. This box plot depicts the positional differences between the automated workflow outputs and manual annotations across the timelapse for each edge position of the regenerating tubules. For each box plot, the annotations were done for 15 samples (approx. 195 images), showing the mean and intervals across the sample space for each case: expert versus workflow, non-expert versus workflow, and expert versus non-expert, highlighting the variability and accuracy in edge detection.

3.5. Validating the high throughput screening workflow for quantifying kidney regeneration

After developing the imaging and analysis workflow for high-throughput screening to quantify kidney regeneration following laser-induced injury (See Results Section 3.1-3.4), I aimed to validate its applicability by evaluating its capacity to identify significant biological changes. A straightforward approach to evaluating biological activity is introducing controlled environmental perturbations, among which temperature is the most fundamental variable influencing metabolic processes. It is well established in zoology that changes in temperature directly affect metabolic activity; however, in the context of kidney regeneration in zebrafish embryos, this relationship has not been precisely quantified, particularly with the level of temporal resolution offered by this workflow. Therefore, initially, I explored the regeneration dynamics across different temperature conditions to investigate the influence of temperature on kidney regeneration.

As a second validation study, I examined the effect of different DMSO levels on kidney regeneration. This study was vital, as knowledge of whether DMSO affects regeneration kinetics would help ensure that future drug studies using this workflow account for potential solvent effects.

I applied the standardized experimental protocol developed during workflow construction to conduct these validations. Within the regeneration tracking workflow (See results Section 3.4), I further enhanced the process by creating an experiment overview panel (See Figure 24). I developed custom python scripts which I integrated into this panel which automated the organization and analysis of large experimental datasets. For every experiment, these scripts calculated important dynamic characteristics of regeneration and produced an comprehensive experiment overview consisting:

- Regeneration Status: Categorizing whether regeneration was complete or partial.
- Laser Injury Length: Measure the length of the drawn laser ROI.
- Average Regeneration Speed: Quantifying the average regeneration speed.
- Closure Timepoint: Recording the tubule closure timepoint.

In the corresponding upcoming subsections, I show how I validated the workflow's ability to investigate the environmental and chemical perturbations and offer a thorough investigation of how these parameters affect regeneration kinetics.

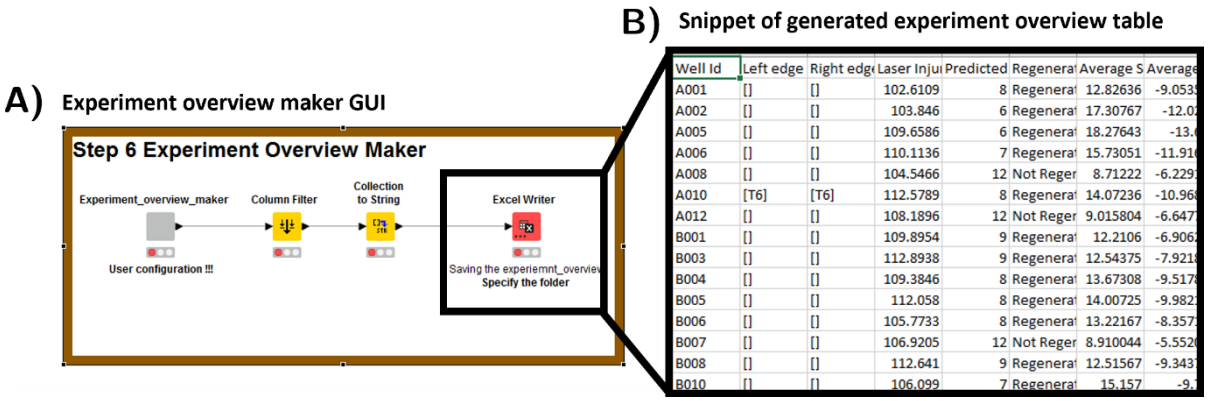

Figure 24: Experiment overview maker panel and generated data table. A) This figure displays the experiment overview maker's graphical user interface (GUI), which is used to create an organized experimental data overview. It consists of only two user-configurable nodes to input the analysis files and to export the generated experiment overview Excel sheet. B) This figure shows a snippet of the generated experiment overview table sample. This table consists of columns depicting well IDs and measured and calculated attributes such as laser injury lengths, predicted regeneration status, and average regeneration speeds.

3.5.1. Investigating kidney regeneration at different temperatures

Temperature is a fundamental physiological parameter that affects metabolic and cellular processes, including regeneration. Since zebrafish are ectothermic organisms, their developmental and regenerative processes are temperature-dependent (Scott & Johnston, 2012)Although temperature has a known influence on metabolism and development, a systematic and high-resolution dynamic study of its effect on kidney regeneration has not yet been carried out. This knowledge gap motivated me to explore the temperature-dependent effects on kidney regeneration following laser damage and thereby verify the created workflow.

To examine how temperature influences kidney regeneration, I conducted experiments in which I observed the regeneration of the distal renal tubule in 3 days post-fertilization (dpf) zebrafish embryos following laser injury. Embryos were kept at four different temperatures during the regeneration phase: 20°C, 24°C, 28°C (control/standard developmental temperature)(Kimmel et al., 1995), and 33°C. These settings were chosen to span relative to the control condition (28°C, both lower

and upper extremes). The upper-temperature limit was set at 33°C, as previous studies reported that temperatures above 33°C had high embryonic lethality (Urushibata et al., 2021). For the lower extreme, while previous research has shown studies where 18°C was used to investigate temperature-dependent metabolism, I opted for 20°C. As the work was carried out in the summer, room temperature changes made reaching and maintaining 18°C in the microscope incubator difficult.

For each temperature condition, I conducted a 96-well plate experiment, where each plate contained six rows of embryos that underwent laser injury, while the remaining two rows served as non-injured controls to account for any temperature-related developmental changes independent of injury(See Figure 25A). Each temperature condition was tested in two independent experimental repeats to ensure reproducibility. Following laser injury, the regeneration of the distal renal tubule was tracked and quantified using the developed image analysis pipeline.

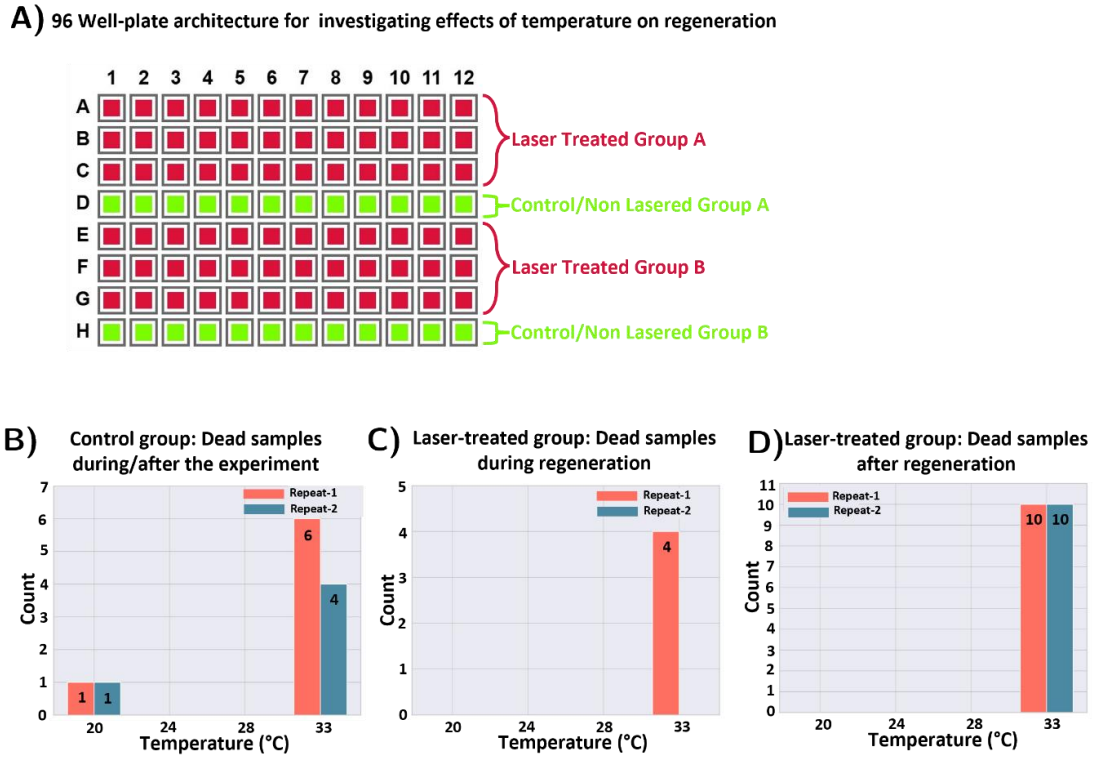

Figure 25: Investigating the impact of temperature on kidney regeneration: Plate architecture and sample viability. A) 96-well-plate architecture for temperature experiments: This panel displays the layout of a 96-well plate used to study the effects of temperature on zebrafish kidney regeneration. Each plate has specific rows designated for laser-treated (in red) and control/non-lasered (in green) groups to facilitate a systematic analysis of temperature influences. B) Graphs illustrating the count of dead embryos at different temperatures for control groups (no laser injury). C) Separated by temperature, this graph shows the count of dead embryos within the laser-treated samples during regeneration. D) The final graph details the counts of dead embryos within the laser-treated samples after regeneration.

3.5.1.1. Impact of temperature on sample viability

During long time-lapse experiments, temperature becomes a crucial factor influencing the survivability of zebrafish embryos. I evaluated the sample viability under different temperatures to filter out non-viable samples from further analysis and ensure the accuracy of my measurements. I examined post-screen imaging data for every sample to establish if it was dead, by confirming the absence of a heartbeat. This step ensured accurate classification of viable and non-viable samples.

I classified sample viability into three distinct categories based on their condition and timing of death. First, I evaluated control samples (embryos that did not undergo laser injury) to determine the number of dead samples during the experiment (See Figure 25B). This served as a baseline to assess whether temperature had a general impact on survival without the additional stress of injury. Then, I classified laser-treated samples into two categories: those that died during the regeneration phase (See Figure 25C) and those that died after regeneration had been completed (See Figure 25D).

Identifying samples that died during regeneration was critical because these samples were excluded from further analysis, as death could confound the regeneration measurements. Conversely, samples that died after the regeneration process were retained for analysis, as their death did not affect the tracking and quantification of regeneration.

The viability assessment revealed that at 33°C, the highest number of nonviable samples existed in both control and laser-treated groups. With minimum non-viable samples seen below 33°C they all showed better survival rates.

3.5.1.2. Analysis of laser injury ROI lengths across different temperatures

The length of the laser injury ROI is an important measure because it directly reflects the initial length of the injury. To ensure consistency in laser-induced injuries and to evaluate the accuracy of the manually drawn laser regions of interest (ROIs), I quantified the lengths of the laser ROIs across different temperature conditions. For each experiment, the coordinates of the laser-drawn ROI were automatically saved as part of the experiment logs through the imaging microscope's software. To compute the ROI length from these coordinates, I developed a Python script that computes and records the injury lengths for each sample. I subsequently integrated this calculation step into the smart imaging workflow (See results Section 3.1.5), as

measuring injury size is a routine aspect of experimental validation. The computed laser injury lengths was later integrated to respective experiment overview table using the experiment overview maker panel in the regeneration tracking workflow (See results Section 3.5).

Using the developed script, I evaluated the laser injury lengths across all temperature conditions and experimental repeats (See Figure 26A-B). While manually marking the laser ROI, I aimed for a target injury length of 105 µm during the experiments. However, I observed variability in the measured lengths, often within a range of ±15 µm. In 1st Repeat (See Figure 26A), I observed considerable differences in the mean laser ROI lengths across the temperature conditions, with some conditions deviating by more than 10 µm from the target length. However, in 2nd Repeat (See Figure 26B), the mean laser ROI lengths were more consistent, clustering closely around the target length of 105 µm across all temperature conditions. Despite these differences, the overall range of laser injury lengths across both repeats fell within the interval of 90 µm to 120 µm, with most samples falling near the target range.

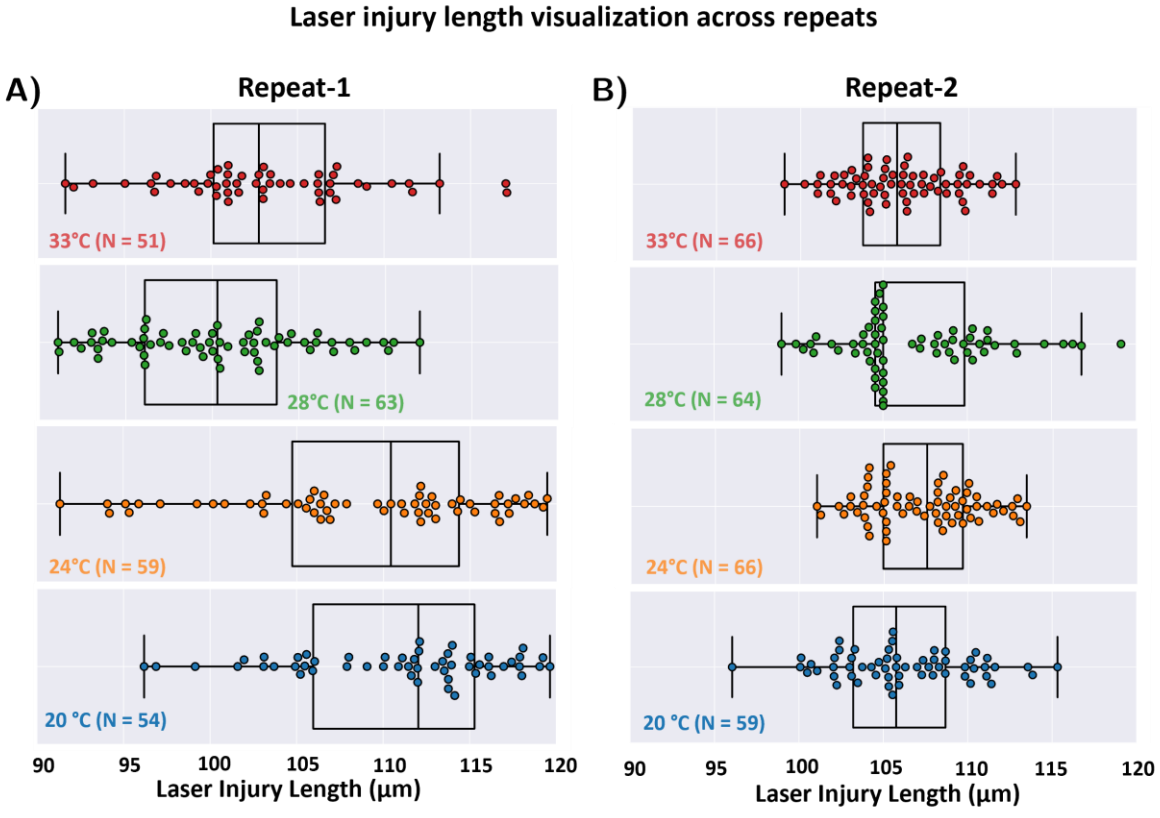

Figure 26: **Laser injury ROI lengths across different temperatures.** A) Repeat-1 and B) Repeat-2 Laser Injury These panels display the lengths of laser-induced injuries in zebrafish embryos at different temperatures across two experimental repeats. Each plot represents a different temperature condition (20°C (blue), 24°C (orange), 28°C (green), and 33°C (red)) with corresponding laser injury lengths depicted as individual points. This provides insights into the precision of the laser injury process under varying temperature.

3.5.1.3. Evaluating regeneration success across temperature variations

The regeneration status of each sample is a critical factor in evaluating the impact of temperature on kidney regeneration following laser injury. By evaluating the regeneration status for each sample across temperatures, I aimed to quantify the capacity of zebrafish embryos to repair injuries under different temperature conditions and across experimental repeats. After analyzing the time-lapse images using the developed analysis workflow (See Results Sections 3.3-3.4), the experiment overview maker (See results Section 3.5) panel within the regeneration tracking workflow categorized each sample into one of two statuses: regenerated (R) or not regenerated (NR). Regenerated samples successfully repaired the injury within the experimental timeframe, while non-regenerated samples failed to do so within the same period.

I quantified the regeneration statuses for each temperature and compared them across experimental repeats (See Figure 27A-B). At 20°C, I noted many non-regenerated samples, with 40 out of 54 samples in Repeat-1 and 51 out of 59 in Repeat-2. For 24°C, regeneration outcomes improved, with fewer non-regenerated samples: 15 out of 59 samples in Repeat-1 and 11 out of 66 in Repeat-2 failing to regenerate. This indicates that temperatures closer to the developmental standard of 28°C begin to support more successful regeneration outcomes. Within the standard developmental temperature of 28°C, regeneration was highly efficient, with only 1 sample in Repeat-1 and 2 samples in Repeat-2 failing to regenerate. Finally, at 33°C, I observed no non-regenerated samples in either repeat.

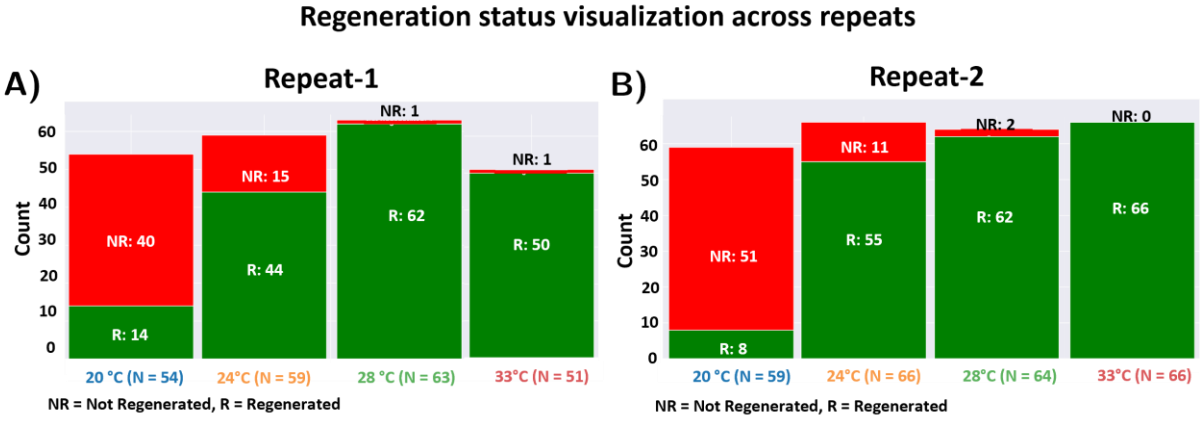

Figure 27: **Regeneration outcomes across temperature conditions**. A) Repeat-1 and B) Repeat-2 Regeneration status visualization: These bar charts illustrate the count of regeneration status of zebrafish embryos across different temperature treatments in two experimental repeats. Each bar represents the number of embryos that either regenerated (R) or did not regenerate (NR) at 20°C, 24°C, 28°C, and 33°C.

3.5.1.4. Impact of temperature on closure timepoints during kidney regeneration

I defined the closure timepoint as the time required for the injury gap to regenerate and close completely. To investigate how temperature affected the closure timepoints I computed the closure timepoints across temperature for each sample using the regeneration tracking workflow (See Results Section 3.5). For this analysis, only samples classified as regenerated (R) were included, as non-regenerated samples did not exhibit closure events and were therefore excluded from this measurement.

I compared the distribution of closure timepoints across temperature conditions for both experimental repeats (See Figure 28A-B). The distribution shifted towards longer closure periods at 20°C; most closure events occurred between 8 and 12 hours. The distribution shifted toward shorter times for 24°C, with most samples completing regeneration within 6 to 10 hours, indicating better regenerative efficiency as the temperature approached optimal developmental conditions. At 28°C, most samples completed regeneration within 4 to 8 hours. Finally, at 33°C, the closure times were the shortest, with most samples completing regeneration within 2 to 6 hours.

To further quantify these observations, I calculated the average closure timepoint for each temperature across both experimental repeats (See Figure 28C). The average closure time consistently decreased linearly as temperature increased, with 20°C exhibiting the longest average closure time and 33°C the shortest.

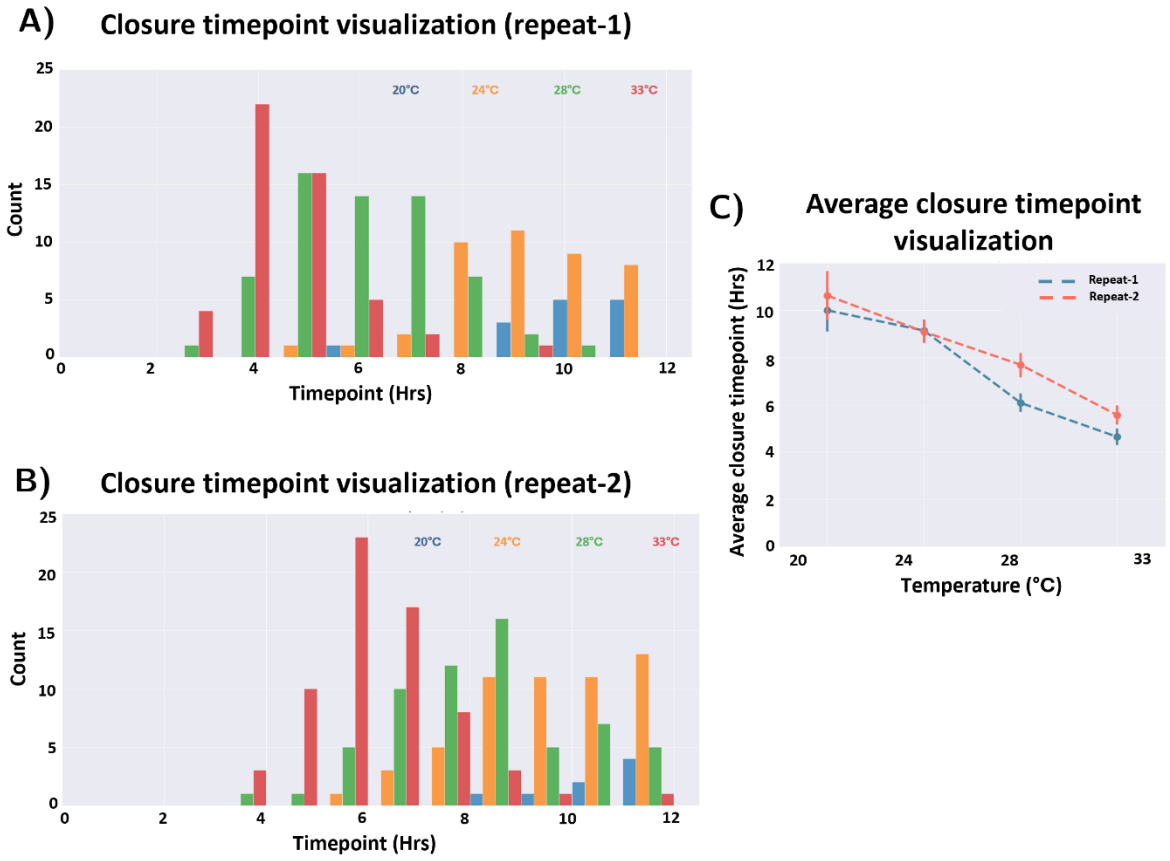

Figure 28: Impact of temperature on closure timepoints during kidney regeneration. A) and B) display the distribution of closure times for regenerated samples in Repeat-1 and Repeat-2, respectively, across four temperatures (20°C (blue), 24°C (orange), 28°C (green), and 33°C (red)). C) This graph shows the average closure timepoints calculated for each temperature, highlighting the shorter closure timepoints at higher temperatures.

3.5.1.5. Impact of temperature on the regeneration dynamics

The tubule gap size is a fundamental measure for tracking the progression of regeneration, as it reflects the physical distance between the regenerating left and right tubule edges. By monitoring how this gap size evolves, it is possible to capture the dynamic nature of regeneration. To analyze this temporal evolution in detail, I developed custom Python scripts, integrated into the visualization panel of the regeneration tracking workflow, to compute the tubule gap size at each timepoint and generate comprehensive profiles of gap size evolution and regeneration rate.

The tubule gap size for each sample was computed by taking the difference between the positions of the left and right regenerating edges obtained through the regeneration tracking workflow. Since the initial gap sizes varied between samples, I normalized the data by setting the gap size at the first timepoint to 1 and dividing the subsequent gap sizes by this initial value. This normalization allowed for comparing regeneration dynamics across samples regardless of their initial injury size.

The normalized gap size profiles for individual samples across different temperatures are shown in Figure 29A and Figure 29B . To provide a clearer overview of the average regeneration dynamics at each temperature, I plotted the aggregated normalized gap size evolution with the graphs displaying average and 95% confidence intervals for each temperature condition across both experimental repeats (See Figure 29 Figure 30C and Figure 29D). These line plots summarize how the average tubule gap size decreased over time across different temperatures. The profiles highlighted that at 33°C, the gap size decreased rapidly, reaching zero by 6 hours. At 28°C, the gap size approached zero around 8 hours, while at 24°C, the gap size decreased more slowly, taking approximately 9 hours. In contrast, at 20°C, the gap size decreased slowly but did not reach zero within the 12-hour, reflecting slower regeneration in most samples.

In addition to gap size evolution, I also generated the tubule regeneration rate, which is calculated as the rate of change in the gap size over time. I used the non-normalized gap size data for this calculation to capture the regeneration rate at each timepoint. The regeneration rate profiles were computed for individual samples and were aggregated, and the mean regeneration rate with 95% confidence intervals was plotted for each temperature (See Figure 30A and Figure 30B).The regeneration rate profiles revealed that at 20°C, the rate remained constant and low throughout the 12 hours. At 24°C, although the rate improved slightly, it remained relatively constant without significant fluctuations. In contrast, at 28°C and 33°C, I observed a sharp increase in regeneration rate within the first few hours. The peak regeneration rate was higher at 33°C compared to 28°C, but both temperatures showed a similar pattern of an early rate surge followed by a gradual decline as the injury gap approached closure.

To have an overall trend of the regeneration rate, I also computed and compared the average speed across the temperatures for each samples (See Figure 31A-B). At 20°C, the regeneration speed was the slowest, the average regeneration speed clustered between 4 to 8 µm/hr. For 24°C, the regeneration speed improved, with most samples exhibiting average speeds between 8 to 12 µm/hr. At 28°C, most samples achieved speeds between 12 to 18 µm/hr, and finally, at 33°C, the regeneration speed was the highest, with many samples exhibiting speeds between 18 to 25 µm/hr.

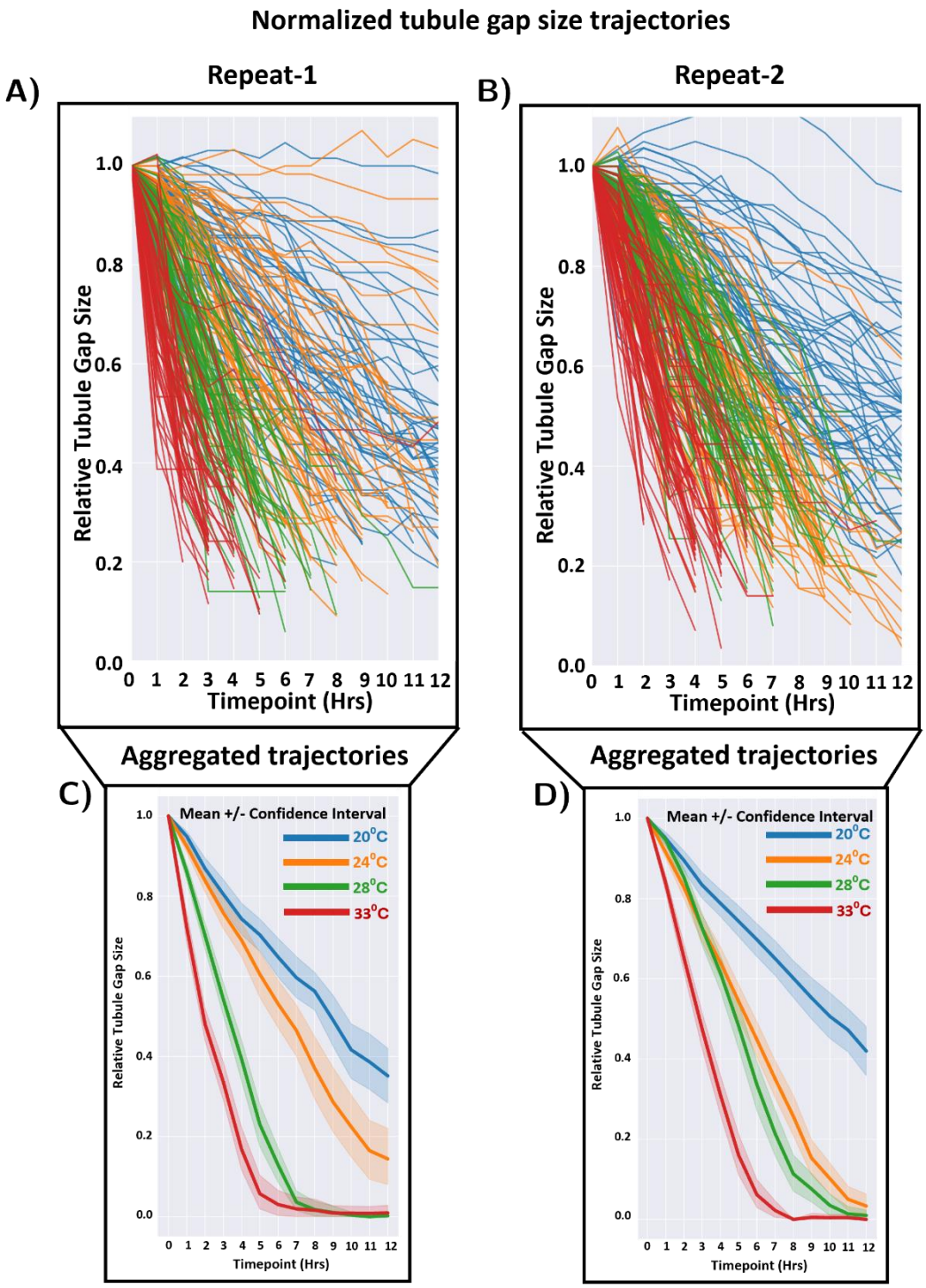

Figure 29: Comprehensive analysis of regenerating tubule gap size evolution across different temperatures. Panels A) & B) Display individual sample trajectories for normalized tubule gap sizes over time during kidney regeneration, across two experimental repeats. Each trajectory represents the closure process of the tubular gap with colors indicative of different temperature conditions: blue for 20°C, orange for 24°C, green for 28°C, and red for 33°C. Panels C) & D): Show the average evolution of normalized gap sizes over time for each temperature, aggregated from individual sample data in Panels A) & B). These plots include 95% confidence intervals, illustrating the average pace at which the tubular gap closes at different temperatures: blue for 20°C, orange for 24°C, green for 28°C, and red for 33°C.

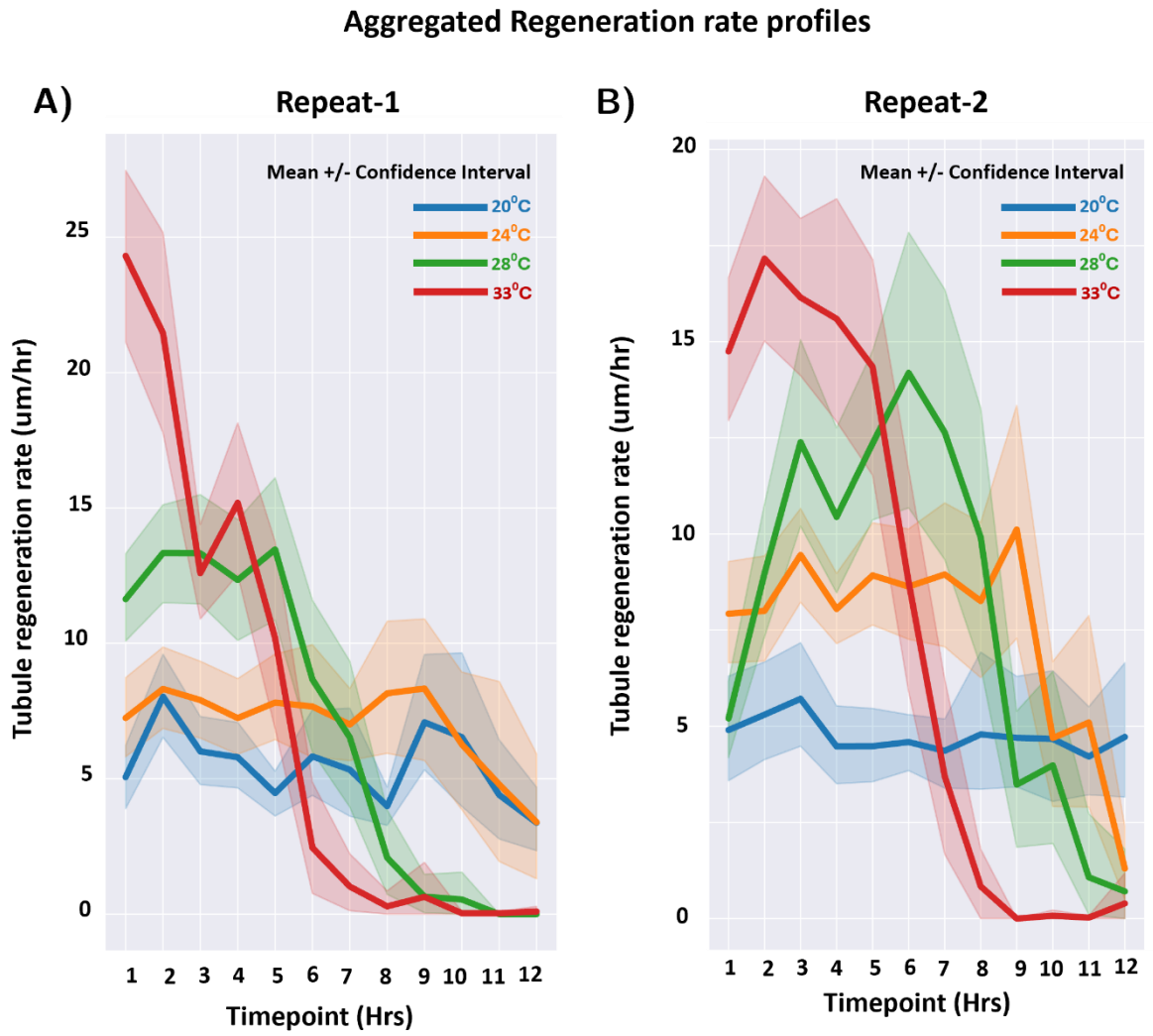

Figure 30: Comprehensive analysis of regeneration rate profiles across different temperatures. Panels A) & B) presents the regeneration rates calculated from the rate of change of the non-normalized tubule gap size, with mean values and 95% confidence intervals for each temperature conditions: blue for 20°C, orange for 24°C, green for 28°C, and red for 33°C

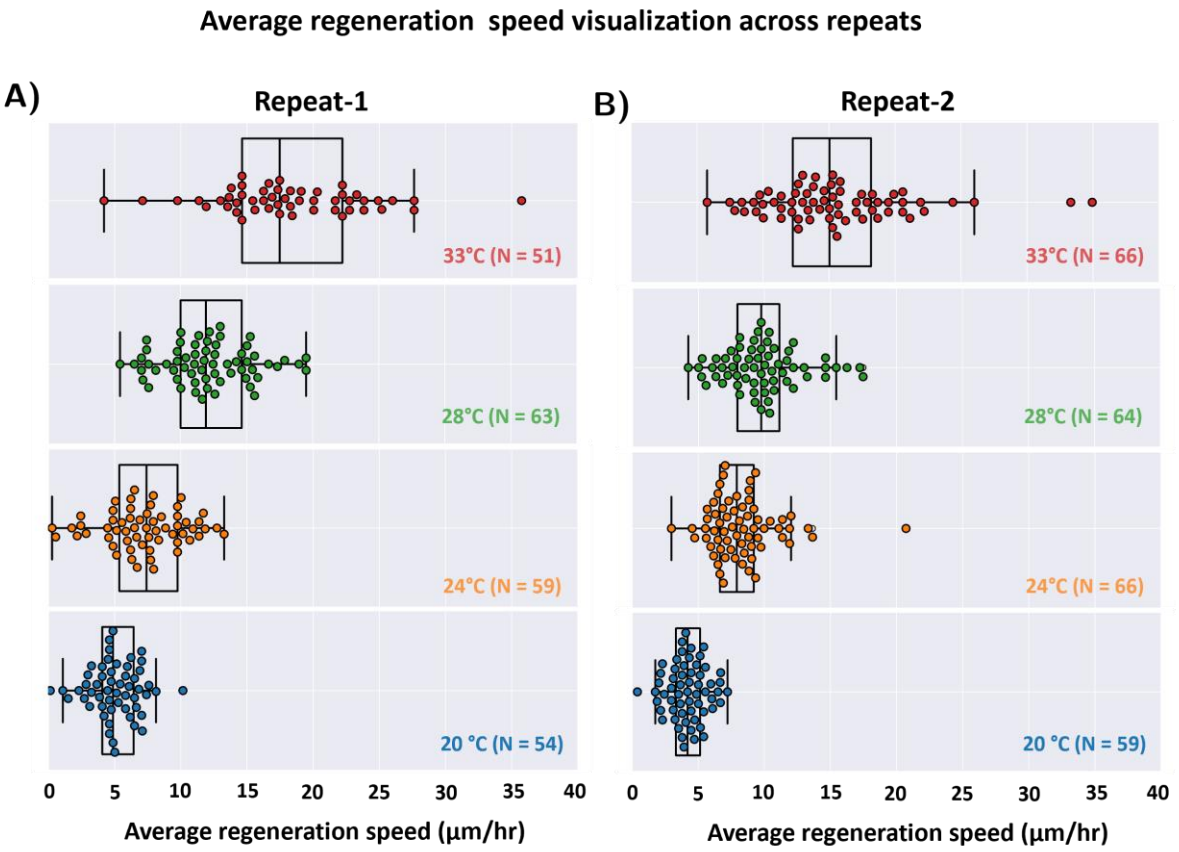

Figure 31: Average regeneration speed analysis across temperatures A) & B) Visualization of average regeneration speeds across experimental repeats for different temperatures. Each plot corresponds to temperatures of 20°C (blue), 24°C (orange), 28°C (green), and 33°C (red). Each dot represents the average regeneration speed of a single sample with the spread indicating variability within each group.

3.5.2. Investigating kidney regeneration at varying DMSO concentrations

Dimethyl sulfoxide (DMSO) employed as a solvent in biological experiments due to its ability to solubilize many hydrophobic compounds in aqueous solutions. Nevertheless, its concentration requires careful evaluation, particularly in developmental research utilizing sensitive models like zebrafish embryos as it may affect physiological systems and cause developmental toxicity at high doses (Hoyberghs et al., 2021). The widespread use and probable effects of DMSO motivated me to do this second validation experiment to examine if varying levels of DMSO influence kidney regeneration dynamics. To examine how DMSO influences kidney regeneration, I conducted experiments in which I observed the regeneration of the distal renal tubule in 3 days post-fertilization (dpf) zebrafish embryos following laser injury at varying DMSO concentrations (0%-1.5%). Selected DMSO concentration ranges were commonly utilized in biological research, including levels approaching the top safety criteria (typically 0-1%) (Hoyberghs et al., 2021). All experiments were conducted at 28°C, the standard temperature for zebrafish development and regeneration in laboratories.

For every DMSO concentration, I conducted a 96-well plate experiment ensuring uniform sample distribution. As seen in Figure 32, every well plate was arranged with rows indicating different DMSO concentrations. Specifically, each row contained 10 laser-injured samples and 2 non-lasered control samples to account for potential effects unrelated to the laser-induced injury. Each row included two non-lasered control samples and ten laser-injured samples to consider any possible impacts unrelated to the laser-induced damage. Each row included two non-lasered control samples and ten laser-injured samples to account for any possible effects unrelated to the laser-induced damage. Each DMSO concentration was evaluated in two separate experimental replicates to ensure reproducibility. The laser-induced injury and regeneration tracking were performed using the same high-throughput screening workflow employed in the temperature experiments, thereby ensuring consistent and comparable measurement of regeneration outcomes across all DMSO concentrations tested.

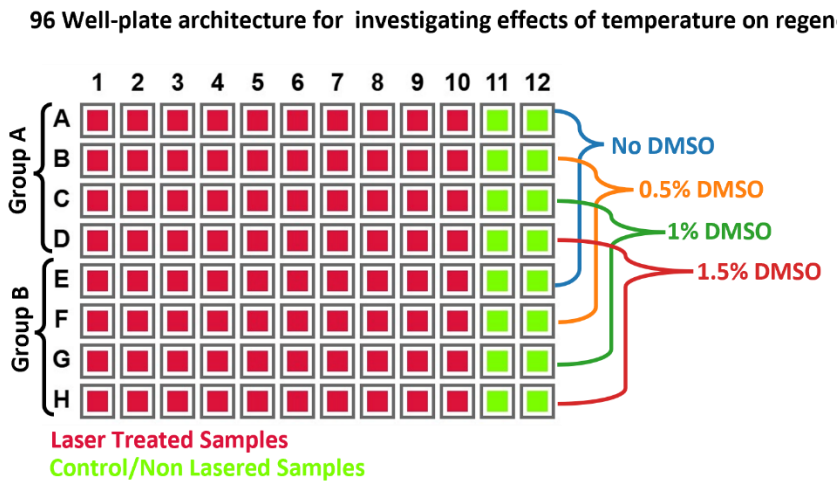

Figure 32: 96 Well-plate layout for evaluating the effects of DMSO on kidney regeneration dynamics in zebrafish embryos. The figure portrays the schematic layout of the 96-well plate used to test various concentrations of DMSO. Each plate has specific rows designated for each DMSO concentration, starting from no DMSO to 1.5% DMSO (rows A-D for Group A and rows E-H for Group B). Within each row, 10 samples (in red) were lasered and 2 samples (in green) were non-lasered and used as control groups to facilitate a systematic analysis of DMSO's influences

3.5.2.1. Impact of DMSO on sample viability

Unlike the temperature experiments where viability was a critical issue (See Results Section 3.5.1.1), no sample deaths were observed during the DMSO experiments across any concentration. This indicates that even the highest DMSO concentration tested (1.5%) was not acutely toxic to the samples under the experimental timeframe. Thus, all samples were kept for further analysis instead of requiring viability filtration.

3.5.2.2. Analysis of laser injury ROI lengths across different DMSO concentrations

The length of the laser injury ROI is an important measure because it directly reflects the initial length of the injury. To ensure consistency in the injury size across all DMSO concentrations, I compared the lengths of the laser-drawn regions of interest (ROIs) using the same approach as in the temperature experiments. While manually marking the laser ROI, I aimed for a target injury length of 105 µm during the experiments. Figure 33A-B show the distributions of laser injury lengths for each DMSO condition across the two experimental repeats. Across all concentrations, the average laser injury length remained close to the target of 105 µm, with minimal variation between conditions. After quantifying and understanding the variability in

laser injury lengths, I established that the initial injury size was well controlled and did not introduce significant variability for subsequent downstream analysis.

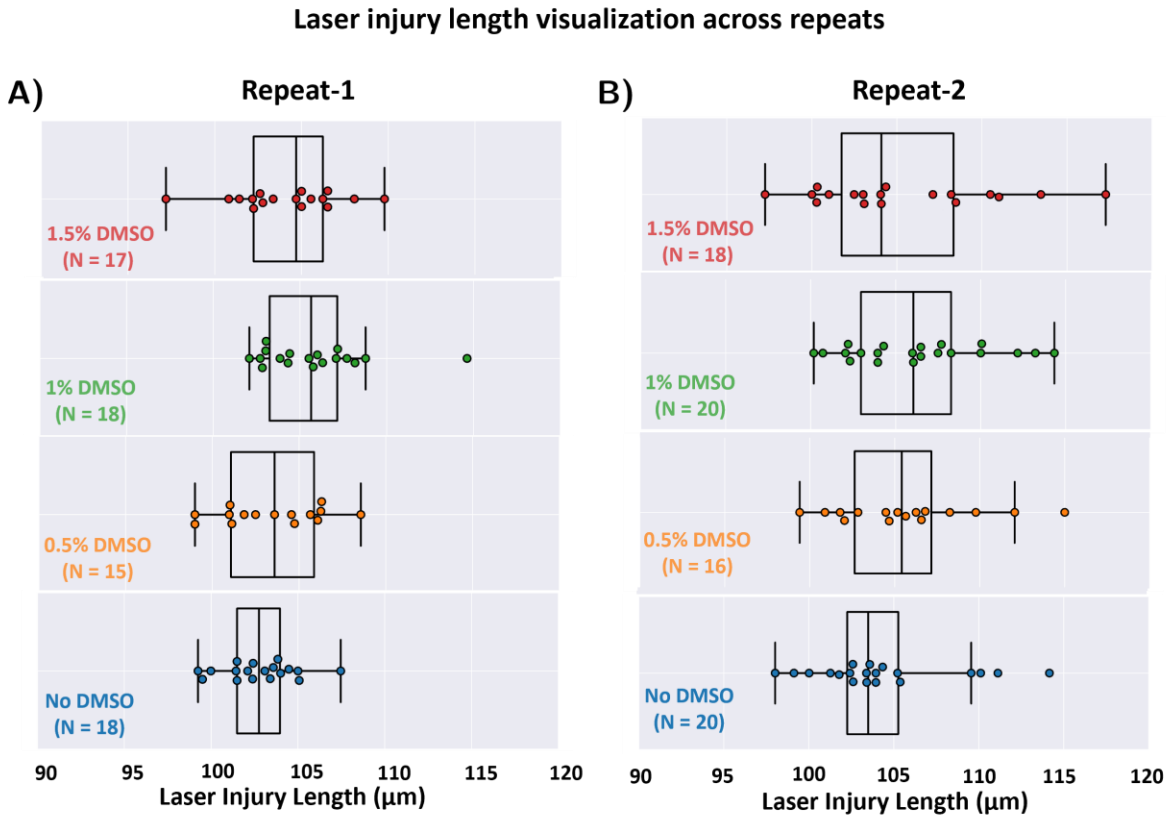

Figure 33: Laser injury ROI lengths across at different DMSO concentrations. A) Repeat-1 and B) Repeat-2 Laser Injury These panels display the lengths of laser-induced injuries in zebrafish embryos at different DMSO concentrations across two experimental repeats. Each plot represents a different DMSO concentrations (No DMSO (blue), 0.5% DMSO (orange), 1% DMSO (green), and 1.5% DMSO (red)) with corresponding laser injury lengths depicted as individual points. This provides insights into the precision of the laser injury process under varying DMSO concentrations.

3.5.2.3. Evaluating regeneration success across DMSO concentrations

An important indicator of how DMSO concentrations affect the potential of zebrafish embryos to heal damage caused by laser-induced damage is the status of regeneration of every sample. By assessing whether samples successfully closed the injury gap within the experimental timeframe, I aimed to quantify the overall regeneration efficiency under different DMSO conditions. I used the experiment overview panel, as described in the temperature experiments (See Results Section 3.5), to classify samples as either regenerated (R) or not regenerated (NR) based on their closure status.

Figure 34A-B illustrate the distribution of regenerated and non-regenerated samples across DMSO concentrations for both repeats. At 0% DMSO, 15 out of 18 samples regenerated successfully in Repeat-1, while 18 out of 20 samples regenerated in Repeat-2. Similarly, at 0.5%, 1%, and 1.5% DMSO, most samples demonstrated successful regeneration, with only a few classified as non-regenerated. The overall regeneration success across all concentrations was high, indicating that DMSO levels within the tested range do not drastically impair the ability of zebrafish embryos to repair injuries.

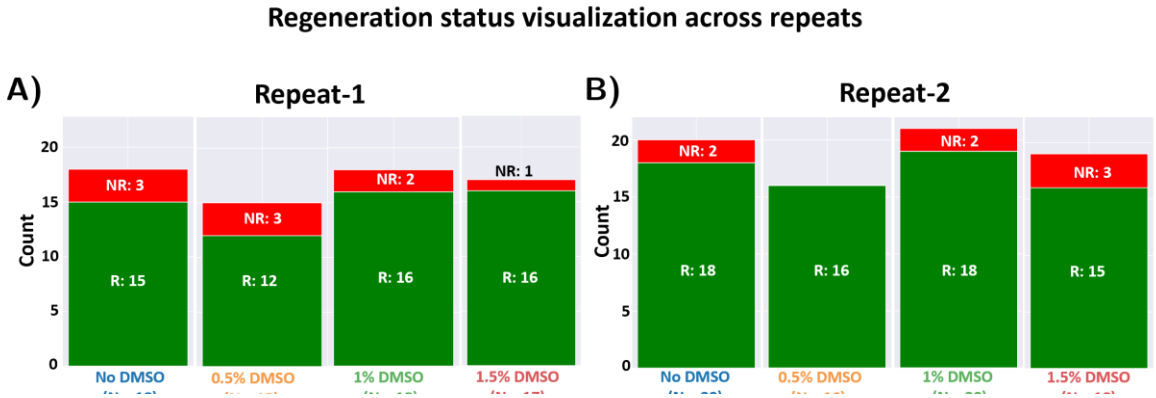

Figure 34: Regeneration outcomes across different DMSO concentrations. A) Repeat-1 and B) Repeat-2 Regeneration status visualization: These bar charts illustrate the count of regeneration status of zebrafish embryos across different DMSO concentrations in two experimental repeats. Each bar represents the number of embryos that either regenerated (R) or did not regenerate (NR) at No DMSO, 0.5% DMSO, 1% DMSO, and 1.5% DMSO.

3.5.2.4. Impact of DMSO on closure timepoints during kidney regeneration

The closure timepoint is a critical measure of regeneration efficiency, representing the time taken for the injury gap to close completely. To investigate how different DMSO concentrations influence the timing of this process, I analyzed the closure timepoints of the regenerating tubule edges across the various concentrations. The closure timepoints for each sample were computed using the regeneration tracking workflow. For this analysis, only samples classified as regenerated (R) were included, as non-regenerated samples did not exhibit closure events and were therefore excluded. I compared the distribution of closure timepoints across DMSO concentrations for both experimental repeats (See Figure 35A-B). At 0% DMSO (no DMSO). As the DMSO concentration increased to 0.5%, 1%, and 1.5%, the distribution of closure timepoints remained relatively stable, with most samples completing regeneration within a similar timeframe. I computed the average closure times for every DMSO concentration across both experimental repeats (See Figure 35C). The average closing time was constant at the studied concentrations—between 7.5 and 8 hours. This stability implies that DMSO doses within the investigated range do not notably affect the usual closure routine or postpone regeneration. The closure times stayed like those recorded at lower concentrations (no DMSO), even at the maximum concentration of 1.5% DMSO, suggesting that the embryos maintained their regeneration efficiency despite the rising DMSO levels.

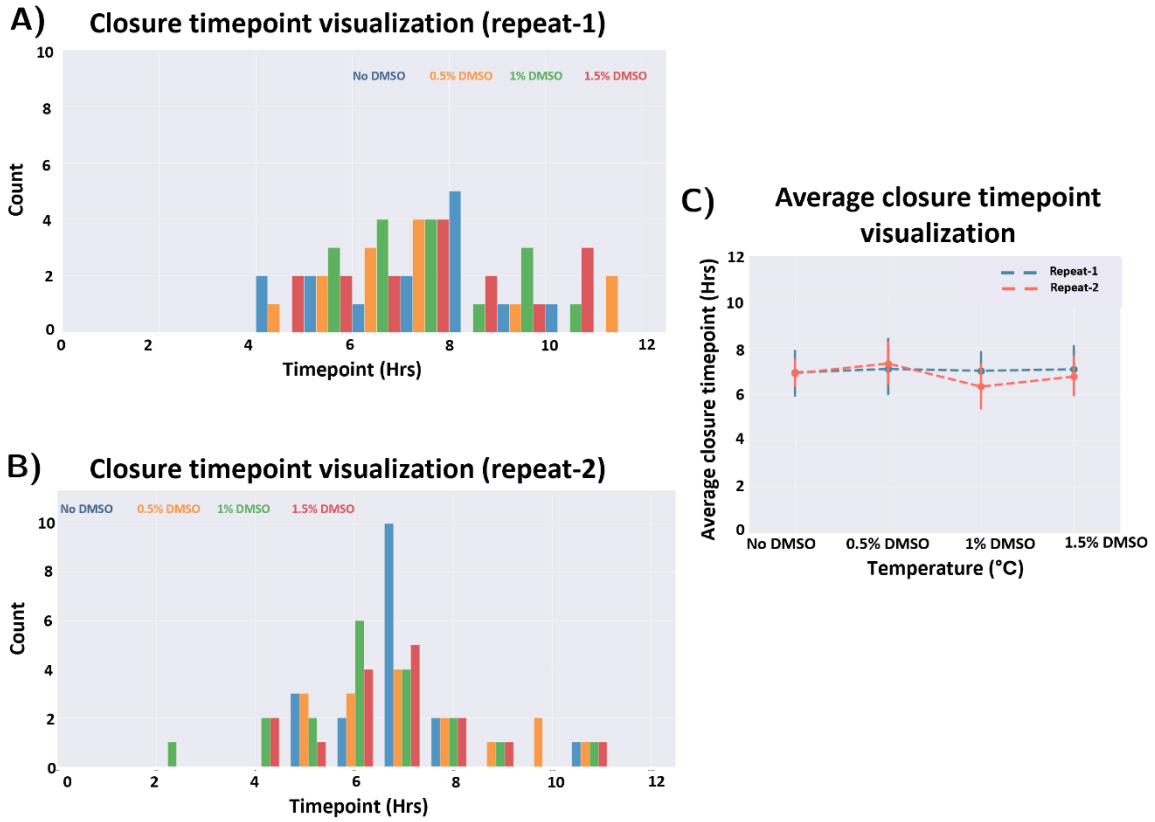

Figure 35: Impact of DMSO on closure timepoints during kidney regeneration. A) and B) display the distribution of closure times for regenerated samples in Repeat-1 and Repeat-2, respectively, across four DMSO concentrations (No DMSO (blue), 0.5% DMSO (orange), 1% DMSO (green), and 1.5% DMSO (red)). C) This graph shows the average closure timepoints calculated for each DMSO concentration, highlighting the uniform closure timepoints across the DMSO concentrations.

3.5.2.5. Impact of DMSO on the regeneration dynamics

To understand the detailed temporal dynamics of regeneration beyond the average speed, I analyzed the evolution of the tubule gap size and regeneration rate over time for different DMSO concentrations. I followed the same methodology described in the temperature experiments (See Results Section 3.5.1.5). The tubule gap size for each sample was computed based on the positions of the regenerating left and right edges, and the data were normalized to enable comparisons across samples with different initial injury sizes. This analysis was performed using the custom Python scripts I developed and integrated into the visualization panel of the regeneration tracking workflow. These scripts generated comprehensive profiles of gap size evolution and regeneration rates over time. Figure 36A-B displays the normalized tubule gap size evolution for individual samples across the tested DMSO concentrations, while Figure 36C-D presents the mean gap size profiles with 95% confidence intervals. Across all concentrations, I observed that the gap size evolution profiles were highly similar and superimposed on each other, indicating a consistent regeneration pattern.

Similarly, the regeneration rate profiles for different DMSO concentrations were computed using the non-normalized gap size data, following the same procedure as in the temperature experiments (See Results Section 3.5.1.5). Figure 37A-B illustrates the mean regeneration rate profiles with 95% confidence intervals. I observed that all DMSO concentrations followed a similar trend and were almost superimposed on each other. To have an overall trend of the regeneration rate, I also computed and compared the average speed across the DMSO concentrations for each sample (See Figure 38A-B). Across both experimental repeats, the regeneration speed across DMSO concentrations varied from 6 - 12 µm/hr. While mean average

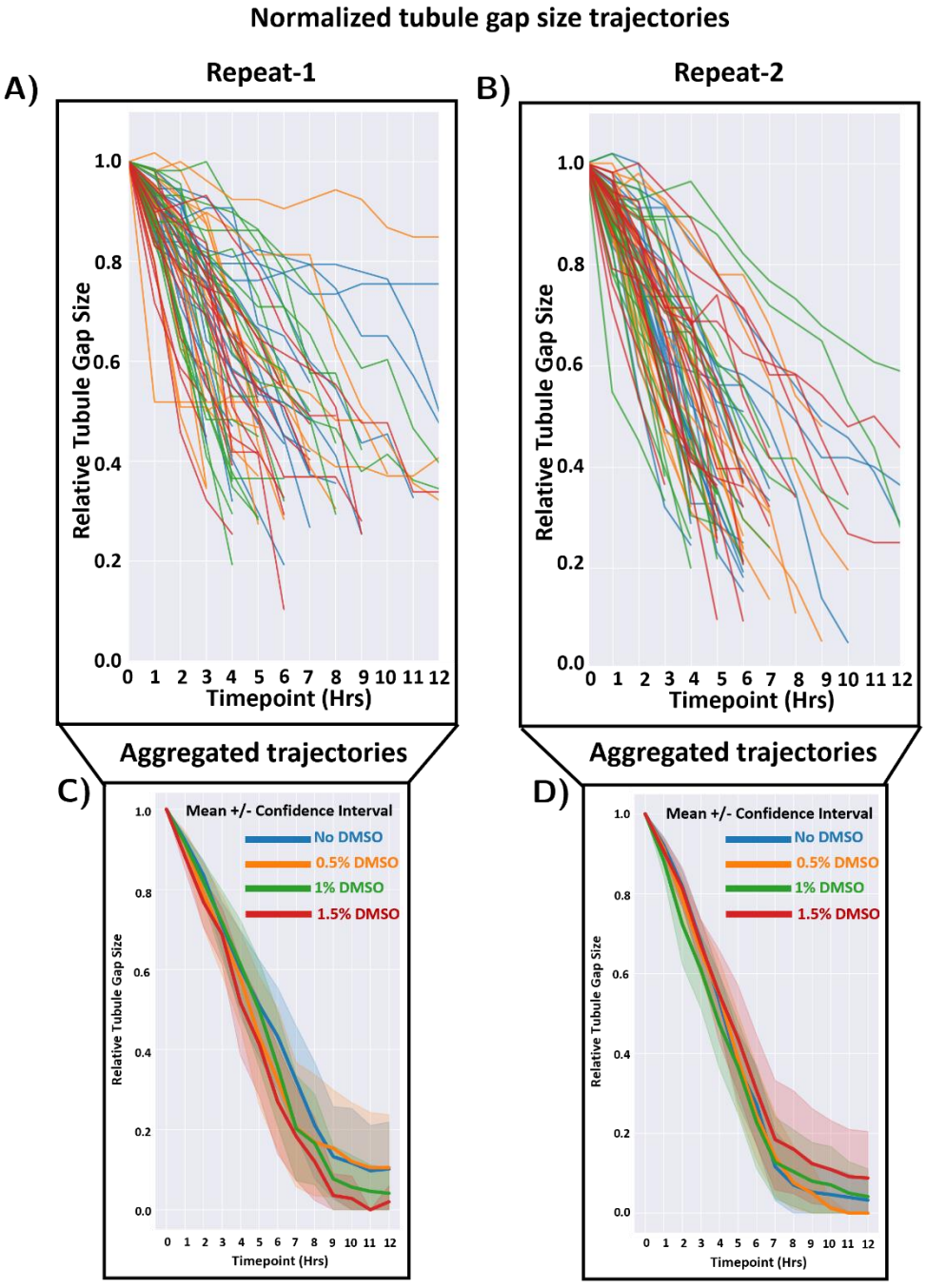

Figure 36:Comprehensive analysis of regenerating tubule gap size evolution across different DMSO concentrations. Panels A) & B) Display individual sample trajectories for normalized tubule gap sizes over time during kidney regeneration across two experimental repeats. Each trajectory represents the closure process of the tubular gap with colors indicative of different DMSO concentrations: blue for No DMSO, orange for 0.5% DMSO, green for 1% DMSO, and red for 1.5% DMSO. Panels C) & D): Show the average evolution of normalized gap sizes over time for each DMSO concentration, aggregated from individual sample data in Panels A) & B). These plots include 95% confidence intervals, illustrating the average pace at which the tubular gap closes at different temperatures: blue for No DMSO, orange for 0.5% DMSO, green for 1% DMSO, and red for 1.5% DMSO.

regeneration speeds had slight variations across DMSO concentrations, but the overall range was consistent throughout all investigated concentrations.

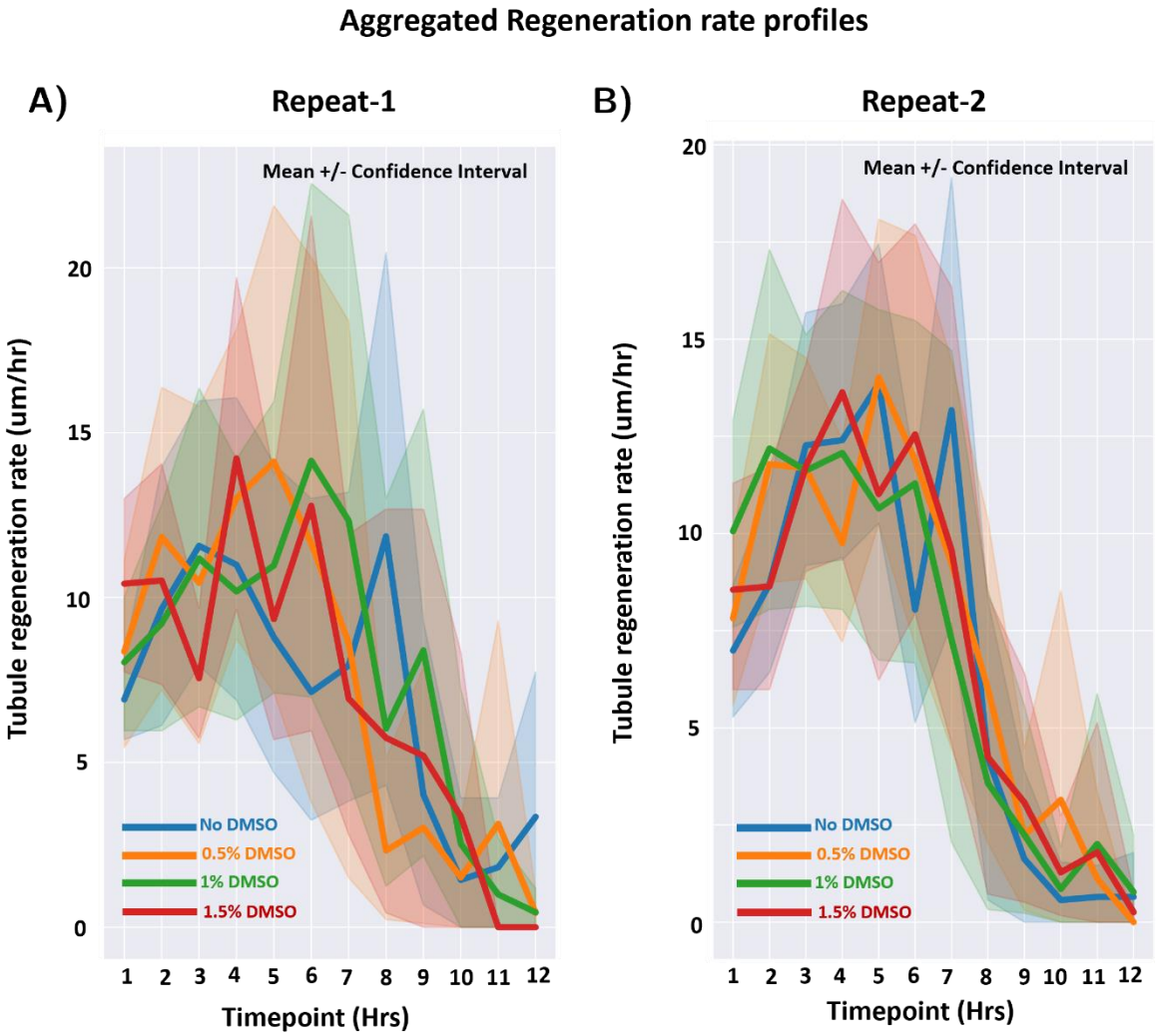

Figure 37:Comprehensive analysis of regeneration rate profiles across different DMSO concentrations. Panels A) & B) presents the regeneration rates calculated from the rate of change of the non-normalized tubule gap size, with mean values and 95% confidence intervals for each DMSO concentrations: blue for No DMSO, orange for 0.5% DMSO, green for 1% DMSO, and red for 1.5% DMSO

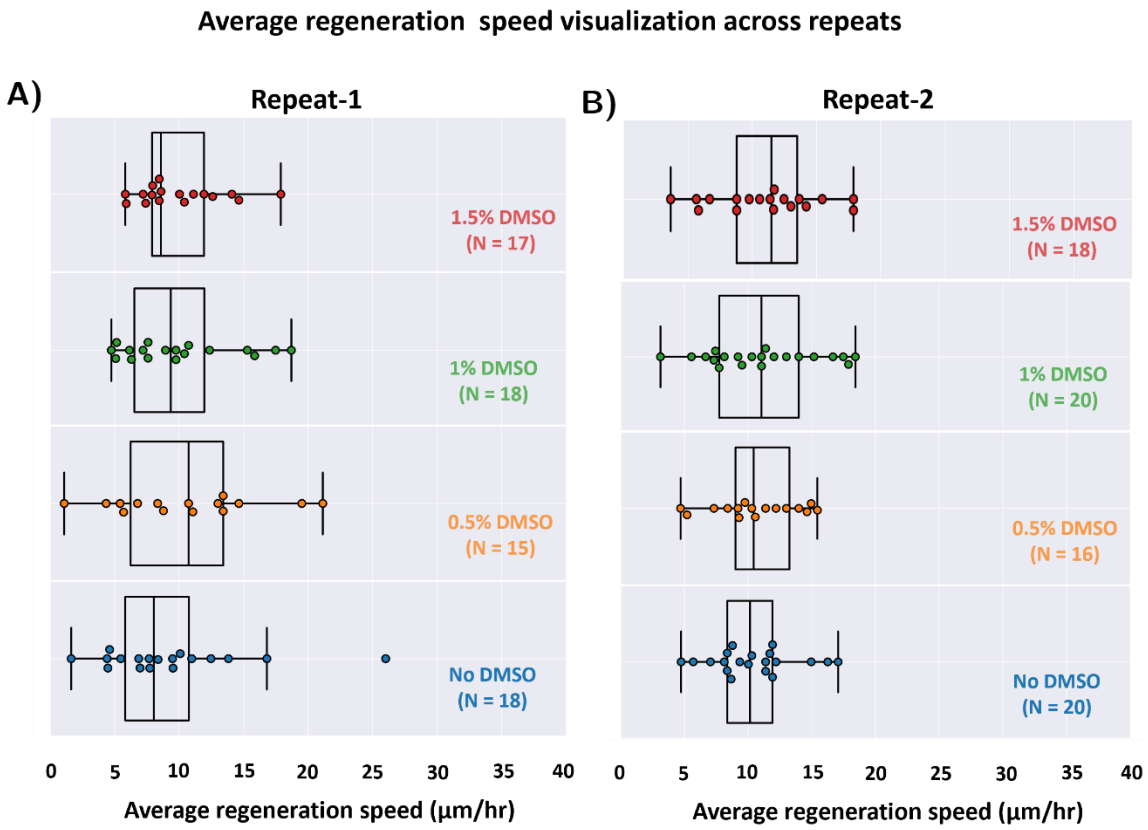

Figure 38:Average regeneration speed analysis across DMSO concentrations A) & B) Visualization of average regeneration speeds across experimental repeats for different DMSO concentrations. Each plot corresponds to temperatures of No DMSO (blue), 0.5% DMSO (orange), 1% DMSO (green), and 1.5% DMSO (red). Each dot represents the average regeneration speed of a single sample, with the spread indicating variability within each group.

4

Discussion

4.1. High throughput time-lapse imaging workflow to study regenerating distal renal tubules post-laser-induced injury

4.1.1. Achieved reliable embryo orientation and mounting approach

Given the zebrafish embryo's complex 3D shape and size, evaluating the ideal orientation and mounting approach becomes crucial for microscopy imaging. (Kleinhans & Lecaudey, 2019; Nagarajan et al., 2024). I established that the tilted dorsal orientation of embryos mounted in low melting agarose molds within cycloolefin film bottom well plates created an ideal scheme for visualizing GFP-expressing distal renal tubules in zebrafish embryos (See Results Section 3.1.1). The titled dorsal orientation balanced tubule visibility and contrast, avoiding the autofluorescence artifacts seen with the fully dorsal orientation and the incomplete visualization observed with the lateral orientation (See Figure 6A). I tried a series of established approaches to orient the embryos in a tilted dorsal manner for long imaging periods (Gehrig et al., 2018; Lubin et al., 2021; Wittbrodt et al., 2014). The ZF plate (Lubin et al., 2021) looked optimal, imparting high signal-to-noise ratio images. However, I rejected that strategy due to the instability of the desired orientation and difficulty with embryo handling. Optimizing the embryo mounting using the orientation-tools (Wittbrodt et al., 2014) gave me greater control over the orientation and handling of the embryos. I further enhanced the orientation tools approach by replacing the agarose molds with low melting agarose molds, imparting their good optical properties and wide use in other microscopy techniques like light-sheet and confocal microscopy (Hirsinger & Steventon, 2017). Tilted dorsal orientation offers an optimal visualization of the distal renal tubules, but it is a non-

trivial orientation limited to specific problems. A key limitation of my approach is the time and skill required to orient the samples, especially as the desired orientation demands significant embryo manipulation. To improve my current approach, geometry-specific molds could be designed based on orientation tools (Wittbrodt et al., 2014) and accounting for tilt. Although it would still demand embryo manipulation, it would reduce the effort and time, as the orientation tools did for standard orientation, such as dorsal and lateral. Alternative automated systems with flexible orientation and mounting include microfluidics and VAST (Khalili & Rezai, 2019; Pardo-Martin et al., 2010). However, their current designs often prioritize static or perfusion-based imaging over this study's long-term, high-throughput time-lapse needs. Future developments in these tools would also accommodate time-lapse imaging.

4.1.2. High throughput laser-induced injury workflow to study kidney regeneration

A precise and reproducible injury model is essential to study kidney regeneration dynamics effectively. Previously established methods involving nephrotoxic agents (gentamicin, aristolochic acid (Ding & Chen, 2012; Hentschel et al., 2005)) and NTR-mediated genetic ablation (B. E. Drummond & Wingert, 2016) resulted in very sparse and uncontrolled injury, leading to high lethality of the samples. Moreover, these studies concentrated on injury modeling rather than tracking regeneration dynamics. Laser-induced injury addressed and overcome these limitations by providing a precise and reproducible spatiotemporal controlled injury (Datta et al., 2017; C. S. Johnson et al., 2011a), but a high throughput approach was still lacking. Through my workflow, I addressed this gap by introducing a high-throughput laser-induced injury workflow to target and injure one of the distal renal tubules in a controlled and reproducible manner (See Sections 3.1.2-3.1.3).

However, while scaling up the laser injury workflow, I noticed a major failure rate(See Figure 8). Analyzing the failed laser attempts revealed that the embryo movement of 1–2 tubule diameters during the process of annotation and lasering was the major reason. Iterative refinements—incorporating methylcellulose to increase media viscosity, lowering incubation temperature to 20°C to reduce metabolic activity, and adopting a modular two-group approach—collectively reduced the failure rate of laser injuries (See Figure 9C). Methyl cellulose is a known mounting agent that enhances

media viscosity for better sample stability for extended time-lapse microscopy (Weber et al., 2014). Prior research indicated that development is slowed at lower temperatures, reducing the metabolism and resulting in minimal movement (Urushibata et al., 2021). Combining these two strategies, I enhanced the high throughput laser injuries. Finally, the two-group approach streamlined the process, cutting the time between imaging and lasering. In conclusion, I introduced a novel high-throughput workflow for inducing laser injuries and how to optimize it for non-standard orientations.

While the two-group approach added efficiency to the workflow, it introduced a potential issue. Embryos in group A (lasered first) spend more time at 20°C after injury than group B before returning to 28°C for regeneration. I explored this issue by comparing the group-wise data from one of the repeats of temperature experiments, I specifically went for 28°C and 33°C exp (upper extreme from the temperature experiments) and found no detectable differences in the regeneration dynamics (See Figure 39). However, this temperature modulation could be a limitation for drug screening, if certain compounds exhibit temperature-dependent effects. Another potential optimization for the developed workflow would be the automated laser ROI annotation. Currently, the annotation is carried out manually, introducing a 10-20 µm difference in the laser injury lengths (See Figure 26 and Figure 33). An automated solution for annotation could address this inaccuracy while reducing the time spent annotating. Specifically, a machine learning-based model to annotate the laser ROI can enhance the precision and speed of the overall developed workflow. Beyond these technical constraints, laser-based studies present a broader challenge. Although the workflow provides a model for acute kidney injury (AKI), laser-induced injury does not fully replicate the complex pathophysiology of AKI in humans(I. A. Drummond & Davidson, 2010).

Despite these limitations, the established approach provides flexibility for investigating regeneration in other areas of the zebrafish kidney, including the proximal tubules. Although the mounting technique and orientation were optimized for imaging the distal tubules, changes would be needed to visualize proximal tubule regeneration. However, the analysis workflow could readily be applied to images of the proximal tubules. I also demonstrated the workflow's adaptability beyond kidney regeneration studies. I utilized the established prescreen and prelaser imaging workflow to induce ventral fin injury to study neutrophil swarming in zebrafish embryos (See Appendix Section 7.1.2). This emphasizes the possibility for broader

applications, as the workflow could be extended to other injury models, such as spinal cord damage, with appropriate modifications to the laser settings.

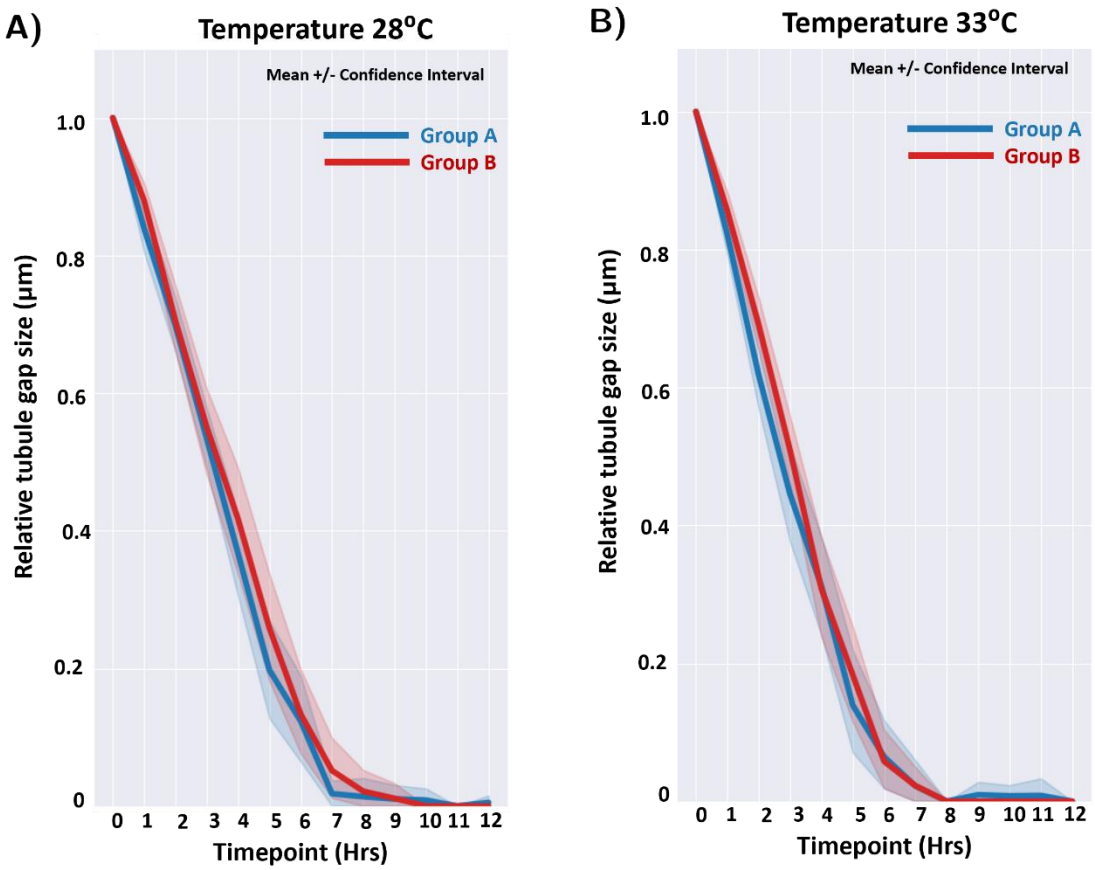

Figure 39:Comprehensive analysis of normalized regenerating tubule gap size evolution across two groups for different temperatures. Panels A) & B) Display individual sample trajectories for normalized tubule gap sizes over time during kidney regeneration mean values and 95% confidence intervals, across the groups for each temperature 28°C and 33°C respectively. The blue line indicates the trajectory for group A and the red line depicts for group B. Group A and B are just the top and bottom rows of a given plate

4.1.3. Computer-guided imaging workflow

Automating various aspects of an imaging workflow becomes crucial, especially those involving complex steps, which are time-consuming and error-prone for the end user when performed manually. Smarter microscopes and imaging workflows through automation bring robustness and efficiency, ensuring consistency in the assay (Balasubramanian et al., 2023; Carpenter et al., 2023; Strack, 2020). Given the complexity of my workflow, including steps like the temperature modulation group approach and long-term imaging of regenerating tubules, I introduced a computer

guided imaging workflow, automating almost every aspect and providing step-by-step instructions to guide users through the acquisition (See Section 3.1.4-3.1.5).

Following the development of individual workflow steps, I integrated them into a unified computer-guided imaging workflow. I developed an overarching Python script centrally controlling all the individual subprocesses and subscripts for seamless workflow execution, as shown in Figure 11. Python-based smart imaging-based workflow is currently a flourishing landscape (Pinkard et al., 2021). My workflow also adds to this landscape by providing open-source solutions focusing on the automation of complex high-throughput studies, time-lapse imaging, and workflow management. The scripting domain may vary across microscopy systems, but the overarching Python script's framework could be adapted specifically for imaging studies involving temperature-dependent experiments and differential group imaging workflows. The automated post-acquisition processing using Fiji incorporated within my workflow is a generic feature that could be an adaptable model for various imaging workflows, like max projections, making consolidated hyperstacks, etc. The developed workflow also sets an example for smart microscopy (Scherf & Huisken, 2015) in general and could be used to make the imaging conditions more gentle for living samples.

As discussed, the developed workflow could be further optimized by implementing an automated laser annotation. Implementing this feature would completely automate the current workflow. Another potential feature to add to the workflow was a sample viability report after each assay run. Currently, the workflow generates an analysis report of the laser annotations, time spent for performing each step, and temperature profiles throughout the assay, and reports any potential errors. This feature would be very relevant for screening assays, dealing with vast datasets, offering an overview of sample space, and rejecting the dead samples prior to analysis of the dataset (Kraus et al., 2017).

4.2. Virtual Orientation Tools (VOTj)

Standardizing the positioning (centering) and orientation of the object of interest is essential to ensure uniformity across the dataset. This enhances the results of object detection and classification outcomes and facilitates simple visual comparisons (Chen et al., 2022; Erickson et al., 2007). To address this, I developed a set of Fiji plugins (Schindelin et al., 2012) for centering and orienting an object of interest in an image, Virtual Orientation Tools (VOTj) (See Results Section 3.2). Compared to the traditional approaches, I aimed to provide a flexible, intuitive, and user-friendly

approach for alignment using VOTj (see Figure 13). The tool utilized Principal Component Analysis (PCA) to compute rotation and translation factors for object centering and orientation, eliminating the time-consuming pixel-by-pixel computations in conventional techniques (Satheesan et al., 2024).

Particularly in studies where consistent embryo placement and orientation would support empirical observation, such as zebrafish embryo-based toxicity and pharmacology screens (Bauer et al., 2021; Teixidó et al., 2019), VOTj is a crucial tool for addressing inconsistencies in sample mounting. By allowing post-acquisition correction of misaligned samples, VOTj would also reduce the reliance on hardware-based mounting solutions, which may be expensive, time-consuming, and stressful for embryos. The tool's capacity to identify an object's polarity ensures continuous head-tail (top-bottom/left-right) orientation for asymmetric objects like zebrafish embryos (See Figure 14A). For segmentation and object recognition, properly centered and aligned images result in better prediction (Hesamian et al., 2019; Wang et al., 2022). VOTj generates more robust datasets by standardizing the image datasets by orienting and centering the object of interest. I developed VOTj to detect and adjust the orientation of an object of interest, but the tool can also be used to determine an object's orientation. Moreover, VOTj built within the Fiji environment integrates seamlessly into various imaging workflows, aiding orientation and centering across dimensions (See Figure 14B-C).

Currently, the plugin requires user input for object annotation or mask generation, which may introduce variability. However, within the tool, I also incorporated an option to integrate automated segmentation routines to generate object-specific masks, as discussed in the results Section 3.3.3. However, situations where automated segmentation is challenging may still require manual annotations, making the process more tedious and a potential limitation. Another key limitation of the tool is that it is optimized for centering and orienting single objects per image; the ability to center and orient multiple objects within the image would be a good upgrade. Being an open-source tool developed inside the Fiji ecosystem, VOTj is still flexible and extendable for incorporating future improvements that can be made to overcome these constraints and increase the usability of the tool.

4.3. Image processing workflow for stabilizing and segmenting regenerating tubules

Accurate detection and tracking of tubule regeneration growth over time demands that the regenerating tubules within the acquired images be stable and aligned throughout the time-lapse . I developed an image processing workflow integrating standardization and segmentation pipelines for the regenerating tubules (See Results Section 3.3). Initially, I addressed the stabilization issues by employing a common and single approach, registration-based stack alignment (Thevenaz et al., 1998), and template matching methods (Thomas & Gehrig, 2020a). However, the misalignment was still considerably high, and the computation time for stabilization was high, particularly for the stack registration . Combining these two approaches enhanced the alignment, speeding processing by reducing the size of the input image (See Figure 15). The novelty of the proposed standardization pipeline (See Figure 16) lies in its three-step approach heading individual tasks, where the template matching and stack registration dealt with the stabilization of the time-lapse. Followed by VOTj centering and orienting the object of interest (regenerating tubules) within the time-lapse (See Results Section 3.3.1-3.3.3). I also noticed that the sequence of the execution of both steps impacted the final output. Initially, I applied standardization (centering and orientation) before stabilization. However, I observed that it affected the stabilization process, I speculated that the black pixel artifacts generated from transformations during standardization were skewing computations for stabilization.

Through the developed standardization pipeline, I aimed to resolve the stabilization and standardization hurdles beyond regeneration, establishing a flexible framework for stabilizing and standardizing time-lapses within the Fiji environment. I successfully employed a similar framework for stabilizing time-lapse stacks to study neutrophil swarming post-injury (See Appendix Section 7.1.3.1-7.1.3.2) and neutrophil recruitment post-substrate injection (See Appendix Section 7.2.2). In these experiments, template matching was employed for initial localization and stabilization, followed by stack registration for additional refinement. In contrast to the tubule regeneration process, I integrated the HyperStackReg plugin to execute stack registration on a designated channel (See Figure 44 &Figure 50), which could then be applied to additional channels, portraying the framework's flexibility for broader applications.

After stabilization and standardization, the segmentation pipeline facilitated the automated segmentation of regenerating tubules. I developed a conventional intensity-based threshold segmentation method within Fiji (See Results Section 3.3.4). Initially, I had also developed an Ilastik-based segmentation approach (integrated within Fiji), but I did not pursue it for the newer datasets as the intensity-based threshold segmentation was faster and computationally less demanding.

However, I observed that the current segmentation workflow required tuning the segmentation parameters a couple of times to achieve optimal results for 5–7% of samples per experiment. So, as a potential future optimization and to address the current limitations, the existing Ilastik model could be refined, or deep-learning-based segmentation approaches could be integrated. DeepImageJ (Gómez-de-Mariscal et al., 2021), a recent and now widely used Fiji plugin, offers access to pre-trained models from the BioImage Model Zoo (Ouyang et al., 2022). This could be utilized for more robust segmentation as it consists of models across biological imaging scenarios. Alternatively, a new model specifically for segmenting regenerating tubules could be trained and integrated within the plugin for segmentation. Generating such a model and making it public could extend its applicability beyond the renal tubules to other tubular structures, including spinal cord and vascular structures.

4.4. KNIME-based regeneration tracking workflow

The crucial output from a regeneration assay is tracking injury repair over time. I developed a KNIME-based regeneration tracking workflow to detect and track the regenerating edges from the standardized and segmented time-lapses (See Results Section 3.4). Through the developed workflow, I introduced a novel, simple, and user-friendly approach for detecting and tracking longitudinal regeneration/growth. The workflow was constituted by a modular structure consisting of four components: three user-configurable modules (Managing Inputs, Parameter configuration, visualizing tracking overlay, and saving outputs) and one non-configurable module (Detection and tracking).

I devised a straightforward and novel profile-based detection and tracking approach, where the regenerating tubule edges were identified based on prominent dips in the horizontal profile plots derived from segmented time-lapses (See Figure 19). I selected KNIME (Berthold et al., 2009) to implement this idea and develop the workflow mostly because it could offer end users a no-code, click-and-proceed solution and flexibility in integrating other programming languages. The first component of the workflow (See Results Section 3.4.1) organized the inputs. It automated the file matching (Selecting profiles and corresponding time-lapse automatically), eliminating potential user errors associated with manual file selection for such large datasets. Within the second component (See Results Section 3.4.2), I introduced options to allow users to define the region of interest (ROI) within the generated collated profile plot and manually include or exclude specific timepoints for the tracking and detection. This level of control made the developed workflow handle variations within the datasets. Although the option to define the region of interest existed, I noted that this was not used often while analyzing, showing the stabilization and standardization workflow's effectiveness in centering and orienting the time-lapses (See Results Section 3.3 and Discussions Section 4.3) and allowing the analysis to be performed with minimal configuration. Finally, after detection and tracking (See Results Section 3.4.3), the component responsible for visualization and saving the outputs (See Results Section 3.4.4) bridged the gap between analysis and validation by incorporating real-time visualization of tracking results. I ensured that the workflow provided an intuitive and interactive way to review the accuracy of the detection and tracking process. Additionally, automated and structured saving of results ensured that all relevant outputs were systematic, which is often a bottleneck for studies involving huge datasets. Validation against manual annotations showed

some differences in the workflow's automated annotations (See Figure 23). However, a comparable level of variation was also observed between expert and non-expert manual annotations, demonstrating that such discrepancies are inherent to human annotation. By contrast, the workflow eliminates this subjectivity, providing a bias-free and more consistent analysis.

Pose estimation is an alternative approach (Cao et al., 2021; Mathis et al., 2018; Pereira et al., 2019) to address the detection and tracking of the regenerating tubule. It is a well-established approach within the biological context, involving detecting landmarks/key points (regenerating tubule edges) and tracking their movement across time. However, this approach requires a large training dataset with manually annotated key points, followed by extensive model training and optimization, demanding significant computational resources and expertise. Additionally, widely used pose estimation-based detection and tracking tools such as DeepLabCut (Mathis et al., 2018) support only a limited number of image formats (e.g., PNG), making their direct application to fluorescence microscopy datasets challenging due to potential information loss during format conversion. The KNIME workflow that I developed provides an easy-to-use, training-free alternative that automates edge detection and tracking with minimal computational requirements. Another potential alternative to detect and track the regenerating tubules is utilizing Fiji based scratch wound healing analysis plugins (Suarez-Arnedo et al., 2020). These tools primarily detect and quantify the wound gaps in confluent cell layers. A straightforward use of this tool to detect and track the regenerating tubule is impractical, however future advancements in this tool, generalizing edge tracking would serve as an alternative to my workflow. However, my approach of analyzing the regeneration dynamics by compartmentalizing the image processing (in Fiji) and tubule detection and tracking (in KNIME) has a distinct advantage. This separation offers clear checkpoints for error detection and allows troubleshooting of individual processing steps more effectively than workflows where all steps are carried out in a single platform.

Observing hundreds of time-lapses of regenerating tubules, I noticed a consistent pattern in the tubule closure. After the tubules fused, it appeared dilated before the fluid flow was fully re-established, which subsided once the flow was restored (See Figure 40). This phenomenon has not been previously reported, likely due to the limited sample sizes in earlier studies. In the current workflow context, the completion of regeneration is marked by the closure of the injury gap. However, based on these observations, I speculate that regeneration is incomplete until fluid flow is re-established. This distinct event offers a more precise marker for regeneration

completion. Incorporating the detection of the dilation event in the workflow could improve the reporting of regeneration events. Although not necessarily for the current dataset, as it would potentially require higher-resolution imaging for accurate detection. However, such an addition would further strengthen the workflow's effectiveness and make its reporting more precise.

Beyond kidney regeneration, the developed workflow can also be utilized for other tubular regeneration (longitudinal) studies, such as spinal cord repair or vascular regeneration (Ghosh & Hui, 2018). The workflow can also be extended to handle multiple injury sites, though modifications in the current workflow would be needed to handle more than two edges. Additionally, I think the workflow has potential applications in plant developmental biology, especially in tracking shoot and root development, where the workflow needs to be adapted to detect and track just one dominant edge (Efroni et al., 2016).

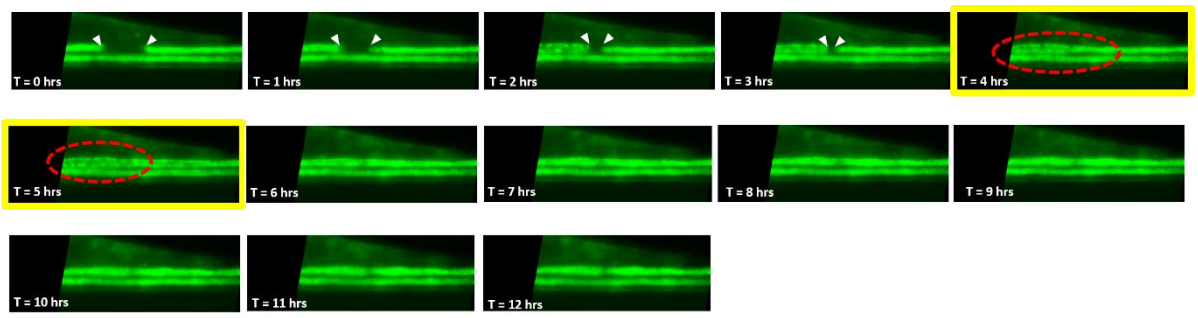

Figure 40: Time-lapse montage of regenerating tubule. This figure consists of a series of regenerating tubule images showing the regeneration process. Timepoint 4 and 5 are highlighted with a yellow box to show the dilation event (see the red circle), in the later timepoints the dilation subsides. The white spokes marked in the initial timepoints depicts the regenerating tubule edges.

4.5. Investigation of kidney regeneration at different temperatures, DMSO concentrations, and beyond

Using the developed high-throughput imaging and analysis platform, I explored the roles of temperature and DMSO levels on kidney regeneration dynamics (See results Section 3.5). Through this investigation, I also tested the developed platform's ability to validate the developed workflow's sensitivity in detecting biologically relevant changes.

I explored regeneration at four different temperatures, 20°C, 24°C, 28°C and 33°C, using the established platform (See results Section 3.5.1). The analysis of the sample viability across the temperatures showed a similar trend as shown in previous studies (Pype et al., 2015; Scott & Johnston, 2012; Urushibata et al., 2021). Embryos at 33°C showed the highest mortality during and after regeneration, whereas samples below 33°C showed no mortality during regeneration and post-regeneration (See Figure 25B). The regeneration efficiency across temperatures was established by analyzing the number of successful and unsuccessful regeneration samples. The lower temperature impaired the regeneration in samples, while as the temperature approached 28°C (the optimal developmental temperature), regeneration success improved, reaching its peak at 33°C. This trend was also reflected in the average speeds of regeneration and average closure times. The average speed of regeneration at 33°C was the fastest, followed by 28°C and 24°C, whereas 20°C had the slowest (See Figure 31). This trend was also evident for average closure time, it decreased from 20°C-33°C (See Figure 28). At 20°C, the regeneration rate remained low and constant throughout the time-lapse, reflecting a steady but slow regenerative process. 24°C showed a similar trend but with a higher rate than 20°C, indicating an intermediate regenerative capacity. However, at 28°C and 33°C, a distinct profile emerged, the regeneration velocity peaked early, followed by a gradual decline as the injury gap approached closure (See Figure 30). This pattern suggests that regeneration initiates rapidly at optimal and elevated temperatures before slowing as tubule edges close, compared to lower temperatures, where it was stagnant and no distinct peak or rapidness was employed. The platform established and confirmed a clear temperature-dependent trend for kidney regeneration dynamics.

Studies exploring the kidney regeneration dynamics across temperatures in zebrafish embryos using a laser injury are non-existent, making my investigation novel. However, studies in adult zebrafish using gentamicin-induced nephrotoxicity have

shown that higher temperatures (37°C) accelerate kidney regeneration, whereas lower temperatures (26°C) slow the process (Kamei et al., 2015). While my findings align with these observations, the injury models differ significantly. Studies report that gentamicin-induced nephrotoxicity results in diffuse kidney injury, engaging epithelial and immune-driven repair mechanisms. In the case of laser-induced injury, the injury is precise and localized but engages only the epithelial repair mechanism. However, both models capture key processes such as rapid proliferation and migration of renal tubular epithelial cells (RTECs) during regeneration (Brilli Skvarca et al., 2019; Datta et al., 2017; C. S. Johnson et al., 2011b; McKee & Wingert, 2015). As the developed platform is also based on laser-induced injury, I speculate it may exhibit regenerative phenomena similar to those observed in previous laser ablation studies.

Beyond kidney regeneration, temperature-dependent effects on regeneration have been observed in other zebrafish models. For example, in larval tail regeneration (S. L. Johnson & Weston, 1995; Sinclair et al., 2021) at 28°C, glycolysis-driven metabolic activity facilitates blastema formation, contributing to faster tissue regrowth (Sinclair et al., 2021). Similarly, reduced metabolic rates at lower temperatures slow dedifferentiation and blastema formation, delaying regeneration (D'Costa & Shepherd, 2009). Since proliferation is a key event in kidney regeneration (Toback, 1992; Witzgall et al., 1994), the observed temperature-dependent differences likely reflect cellular division and migration rate alterations. My findings suggest a similar mechanistic basis for kidney regeneration, where higher temperatures enhance cellular proliferation and tissue repair while lower temperatures suppress these processes. However, the higher temperatures enhanced regeneration at lower sample viability.

While my study confirmed a clear temperature-dependent trend in kidney regeneration, it did not directly investigate how temperature affects the underlying biological processes, such as cell proliferation and migration. Previous studies have demonstrated that proliferation and collective epithelial migration contribute to kidney repair following acute injury (Palmyre et al., 2014). However, it remains unclear whether temperature predominantly influences early migration events, later proliferation dynamics, or both. A potential future study could incorporate live-cell imaging of cellular proliferation markers alongside real-time tracking of RTEC migration, to determine whether temperature primarily alters cell migration speed, cell division rate, or both processes in parallel.

As a second validation experiment, I investigated the kidney regeneration dynamics at different DMSO concentrations (See Results Section 3.5.2). No sample deaths were observed across any of the DMSO concentrations tested, suggesting that DMSO within this range was not toxic to zebrafish embryos under these conditions. Regeneration success rates, average regeneration speeds, and closure timepoints remained highly consistent across all concentrations, with only minor fluctuations (See Figure 35 and Figure 38). The regeneration rate profiles were nearly superimposable across all DMSO concentrations, indicating that DMSO within the tested levels did not affect regeneration (See Figure 36 and Figure 37). While no direct studies on the effects of DMSO on kidney regeneration exist, previous studies using DMSO as a solvent for drug screening in zebrafish embryos have reported no significant effects on development at concentrations up to 0.5% (Brilli Skvarca et al., 2019). Studies have shown 1% as a suitable range for DMSO, citing no adverse effects on cellular processes (e.g., proliferation), critical for regeneration (Hallare et al., 2006; Hoyberghs et al., 2021). My findings align with these reports, as DMSO up to 1% did not affect kidney regeneration dynamics. For 1.5% DMSO, studies have shown that development proceeded usually, but some embryos showed minor edema. However, higher concentrations (>2%) are lethal to the embryos (Xiong et al., 2017).

For all the validation experiments, I conducted two independent repeats for each experimental condition (different temperatures and different DMSO concentrations). I observed considerable differences in nearly all quantitative attributes between the replicates across most conditions. For instance, the closure timepoints in repeat 1 for 28°Cwas 4-8 hours, and in repeat 2 was 6-10 hrs (See the green bars in Figure 28A-B), suggesting slower regeneration in the second replicate. This trend was also apparent in the average regeneration speed and profiles (Figure 29, Figure 30, and Figure 31). Due to this inherent difference among the replicates, I opted not to combine the data from the two replicates into a single dataset. Despite these differences, the overall trends remained consistent across repeats. The variability among replicates in such a large screen is expected to arise from biological and technical sources. Zebrafish embryos from the same tank show natural genetic, epigenetic, or developmental differences. With subtle variations in staging and health, the inherent dynamics can differ. Technically, factors like inconsistencies in laser injury length or measurement errors in the workflow also play a role. Incorporating experiment-specific controls (untreated but lasered samples) is essential to address this in future screening experiments. These controls would normalize each replicate's data, providing a uniform baseline for comparison or combination across experiments.

Beyond validating the platform for environmental influence on regeneration, a key step in demonstrating its practical utility is its application in a real-world compound screening study. Currently, the platform is being utilized by Leon Rapp (Westhoff lab) as part of his MD thesis, where it is being employed to screen a small 43-compound library (SCREEN-WELL® Epigenetics Library BML-2836) to identify potential drugs that influence kidney regeneration. The platform has been used to successfully screened up to 2000 embryos, with final screens underway. This study serves as a proof of concept for using the developed platform in pharmacological screening. Future works could utilize this platform for larger-scale drug screening, environmental toxins, or genetic perturbations, further establishing the platform as a valuable tool for high-throughput regeneration studies.

5

Conclusion

In this thesis, I established a novel high-throughput imaging platform for quantifying kidney regeneration in zebrafish embryos post-laser-induced injury as a benchmark for multiplexed time-lapse screening. As part of the platform's development, I have approached three major goals.

First, I established a novel lasering and imaging workflow for injuring and imaging distal renal tubules in a high-throughput manner. Automated lasering, adaptive imaging strategies, and integrating smart imaging approaches ensured robust, reproducible, and high-content data acquisition, which is crucial for screening purposes. This makes my workflow a cutting-edge framework for large-scale regenerative studies.

Second, to quantify the regeneration dynamics post-image acquisition, I established a Fiji-based image processing workflow and a KNIME-based workflow to detect and track the regenerating tubules. Virtual Orientation Tools (VOTj), a Fiji plugin I developed to standardize sample alignment across experiments as part of the image processing workflow, has broader applications and is already being adopted beyond my original assay.

Finally, the developed platform was validated by investigating the kidney regeneration dynamics at different temperatures and DMSO levels. Temperature strongly influenced the regeneration, whereas DMSO within the tested ranges did not have any influence. As a next step to establishing the platform for clinical studies, it is currently being utilized for drug screening of a small compound library.

In summary, I provide critical methodological advancements through this thesis by addressing previously unresolved technical challenges and developing a comprehensive, validated imaging and analysis platform. These contributions will facilitate new avenues for large-scale regenerative biology research and multiplexed time-lapse imaging, establishing a foundation for innovative future screening projects.

6

Materials & Methods

6.1. Ethics Statement

Zebrafish husbandry and experimental procedures were conducted in compliance with German animal welfare standards (Tierschutzgesetz 11, Abs. 1, Nr. 1, husbandry permit number 35-9185.64/BHWittbrodt)(Suzuki et al., 2024) and European Union animal welfare guidelines. The local representative of the animal welfare agency supervised the fish facility.

6.2. Materials

6.2.1. Zebrafish Lines

The wild-type strains AB and AB/Beck were used for outcross, and the following transgenic lines were used as part of the thesis.

Table 1: Transgenic fish lines used in this thesis.

Fish line name	Source
Tg(cdh17:GFP)	(Sanker et al., 2013)
Tg(mpx:GFP)	(Renshaw et al., 2006)
Tg(lysC:EGFP)	(Hall et al., 2007)

6.2.2. Chemicals and Reagents

Table 2: Chemicals and reagents used in this thesis.

Chemical/Reagents	Abbreviation/Synonym	Supplier
Agarose		Roth
Agarose Low Melting	LMA	Roth
N-Phenylthiourea	PTU	Sigma
Paraformaldehyde	PFA	Sigma
Tricaine	MS-222	Aldrich
Tris-hydrochloride	Tris-HCl	Sigma
Methyl Cellulose		Sigma
Methylene blue trihydrate		Sigma

6.2.3. Buffers and Solutions

Table 3: Buffers and solutions prepared for this thesis.

Name	Composition	Concentration
60x E3	NaCl KCl CaCl2.2H2O MgSO4.7H2O	17.2 g/l 0.76 g/l 2.9 g/l 4.9 g/l
Working E3 media (With Methylene blue)	Diluting 60x E3 Methylene blue	1x 2 mg/l
Working E3 media	Diluting 60x E3	1x
20x PTU	PTU in E3	0.06% (w/v)
Working PTU media	Diluting 20x PTU With working E3 media	0.003% (w/v)
20x Tricane	Tricane Tris-HCl 1x E3	400 mg 2.1 ml 97.9 ml

1% Agarose	Agarose 1x E3	1 g 100 ml
1% Low Melting Agarose	Low Melting Agarose 1x E3	1 g 100 ml

6.2.4. Consumables and Equipment

Table 4: Consumables used in this thesis.

Consumables	Supplier
Filter Tips 20µl,200µl,1ml	Starlab
Nitrile Gloves	Stralab
Pasteur Pipettes	Sarstedt
Petri Dishes	Greiner
Tubes 15ml, 50ml	Sarstedt
Cycloolefin film bottom Well Plates (96 wells) (655891)	Greiner bio-one
Plastic bottom Well Plates (96 wells) (655101)	Greiner bio-one
ZF Plates (96 wells) (HDK-ZFA101-02a)	Hashimoto

Table 5: Equipment used in this thesis.

Equipment	Supplier
ACQUIFER IM	ACQUIFER
Freezer -20 °C	Liebherr
Freezer -80 °C	Thermo Fisher Scientific
Fridge 4 °C	Liebherr
Microwave R-939	Sharp
Pipettes 2µl, 10µl, 20µl, 200µl, 1 ml	Eppendorf
Parafilm	Pechiney Plastic Packaging
Multipette plus	Eppendorf

Stereomicroscope SMZ18	Nikon
Epi microscope	Nikon
Fish Incubator	VWR
Forceps 5, 55 Inox stainless steel	Dumont
Microinjection needle puller	Sutter Instrument P-87
Microinjector	Eppendorf FemtoJet

6.3. Hardware and Software

6.3.1. Hardware configuration

This thesis's workflow pipelines and software depend on freely available open-source projects that function uniformly across major operating systems (Windows, Mac, Linux). While no specific hardware requirements are needed to run the developed pipelines and software, a list of the hardware configurations used for this thesis is provided below.

Table 6: List of the hardware configurations used for this thesis.

Component	Laptop	Workstation- I	Workstation-II
Main purpose	General	Workflow development, Processing	Imaging, Visualization
Processor	11th Gen Intel(R) Core(TM) i5-1135G7 @ 2.40GHz	Intel(R) Xenon(R) CPU E5-1650 v3 @ 3.50GHz	Intel(R) Xenon(R) CPU E5-1650 v3 @ 3.50GHz
OS	Windows 10 64-bit	Windows Server 2012 R2	Windows Server 2012 R2
RAM	16 GB	128 GB	128 GB
GPU	Intel(R) Iris(R) Xe Graphics	NVIDIA Quadro P4000	
Storage capacity	500 GB	22 TB	13 TB

Vendor	HP	ACQUIFER Imaging	ACQUIFER Imaging

6.3.2. FIJI

FIJI/ImageJ (Schindelin et al., 2012) is user-friendly cross-platform software for scientific image analysis. Fiji is built on top of ImageJ and has additional functionalities and libraries. Most plugins reported here require some of these libraries and are, thus, incompatible with ImageJ.

The archived version of FIJI used in the thesis can be downloaded from the provided link (https://doi.org/10.5281/zenodo.15046681). Below is a list of additional plugins installed as part of this thesis. To install them, activate the dedicated update sites through Menu Help > Update… then Manage update sites and select the corresponding sites.

Table 7: List of Fiji plugins/libraries used for this thesis.

Plugin/Library	Reference
ImageJ API	(Rasband & and ImageJ contributors, n.d.)
IJ-OpenCV-plugins	(Domínguez et al., 2017)
IJPB Plugins	(MorphoLibJ: Integrated Library and Plugins for Mathematical Morphology with ImageJ | Bioinformatics | Oxford Academic, n.d.)
StarDist	(Schmidt et al., 2018)
Virtual-Orientation-Tool-VOTj	(Satheesan et al., 2024)
StackReg	(Thevenaz et al., 1998)
Multi-Template-Matching	(Thomas & Gehrig, 2020b)

6.3.3. Ilastik

Ilastik (Berg et al., 2019) is a user-friendly tool for interactive image segmentation and classification. This software was used for the segmentation step in the image analysis pipelines in this thesis, and the results Section 3.3.4 describe the use case in detail. The archived version of the used Ilastik software and trained model can be found here

(https://github.com/sankeert1999/RenalRegenToolkit/tree/main/Fiji_Macros/Segmentation/Ilastik).

6.3.4. Python

The solutions developed in this thesis were built on Python 3.9.16. Python was installed with the free Anaconda individual Python distribution available at https://www.anaconda.com/products/individual. Either Pip or Anaconda was used to install packages. Below is a list of packages installed as part of this thesis

Table 8: List of python libraries/packages used for this thesis.

Package	Reference
NumPy	(Harris et al., 2020)
Pandas	(McKinney, 2010)
OpenCV	(Bradski, G., n.d.)
KNIPImage	(KNIME Image Processing | KNIME, n.d.)
Matplotlib	(Hunter, 2007)
Seaborn	(Waskom, 2021)
Ruptures	(Truong, 2018/2024)

6.3.5. KNIME

The Konstanz Information Miner (KNIME analytics platform)(Berthold et al., 2009) is a graphical data analysis environment written in Java and built on eclipse. It allows for building complex data processing workflows by linking single processing units called nodes. Also, it enables the bridging of definite programming languages in one place. KNIME was extensively used to build the analysis workflows as part of this thesis. KNIME 4.7.8 version was used for the development of all the workflow described in this thesis. The analysis workflows developed are mentioned in the corresponding the results Sections 3.4,3.5.

6.4. Fish Husbandry

6.4.1. Maintaining adult zebrafish

The adult zebrafish stocks were kept in a controlled day/night cycle of 14 hours light/10 hours dark phase. Each zebrafish rearing tank housed 5-8 pairs of fish. Water parameters were carefully monitored, with conductivity maintained at 400-500 µS, hardness at 5° dH, pH levels between 7.0 and 7.5, and temperature within the range of 26°C to 28°C. The zebrafish were fed three times daily, and rigorous monthly assessments of water quality, including levels of ammonium and nitrate, were conducted.

6.4.2. Embryo production and collection

The adult zebrafish crosses were carried out for embryo production in Techniplast beach-style polycarbonate 1.7 l crossing cages. The crossing cages contained a sloped mesh as an inlay, which provided a shallow end in the tank as the laying activity of the fish tends to be higher in the shallow waters. This mesh also separated the eggs from the parent's post-egg laying, preventing parental egg cannibalism. Male-female zebrafish pairs were transferred in these tanks with the sloped mesh inlay in the evening before crossing. The following morning, the fish laid eggs after the lights were turned on. After egg laying, the water was drained from the tanks through a small net to collect the eggs, which were then transferred to a petri dish.

6.4.3. Raising embryos and larvae

Post-embryo production, the laid eggs were collected in a petri dish, removing dirt and debris. The embryos were then transferred to Petri dishes containing E3 media (with Methylene blue), with 60-80 eggs in each dish, and placed in fish incubators. The media was regularly cleaned, and dead embryos were removed till the onset of the experiment. Optionally, the embryos were transferred to PTU media at 24 hpf to prevent pigment formation for specific experiments. As the transgenic fish population was heterozygous, the embryos were sorted under a fluorescence microscope at 24 hpf before downstream steps.

6.5. High Throughput Imaging and Analysis Protocols

Image acquisition for all the screening experiments was done using the ACQUIFER Imaging Machine (Luxendo GmbH, Heidelberg, Germany). The imaging machine was a wide-field (inverted) high-content screening microscope featuring a white LED array for bright-field imaging, a LED fluorescence excitation light source, a CMOS (2048 x 2048 pixel) camera, a stationary plate holder in combination with movable optics, and a temperature-controlled incubation lid. The imaging machine's general scheme involved initially acquiring low-magnification images during a prescreen (2X objective), which helped identify the sample within each well and annotate the region of interest for subsequent high-magnification acquisitions (4X,10X,20X objectives) using PlateViewer software provided by ACQUIFER. The imaging machine also offered a Smart Imaging (SI) platform known as feedback microscopy, allowing the ability to script each acquisition step and automate the acquisition.

The acquired data was managed and processed using the ACQUIFER HIVE Core (Luxendo GmbH, Heidelberg, Germany). After microscopy obtained images were temporarily saved in Workstation-II (see Section 6.3.1) and later transferred to Workstation-I (see Section 6.3.1) for further downstream processing. A custom combination of Fiji, python scripts, and KNIME workflows was utilized to construct and refine the analysis pipelines. While the image processing aspect was exclusively developed in Fiji, the feature detection, tracking, and data analysis were executed through Python integrations within Knime. Please refer the following link https://www.youtube.com/watch?v=6XF1xtDSk4I&ab_channel=KNIMETV

6.5.1. Sample preparation and mounting

6.5.1.1. Preparation of 96-well plates for imaging

96-well microplates with cycloolefin bottoms (Greiner bio-one SCREENSTAR Cat.-No. 655866) were used for imaging purposes. Using a multichannel pipette, 50 µl of hot 1% low melting agarose prepared in working E3 media was pipetted into all the rows of the 96-well microplates. The low-melting agarose was allowed to cool down for 1-3 minutes, and then a 3D printed tool for dorsal orientation (Wittbrodt et al., 2014) was inserted in the low-melting agarose-filled plates for an hour. The 3D-printed tool, comprising a base plate with 96 pins, each with a cylindrical structure and a narrow top, was used to create cavities inside the low-melting agarose molds where the embryos were placed for imaging. After solidification of the low melting

agarose, the tool was removed from the imaging plate. The imaging plates were always prepared prior to the experiment.

6.5.1.2. Embryo mounting for imaging

The *Tg(cdh17*:GFP) embryos were collected from the incubator for the experiment at 3 dpf, and the chlorinated embryos were dechorionated using forceps. The embryos were transferred to a new petri dish containing the imaging media, consisting of working PTU media, tricaine (200 µg/ml), and methylcellulose (3 mg/ml). Using a 200 µl pipette tip with a small cut at the top to ensure the embryos' safety, 150 µl of imaging medium with the embryos were pipetted and transferred to the individual wells of the imaging plate. Using a bent subcutaneous injection needle, the embryos were carefully positioned in a tilted dorsal manner under a stereomicroscope. A consistent embryo orientation was maintained throughout the screening experiments and the preparation of a single imaging plate typically took 1.5-2 hours.

6.5.2. Image acquisition workflow

The imaging machine's temperature was set to 20^0C, and the imaging plate was inserted for imaging. In the initial prescreening, a single z-slice per well was acquired using a 2x 0.06 objective in a bright-field and 470nm (GFP) channel (See Table 9). The acquired prescreen data was visualized using Plateviewer (provided by ACQUIFER), and the distal renal tubule region of the Tg(cdh17:GFP) embryos was marked using the click tool for higher magnification acquisition. The coordinates of the selected region were saved within the acquisition script, and 20x prelaser images were acquired. The 20x prelaser acquisition utilized a 20x 0.45 objective in bright-field and 470nm (GFP) channel, acquiring 15 z-slices with a ΔZ of 3µm per well (See Table 10). A 2-step software autofocus was used to find the optimal focal plane in the Z-axis (See Table 11). Subsequently, the images were used for laser annotation to perform laser injury in the annotated region (section 6.5.3).

The prescreen, prelaser acquisitions, laser injury were conducted in two groups. Group A (first four rows of the imaging plate) underwent the entire imaging and laser ablation process first, followed by Group B (remaining four rows of the imaging plate).

Table 9: Imaging parameters for 2x prescreen acquisition for kidney regeneration screens.

Channel	Power	Exposure Time
Bright-Field (BF)	30%	20 ms
470nm (GFP)	50%	50 ms

Table 10: Imaging parameters for 20x prelaser and time-lapse acquisitions for kidney regeneration screens.

Channel	Power	Exposure Time	Stack step Size ΔZ	No. Z Slices
Bright-Field (BF)	30%	20 ms	3 µm	15
470nm (GFP)	50%	100 ms	3 µm	15

Table 11: Optimized 2-step Autofocus parameters for kidney regeneration screens.

Attribute	Coarse Auto Focus	Fine Auto Focus
Channel	470nm (GFP)	470nm (GFP)
Power	5%	20%
Exposure Time	5 ms	20 ms
ΔZ	50 µm	5 µm
No. Z Slices	20	10

Following laser injury of both groups, the imaging machine's temperature was set to 28^0C (corresponding temperatures were used for experiments investigating the effects of temperature on regeneration). After the temperature adjustment, the time-lapse acquisition was initiated, involving the acquisition of 15 z-slices with a ΔZ of 3µm per well. A 2-step software autofocus was used for each time point to find the optimal focal plane in the Z-axis (See Table 11), utilizing a 20x 0.45 objective in bright-field and 470nm channel. Images were acquired every hour for 12 hours (See Table 10).

To synchronize the timeline between the two groups, a 30-minute delay was introduced between the acquisitions. Group A was imaged first, followed by Group B after the delay. After the time-lapse acquisition, a 2x post-screening of the whole plate was performed. This involved acquiring 15 z-slices with a ΔZ of 3µm per well using a 2x 0.06 objective in bright-field and 470nm channel (See Table 9)

The smart imaging platform was extensively used to script each acquisition step mentioned above. These individual scripts were then integrated into a master script using Python, automating the entire workflow. The imaging machine scripts and the master Python script are available at this link (https://github.com/sankeert1999/RenalRegenToolkit/tree/main/Smart_Imaging_Scripts).

6.5.3. Laser-induced kidney tubule injury

After successfully mounting and tilted dorsally orienting and acquiring higher magnified images marking the distal renal tubule region. (kidney tubule injury, see section 6.5.1 and section 6.5.2) the images were visualized using Plateviewer, provided by ACQUIFER. Utilizing the laser annotation tool within the Plateviewer software, the images in the green channel were annotated with a rectangular region of interest with length 100 µm and tubular width encompassing the targeted area for laser-induced injury on one of the distal renal tubules (see the red box in Figure 7A).

For assay optimization, experiments used varying laser power and repeat cycles, which were configured accordingly for each experiment. The annotated regions and laser settings were then transferred to ACQUIFER's photomanipulation module (developed with Rapp Optoelectronic, Wedel, Germany), which performed automated laser injury on each embryo in the corresponding wells without further user interaction.

6.5.4. Image analysis workflow pipelines and scripts

The analysis pipeline primarily comprised an image processing segment and a segment dedicated to detecting and tracking regenerating tubules alongside data visualization and analysis. The analysis pipeline was designed to be user-friendly and tailored to users in an open-source environment. The entire pipeline is available on GitHub and can be accessed using this link (https://github.com/sankeert1999/RenalRegenToolkit).

6.5.4.1. Image preprocessing

The acquired time-lapse data was subjected to maximum intensity projection along the Z-axis for each timepoint in the green fluorescent channel. A custom Fiji macro, "Timelapse_preprocessor.ijm," was created to preprocess the maximum projected timelapse of the maximum projection. The process begins with template matching

(Thomas & Gehrig, 2020b), utilizing the first frame of the time-lapse that encompasses the tubules as the template. This template is then searched throughout the entire time-lapse. Following template matching stack registration is carried out using the StackReg plugin (Thevenaz et al., 1998). Due to the dorsal orientation, the tubules within the template-matched and registered stack displayed a tilt. To align the images along the horizontal axis and to further center them, the script used Virtual Orientation Tools (Section 6.6) (Satheesan et al., 2024) in a two-step process. First, the time-lapses were centered using user annotation (marking the injury site), and then the centered time-lapse was further aligned. The aligned and centered time-lapse was further cropped using the crop function within Fiji, enclosing only the regenerating tubule region. The cropping dimensions are consistent and uniform across all samples. The script was designed to process images in batches and takes a folder of maximum projected images as input. The entire preprocessing process is automated, requiring user intervention only to mark the injury site to center the time lapses.

6.5.4.2. Image segmentation

Preprocessed time-lapses were subjected to segmentation to segment regenerating tubules. A custom Fiji macro, "Tubule_segmentation_profile_plot_batch.ijm, " processed the aligned, stabilized, and cropped time-lapse stack. The script begins with a pre-segmentation preprocessing involving a mean blur and background subtraction, with adjustable parameters that allow users to configure settings for different image sets. After pre-segmentation preprocessing, the stack was subjected to segmentation.

For experiments utilizing Ilastik, a pre-trained Ilastik model generated segmentation masks. The Ilastik software was called directly from Fiji using the Ilastik Fiji plugin (“Ilastik_Tubule_segmentation_Profile_plot_batch.ijm”), and the segmentation masks were generated. Classical default threshold within FIJI was applied in most experiments, with tunable threshold parameters adjusted according to specific experimental needs.

Once the segmentation masks were generated, they were refined using the Analyze Particles function in Fiji. The final masks were further smoothed with the MorphoLibJ plugin (*MorphoLibJ: Integrated Library and Plugins for Mathematical Morphology with ImageJ | Bioinformatics | Oxford Academic*, n.d.), and the smoothness parameters were made user-adjustable.

The final segmentation masks extracted horizontal intensity profiles from each time point and saved them as CSV files. The segmentation masks, overlays, and detected ROIs were also saved for future reference.

The script was designed to process images in batches, taking a folder of cropped, aligned, and stabilized stacks as input. The entire preprocessing workflow was automated, requiring user input only to configure the segmentation parameters before processing.

6.5.4.3. Regenerating tubule edge detection and tracking

To detect the regenerating tubule edge from the horizontal intensity profiles generated for each timepoint after segmentation, a user-friendly KNIME workflow called "Injury_Detector_Tracker.knwf" was developed.

The workflow is initiated by inputting the intensity profile and corresponding cropped and aligned time-lapse images. The loaded intensity profile is smoothed and filtered for noise reduction. With noise-reduced profiles, the workflow applies change-point detection (a Python-based "ruptures" package function) to identify the tubule edge. Once the edge is detected, the corresponding image stack with the detection overlay is displayed for user validation, the results are saved after validation.

The saved output included the tracks of both tubule edges, plots, and calculated metrics such as velocity and other parameters. The workflow also provided an option to refine the detection by allowing the user to manually adjust the search region for the tubule edge and add missing timepoints.

Additionally, the workflow featured a section dedicated to visualizing and further analyzing detection and tracking results, detailed in the Results Section 3.2 and 3.3.3.

6.6. Virtual orientation tools -VOTj

The VOTj plugins are included in a collection of Jython codes for Fiji. They are not compatible with the standalone ImageJ installation. The source code and documentation are on GitHub at the following link (https://github.com/sankeert1999/Virtual-Orientation-Tools-VOTj).

6.6.1. Installation in Fiji

The virtual orientation tools plugins can be installed in Fiji by activating the "Virtual-Orientation-Tools-VOTj" and "IJ-OpenCV" update sites. After installation, the plugins are listed in the entry Virtual Orientation Tools at the bottom of the Plugin menu list. A preconfigured Fiji bundle for Mac and Windows is also archived on Zenodo (https://zenodo.org/records/11093038). A video tutorial demonstrating the installation and usage is also available on YouTube (https://www.youtube.com/watch?v=WHeDhn1Mnpc&ab_channel=ImageJFiji)

References

Arlt, V. M., Stiborova, M., & Schmeiser, H. H. (2002). Aristolochic acid as a probable human cancer hazard in herbal remedies: A review. *Mutagenesis*, *17*(4), 265–277. https://doi.org/10.1093/mutage/17.4.265

Avanesov, A., & Malicki, J. (2010). Analysis of the Retina in the Zebrafish Model. *Methods in Cell Biology*, *100*, 153–204. https://doi.org/10.1016/B978-0-12-384892-5.00006-2

Bakkers, J. (2011). Zebrafish as a model to study cardiac development and human cardiac disease. *Cardiovascular Research*, *91*(2), 279–288. https://doi.org/10.1093/cvr/cvr098

Balasubramanian, H., Hobson, C. M., Chew, T.-L., & Aaron, J. S. (2023). Imagining the future of optical microscopy: Everything, everywhere, all at once. *Communications Biology*, *6*(1), 1–12. https://doi.org/10.1038/s42003-023-05468-9

Berg, S., Kutra, D., Kroeger, T., Straehle, C. N., Kausler, B. X., Haubold, C., Schiegg, M., Ales, J., Beier, T., Rudy, M., Eren, K., Cervantes, J. I., Xu, B., Beuttenmueller, F., Wolny, A., Zhang, C., Koethe, U., Hamprecht, F. A., & Kreshuk, A. (2019). ilastik: Interactive machine learning for (bio)image

analysis. *Nature Methods*, *16*(12), 1226–1232. https://doi.org/10.1038/s41592-019-0582-9

Bernut, A., Dupont, C., Sahuquet, A., Herrmann, J.-L., Lutfalla, G., & Kremer, L. (2015). Deciphering and Imaging Pathogenesis and Cording of Mycobacterium abscessus in Zebrafish Embryos. *Journal of Visualized Experiments : JoVE*, *103*, 53130. https://doi.org/10.3791/53130

Berthold, M. R., Cebron, N., Dill, F., Gabriel, T. R., Kötter, T., Meinl, T., Ohl, P., Thiel, K., & Wiswedel, B. (2009). KNIME - the Konstanz information miner: Version 2.0 and beyond. *ACM SIGKDD Explorations Newsletter*, *11*(1), 26–31. https://doi.org/10.1145/1656274.1656280

Bibliowicz, J., Tittle, R. K., & Gross, J. M. (2011). Toward a better understanding of human eye disease insights from the zebrafish, Danio rerio. *Progress in Molecular Biology and Translational Science*, *100*, 287–330. https://doi.org/10.1016/B978-0-12-384878-9.00007-8

Bonventre, J. V. (2003). Dedifferentiation and proliferation of surviving epithelial cells in acute renal failure. *Journal of the American Society of Nephrology: JASN*, *14 Suppl 1*, S55-61. https://doi.org/10.1097/01.asn.0000067652.51441.21

Bradski, G. (n.d.). *Opencv_library*. Dr. Dobb's Journal of Software Tools. 2236121

Breitwieser, H., Dickmeis, T., Vogt, M., Ferg, M., & Pylatiuk, C. (2018). Fully Automated Pipetting Sorting System for Different Morphological Phenotypes of Zebrafish Embryos. *SLAS Technology*, *23*(2), 128–133. https://doi.org/10.1177/2472630317745780

Brilli Skvarca, L., Han, H. I., Espiritu, E. B., Missinato, M. A., Rochon, E. R., McDaniels, M. D., Bais, A. S., Roman, B. L., Waxman, J. S., Watkins, S. C., Davidson, A. J., Tsang, M., & Hukriede, N. A. (2019). Enhancing regeneration after acute kidney injury by promoting cellular dedifferentiation in zebrafish. *Disease Models & Mechanisms*, *12*(4), dmm037390. https://doi.org/10.1242/dmm.037390

Bullen, A. (2008). Microscopic imaging techniques for drug discovery. *Nature Reviews Drug Discovery*, *7*(1), 54–67. https://doi.org/10.1038/nrd2446

Cao, Z., Hidalgo, G., Simon, T., Wei, S.-E., & Sheikh, Y. (2021). OpenPose: Realtime Multi-Person 2D Pose Estimation Using Part Affinity Fields. *IEEE Transactions on Pattern Analysis and Machine Intelligence*, *43*(1), 172–186. https://doi.org/10.1109/TPAMI.2019.2929257

Čapek, D., Safroshkin, M., Morales-Navarrete, H., Toulany, N., Arutyunov, G., Kurzbach, A., Bihler, J., Hagauer, J., Kick, S., Jones, F., Jordan, B., & Müller, P. (2023). EmbryoNet: Using deep learning to link embryonic

phenotypes to signaling pathways. *Nature Methods*, *20*(6), 815–823. https://doi.org/10.1038/s41592-023-01873-4

Carpenter, A. E., Cimini, B. A., & Eliceiri, K. W. (2023). Smart microscopes of the future. *Nature Methods*, *20*(7), 962–964. https://doi.org/10.1038/s41592-023-01912-0

Chen, Z., Li, Z., Zhang, S., Fang, L., Jiang, Q., Zhao, F., Zhou, B., & Zhao, H. (2022). *AutoAlign: Pixel-Instance Feature Aggregation for Multi-Modal 3D Object Detection*. *2*, 827–833. https://doi.org/10.24963/ijcai.2022/116

Cimini, B. A., Nørrelykke, S. F., Louveaux, M., Sladoje, N., Paul-Gilloteaux, P., Colombelli, J., & Miura, K. (2020). The NEUBIAS Gateway: A hub for bioimage analysis methods and materials. *F1000Research*, *9*, 613. https://doi.org/10.12688/f1000research.24759.1

Cirio, M. C., de Caestecker, M. P., & Hukriede, N. A. (2015). Zebrafish Models of Kidney Damage and Repair. *Current Pathobiology Reports*, *3*(2), 163–170. https://doi.org/10.1007/s40139-015-0080-4

Collins, J. L., Knippenberg, B. van, Ding, K., V.Kofman, A., Collins, J. L., Knippenberg, B. van, Ding, K., & V.Kofman, A. (2018). Time-Lapse Microscopy. In *Cell Culture*. IntechOpen. https://doi.org/10.5772/intechopen.81199

Coutu, D. L., & Schroeder, T. (2013). Probing cellular processes by long-term live imaging – historic problems and current solutions. *Journal of Cell Science*, *126*(17), 3805–3815. https://doi.org/10.1242/jcs.118349

Culley, S., Tosheva, K. L., Matos Pereira, P., & Henriques, R. (2018). SRRF: Universal live-cell super-resolution microscopy. *The International Journal of Biochemistry & Cell Biology*, *101*, 74–79. https://doi.org/10.1016/j.biocel.2018.05.014

Danuser, G. (2011). Computer Vision in Cell Biology. *Cell*, *147*(5), 973–978. https://doi.org/10.1016/j.cell.2011.11.001

Datta, R., Wong, A., Camarata, T., Tamanna, F., Ilahi, I., & Vasilyev, A. (2017). Precise Cellular Ablation Approach for Modeling Acute Kidney Injury in Developing Zebrafish. *Journal of Visualized Experiments : JoVE*, *124*, 55606. https://doi.org/10.3791/55606

D'Costa, A., & Shepherd, I. T. (2009). Zebrafish Development and Genetics: Introducing Undergraduates to Developmental Biology and Genetics in a Large Introductory Laboratory Class. *Zebrafish*, *6*(2), 169–177. https://doi.org/10.1089/zeb.2008.0562

Deindoerfer, F. H., Boris, W. B., Gangwer, J. R., Laird, C. W., & Tittsler, J. W. (1982). Automated intelligent microscopy (AIM) and its potential application in the clinical laboratory. *Clinical Chemistry*, *28*(9), 1910–1916.

Diep, C. Q., Ma, D., Deo, R. C., Holm, T. M., Naylor, R. W., Arora, N., Wingert, R. A., Bollig, F., Djordjevic, G., Lichman, B., Zhu, H., Ikenaga, T., Ono, F., Englert, C., Cowan, C. A., Hukriede, N. A., Handin, R. I., & Davidson, A. J. (2011). Identification of adult nephron progenitors capable of kidney regeneration in zebrafish. *Nature*, *470*(7332), 95–100. https://doi.org/10.1038/nature09669

Ding, Y.-J., & Chen, Y.-H. (2012). Developmental nephrotoxicity of aristolochic acid in a zebrafish model. *Toxicology and Applied Pharmacology*, *261*(1), 59–65. https://doi.org/10.1016/j.taap.2012.03.011

Domínguez, C., Heras, J., & Pascual, V. (2017). IJ-OpenCV: Combining ImageJ and OpenCV for processing images in biomedicine. *Computers in Biology and Medicine*, *84*, 189–194. https://doi.org/10.1016/j.compbiomed.2017.03.027

Dooley, K., & Zon, L. I. (2000). Zebrafish: A model system for the study of human disease. *Current Opinion in Genetics & Development*, *10*(3), 252–256. https://doi.org/10.1016/s0959-437x(00)00074-5

Driever, W., Solnica-Krezel, L., Schier, A. F., Neuhauss, S. C., Malicki, J., Stemple, D. L., Stainier, D. Y., Zwartkruis, F., Abdelilah, S., Rangini, Z., Belak, J., & Boggs, C. (1996). A genetic screen for mutations affecting embryogenesis in

zebrafish. *Development (Cambridge, England)*, *123*, 37–46. https://doi.org/10.1242/dev.123.1.37

Drummond, B. E., & Wingert, R. A. (2016). Insights into kidney stem cell development and regeneration using zebrafish. *World Journal of Stem Cells*, *8*(2), 22–31. https://doi.org/10.4252/wjsc.v8.i2.22

Drummond, I. A., & Davidson, A. J. (2010). Zebrafish kidney development. *Methods in Cell Biology*, *100*, 233–260. https://doi.org/10.1016/B978-0-12-384892-5.00009-8

Ebarasi, L., Oddsson, A., Hultenby, K., Betsholtz, C., & Tryggvason, K. (2011). Zebrafish: A model system for the study of vertebrate renal development, function, and pathophysiology. *Current Opinion in Nephrology and Hypertension*, *20*(4), 416–424. https://doi.org/10.1097/MNH.0b013e3283477797

Efroni, I., Mello, A., Nawy, T., Ip, P.-L., Rahni, R., DelRose, N., Powers, A., Satija, R., & Birnbaum, K. D. (2016). Root Regeneration Triggers an Embryo-like Sequence Guided by Hormonal Interactions. *Cell*, *165*(7), 1721–1733. https://doi.org/10.1016/j.cell.2016.04.046

Erickson, B. J., Mandrekar, J., Wang, L., Patriarche, J. W., Bartholmai, B. J., Wood, C. P., Lindell, E. P., Sykes, A.-M., Harms, G. F., Lindell, R. M., & Andirole, K. (2007). Effect of Automated Image Registration on Radiologist

Interpretation. *Journal of Digital Imaging*, *20*(2), 105–113. https://doi.org/10.1007/s10278-007-9023-x

Esner, M., Meyenhofer, F., & Bickle, M. (2018). Live-Cell High Content Screening in Drug Development. *Methods in Molecular Biology (Clifton, N.J.)*, *1683*, 149–164. https://doi.org/10.1007/978-1-4939-7357-6_10

Fadool, J. M., & Dowling, J. E. (2008). Zebrafish: A Model System for the Study of Eye Genetics. *Progress in Retinal and Eye Research*, *27*(1), 89–110. https://doi.org/10.1016/j.preteyeres.2007.08.002

Flores, E. M., Nguyen, A. T., Odem, M. A., Eisenhoffer, G. T., & Krachler, A. M. (2020). The Zebrafish as a Model for Gastrointestinal Tract—Microbe Interactions. *Cellular Microbiology*, *22*(3), e13152. https://doi.org/10.1111/cmi.13152

Frisby, J. P., & Stone, J. V. (2010). *Seeing, Second Edition: The Computational Approach to Biological Vision* (2nd ed.). The MIT Press.

Futamura, Y., Kawatani, M., Kazami, S., Tanaka, K., Muroi, M., Shimizu, T., Tomita, K., Watanabe, N., & Osada, H. (2012). Morphobase, an encyclopedic cell morphology database, and its use for drug target identification. *Chemistry & Biology*, *19*(12), 1620–1630. https://doi.org/10.1016/j.chembiol.2012.10.014

Garcia, G. R., Noyes, P. D., & Tanguay, R. L. (2016). Advancements in zebrafish applications for 21st century toxicology. *Pharmacology & Therapeutics*, *161*, 11–21. https://doi.org/10.1016/j.pharmthera.2016.03.009

Gehrig, J., Pandey, G., & Westhoff, J. H. (2018). Zebrafish as a Model for Drug Screening in Genetic Kidney Diseases. *Frontiers in Pediatrics*, *6*, 183. https://doi.org/10.3389/fped.2018.00183

Ghosh, S., & Hui, S. P. (2018). Axonal regeneration in zebrafish spinal cord. *Regeneration*, *5*(1), 43–60. https://doi.org/10.1002/reg2.99

Gierten, J., Pylatiuk, C., Hammouda, O. T., Schock, C., Stegmaier, J., Wittbrodt, J., Gehrig, J., & Loosli, F. (2020). Automated high-throughput heartbeat quantification in medaka and zebrafish embryos under physiological conditions. *Scientific Reports*, *10*(1), 2046. https://doi.org/10.1038/s41598-020-58563-w

Gómez-de-Mariscal, E., García-López-de-Haro, C., Ouyang, W., Donati, L., Lundberg, E., Unser, M., Muñoz-Barrutia, A., & Sage, D. (2021). DeepImageJ: A user-friendly environment to run deep learning models in ImageJ. *Nature Methods*, *18*(10), 1192–1195. https://doi.org/10.1038/s41592-021-01262-9

Gunnarsson, L., Jauhiainen, A., Kristiansson, E., Nerman, O., & Larsson, D. G. J. (2008). Evolutionary conservation of human drug targets in organisms used

for environmental risk assessments. *Environmental Science & Technology*, *42*(15), 5807–5813. https://doi.org/10.1021/es8005173

Guo, Y., Veneman, W. J., Spaink, H. P., & Verbeek, F. J. (2017). Three-dimensional reconstruction and measurements of zebrafish larvae from high-throughput axial-view in vivo imaging. *Biomedical Optics Express*, *8*(5), 2611–2634. https://doi.org/10.1364/BOE.8.002611

Hale, C. M., & Nojima, D. (2016). *Approaches to High Content Imaging and Multi-feature Analysis*. https://doi.org/10.1039/9781782626770-00162

Hall, C., Flores, M. V., Storm, T., Crosier, K., & Crosier, P. (2007). The zebrafish lysozyme C promoter drives myeloid-specific expression in transgenic fish. *BMC Developmental Biology*, *7*(1), 42. https://doi.org/10.1186/1471-213X-7-42

Hallare, A., Nagel, K., Köhler, H.-R., & Triebskorn, R. (2006). Comparative embryotoxicity and proteotoxicity of three carrier solvents to zebrafish (Danio rerio) embryos. *Ecotoxicology and Environmental Safety*, *63*(3), 378–388. https://doi.org/10.1016/j.ecoenv.2005.07.006

Hallou, A., Yevick, H. G., Dumitrascu, B., & Uhlmann, V. (2021). Deep learning for bioimage analysis in developmental biology. *Development*, *148*(18), dev199616. https://doi.org/10.1242/dev.199616

Harris, C. R., Millman, K. J., van der Walt, S. J., Gommers, R., Virtanen, P., Cournapeau, D., Wieser, E., Taylor, J., Berg, S., Smith, N. J., Kern, R., Picus, M., Hoyer, S., van Kerkwijk, M. H., Brett, M., Haldane, A., del Río, J. F., Wiebe, M., Peterson, P., … Oliphant, T. E. (2020). Array programming with NumPy. *Nature*, *585*(7825), 357–362. https://doi.org/10.1038/s41586-020-2649-2

Harrold, I., Carbonneau, S., Moore, B. M., Nguyen, G., Anderson, N. M., Saini, A. S., Kanki, J. P., Jette, C. A., & Feng, H. (2016). Efficient transgenesis mediated by pigmentation rescue in zebrafish. *BioTechniques*, *60*(1), 13–20. https://doi.org/10.2144/000114368

He, B., Ebarasi, L., Hultenby, K., Tryggvason, K., & Betsholtz, C. (2011). Podocin-Green Fluorescence Protein Allows Visualization and Functional Analysis of Podocytes. *Journal of the American Society of Nephrology : JASN*, *22*(6), 1019. https://doi.org/10.1681/ASN.2010121291

Hentschel, D. M., Park, K. M., Cilenti, L., Zervos, A. S., Drummond, I., & Bonventre, J. V. (2005). Acute renal failure in zebrafish: A novel system to study a complex disease. *American Journal of Physiology-Renal Physiology*, *288*(5), F923–F929. https://doi.org/10.1152/ajprenal.00386.2004

Hesamian, M. H., Jia, W., He, X., & Kennedy, P. (2019). Deep Learning Techniques for Medical Image Segmentation: Achievements and Challenges.

Journal of Digital Imaging, *32*(4), 582–596. https://doi.org/10.1007/s10278-019-00227-x

Hmeljak, J., & Agullo-Pascual, E. (2021). Celebrating FocalPlane and microscopy in Disease Models & Mechanisms. *Disease Models & Mechanisms*, *14*(7), dmm049183. https://doi.org/10.1242/dmm.049183

Hooke, R., Hooke, R., Allestry, J., & Martyn, J. (1665). *Micrographia, or, Some physiological descriptions of minute bodies made by magnifying glasses :with observations and inquiries thereupon* (pp. 1–323). Printed by Jo. Martyn and Ja. Allestry, printers to the Royal Society. https://doi.org/10.5962/bhl.title.904

Hostetter, C. L., Sullivan-Brown, J. L., & Burdine, R. D. (2003). Zebrafish pronephros: A model for understanding cystic kidney disease. *Developmental Dynamics: An Official Publication of the American Association of Anatomists*, *228*(3), 514–522. https://doi.org/10.1002/dvdy.10371

Howe, K., Clark, M. D., Torroja, C. F., Torrance, J., Berthelot, C., Muffato, M., Collins, J. E., Humphray, S., McLaren, K., Matthews, L., McLaren, S., Sealy, I., Caccamo, M., Churcher, C., Scott, C., Barrett, J. C., Koch, R., Rauch, G.-J., White, S., … Stemple, D. L. (2013). The zebrafish reference genome sequence and its relationship to the human genome. *Nature*, *496*(7446), 498–503. https://doi.org/10.1038/nature12111

Hoyberghs, J., Bars, C., Ayuso, M., Ginneken, C. V., Foubert, K., & Cruchten, S. V. (2021). DMSO Concentrations up to 1% are Safe to be Used in the Zebrafish Embryo Developmental Toxicity Assay. *Frontiers in Toxicology*, *3*, 804033. https://doi.org/10.3389/ftox.2021.804033

Hunter, J. D. (2007). Matplotlib: A 2D Graphics Environment. *Computing in Science & Engineering*, *9*(3), 90–95. Computing in Science & Engineering. https://doi.org/10.1109/MCSE.2007.55

Jan, M., Spangaro, A., Lenartowicz, M., & Mattiazzi Usaj, M. (2024). From pixels to insights: Machine learning and deep learning for bioimage analysis. *BioEssays*, *46*(2), 2300114. https://doi.org/10.1002/bies.202300114

Johnson, C. S., Holzemer, N. F., & Wingert, R. A. (2011a). Laser Ablation of the Zebrafish Pronephros to Study Renal Epithelial Regeneration. *Journal of Visualized Experiments : JoVE*, *54*, 2845. https://doi.org/10.3791/2845

Johnson, C. S., Holzemer, N. F., & Wingert, R. A. (2011b). Laser Ablation of the Zebrafish Pronephros to Study Renal Epithelial Regeneration. *Journal of Visualized Experiments : JoVE*, *54*, 2845. https://doi.org/10.3791/2845

Johnson, S. L., & Weston, J. A. (1995). Temperature-sensitive mutations that cause stage-specific defects in Zebrafish fin regeneration. *Genetics*, *141*(4), 1583–1595. https://doi.org/10.1093/genetics/141.4.1583

Kamei, C. N., Liu, Y., & Drummond, I. A. (2015). Kidney Regeneration in Adult Zebrafish by Gentamicin Induced Injury. *Journal of Visualized Experiments: JoVE*, *102*, e51912. https://doi.org/10.3791/51912

Kanther, M., Sun, X., Mühlbauer, M., Mackey, L. C., Flynn, E. J., Bagnat, M., Jobin, C., & Rawls, J. F. (2011). Microbial colonization induces dynamic temporal and spatial patterns of NF-κB activation in the zebrafish digestive tract. *Gastroenterology*, *141*(1), 197–207. https://doi.org/10.1053/j.gastro.2011.03.042

Keller, P. J., Schmidt, A. D., Wittbrodt, J., & Stelzer, E. H. K. (2008). Reconstruction of zebrafish early embryonic development by scanned light sheet microscopy. *Science (New York, N.Y.)*, *322*(5904), 1065–1069. https://doi.org/10.1126/science.1162493

Khalili, A., & Rezai, P. (2019). Microfluidic devices for embryonic and larval zebrafish studies. *Briefings in Functional Genomics*, *18*(6), 419–432. https://doi.org/10.1093/bfgp/elz006

Kimmel, C. B., Ballard, W. W., Kimmel, S. R., Ullmann, B., & Schilling, T. F. (1995). Stages of embryonic development of the zebrafish. *Developmental Dynamics*, *203*(3), 253–310. https://doi.org/10.1002/aja.1002030302

KNIME Image Processing / KNIME. (n.d.). Retrieved 22 August 2024, from https://www.knime.com/community/image-processing

Kraus, O. Z., Grys, B. T., Ba, J., Chong, Y., Frey, B. J., Boone, C., & Andrews, B. J. (2017). Automated analysis of high-content microscopy data with deep learning. *Molecular Systems Biology*, *13*(4), 924. https://doi.org/10.15252/msb.20177551

Kumar, S., Dunsby, C., De Beule, P. a. A., Owen, D. M., Anand, U., Lanigan, P. M. P., Benninger, R. K. P., Davis, D. M., Neil, M. a. A., Anand, P., Benham, C., Naylor, A., & French, P. M. W. (2007). Multifocal multiphoton excitation and time correlated single photon counting detection for 3-D fluorescence lifetime imaging. *Optics Express*, *15*(20), 12548–12561. https://doi.org/10.1364/oe.15.012548

Letamendia, A., Quevedo, C., Ibarbia, I., Virto, J. M., Holgado, O., Diez, M., Belmonte, J. C. I., & Callol-Massot, C. (2012). Development and Validation of an Automated High-Throughput System for Zebrafish In Vivo Screenings. *PLOS ONE*, *7*(5), e36690. https://doi.org/10.1371/journal.pone.0036690

Levet, F., Carpenter, A. E., Eliceiri, K. W., Kreshuk, A., Bankhead, P., & Haase, R. (2021). *Developing open-source software for bioimage analysis: Opportunities and challenges* (10:302). F1000Research. https://doi.org/10.12688/f1000research.52531.1

Li, Y., & Hu, B. (2012). Establishment of multi-site infection model in zebrafish larvae for studying Staphylococcus aureus infectious disease. *Journal of*

Genetics and Genomics = Yi Chuan Xue Bao, *39*(9), 521–534. https://doi.org/10.1016/j.jgg.2012.07.006

Lischik, C. Q., Adelmann, L., & Wittbrodt, J. (2019). Enhanced in vivo-imaging in medaka by optimized anaesthesia, fluorescent protein selection and removal of pigmentation. *PLoS ONE*, *14*(3), e0212956. https://doi.org/10.1371/journal.pone.0212956

Lopez-Novoa, J. M., Quiros, Y., Vicente, L., Morales, A. I., & Lopez-Hernandez, F. J. (2011). New insights into the mechanism of aminoglycoside nephrotoxicity: An integrative point of view. *Kidney International*, *79*(1), 33–45. https://doi.org/10.1038/ki.2010.337

Lubin, A., Otterstrom, J., Hoade, Y., Bjedov, I., Stead, E., Whelan, M., Gestri, G., Paran, Y., & Payne, E. (2021). A versatile, automated and high-throughput drug screening platform for zebrafish embryos. *Biology Open*, *10*(9), bio058513. https://doi.org/10.1242/bio.058513

Lucas, A. M., Ryder, P. V., Li, B., Cimini, B. A., Eliceiri, K. W., & Carpenter, A. E. (2021). Open-source deep-learning software for bioimage segmentation. *Molecular Biology of the Cell*, *32*(9), 823–829. https://doi.org/10.1091/mbc.E20-10-0660

Lukonin, I., Serra, D., Challet Meylan, L., Volkmann, K., Baaten, J., Zhao, R., Meeusen, S., Colman, K., Maurer, F., Stadler, M. B., Jenkins, J., & Liberali,

P. (2020). Phenotypic landscape of intestinal organoid regeneration. *Nature*, *586*(7828), 275–280. https://doi.org/10.1038/s41586-020-2776-9

Ma, J., He, Y., Li, F., Han, L., You, C., & Wang, B. (2024). Segment anything in medical images. *Nature Communications*, *15*(1), 654. https://doi.org/10.1038/s41467-024-44824-z

Marques, I. J., Lupi, E., & Mercader, N. (2019). Model systems for regeneration: Zebrafish. *Development (Cambridge, England)*, *146*(18), dev167692. https://doi.org/10.1242/dev.167692

Marr, D. (2010). *Vision: A Computational Investigation into the Human Representation and Processing of Visual Information*. The MIT Press. https://doi.org/10.7551/mitpress/9780262514620.001.0001

Masud, S., Torraca, V., & Meijer, A. H. (2017). Modeling Infectious Diseases in the Context of a Developing Immune System. *Current Topics in Developmental Biology*, *124*, 277–329. https://doi.org/10.1016/bs.ctdb.2016.10.006

Mathis, A., Mamidanna, P., Cury, K. M., Abe, T., Murthy, V. N., Mathis, M. W., & Bethge, M. (2018). DeepLabCut: Markerless pose estimation of user-defined body parts with deep learning. *Nature Neuroscience*, *21*(9), 1281–1289. https://doi.org/10.1038/s41593-018-0209-y

Mattiazzi Usaj, M., Styles, E. B., Verster, A. J., Friesen, H., Boone, C., & Andrews, B. J. (2016). High-Content Screening for Quantitative Cell

Biology. *Trends in Cell Biology*, *26*(8), 598–611. https://doi.org/10.1016/j.tcb.2016.03.008

McCampbell, K. K., & Wingert, R. A. (2014). New tides: Using zebrafish to study renal regeneration. *Translational Research*, *163*(2), 109–122. https://doi.org/10.1016/j.trsl.2013.10.003

McKee, R. A., & Wingert, R. A. (2015). Zebrafish Renal Pathology: Emerging Models of Acute Kidney Injury. *Current Pathobiology Reports*, *3*(2), 171–181. https://doi.org/10.1007/s40139-015-0082-2

McKinney, W. (2010). *Data Structures for Statistical Computing in Python*. 56–61. https://doi.org/10.25080/Majora-92bf1922-00a

McNamara, G., Difilippantonio, M. J., & Ried, T. (2005). Microscopy and Image Analysis. *Current Protocols in Human Genetics*, *46*(1), 4.4.1-4.4.34. https://doi.org/10.1002/0471142905.hg0404s46

Meijering, E. (n.d.). *Time-Lapse Imaging*.

Meijering, E. (2012). Cell Segmentation: 50 Years Down the Road [Life Sciences]. *IEEE Signal Processing Magazine*, *29*(5), 140–145. IEEE Signal Processing Magazine. https://doi.org/10.1109/MSP.2012.2204190

Meijering, E., Carpenter, A. E., Peng, H., Hamprecht, F. A., & Olivo-Marin, J.-C. (2016). Imagining the future of bioimage analysis. *Nature Biotechnology*, *34*(12), 1250–1255. https://doi.org/10.1038/nbt.3722

Mohd Fuad, N., Carve, M., Kaslin, J., & Wlodkowic, D. (2018). Characterization of 3D-Printed Moulds for Soft Lithography of Millifluidic Devices. *Micromachines*, *9*(3), 116. https://doi.org/10.3390/mi9030116

MorphoLibJ: integrated library and plugins for mathematical morphology with ImageJ | Bioinformatics | Oxford Academic. (n.d.). Retrieved 22 August 2024, from https://academic.oup.com/bioinformatics/article/32/22/3532/2525592?login=false

Muzzey, D., & van Oudenaarden, A. (2009). Quantitative Time-Lapse Fluorescence Microscopy in Single Cells. *Annual Review of Cell and Developmental Biology*, *25*, 301–327. https://doi.org/10.1146/annurev.cellbio.042308.113408

Nagy, G., Kiraly, G., & Banfalvi, G. (2012). Chapter 7—Optimization of Cell Cycle Measurement by Time-Lapse Microscopy. In P. M. Conn (Ed.), *Methods in Cell Biology* (Vol. 112, pp. 143–161). Academic Press. https://doi.org/10.1016/B978-0-12-405914-6.00007-X

Nguyen, C. T., Lu, Q., Wang, Y., & Chen, J.-N. (2008). Zebrafish as a model for cardiovascular development and disease. *Drug Discovery Today. Disease Models*, *5*(3), 135–140. https://doi.org/10.1016/j.ddmod.2009.02.003

North, A. J. (2006). Seeing is believing? A beginners' guide to practical pitfalls in image acquisition. *The Journal of Cell Biology*, *172*(1), 9–18. https://doi.org/10.1083/jcb.200507103

Nüsslein-Volhard, C. (2012). The zebrafish issue of Development. *Development (Cambridge, England)*, *139*(22), 4099–4103. https://doi.org/10.1242/dev.085217

Oheim, M. (2007). High-throughput microscopy must re-invent the microscope rather than speed up its functions. *British Journal of Pharmacology*, *152*(1), 1–4. https://doi.org/10.1038/sj.bjp.0707348

Oheim, M. (2011). Advances and challenges in high-throughput microscopy for live-cell subcellular imaging. *Expert Opinion on Drug Discovery*, *6*(12), 1299–1315. https://doi.org/10.1517/17460441.2011.637105

Opris¸oreanu, A.-M., Smith, H. L., Krix, S., Chaytow, H., Carragher, N. O., Gillingwater, T. H., Becker, C. G., & Becker, T. (2021). Automated in vivo drug screen in zebrafish identifies synapse-stabilising drugs with relevance to spinal muscular atrophy. *Disease Models & Mechanisms*, *14*(4), dmm047761. https://doi.org/10.1242/dmm.047761

Ouyang, W., Beuttenmueller, F., Gómez-de-Mariscal, E., Pape, C., Burke, T., Garcia-López-de-Haro, C., Russell, C., Moya-Sans, L., de-la-Torre-Gutiérrez, C., Schmidt, D., Kutra, D., Novikov, M., Weigert, M., Schmidt, U.,

Bankhead, P., Jacquemet, G., Sage, D., Henriques, R., Muñoz-Barrutia, A., … Kreshuk, A. (2022). *BioImage Model Zoo: A Community-Driven Resource for Accessible Deep Learning in BioImage Analysis* (p. 2022.06.07.495102). bioRxiv. https://doi.org/10.1101/2022.06.07.495102

Palmyre, A., Lee, J., Ryklin, G., Camarata, T., Selig, M. K., Duchemin, A.-L., Nowak, P., Arnaout, M. A., Drummond, I. A., & Vasilyev, A. (2014). Collective Epithelial Migration Drives Kidney Repair after Acute Injury. *PLOS ONE*, *9*(7), e101304. https://doi.org/10.1371/journal.pone.0101304

Pandey, G., Westhoff, J. H., Schaefer, F., & Gehrig, J. (2019). A Smart Imaging Workflow for Organ-Specific Screening in a Cystic Kidney Zebrafish Disease Model. *International Journal of Molecular Sciences*, *20*(6), Article 6. https://doi.org/10.3390/ijms20061290

Pantanowitz, L., Valenstein, P. N., Evans, A. J., Kaplan, K. J., Pfeifer, J. D., Wilbur, D. C., Collins, L. C., & Colgan, T. J. (2011). Review of the current state of whole slide imaging in pathology. *Journal of Pathology Informatics*, *2*(1), 36. https://doi.org/10.4103/2153-3539.83746

Pardo-Martin, C., Chang, T.-Y., Koo, B. K., Gilleland, C. L., Wasserman, S. C., & Yanik, M. F. (2010). High-throughput in vivo vertebrate screening. *Nature Methods*, *7*(8), 634–636. https://doi.org/10.1038/nmeth.1481

Peng, H., Zhou, J., Zhou, Z., Bria, A., Li, Y., Kleissas, D. M., Drenkow, N. G., Long, B., Liu, X., & Chen, H. (2016). Bioimage Informatics for Big Data. *Advances in Anatomy, Embryology, and Cell Biology*, *219*, 263–272. https://doi.org/10.1007/978-3-319-28549-8_10

Pepperkok, R., & Ellenberg, J. (2006). High-throughput fluorescence microscopy for systems biology. *Nature Reviews. Molecular Cell Biology*, *7*(9), 690–696. https://doi.org/10.1038/nrm1979

Pereira, T. D., Aldarondo, D. E., Willmore, L., Kislin, M., Wang, S. S.-H., Murthy, M., & Shaevitz, J. W. (2019). Fast animal pose estimation using deep neural networks. *Nature Methods*, *16*(1), 117–125. https://doi.org/10.1038/s41592-018-0234-5

Pincus, Z., & Theriot, J. A. (2007). Comparison of quantitative methods for cell-shape analysis. *Journal of Microscopy*, *227*(Pt 2), 140–156. https://doi.org/10.1111/j.1365-2818.2007.01799.x

Pinkard, H., Stuurman, N., Ivanov, I. E., Anthony, N. M., Ouyang, W., Li, B., Yang, B., Tsuchida, M. A., Chhun, B., Zhang, G., Mei, R., Anderson, M., Shepherd, D. P., Hunt-Isaak, I., Dunn, R. L., Jahr, W., Kato, S., Royer, L. A., Thiagarajah, J. R., … Waller, L. (2021). Pycro-Manager: Open-source software for customized and reproducible microscope control. *Nature Methods*, *18*(3), 226–228. https://doi.org/10.1038/s41592-021-01087-6

Poureetezadi, S. J., & Wingert, R. A. (2016). Little fish, big catch: Zebrafish as a model for kidney disease. *Kidney International*, *89*(6), 1204–1210. https://doi.org/10.1016/j.kint.2016.01.031

Prewitt, J. M., & Mendelsohn, M. L. (1966). The analysis of cell images. *Annals of the New York Academy of Sciences*, *128*(3), 1035–1053. https://doi.org/10.1111/j.1749-6632.1965.tb11715.x

Pulak, R. (2016). Tools for automating the imaging of zebrafish larvae. *Methods*, *96*, 118–126. https://doi.org/10.1016/j.ymeth.2015.11.021

Pylatiuk, C., Sanchez, D., Mikut, R., Alshut, R., Reischl, M., Hirth, S., Rottbauer, W., & Just, S. (2014). Automatic zebrafish heartbeat detection and analysis for zebrafish embryos. *Zebrafish*, *11*(4), 379–383. https://doi.org/10.1089/zeb.2014.1002

Pype, C., Verbueken, E., Saad, M. A., Casteleyn, C. R., Van Ginneken, C. J., Knapen, D., & Van Cruchten, S. J. (2015). Incubation at 32.5°C and above causes malformations in the zebrafish embryo. *Reproductive Toxicology (Elmsford, N.Y.)*, *56*, 56–63. https://doi.org/10.1016/j.reprotox.2015.05.006

Rácz, A., Allan, B., Dwyer, T., Thambithurai, D., Crespel, A., & Killen, S. S. (2021). Identification of Individual Zebrafish (Danio rerio): A Refined Protocol for VIE Tagging Whilst Considering Animal Welfare and the

Principles of the 3Rs. *Animals*, *11*(3), 616. https://doi.org/10.3390/ani11030616

Reigoto, A. M., Andrade, S. A., Seixas, M. C. R. R., Costa, M. L., & Mermelstein, C. (2021). A comparative study on the use of microscopy in pharmacology and cell biology research. *PLOS ONE*, *16*(1), e0245795. https://doi.org/10.1371/journal.pone.0245795

Rennekamp, A. J., & Peterson, R. T. (2015). 15 years of zebrafish chemical screening. *Current Opinion in Chemical Biology*, *24*, 58–70. https://doi.org/10.1016/j.cbpa.2014.10.025

Renshaw, S. A., Loynes, C. A., Trushell, D. M. I., Elworthy, S., Ingham, P. W., & Whyte, M. K. B. (2006). A transgenic zebrafish model of neutrophilic inflammation. *Blood*, *108*(13), 3976–3978. https://doi.org/10.1182/blood-2006-05-024075

Richter, L. M., Daelmans, B., Lombardi, J., Heymann, J., Boo, F. L., Behrman, J. R., Lu, C., Lucas, J. E., Perez-Escamilla, R., Dua, T., Bhutta, Z. A., Stenberg, K., Gertler, P., & Darmstadt, G. L. (2017). Investing in the foundation of sustainable development: Pathways to scale up for early childhood development. *Lancet (London, England)*, *389*(10064), 103–118. https://doi.org/10.1016/S0140-6736(16)31698-1

Rieger, S., Wang, F., & Sagasti, A. (2011). Time-lapse imaging of neural development: Zebrafish lead the way into the fourth dimension. *Genesis (New York, N.Y. : 2000)*, *49*(7), 534–545. https://doi.org/10.1002/dvg.20729

Russell, W. M. S. (1995). The development of the three Rs concept. *Alternatives to Laboratory Animals: ATLA*, *23*(3), 298–304.

Sadik, C. D., Miyabe, Y., Sezin, T., & Luster, A. D. (2018). The critical role of C5a as an initiator of neutrophil-mediated autoimmune inflammation of the joint and skin. *Seminars in Immunology*, *37*, 21–29. https://doi.org/10.1016/j.smim.2018.03.002

Samereier, M., Meyer, I., Koonce, M. P., & Gräf, R. (2010). Live Cell-Imaging Techniques for Analyses of Microtubules in *Dictyostelium*. In L. Cassimeris & P. Tran (Eds.), *Methods in Cell Biology* (Vol. 97, pp. 341–357). Academic Press. https://doi.org/10.1016/S0091-679X(10)97018-0

Sanker, S., Cirio, M. C., Vollmer, L. L., Goldberg, N. D., McDermott, L. A., Hukriede, N. A., & Vogt, A. (2013). Development of High-Content Assays for Kidney Progenitor Cell Expansion in Transgenic Zebrafish. *SLAS Discovery*, *18*(10), 1193–1202. https://doi.org/10.1177/1087057113495296

Sarder, P., & Nehorai, A. (2006). Deconvolution methods for 3-D fluorescence microscopy images. *IEEE Signal Processing Magazine*, *23*(3), 32–45. IEEE Signal Processing Magazine. https://doi.org/10.1109/MSP.2006.1628876

Satheesan, S., Gehrig, J., & Thomas, L. S. V. (2024). Virtual Orientation Tools (VOTj): Fiji plugins for object centering and alignment. *microPublication Biology*, *2024*. https://doi.org/10.17912/micropub.biology.001221

Scherf, N., & Huisken, J. (2015). The smart and gentle microscope. *Nature Biotechnology*, *33*(8), 815–818. https://doi.org/10.1038/nbt.3310

Schindelin, J., Arganda-Carreras, I., Frise, E., Kaynig, V., Longair, M., Pietzsch, T., Preibisch, S., Rueden, C., Saalfeld, S., Schmid, B., Tinevez, J.-Y., White, D. J., Hartenstein, V., Eliceiri, K., Tomancak, P., & Cardona, A. (2012). Fiji: An open-source platform for biological-image analysis. *Nature Methods*, *9*(7), 676–682. https://doi.org/10.1038/nmeth.2019

Schlaeppi, A., Adams, W., Haase, R., Huisken, J., MacDonald, R. B., Eliceiri, K. W., & Kugler, E. C. (2022). Meeting in the Middle: Towards Successful Multidisciplinary Bioimage Analysis Collaboration. *Frontiers in Bioinformatics*, *2*. https://doi.org/10.3389/fbinf.2022.889755

Schmidt, U., Weigert, M., Broaddus, C., & Myers, G. (2018). Cell Detection with Star-Convex Polygons. In A. F. Frangi, J. A. Schnabel, C. Davatzikos, C. Alberola-López, & G. Fichtinger (Eds.), *Medical Image Computing and Computer Assisted Intervention – MICCAI 2018* (pp. 265–273). Springer International Publishing. https://doi.org/10.1007/978-3-030-00934-2_30

Scott, G. R., & Johnston, I. A. (2012). Temperature during embryonic development has persistent effects on thermal acclimation capacity in zebrafish. *Proceedings of the National Academy of Sciences of the United States of America*, *109*(35), 14247–14252. https://doi.org/10.1073/pnas.1205012109

Serghiou, S., & Ioannidis, J. P. A. (2018). Altmetric Scores, Citations, and Publication of Studies Posted as Preprints. *JAMA*, *319*(4), 402. https://doi.org/10.1001/jama.2017.21168

Sharma, P., Sharma, S., Patial, V., Singh, D., & Padwad, Y. S. (2014). Zebrafish (Danio rerio): A potential model for nephroprotective drug screening. *Clinical Queries: Nephrology*, *3*(2–4), 97–105. https://doi.org/10.1016/j.cqn.2014.11.002

Sharma, V. (2018). *ImageJ plugin HyperStackReg V5.6* (Version v5.6) [Computer software]. Zenodo. https://doi.org/10.5281/zenodo.2252521

Sinclair, J. W., Hoying, D. R., Bresciani, E., Nogare, D. D., Needle, C. D., Berger, A., Wu, W., Bishop, K., Elkahloun, A. G., Chitnis, A., Liu, P., & Burgess, S. M. (2021). The Warburg effect is necessary to promote glycosylation in the blastema during zebrafish tail regeneration. *NPJ Regenerative Medicine*, *6*(1), 55. https://doi.org/10.1038/s41536-021-00163-x

Soda, P. (2014). BioImage Informatics: The challenge of knowledge extraction from biological images. *The 10th International Conference on Digital Technologies 2014*, 311–320. https://doi.org/10.1109/DT.2014.6868733

Sofroniew, N., Lambert, T., Bokota, G., Nunez-Iglesias, J., Sobolewski, P., Sweet, A., Gaifas, L., Evans, K., Burt, A., Doncila Pop, D., Yamauchi, K., Weber Mendonça, M., Buckley, G., Vierdag, W.-M., Royer, L., Can Solak, A., Harrington, K. I. S., Ahlers, J., Althviz Moré, D., … Zhao, R. (2024). *napari: A multi-dimensional image viewer for Python* (Version v0.5.4) [Computer software]. Zenodo. https://doi.org/10.5281/zenodo.13863809

Sönnichsen, B., Koski, L. B., Walsh, A., Marschall, P., Neumann, B., Brehm, M., Alleaume, A.-M., Artelt, J., Bettencourt, P., Cassin, E., Hewitson, M., Holz, C., Khan, M., Lazik, S., Martin, C., Nitzsche, B., Ruer, M., Stamford, J., Winzi, M., … Echeverri, C. J. (2005). Full-genome RNAi profiling of early embryogenesis in Caenorhabditis elegans. *Nature*, *434*(7032), 462–469. https://doi.org/10.1038/nature03353

Stelzer, E. H. K. (2015). Light-sheet fluorescence microscopy for quantitative biology. *Nature Methods*, *12*(1), 23–26. https://doi.org/10.1038/nmeth.3219

Strack, R. (2020). Smarter microscopes. *Nature Methods*, *17*(1), 23. https://doi.org/10.1038/s41592-019-0708-0

Streisinger, G., Walker, C., Dower, N., Knauber, D., & Singer, F. (1981). Production of clones of homozygous diploid zebra fish (Brachydanio rerio). *Nature*, *291*(5813), 293–296. https://doi.org/10.1038/291293a0

Stuart, G. W., Mcmurray, J. V., & Westerfield, M. (1988). Replication, integration and stable germ-line transmission of foreign sequences injected into early zebrafish embryos. *Development*, *103*(2), 403–412. https://doi.org/10.1242/dev.103.2.403

Suarez-Arnedo, A., Figueroa, F. T., Clavijo, C., Arbeláez, P., Cruz, J. C., & Muñoz-Camargo, C. (2020). An image J plugin for the high throughput image analysis of in vitro scratch wound healing assays. *PLOS ONE*, *15*(7), e0232565. https://doi.org/10.1371/journal.pone.0232565

Suzuki, R., Woo, J. Z., Thumberger, T., Hofmann, G., Wittbrodt, J., & Tavhelidse-Suck, T. (2024). Characterizing medaka visual features using a high-throughput optomotor response assay. *PloS One*, *19*(6), e0302092. https://doi.org/10.1371/journal.pone.0302092

Swanhart, L. M., Cosentino, C. C., Diep, C. Q., Davidson, A. J., de Caestecker, M., & Hukriede, N. A. (2011). Zebrafish kidney development: Basic science to translational research. *Birth Defects Research. Part C, Embryo Today: Reviews*, *93*(2), 141–156. https://doi.org/10.1002/bdrc.20209

Thevenaz, P., Ruttimann, U. E., & Unser, M. (1998). A pyramid approach to subpixel registration based on intensity. *IEEE Transactions on Image Processing*, *7*(1), 27–41. https://doi.org/10.1109/83.650848

Thomas, L. S. V., & Gehrig, J. (2020a). Multi-template matching: A versatile tool for object-localization in microscopy images. *BMC Bioinformatics*, *21*(1), 44. https://doi.org/10.1186/s12859-020-3363-7

Thomas, L. S. V., & Gehrig, J. (2020b). Multi-template matching: A versatile tool for object-localization in microscopy images. *BMC Bioinformatics*, *21*(1), 44. https://doi.org/10.1186/s12859-020-3363-7

Toback, F. G. (1992). Regeneration after acute tubular necrosis. *Kidney International*, *41*(1), 226–246. https://doi.org/10.1038/ki.1992.32

Truong, C. (2024). *Deepcharles/ruptures* [Python]. https://github.com/deepcharles/ruptures (Original work published 2018)

Urushibata, H., Sasaki, K., Takahashi, E., Hanada, T., Fujimoto, T., Arai, K., & Yamaha, E. (2021). Control of Developmental Speed in Zebrafish Embryos Using Different Incubation Temperatures. *Zebrafish*, *18*(5), 316–325. https://doi.org/10.1089/zeb.2021.0022

Vaisberg, E. A., Lenzi, D., Hansen, R. L., Keon, B. H., & Finer, J. T. (2006). [26] - An Infrastructure for High-Throughput Microscopy: Instrumentation, Informatics, and Integration. In J. Inglese (Ed.), *Methods in Enzymology*

(Vol. 414, pp. 484–512). Academic Press. https://doi.org/10.1016/S0076-6879(06)14026-4

Verghese, E., Weidenfeld, R., Bertram, J. F., Ricardo, S. D., & Deane, J. A. (2008). Renal cilia display length alterations following tubular injury and are present early in epithelial repair. *Nephrology, Dialysis, Transplantation: Official Publication of the European Dialysis and Transplant Association - European Renal Association*, *23*(3), 834–841. https://doi.org/10.1093/ndt/gfm743

Vierdag, W.-M. A. M., & Saka, S. K. (2024). A perspective on FAIR quality control in multiplexed imaging data processing. *Frontiers in Bioinformatics*, *4*, 1336257. https://doi.org/10.3389/fbinf.2024.1336257

von Chamier, L., Laine, R. F., Jukkala, J., Spahn, C., Krentzel, D., Nehme, E., Lerche, M., Hernández-Pérez, S., Mattila, P. K., Karinou, E., Holden, S., Solak, A. C., Krull, A., Buchholz, T.-O., Jones, M. L., Royer, L. A., Leterrier, C., Shechtman, Y., Jug, F., … Henriques, R. (2021). Democratising deep learning for microscopy with ZeroCostDL4Mic. *Nature Communications*, *12*(1), 2276. https://doi.org/10.1038/s41467-021-22518-0

Wang, A., Zhang, Q., Han, Y., Megason, S., Hormoz, S., Mosaliganti, K. R., Lam, J. C. K., & Li, V. O. K. (2022). A novel deep learning-based 3D cell segmentation framework for future image-based disease detection. *Scientific Reports*, *12*(1), 342. https://doi.org/10.1038/s41598-021-04048-3

Waskom, M. L. (2021). seaborn: Statistical data visualization. *Journal of Open Source Software*, *6*(60), 3021. https://doi.org/10.21105/joss.03021

Way, G. P., Sailem, H., Shave, S., Kasprowicz, R., & Carragher, N. O. (2023). Evolution and impact of high content imaging. *SLAS Discovery*, *28*(7), 292–305. https://doi.org/10.1016/j.slasd.2023.08.009

Weber, M., Mickoleit, M., & Huisken, J. (2014). Multilayer Mounting for Long-term Light Sheet Microscopy of Zebrafish. *Journal of Visualized Experiments : JoVE*, *84*, 51119. https://doi.org/10.3791/51119

Wittbrodt, J. N., Liebel, U., & Gehrig, J. (2014). Generation of orientation tools for automated zebrafish screening assays using desktop 3D printing. *BMC Biotechnology*, *14*(1), 36. https://doi.org/10.1186/1472-6750-14-36

Witzgall, R., Brown, D., Schwarz, C., & Bonventre, J. V. (1994). Localization of proliferating cell nuclear antigen, vimentin, c-Fos, and clusterin in the postischemic kidney. Evidence for a heterogenous genetic response among nephron segments, and a large pool of mitotically active and dedifferentiated cells. *The Journal of Clinical Investigation*, *93*(5), 2175–2188. https://doi.org/10.1172/JCI117214

Wong, C. C., Loewke, K. E., Bossert, N. L., Behr, B., De Jonge, C. J., Baer, T. M., & Pera, R. A. R. (2010). Non-invasive imaging of human embryos before

embryonic genome activation predicts development to the blastocyst stage. *Nature Biotechnology*, *28*(10), 1115–1121. https://doi.org/10.1038/nbt.1686

Wong, C., Chen, A. A., Behr, B., & Shen, S. (2013). Time-lapse microscopy and image analysis in basic and clinical embryo development research. *Reproductive Biomedicine Online*, *26*(2), 120–129. https://doi.org/10.1016/j.rbmo.2012.11.003

Xiong, X., Luo, S., Wu, B., & Wang, J. (2017). Comparative Developmental Toxicity and Stress Protein Responses of Dimethyl Sulfoxide to Rare Minnow and Zebrafish Embryos/Larvae. *Zebrafish*, *14*(1), 60–68. https://doi.org/10.1089/zeb.2016.1287

Yao, Y., Smal, I., Grigoriev, I., Martin, M., Akhmanova, A., & Meijering, E. (2017). Automated Analysis of Intracellular Dynamic Processes. In Y. Markaki & H. Harz (Eds.), *Light Microscopy: Methods and Protocols* (pp. 209–228). Springer. https://doi.org/10.1007/978-1-4939-6810-7_14

Zanella, F., Lorens, J. B., & Link, W. (2010). High content screening: Seeing is believing. *Trends in Biotechnology*, *28*(5), 237–245. https://doi.org/10.1016/j.tibtech.2010.02.005

Zhou, W., Boucher, R. C., Bollig, F., Englert, C., & Hildebrandt, F. (2010). Characterization of mesonephric development and regeneration using

transgenic zebrafish. *American Journal of Physiology. Renal Physiology*, *299*(5), F1040-1047. https://doi.org/10.1152/ajprenal.00394.2010

Appendix

In this section, I present my collaborative works that were not directly related to the stated aims of the thesis.

7.1. Developing a medium throughput time-lapse workflow for quantitatively analyzing the neutrophil swarming response in zebrafish embryos

Neutrophil swarming is a critical component of the immune response characterized by the active recruitment and aggregation of neutrophils at sites of damage. This process plays a crucial role in containing infections and initiating inflammation. Although the molecular processes regulating neutrophil swarming have been examined, quantitative approaches for delineating its temporal and spatial dynamics are still constrained, especially in vivo. This was the primary motivation behind the PhD research of my collaborator, Nils Olijhoek, from the University of Sheffield, Department of Infection, Immunity & Cardiovascular Disease (United Kingdom). Nils and I were part of INFLANET network, which encouraged and provided opportunities for collaborative research and allowed us to support each other's work.

While neutrophil mono-culture assays have been developed for screening swarming responses, no large-scale in vivo screening workflows for neutrophil swarming have been established. Nils collaborated with me to design and develop a medium-throughput imaging technique for capturing neutrophil swarming in zebrafish embryos following post-injury and an associated image analysis workflow for automated quantification. My role in this collaboration focused on developing robust and reproducible imaging workflows and quantitative analysis pipelines. Although this project complements the broader focus of my PhD, which centers on designing imaging and analysis workflows for zebrafish screening experiments, the biological interpretation of the swarming response falls beyond my core research and is described in detail in Nils Olijhoek's thesis.

The sections below detail the results of this collaboration, specifically highlighting my contributions to the development of the imaging and analysis workflows.

7.1.1. Designing optimal sample mounting approach for imaging neutrophil swarming

Developing an optimum sample mounting technique was a crucial initial step in this project, since it directly influenced the quality and repeatability of time-lapse imaging necessary for examining neutrophil swarming following injury. In the absence of a robust and reproducible setup, reliable images for further analysis would be unachievable.

The experiments were performed using 3 days post-fertilization (dpf) zebrafish embryos from the transgenic lines labelling neutrophils. My collaborator, Nils Olijhoek, had previously compared two different injury sites—tail fin and ventral fin—and found that ventral fin injuries allowed for capturing the entire inflammatory response within shorter timeframes. This result was crucial for creating a medium-throughput imaging assay, as reduced time-lapses facilitate increased sample throughput and mitigate data management issues linked to prolonged imaging durations. Consequent to these findings, we selected ventral fin injury as the standardized method for visualizing neutrophil swarming in these experiments.

To ensure effective imaging of neutrophil swarming, I needed to stabilize the embryos in a lateral orientation, which is ideal for visualizing the ventral fin. In contrast to the kidney regeneration studies, which required agarose molds to maintain the embryo's position (See Results Section 3.1.1.2), lateral orientation for the current setup proved to be naturally stable. I developed a simple mounting approach where embryos were pipetted with imaging media (as detailed in Section 7.1.6.1) directly into standard 96-well microplates with cycloolefin bottoms (Greiner bio-one SCREENSTAR Cat.-No. 655866) and gently nudged them into the correct lateral position when necessary (See Figure 41).

This minimal-intervention strategy had benefits, including minimal preparation time, enabling me to mount 30-40 embryos in 10-15 minutes. By avoiding agarose molds, I lowered background noise and optical interference related to the molds, therefore improving signal-to-noise ratio and image quality. This simple and reproducible nature of this mounting setup laid the foundation for reliable data acquisition in the subsequent imaging and analysis steps.

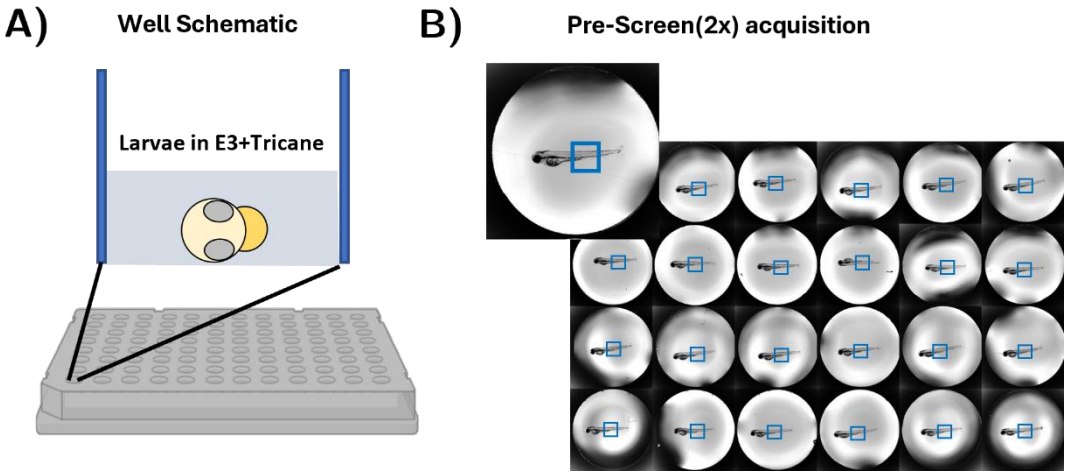

Figure 41: Sample mounting approach for imaging neutrophil swarming. A) Illustrates the schematic representation of laterally positioned zebrafish embryo within a single well, submerged in E3+Tricaine. B) This panel shows the low-magnification pre-screening images from a 96-well plate, with images acquired at 2x magnification and annotated region of interest for subsequent high- magnification imaging steps. The enlarged image highlights a representative embryo in its well, with the blue box denoting the annotated region of interest for higher- magnification imaging. Created with BioRender.com

7.1.2. Laser-induced injury and time-lapse imaging setup for acquiring neutrophil swarming

Neutrophil swarming is triggered by an injury, making it essential to produce precise and uniform injuries to the ventral fin for consistent imaging and analysis. Nils, initially performed mechanical injuries using a scalpel to induce ventral fin wounds. Mechanical injuries presented challenges, including variability in injury sizes, which might influence sample reproducibility. On the other hand, laser-induced injuries, as seen in my kidney regeneration (See Results Sections 3.1.2-3.1.3), provide enhanced accuracy and reproducibility. To overcome the constraints of mechanical injury, I adapted and optimized a laser-induced injury protocol using the photomanipulation module of the ACQUIFER Imaging Machine (IM) for ventral fin injuries (See Section 7.1.6.3).

Prior to assessing the laser parameters, standardized the area of interest (ROI) inside the ventral fin to ensure a consistent and uniform damage site and size across all samples. The injury site was consistently positioned on the ventral fin area, four somites to the right of the urogenital opening, with a set laser ROI length of 150 µm and a width of 50 µm for each sample, as seen in Figure 42. After defining the size and region of interest for laser injury, I conducted a series of trials to identify the optimal laser power and exposure settings required to injure the ventral fin consistently. I tested laser power levels ranging from 80% to 100%, each using a single

iteration of the laser. Through these trials, I found that 100% laser power with a single iteration consistently produced precise and reproducible injuries with minimal variability between samples. In contrast, lower power settings required multiple iterations (2-3) to achieve sufficient injury. However, it significantly prolonged the process, and that would eventually compromise the throughput and temporal resolution, which are critical factors for this assay. Therefore, the 100% power, single iteration setting was selected to balance efficiency and reproducibility.

Following establishing the laser-induced injury protocol, I optimized the time-lapse imaging setup to monitor neutrophil swarming events. Based on Nils's earlier results, I adjusted the imaging duration to 6 hours, which is sufficient to capture the complete swarming process, including initiation, peak neutrophil recruitment, and resolution. I conducted stress tests to evaluate the performance of the Acquifer IM under several settings to find the ideal balance between sample throughput and temporal resolution. The tests revealed that acquiring images every 5 minutes for 30 samples was the best achievable temporal resolution and sample throughput. I decided to image 24 samples for each experiment to ensure reliability and consistency, even though the system could theoretically image 30 samples per run with a 5-minute temporal resolution. This decision accounted for potential variability in acquisition time and ensured sufficient buffer to tackle it.

In contrast to kidney regeneration experiments, where the target structure was fluorescent and readily detected by the autofocus system (See Results Section 3.1.4), imaging the ventral fin posed challenges. The goal was to set the injury site as the plane of focus for time-lapse imaging. However, the injury site was only visible in the brightfield channel, as the neutrophils were imaged in the fluorescent channel and could not be relied upon to set the target for autofocus. Although neutrophils eventually accumulate at the injury site during the swarming process, they are not present immediately after injury, which made it impossible to use the fluorescent signal for autofocus. Within the brightfield channel, I attempted to use the default autofocus system, but it consistently failed to detect the wound site reliably due to interference from other brightfield structures mistakenly prioritized by the autofocus.

To address this, after inducing the injury, the z-plane for each sample was manually set, ensuring that the plane of focus was precisely aligned with the wound site. Additionally, to mitigate the effects of potential z-axis drift during the time-lapse imaging, I acquired a broader z-section of 100 µm, capturing 20 z-slices at 5 µm intervals. This setup ensured that the injury site remained within the imaging range

throughout the experiment, minimizing the risk of missing key events due to sample movement or variability in injury depth.

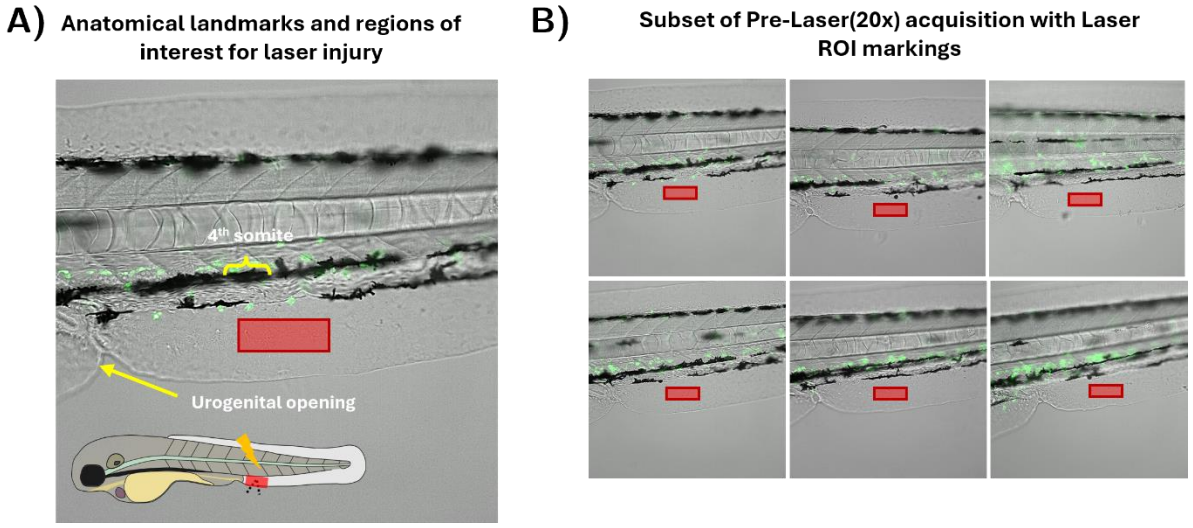

Figure 42: Anatomical landmarks and region of interest for laser-induced injury. A) The figure illustrates the region of interest for laser-induced injury and anatomical landmarks marking it. The ROI is annotated with a red box and is located four somites to the right of the urogenital opening, targeting the ventral fin region. The schematic complements the microscopy image, providing a simplified visual representation of the region of laser-induced injury. The depicted microscopic image is a composite of brightfield and green fluorescent channels, highlighting the ventral fin anatomy and neutrophils respectively. B) This panel depicts a montage of subset of pre-laser images across the plate, demonstrating consistent high- magnification (20x objective) imaging of the ventral fin region with annotated regions of injury for lasering. The images are a composite of brightfield and green fluorescent channels, highlighting the ventral fin anatomy and neutrophils respectively. Created with BioRender.com

7.1.3. Establishing an image processing pipeline to study neutrophil swarming

Following the acquisition of neutrophil swarming events, the generated time-lapses were processed using maximum intensity projection along the z-axis, producing a single plane for every timepoint. Maximum intensity projection guaranteed the preservation of essential spatial and temporal dynamics by combining data from multiple z-slices, despite some neutrophils occupying varying focal planes during the imaging. The maximum projected time-lapses were generated within Fiji and transferred to the respective experiment directories for further processing. Accurate quantification of dynamic biological processes, such as neutrophil swarming or renal tubule regeneration requires precise control over image uniformity and stabilization to minimize variability across samples and deal with motion artifacts and misalignment within time-lapse frames. Neglecting these problems may lead to errors and inconsistencies in downstream studies, especially in extensive datasets where manual adjustments are laborious and unfeasible. To ensure that the acquired time-lapses were stabilized and uniform within time and across samples, I initially started by developing a macro-based image processing pipeline “cluster analyzer.ijm” within FIJI (See Section 7.1.3), building on concepts established in my kidney regeneration experiments (See Results Section 3.3).

7.1.3.1. Template matching based region-of-injury detection

The key emphasis for downstream analysis was the injury site, where neutrophil swarming activity was concentrated within the acquired time-lapses. The injury region accounted for a tiny fraction of the whole field of view within each time-lapse frame. would introduce variability Due to embryo movement and noise from irrelevant regions, analyzing the entire image frame without proper ROI localization would compromise the accuracy and reliability of quantitative measurements. To address this, I employed a template matching-based approach for detecting and localizing the injury region across the time-lapse, an approach adapted from my previous work in kidney regeneration (See Results Section 3.3.2) and based on the plugin developed by (Thomas & Gehrig, 2020a).

The image processing pipeline started with a graphical user interface (GUI) prompting users to input folders containing the maximum projected time-lapse images for both the brightfield and fluorescent (green) channels. The brightfield channel, which captured the injury site and surrounding structures with high

contrast, was used for template matching-based ROI detection. Template matching requires selecting an optimal template to search for and track the injury region across timepoints. Through trial and optimization, I implemented a user-guided approach where the pipeline automatically displayed a rectangular box (950 x 400 pixels) centered around the injury region, and the user was prompted to confirm the box's placement at the middle timepoint of the time-lapse (See Figure 43B yellow box). Another crucial setup while designing the template involved selecting the middle timepoint of a time-lapse for template creation. We saw that using the early or late frames for template creation frequently led to mismatches and incorrect ROI detections, as frames at the beginning and end of the time-lapse often exhibited significant morphological changes in the fin injuries. Once the template was defined, it was used to search and detect the injury region throughout the time-lapse in the brightfield channel. The resulting output stacks contained cropped images with a resolution of 950 x 400 pixels (See Figure 43D), down from the original 2048 x 2048 pixels lapse (See Figure 43A). The detected ROIs in the brightfield channel were then used to crop the corresponding fluorescent (green) channel images, ensuring consistent spatial alignment across both channels. Following template matching and ROI detection, the cropped brightfield and fluorescent images were merged into a hyperstack.

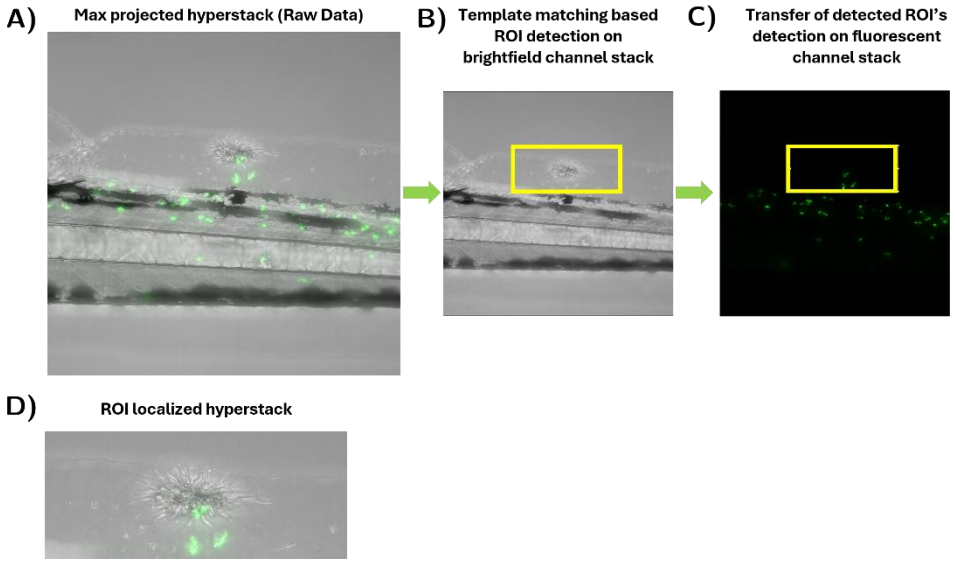

Figure 43: Template matching based region of injury detection workflow. A) This panel displays the max projected hyperstack, capturing both brightfield and fluorescent channels. B) After separating the hyperstack into individual brightfield and fluorescent channels, template matching is applied to the brightfield channel. The yellow bounding box shows the chosen area of damage used as the template to localize the injury location. C) Transferring the detected ROI from the brightfield to the fluorescent channel. D) This figure presents the hyperstack where the region of injury has been isolated and highlighted across both channels using template matching, focusing subsequent analysis on the targeted injury area.

7.1.3.2. Addressing translational drift using HyperStackReg for stack alignment

Following template matching to localize the injury region, I saw translational drift within the hypertstacks (See Results Section 3.3.1.). While template matching effectively identified and localized the region of interest (ROI) in every frame, embryo movement created misalignments between consecutive frames. Such drift artefacts presented a problem by potentially undermining the accuracy and reliability of dynamic downstream quantifications by introducing inconsistencies in tracking neutrophil movements.

To address this issue and ensure consistent alignment throughout the time-lapse hyperstacks, I employed a stack registration-based approach to address these translational drifts as a next step within the image processing pipeline. Unlike the kidney regeneration studies, in which the fluorescent channel, including the regenerating tubule, provided a consistent reference for registration (See Results Section 3.3.1.), this scenario presented additional challenges. The fluorescent channel, which captured individual neutrophils, could not be used as a reference due to the sparse and dynamic nature of neutrophil positions. I chose to base registration on the brightfield channel as it included the injury site and surrounding structures

For the registration process, I employed the HyperStackReg plugin (V. Sharma, 2018), an extension of the StackReg plugin developed by (Thevenaz et al., 1998). In contrast to StackReg, which is tailored for single-channel stacks, HyperStackReg is specifically optimized for multi-channel time-lapse hyperstacks, enabling the alignment executed on the chosen reference channel to be effortlessly applied to the equivalent frames in additional channels. The choice of the reference frame was a major factor in the registration procedure as it affected the general alignment precision. My optimization attempts and the ideas developed during template matching guided me in selecting the middle timepoint of the time-lapse as the reference frame (See Results Section 7.1.3.1), I selected the middle timepoint of the time-lapse as the reference frame. The registration process involved recursively aligning each frame to its subsequent frame, creating a continuous and stable sequence of images within the brightfield channel (See Figure 44A-B). The registration performed within the brightfield channel was seamlessly transferred to the green fluorescent channels (See Figure 44C-D).

Upon localizing the region of injury and successfully eliminating drift artifacts and I was able to produce consistently aligned time-lapse hyperstacks (See Figure 44B&D), which were crucial for accurate downstream analyses of neutrophil swarming.

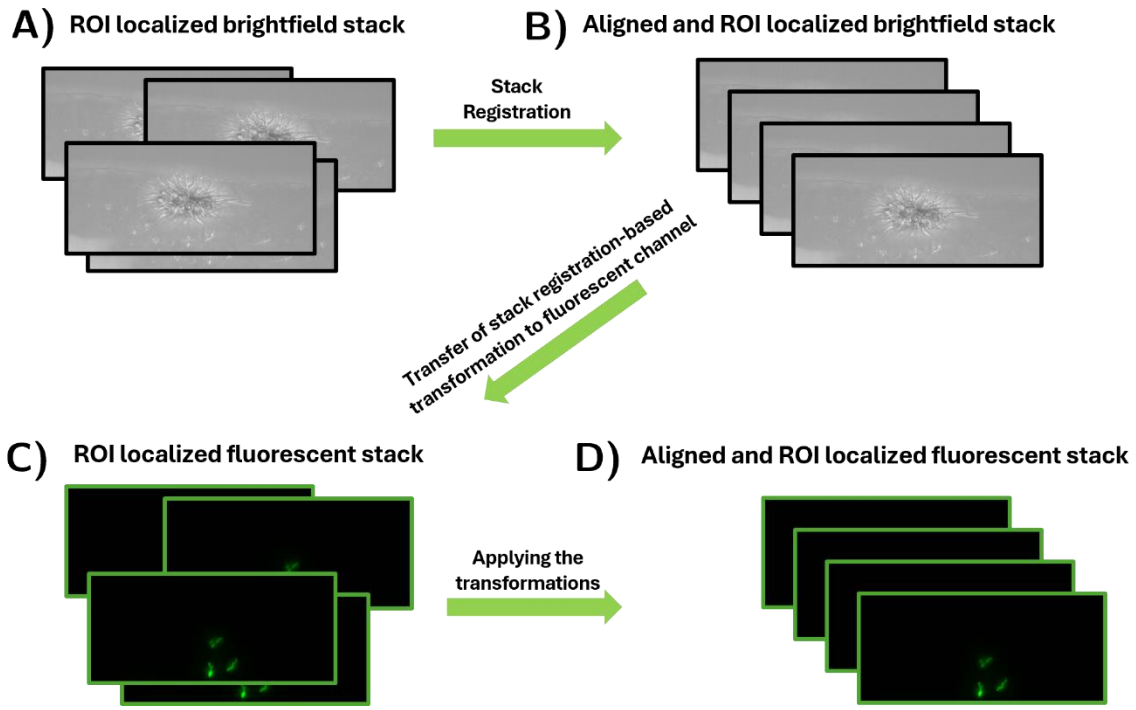

Figure 44: Hyperstackreg based stack registration workflow. After ROI localization, A) and C) show the misalignments noted in the fluorescent stacks and brightfield correspondingly. B) This figure shows the alignment of the brightfield stack using stack registration; the adjustments made here are subsequently applied to the fluorescent stack. D) Displays the aligned fluorescent stack, which has been modified depending on the changes done on the brightfield stack thereby guaranteeing constant alignment throughout both channels.

7.1.3.3. Segmentation and feature extraction

Segmenting and quantifying individual neutrophils, clusters, and swarms came next in the image processing pipeline upon localizing and stabilizing the hyperstacks (See Results Section 7.1.3.1-7.1.3.2). To achieve this, I developed a segmentation pipeline followed by feature extraction from the segmented images and automated output generation, ensuring that results were saved in user-defined directories within the pipeline.

Since segmentation was conducted on the fluorescent channel including neutrophil data, the segmentation procedure started by separating the hyperstack into its individual channels—brightfield and green fluorescent. To enable more precise and consistent segmentation, I pre-processed the fluorescence channel using a sequence of processes comprising background removal followed by a small Gaussian blur to lower noise and improve the contrast between the neutrophils and the background.

Following pre-processing, I applied an intensity-based threshold segmentation method within FIJI to segment the time-lapses and create binary masks representing neutrophils, clusters, and swarms. The thresholding parameters were carefully optimized to exclude small background artifacts or noise while retaining meaningful neutrophil signals. After segmentation, an additional filtering step was applied using the Analyze Particles function in FIJI. Customized parameters, based on the measured size range of individual neutrophils, were used to discard irrelevant objects and spurious detections.

In addition to filtering, the Analyze Particles function performed two critical tasks:

- Outlines of detections: These were saved as regions of interest (ROIs) for visualization and verification purposes (See Figure 45B).
- Quantitative measurements: For each detected neutrophil or cluster and swarms, key measurements—including area, centroid position, and intensity—were extracted and saved in structured output files (See Figure 45C).

To ensure traceability and reproducibility, I designed the pipeline to automatically save both the ROI outlines and the quantitative measurements in user-defined directories. During downstream analyses, I sought to let users quickly traverse the data, confirm found items, and track back the beginnings of any results. This structured output design ensured that the pipeline could be seamlessly integrated into further quantitative analyses of neutrophil swarming dynamics (See Figure 45A).

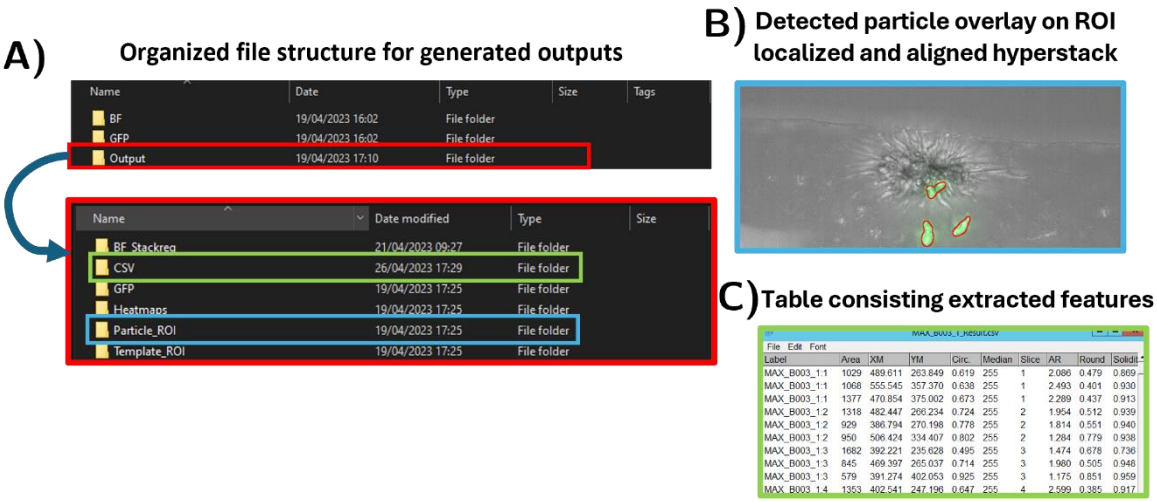

Figure 45:Overview of neutrophil segmentation and feature extraction workflow. A) This figure shows the ordered file structure of the output directory, including how methodically segmented data and analytical results are kept, therefore enabling simple access and reproducibility. Each folder is dedicated to specific outputs such as CSV files for quantitative measurements and ROI data for segmented neutrophils. B) This panel shows a detected particle overlay (in red) on an ROI-localized and aligned hyperstack. C) Illustrating the table of extracted features from the segmented neutrophils, such as area, centroid, and intensity, depicting the detailed quantitative analysis performed on each detected object.

7.1.4. Establishing a KNIME-based neutrophil swarm analysis workflow

Following the segmentation of neutrophils and the systematic extraction of key features from the processed time-lapse images (See Results Section 7.1.3), the final step in the analysis pipeline was establishing a comprehensive summary readout. The summary readout aims to offer a wholistic overview of experimental outcomes in large-scale high-throughput studies, therefore enabling an easy identification of important trends and anomalies without manual interventions. To achieve these objectives, I developed a KNIME-based workflow that integrates the results post image processing to generate summary readouts (See Figure 46A).

One of the primary objectives while designing the workflow was to facilitate data pruning, allowing efficient filtering of swarming and non-swarming samples. Instead of manually reviewing each time-lapse, a classification-based readout could guide researchers by pre-filtering swarming and non-swarming samples based on extracted image features. To classify swarming and non-swarming samples, I focused on the area of detected objects, hypothesizing that swarming samples would exhibit objects with larger areas persisting over time, whereas non-swarming samples would not show such sustained clustering.

To explore this, I computed a set of statistical attributes from the detected object areas across the time-lapse for each sample. These included, mean object area (the average area of detected objects), skewness (measure of the asymmetry of the distribution of object areas), outlier count – area measures detected as outliers), range (difference between the maximum and minimum detected area) and, kurtosis (a measure of tailedness of the distribution, indicating the presence of extreme values).

With these computed attributes, I aimed to automate sample classification using K-means clustering to separate samples into swarming and non-swarming groups. To ensure unbiased validation of the classification, previously acquired time-lapses were blinded, shuffled, and manually assessed for swarming responses. The True Positive Rate (TPR) and True Negative Rate (TNR) were calculated to evaluate classification performance (See Table 12). The TPR ranged from 50% - 87.5% accuracy, while the TNR ranged from 78.57% - 92.86%. The TPR indicated accurate classification of a swarming response, and the TNR indicated accurate classification of a non-swarming

response. Although the TPR was variable and less accurate, the TNR, skewness alone provided the highest TNR (92.86%), making it the most reliable feature for automatically identifying non-responders. For swarming samples the prediction accuracy proved inadequate, hence the automatic classification approach was abandoned.

Considering the limitations of automated classification, I explored other strategies for efficiently reviewing the data. This led to the development of an overview sheet/readout, where instead of relying solely on automated classification, this approach provided a semi-automated way for researchers to quickly assess swarming responses by combining visual and quantitative information. Within the intensity projections, the swarming samples were characterized by distinct clusters of neutrophils accumulating at the injury site, visible as high-intensity regions in the projection. Non-swarming samples, where no persistent accumulation was observed, appeared as diffuse or absent neutrophil clustering in the projection. Finally, for ambiguous cases, samples where swarming could not be classified based on projection alone; were further assessed using the extracted statistical parameters and validated through manual time-lapse review (See Figure 46B). This extensive readout along with the intensity projections, allowed to sort and filter samples efficiently (See Figure 46B). In conclusion, these data readouts fulfil different tasks, ranging from data pruning and accessibility, to aid in classifying inflammatory responses regarding neutrophil swarming, minimizing individual detection biases that can be present.

Table 12: Statistical attributes extracted from the area of detected objects across samples used to classify swarming response employing k-means clustering

Parameters	TNR	TPR
Skewness	92.86%	75%
Outlier count	85.71%	75%
Range	85.71%	50%
Skewness + Outlier count	85.71%	87.5%
Skewness + Range	78.57%	75%
Kurtosis	85.71%	75%

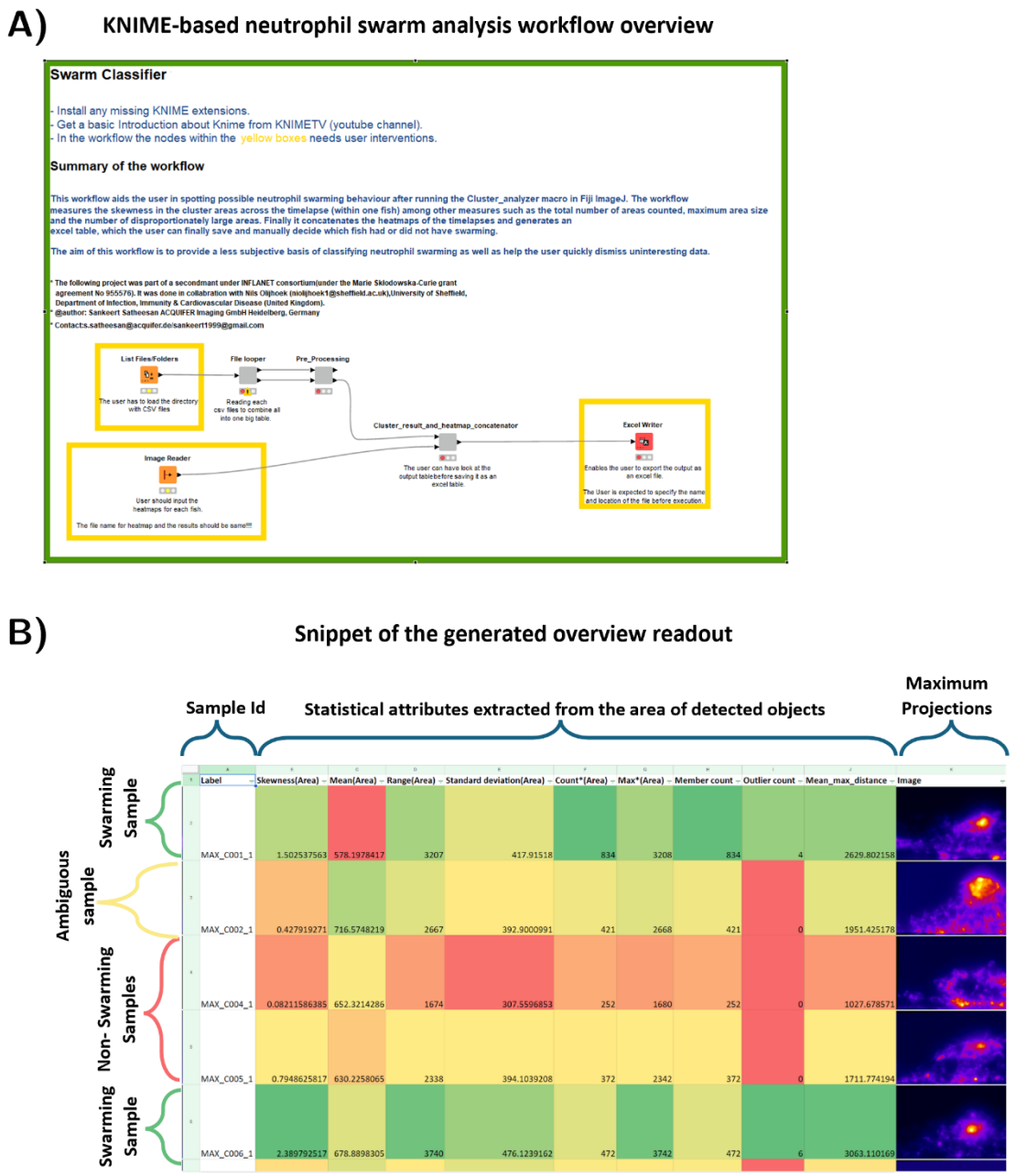

Figure 46:KNIME-based workflow for neutrophil swarm analysis. A) This figure provides a thorough overview of the KNIME based -neutrophil swarm study. Designed for user-friendliness and efficiency in managing complex datasets, it shows the modular architecture of the process. It provides a complete view of the process from initial data input to final output preparation and highlights the user-configurable nodes, marked in yellow, which need user inputs. B) This figure showcases a snippet from the produced overview readout with statistical characteristics collected from the region of identified objects combined with their matching maximum projections. This panel clearly shows the mix of quantitative and visual data, therefore enabling quick assessment of neutrophil swarming behavior across several samples and hence effective data analysis and decision-making based on swarming properties.

7.1.5. Validating the screening workflow for assessing neutrophil swarming across injury types

Following the development and enhancement of the image processing (See Results Section 7.1.1 – 7.1.4), the next step was to confirm if the proposed medium-throughput screening workflow appropriate for studying neutrophil swarming activity. Initially, the aim was to evaluate the impact of immunomodulating drugs on neutrophil swarm activity, hence validating the workflow validation. But unanticipated shipping reagent issues between the UK and Germany prevented us from obtaining the necessary chemicals within the experimental period. During initial experiments Nils had anecdotally observed that mechanical injuries elicited a seemingly stronger inflammatory response, with a greater number of neutrophils recruited to the injury site compared to laser injuries. This observation prompted us to evaluate whether the developed workflow could quantitatively detect these differences, thereby serving as a validation of the assay's capability.

To systematically assess differences in neutrophil swarming dynamics between injury types, we performed both mechanical and laser injuries on the ventral fin of 3 days post-fertilization (dpf) zebrafish larvae. To induce mechanical injuries, Nils used a scalpel to create a controlled wound in the ventral fin (See Figure 47B). Embryos were then mounted and oriented in 96-well plates, following the established sample mounting protocol (See Results Section 7.1.1). For laser injuries (See Figure 47A), embryos were first oriented in 96-well plates following the same mounting procedure, and injuries were performed using the optimized laser injury protocol via the photomanipulation module of the Acquifer Imaging Machine (IM04) (See Results Section 7.2.2). Due to the limited availability of transgenic zebrafish lines throughout the experimental phase, several tests were executed utilizing the Tg(lysC:GFP) transgenic neutrophil reporter line alongside the previously employed *Tg(mpx:GFP)* line. For both laser and mechanical injuries I conducted four independent experimental repeats, with 15–20 samples per repeat per injury type, ensuring a robust dataset for comparative analysis. Nils's thesis covers a comprehensive and detailed analysis of these results. Here, I provide a general overview of the obtained

results, focusing on how the developed workflow was used to assess neutrophil swarming across different injury modalities.

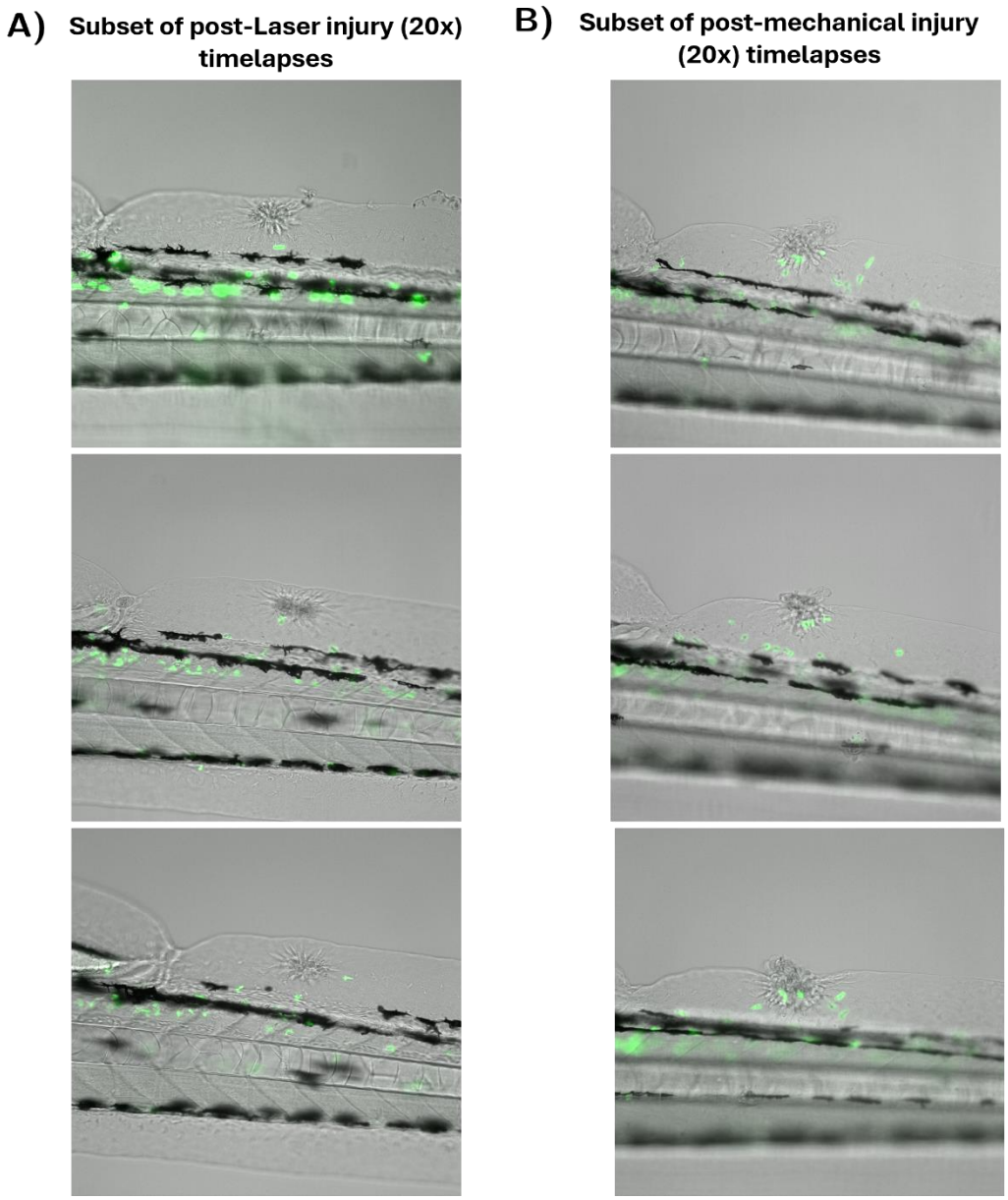

Figure 47: Representative montages consisting of images acquired post injury for A) Laser induced injuries B) Mechanically induced injuries

7.1.5.1. Comparative analysis of neutrophil swarming activity under mechanical and laser injury

The datasets were analysed using the developed image analysis workflow as detailed in results Section 7.1.3-7.1.4, following the acquisition of time-lapse images capturing neutrophil dynamics in both laser- and mechanically-induced injuries .A key challenge in ensuring a direct comparison between the two injury types was aligning the inflammatory response phases captured in each experiment. The acquired time-lapses had an inherent mismatch in the recorded time windows, as the imaging start timings for mechanical and laser injury varied.

Time-lapse imaging started one hour after the first sample was mechanically injured and captured swarming dynamics from 60 minutes post-injury (mpi) to 420 mpi during a six-hour period time-lapse. For laser injuries, imaging started 30 minutes post-injuring the first sample, covering the inflammatory response from 30 mpi to 390 mpi, also over a six-hour period. Since these experimental timelines had an offset, a direct comparison required standardization of the time frames used for analysis (See Figure 48). To address this, I adjusted the analysis window to encompass just the overlapping duration of both datasets, which was from 60 mpi to 390 mpi, (See Figure 48). This adjustment facilitated direct comparisons and guaranteed that the observed variations in neutrophil swarming dynamics were indicative of damage type rather than discrepancies in imaging procedure.

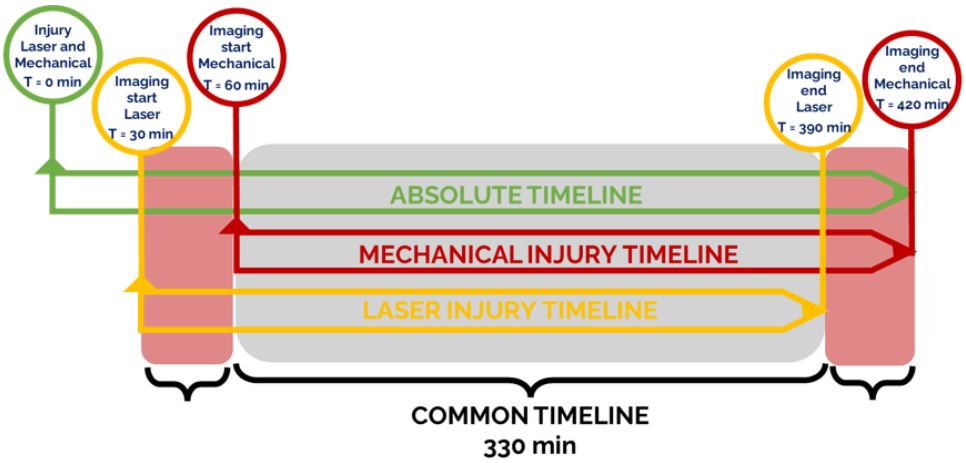

Figure 48:Timeline adjustment for laser and mechanical injury time-lapses. This schematic illustrates the adjusted timelines for capturing the inflammatory response in zebrafish following mechanical and laser-induced injuries. The timelines show the different start times for imaging: 30 minutes post-injury for laser and 60 minutes for mechanical injuries. The red and yellow timelines show the particular times when imaging took place for each type of injury. The common overlapping period from 60 to 390 minutes post-injury is highlighted, showing the standardized window for direct comparison of neutrophil dynamics between the two methods.

Initially I assessed the viability of zebrafish larvae following both mechanical and laser injuries. As shown in Figure 49A, the proportion of viable larvae was lower in the mechanically injured group relative to the laser-injured group. This result was anticipated, as mechanical injuries, executed manually with a scalpel, are intrinsically more susceptible to variability and unintentional damage. Where as in the case of laser injuries, they exhibited more control and precision, resulting in a comparatively elevated survival rate. Nevertheless, a uniform rate of sample death was noted in the laser-injured group, but to a smaller extent than in the mechanical injury group.

After filtering viable samples, as the next step we compared the proportion of larvae exhibiting a neutrophil swarming response between the two injury types using the established image processing pipeline. As seen in (See Figure 49B), neutrophil swarming occurred substantially more often in mechanically wounded larvae than in laser-affected larvae. Moreover, the maximal size of neutrophil clusters was considerably greater in mechanically wounded larvae, indicating an intensified inflammatory response (See Figure 49C). The higher prevalence of swarming in the mechanical damage group most likely indicates the more tissue damage connected to this kind of injury, which would naturally cause a stronger immunological reaction.

To further examine if variations in neutrophil swarming were affected by damage size, Nils quantified the injury size for each sample. After comparing the injury sizes across injury types, I observed that the mechanically induced injuries were larger. Moreover, the variation of wound sizes was more extensive in the mechanically damaged group, underscoring the heterogeneity linked to manual injury methods. Conversely, laser-induced injuries resulted in more uniform wound dimensions, highlighting the reliability and accuracy of laser-based injury induction (See Figure 49D).

In summary, these data demonstrated that the developed workflow could successfully detect biologically relevant differences in neutrophil swarming between injury types. The ability to quantitatively capture these differences based on prior observations highlights the feasibility of this workflow for future high throughput swarming assay studies.

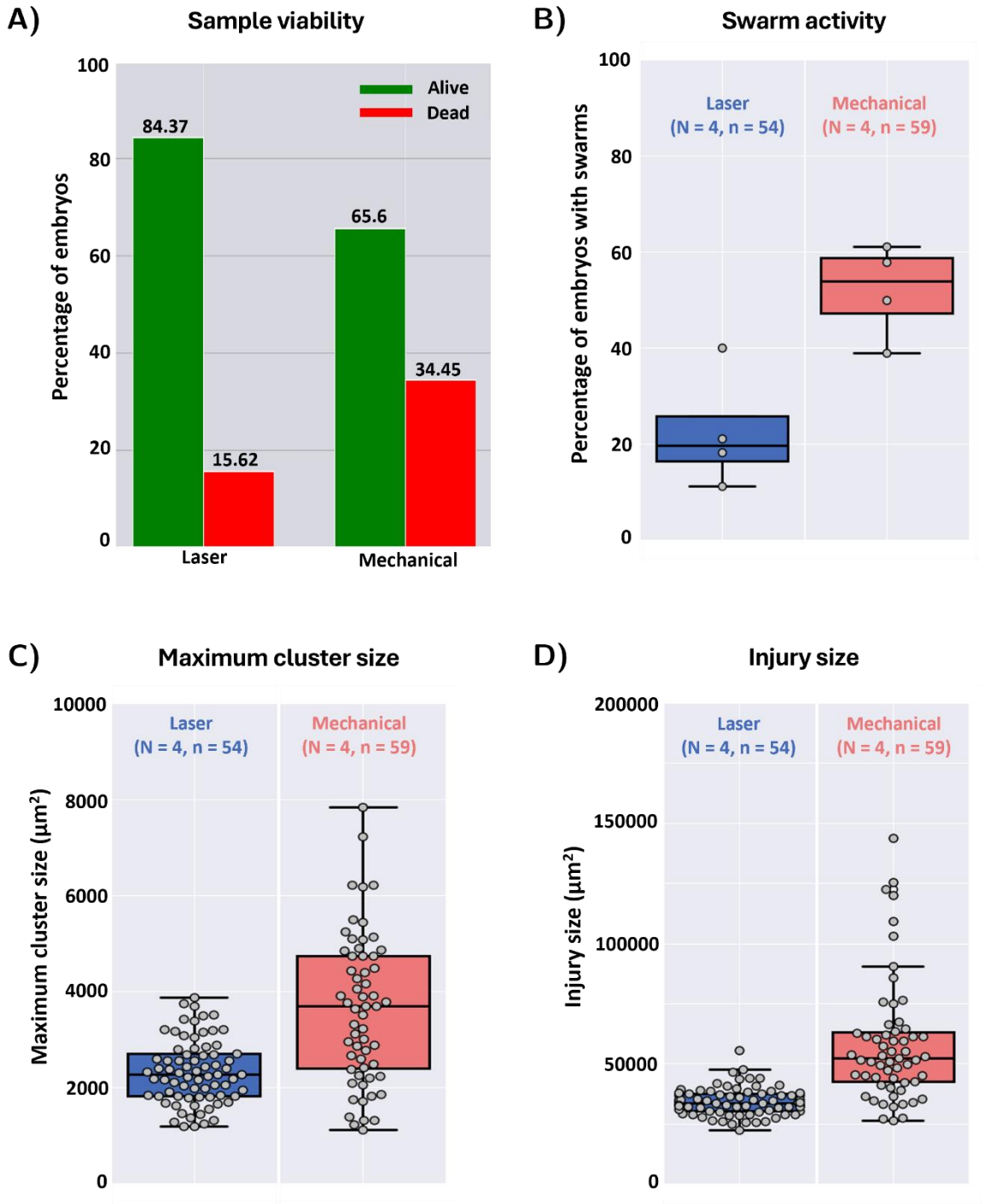

Figure 49:Comparative study of neutrophil swarming activity under laser and mechanical Injury. A) This graph compares mechanical and post-laser survival rates for zebrafish larvae. Whereas the red bars show the proportion of dead samples, the green bars show the proportion of viable embryos. B) The fraction of larvae showing neutrophil swarming following damage is shown by the box plot. Particularly in mechanically damaged larvae, swarming is very common and probably results from the greater and more erratic damage caused by hand techniques. C) The box plot the shows maximum size of neutrophil clusters observed across samples. Larger clusters in mechanically damaged samples point to a stronger inflammatory response most likely brought on by the more tissue disturbance caused by these injuries. D) The box plot represents the wound sizes for each injury type. Mechanical injuries result in larger and more variable wound sizes, while laser injuries are more uniform and precise, reflecting the controlled nature of laser-mediated tissue damage

7.1.6. Methods for neutrophil swarming screen

7.1.6.1. Sample preparation and mounting

Imaging plate preparation and embryo mounting

96-well microplates with cycloolefin bottoms (Greiner bio-one SCREENSTAR Cat.-No. 655866) were used for imaging purposes. The *Tg(mpx*:GFP) embryos were collected from the incubator for the experiment at 2 dpf, and the embryos were dechorionated. The embryos were transferred to a new petri dish containing the imaging media, consisting of working E3 media and tricaine (200 µg/ml). This assay didn't utilize any agarose molds so using a 200 µl pipette tip with a small cut at the top to ensure the embryos' safety, 150 µl of imaging medium with the embryos were pipetted and transferred to the individual wells of the imaging plate. The embryos were carefully positioned laterally under a stereomicroscope using a bent subcutaneous injection needle. Throughout the screening experiments, a consistent embryo orientation was maintained, and preparing a single imaging plate typically took 20-30 minutes.

7.1.6.2. Image acquisition workflow

After positioning the embryos in a 96 well plate, the imaging plate was sealed with a gas-permeable adhesive seal (4titude Cat: 4ti-0517/ST) to prevent media evaporation. The imaging machine's temperature was set to 28^0C, and the imaging plate was inserted for imaging. In the initial prescreening, a single z-slice per well was acquired using a 2x 0.06 objective in a bright-field and 470nm (GFP) channel (See Table 13). The acquired prescreen data was visualized using Plateviewer (provided by ACQUIFER), and the ventral fin region of the *Tg(mpx:GFP*) embryos was marked using the click tool for higher magnification acquisition. The optimal focal plane in the Z-axis was set manually for each well. The coordinates of the selected region and the optimal focal plane were saved within the acquisition script, and sub sequent acquisition was performed. For embryos subjected to laser-induced injury, 20x prelaser images were acquired using a 20x 0.45 objective in bright-field and 470nm (GFP) channel, acquiring 20 z-slices with a ΔZ of 5µm per well (See Table 14). Subsequently, the images were used for laser annotation to perform laser injury in the annotated region (see Section 7.1.6.3). For embryos undergoing mechanical injury, the time-lapse acquisition was initiated immediately after the prescreen acquisition.

The time-lapse acquisition captured 20 z-slices with a ΔZ of 5µm per well. Images were acquired every 5 minutes for 6 hours (See Table 14). The optimal focal plane in the Z-axis was set manually for each well before the start of the time-lapse. Due to the high temporal sampling, the number of wells imaged per plate was 20-30. After the time-lapse acquisition, a 2x post-screening of the whole plate was performed. This involved acquiring 20 z-slices with a ΔZ of 5µm per well using a 2x 0.06 objective in bright-field and 470nm channel (See Table 13). The entire imaging process was controlled using imaging machine scripts to manage various aspects of the experiments.

Table 13: Imaging parameters for 2x prescreen acquisition for neutrophil swarming screen.

Channel	Power	Exposure Time
Bright-Field (BF)	30%	20 ms
470nm (GFP)	50%	50 ms

Table 14: Imaging parameters for 20x prelaser and time-lapse acquisitions for neutrophil swarming screen.

Channel	Power	Exposure Time	ΔZ	No. Z Slices
Bright-Field (BF)	30%	20 ms	5 µm	20
470nm (GFP)	50%	50 ms	5 µm	20

7.1.6.3. Laser-induced ventral fin injury

After successfully mounting orienting and acquiring higher magnified images marking the ventral fin region (ventral fin injury, see section 7.1.6.1 and section 7.1.6.2). The acquired images were visualized using Plateviewer (provided by ACQUIFER); using the laser annotation tool, the images in the brightfield channel were used to uniformly annotate the ventral fin region for laser-induced ventral fin injury.

For assay optimization, experiments used varying laser power and repeat cycles, which were configured accordingly for each experiment. The annotated regions and laser settings were then transferred to ACQUIFER's photomanipulation module (developed with Rapp Optoelectronic, Wedel, Germany), which performed automated laser injury on each embryo in the corresponding wells without further user interaction.

7.1.6.4. Image analysis workflow pipelines and scripts

The analysis pipeline primarily comprised an image processing segment and a segment dedicated to data visualization and analysis, involving identifying samples showing swarming and tracking potential swarm clusters. The analysis pipeline was designed to be user-friendly and tailored to users in an open-source environment. The entire pipeline is available on GitHub and can be accessed using this link (https://github.com/sankeert1999/NeutrophilsSwarmAnalyserKit).

Before image processing, the acquired time-lapse data (see Section 7.1.6.2) was split into brightfield and GFP channels. For the GFP channel, maximum intensity projections were generated along the Z-axis for each timepoint for each time-lapse. For the brightfield channel, the center slice from each timepoint was selected and stitched into a separate stack for each time-lapse.

Image processing

A custom Fiji macro, "cluster analyzer.ijm," was developed to process the images, using the split brightfield stack and max-projected GFP channel stack as inputs. The brightfield stack was subjected to template matching via the Template Matching plugin (Thomas & Gehrig, 2020b), where the user selected a uniform template (across samples) to be searched across the time-lapse sequence. After template matching, the regions of interest (ROIs) were identified across the time-lapse, which were then used to crop both the brightfield and GFP stacks using Fiji's crop tool. The cropped stacks were merged to create a hyperstack.

The obtained hyperstack was then subjected to registration using the HyperStackReg (V. Sharma, 2018) plugin in Fiji. The brightfield channel was utilized for stack registration, and the results of the registrations were transferred to the GFP channel. After registration, the hyperstack was split into individual channels, and neutrophils in the GFP channel were segmented using classical default threshold methods within FIJI, with threshold values adjusted as needed for each experiment.

The segmented masks were further processed using the Analyze Particles function in Fiji, and the resulting data, including mask area, roundness, mean intensity, and other relevant parameters, were exported as a CSV file. The segmentation masks, overlays, and detected ROIs were also saved for future reference.

Data analysis and visualization

A custom, user-friendly Knime workflow named **“**Swarm Classifier.knwf**”** was developed for further data processing. The workflow starts by importing the CSV files generated post-image processing and merging them into a single dataset. It then calculated the statistical parameters—mean, variance, and skewness—of the detected cluster areas over time for different samples. The samples were then ranked based on the likelihood of swarm occurrence, with those having the highest probability at the top. Additionally, maximum intensity projections of the time-lapse data (across time) were combined as a separate column in the final table, and the resulting table was exported as an Excel file.

A second custom user-friendly Knime workflow, “Swarm Tracker,” was created to analyze swarm tracks from the selected samples identified by the Swarm Classifier. This workflow processed individual CSV files for each sample, exporting detailed swarm track data, including position, persistence, and other parameters, as described in the Results Section 7.1.4 .

7.2. Developing a high throughput workflow to assess otic vesicle neutrophil recruitment following substrate injection in zebrafish embryos

Neutrophil recruitment is a fundamental part of the innate immune response which has been linked to several inflammatory disorders via dysregulation. Knowing the mechanisms behind immune responses and choosing a treatment depends on our ability to analyze different treatments objectively by means of in vivo neutrophil migration and accumulation.C5a-C5aR1 signaling axis significantly modulates inflammatory responses by regulating neutrophil recruitment to injury or infection sites (Sadik et al., 2018)While this pathway has been investigated in detail in mammalian models, its function in zebrafish is still mostly unknown.

This knowledge gap was the central focus of my collaborator Liz Hernández from the University of Montpellier, Laboratory of Pathogen-Host Interactions (France). As part of her research, she aimed to investigate C5a-C5aR1 signaling in neutrophil recruitment and develop a zebrafish-based screening assay to evaluate the effects of C5aR inhibitors. She collaborated with me to build the imaging assay and image processing pipeline to measure neutrophil recruitment in the otic vesicle following substrate injections.

Although this project fits the larger scale of my PhD—developing imaging and analysis methods for zebrafish-based screening assays—the biological interpretation of C5aR1 signaling and pharmacological validation of inhibitors falls outside my main research focus and is extensively covered in Liz Hernández's PhD thesis. My particular contributions to this project included, designing a high-throughput imaging workflow and developing an automated image analysis pipeline for reliable and efficient quantification of neutrophil recruitment.

The following sections outline the development of the imaging and analysis workflows, highlighting my contributions to establishing a high-throughput screening assay for neutrophil recruitment in the zebrafish otic vesicle.

7.2.1. Developing the imaging assay to assess neutrophil recruitment following substrate injection in otic vesicles of zebrafish embryos

Accurate detection of neutrophil recruitment and consistent, high-quality data acquisition depended on a standardised imaging assay. Considering that the otic vesicles of zebrafish embryos are positioned laterally, the most effective imaging orientation was lateral placement, similar to the orientation strategy I previously implemented for neutrophil swarming experiments (See Results Section 7.1.1).

The imaging workflow began with substrate injections into the otic vesicles of 2 days post-fertilization (dpf) zebrafish embryos (See Section 7.2.5.3). Liz performed the substrate injection into the otic vesicles, after which the embryos were mounted laterally using the same minimal intervention approach as in my previous experiments (See Section 7.2.5.1).

Getting exact focus on the otic vesicle was essential for this imaging configuration. Similar to the challenges encountered in neutrophil swarming experiments (See Section 7.1.1), the microscope's autofocus (AF) function struggled to detect the otic vesicle, making automated focusing unreliable consistently. To address this, I applied a similar strategy that I had used previously for neutrophil swarming assay to guarantee the optimal focal plane acquisition, where I manually set the z-plane for each sample to ensure that the focal plane aligned with the otic vesicle. I also enlarged the z-section range, obtaining 44 slices at 3 µm intervals, to offset any z-axis drift during time-lapse photography. This method guaranteed that the whole otic vesicle stayed inside the imaging range across the experiment.

Following successful sample orientation and focus adjustment, I initiated time-lapse imaging at 3 hours post-injection (hpi) (See Section 7.2.5.2), acquiring images every hour up to 6 or 8 hours, depending on the specific assay requirements. This flexibility in time-lapse settings allowed us to optimize data collection for different experimental conditions while maintaining high-throughput efficiency.

7.2.2. Establishing an image processing pipeline to investigate neutrophil recruitment

After capturing the neutrophil recruitment events, standardizing image processing to guarantee consistent measurement of neutrophil accumulation in the otic vesicle came next. This project shared many parallels with the neutrophil swarming experiments, as both involved tracking neutrophils post-injury in a time-lapse imaging setup. Consequently, many preprocessing solutions were transferable between both workflows. I built upon the existing analysis pipeline developed for neutrophil swarming (See Section 7.1.3) , leading to a macro-based image processing pipeline "Neutrophil_Population_Estimator.ijm" (See Section 7.2.5.4). Which incorporated key preprocessing steps, including maximum intensity projection (MIP) to create a single plane per timepoint and localizing the otic vesicle as the region of interest (ROI) to extract only the relevant area for analysis followed by aligning the ROI-localized stacks to correct translational drift across timepoints.

Since the otic vesicle occupied only a small portion of the full imaging field, I employed a similar template matching-based approach as discussed in Section 7.1.3.1 to localize the otic vesicle across all timepoints. Using the brightfield channel, which provided a stable structural reference, the pipeline cropped images to 650 x 650 pixels (See Figure 50B) from the original 2048 x 2048 pixels (See Figure 50A), ensuring consistent ROI selection. The corresponding fluorescent (green) channel, which included the neutrophil signal was cropped utilizing the localization results to, maintain the spatial alignment.

As in past experiments, small misalignments were seen in the time-lapse stacks even with good localization. I corrected this using HyperStackReg, a multi-channel registration technique I had earlier tuned for neutrophil swarming studiescontaining the neutrophil signal, was cropped accordingly to maintain spatial alignment.

Despite successful localization, minor misalignments were observed within the time-lapse stacks, as seen in previous projects. To correct this, I applied HyperStackReg, a multi-channel registration tool that I had previously optimized for neutrophil swarming experiments (See Section 7.1.3.2). The brightfield channel served as the reference for alignment, which guaranteed the otic vesicle stayed constant across the time-lapse. The fluorescent channel was subsequently subjected to the resultant

registration change, which preserved alignment across channels and raised downstream quantification accuracy (See Figure 50B).

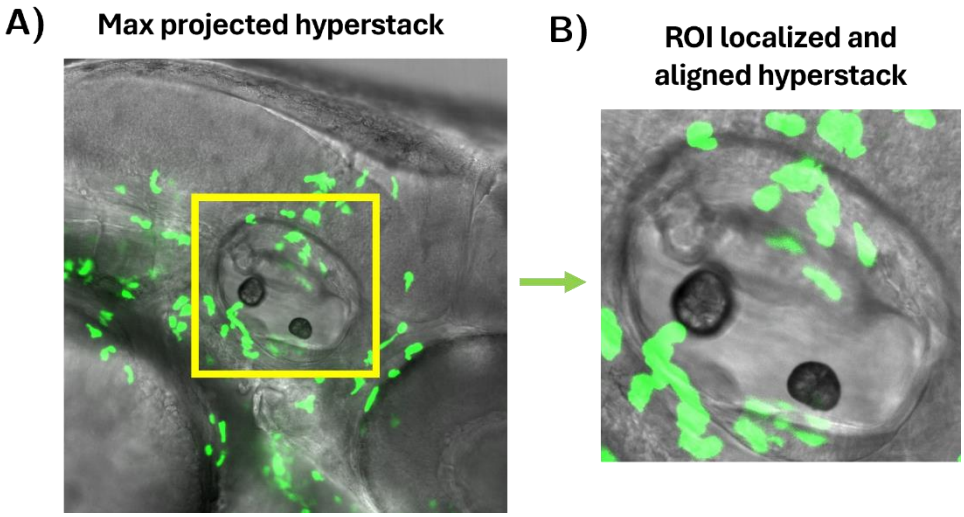

Figure 50: Template matching based otic vesicle detection. A) This panel displays the max projected hyperstack, capturing brightfield and fluorescent channels. B) This figure presents the hyper stack where the otic vesicle has been isolated and highlighted across both channels using template matching, focusing subsequent analysis within the otic vesicle region

After localizing and stabilizing the hyperstacks, the next step as part of the image processing pipeline was to segment and quantify individual neutrophils within the otic vesicle. As in the neutrophil swarming analysis, I followed a similar segmentation routine (See Results Section 7.1.3.3), applying intensity-based thresholding and the Analyze Particles function to detect and extract features from segmented neutrophils (See Figure 51A). Contrary to the swarming experiments, an additional step was necessary to ensure that neutrophil detection was restricted to the otic vesicle region, rather than the entire localized ROI. While the pipeline already restricted the analysis to a cropped region, further refinement was required to exclude detections outside the otic vesicle precisely.

To achieve this, I incorporated a user-guided annotation step within the pipeline. After ROI localization, the user was prompted to manually mark the otic vesicle within the ROI-localized stack across the entire time-lapse. These manually defined otic vesicle ROIs were then automatically saved for subsequent steps (See the yellow outline in Figure 51B). I limited particle detection to the user-defined area using the PTBIOP Fiji plugins once the otic vesicle was marked. This was accomplished by multiplying the detected particle stack with the user-annotated mask stack so that only neutrophils within the annotated otic vesicle were retained for further analysis

(See Figure 51B). Finally, the extracted particle area and otic vesicle area were measured across the time-lapse and stored in separate output tables for downstream quantification (See Figure 51C&D).

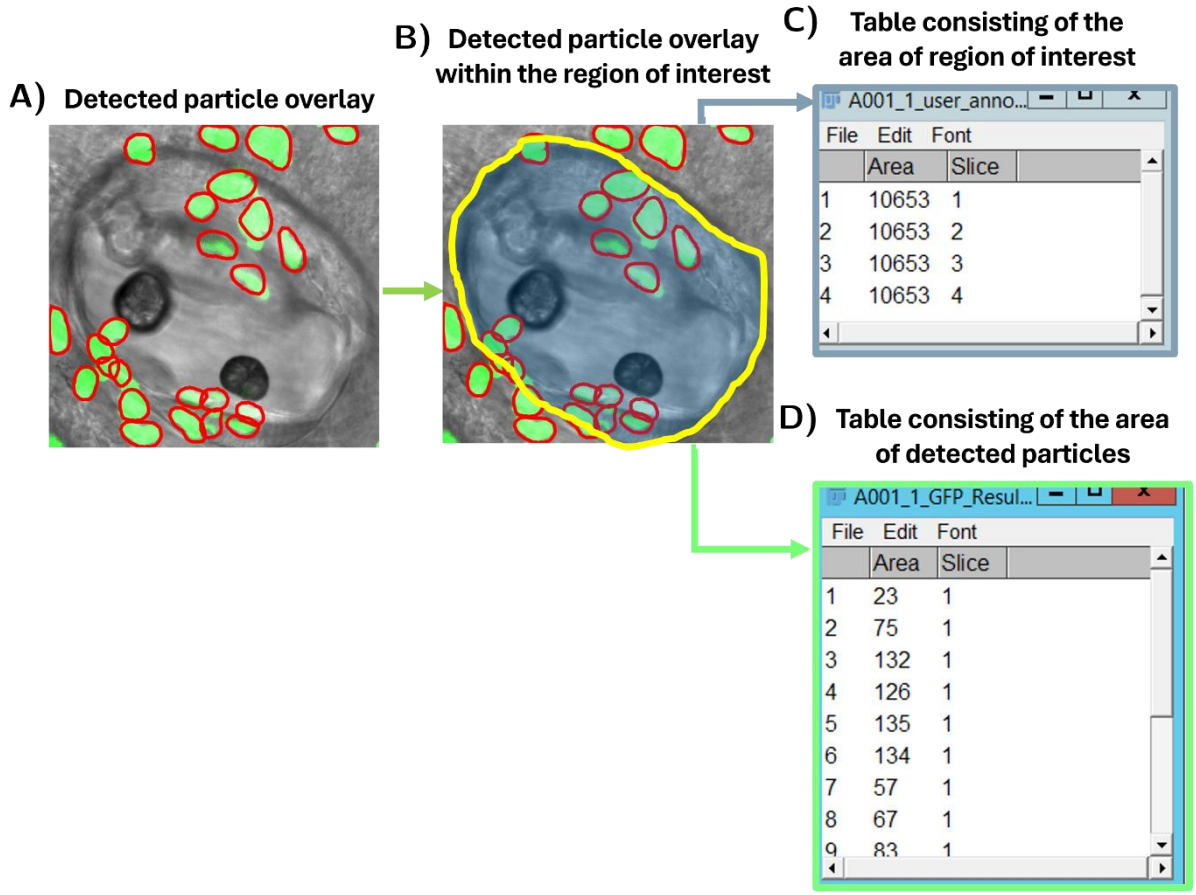

Figure 51: Overview of neutrophil segmentation and feature extraction workflow. A) This panel shows a detected particle overlay (in red) on an ROI-localized and aligned hyperstack. B) This panel shows the detected particle overlay (in red) and the user annotated structure around the otic vesicle (in yellow) on an ROI-localized and aligned hyperstack and the blue shade represents that only the particles within this region would be included as valid detections. C) Illustrating the table consisting of the areas of detected objects within the otic vesicle regions across the timelapse. D) Illustrating the table consisting of the areas the user annotated structure (otic vesicle) across the timelapse.

7.2.3. Establishing a KNIME-based neutrophil recruitment analysis workflow

Following the segmentation of neutrophils and the systematic extraction of the area of the detected neutrophils time-lapse images, the final step in the analysis pipeline was to estimate neutrophil accumulation over time within the otic vesicle. The key objective was to provide a quantitative measure of neutrophil recruitment to the otic vesicle over time post substrate injections. To achieve this, I deduced an approach to estimate the relative accumulation of neutrophils within the otic vesicle over time. I computed the ratio of the total detected neutrophil's area to the otic vesicle area, providing a normalized measurement of neutrophil accumulation (See Figure 52A). I aimed to represent this ratio as a proxy for neutrophil recruitment levels across the time-lapse, allowing for comparisons across different experimental conditions.

To implement this deduced approach, I developed a KNIME-based analysis workflow (See Figure 52B),"Neutrophil_Recruitment_Analyzer.knwf" (See Section 7.2.5.4). It automated the calculation of this accumulation ratio provided with the input files deduced post image processing workflow, including:

- The folder consisting of the list of files with the total detected neutrophil area for each timepoint across samples
- The area of the user-annotated otic vesicle

Using these inputs, the workflow systematically computed the accumulation ratio across time, producing structured output files that could be further analyzed and visualized.

A) Illustrating the approach for neutrophil count estimation in user-defined areas

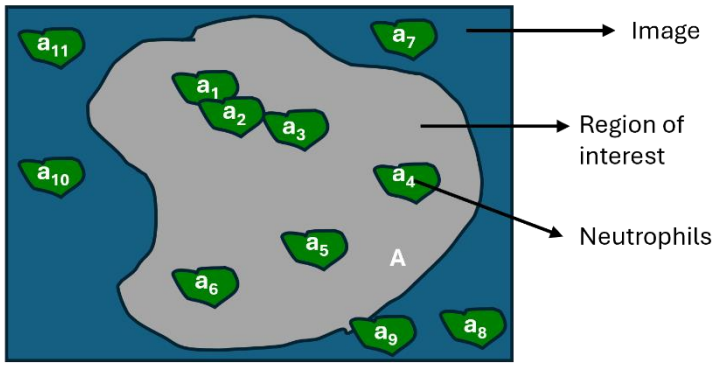

$$Count\ estimate = \frac{Sum\ of\ area\ of\ all\ neutrophils\ within\ the\ region\ of\ interest\ (a_1 + a_2 + a_3 + a_4 + a_5 + a_6)}{Area\ of\ region\ of\ intrest\ (A)} * 100$$

B) KNIME-based neutrophil recruitment analysis workflow overview

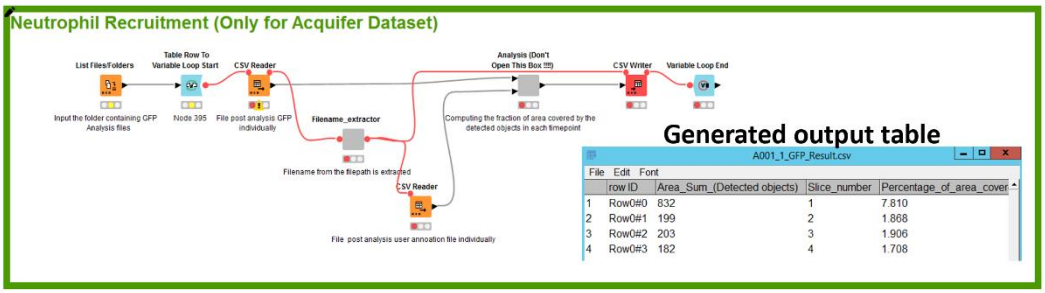

Figure 52: KNIME based neutrophil recruitment analysis workflow overview. A) Schematic representation of the method used for estimating neutrophil counts within user-defined areas of the otic vesicle, emphasizing how the count estimate is calculated as a percentage of the total area covered by neutrophils relative to the entire region of interest. B) Illustrates the KNIME-based workflow overview, the workflow facilitates the computation of neutrophil accumulation ratios using inputs including the detected neutrophil areas and the areas of user-annotated otic vesicles. The panel shows both the schematic of the workflow and a snapshot of the generated output table .

7.2.4. Validating the neutrophil recruitment analysis workflow using manual counts

Following the successful development of the high-throughput imaging assay and the associated analysis workflow for evaluating neutrophil recruitment, the subsequent step was to validate the analysis pipeline to confirm the precision of the calculated neutrophil count estimates. As part of the validation experiments, I designed a comparative study assessing neutrophil recruitment to the otic vesicle following zC5a and buffer injections. Liz had previously performed this experiment, in which buffer injection acted as a control, indicating baseline neutrophil recruitment, whereas zC5a injection was anticipated to elicit a robust neutrophil recruitment response.

To validate the approach, I employed this experimental setting to ascertain whether the proposed workflow could quantitatively discern variations between the two conditions. For this validation, I conducted the imaging and analysis, while Liz performed the injections. The samples were imaged using the previously described high-throughput imaging assay (See Section 7.2.1), capturing neutrophil recruitment from 3 hours post-injection (hpi) to 6 hpi at hourly intervals.

After imaging, the automated analysis pipeline computed the workflow-generated count estimates for every group. To assess the accuracy of the workflow generated count estimates, I compared them against manually counted neutrophils in the otic vesicle for each sample (See Figure 53A-B). Manual counting was performed by Liz, serving as the ground truth for validation. After obtaining the manual counts I computed the Pearson correlation coefficient between the manual counts and the workflow-generated estimates across the time-lapse, to quantitatively compare the results. The correlation association was stronger for the buffer(0.75) over the zC5a (0.65) (See Figure 53C-D). Comparing the counts I observed that the workflow tended to overestimate the neutrophil numbers relative to manual counts. Nevertheless, I found that the workflow effectively caught the general recruitment trends despite the small overestimation, capturing the relative changes in neutrophil accumulation over time is more crucial than reaching perfect agreement in cell counts.

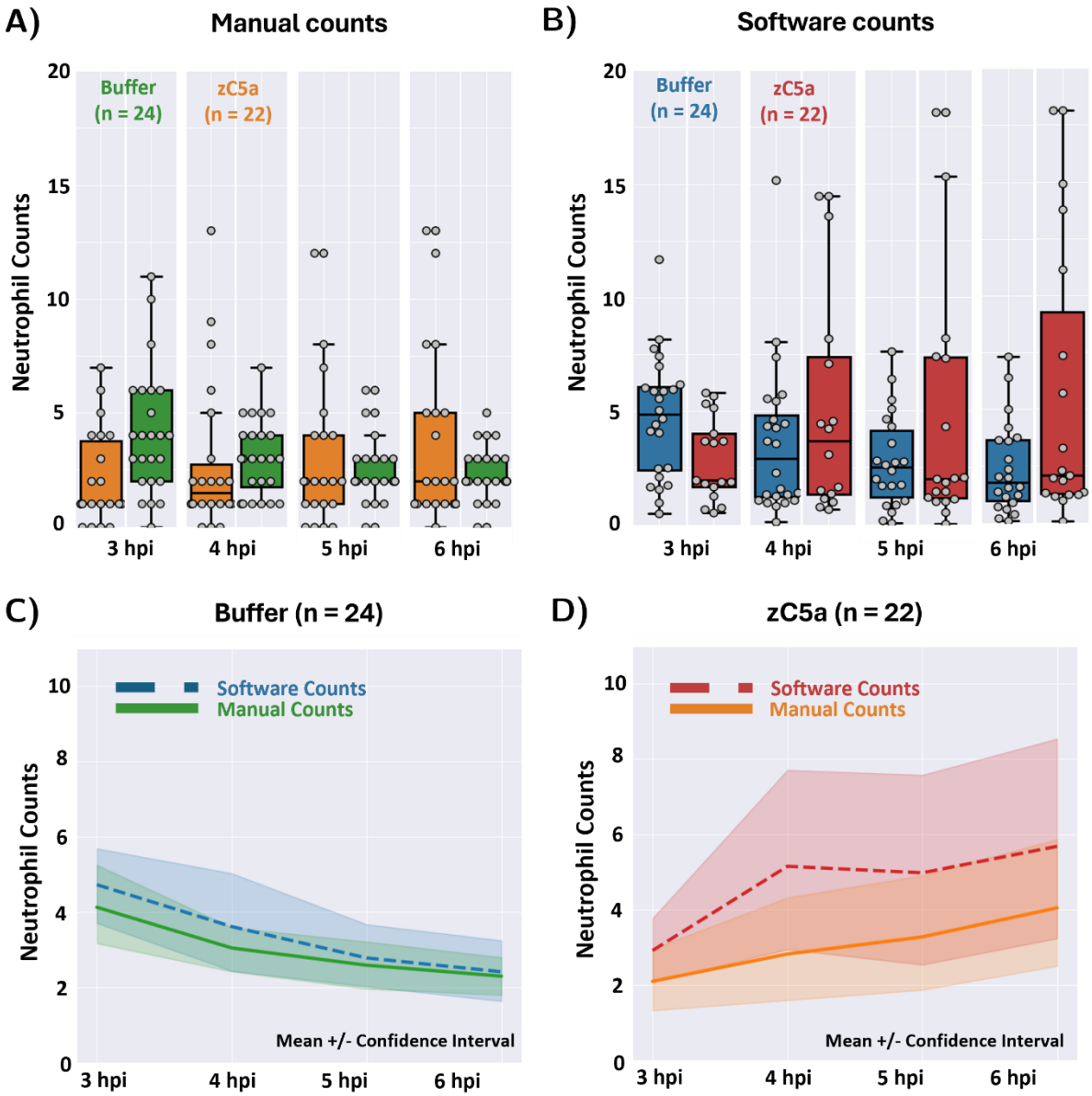

Figure 53: Comparing manual counts with workflow evaluated count estimates. A) Manual counts of neutrophils for buffer and zC5a-treated samples over a timeline from 3 to 6 hours post-injection (hpi). B) Workflow derived count estimates of neutrophils under the same conditions, illustrating variation in count precision between methods. C)&D) Aggregated comparative plots to compare the trendline across buffer and zC5a groups respectively. The Pearson correlation coefficient computed for buffer group was 0.75 and for zC5a was 0.65.

7.2.5. Methods for otic vesicle immune response screen

7.2.5.1. Sample preparation and mounting

Imaging plate preparation and embryo mounting

96-well microplates with plastic bottoms (Greiner bio-one Cat.-No. 655101) were used for imaging purposes. The *Tg(mpx:GFP)* embryos were collected from the incubator for the experiment at 2 dpf, and the embryos were dechorionated. The embryos were transferred to a new petri dish containing the imaging media, consisting of working E3 media and tricaine (200 µg/ml). This assay didn't utilize any agarose molds so using a 200 µl pipette tip with a small cut at the top to ensure the embryos' safety, 150 µl of imaging medium with the embryos were pipetted and transferred to the individual wells of the imaging plate. The embryos were carefully positioned laterally under a stereomicroscope using a bent subcutaneous injection needle. While orienting the embryos, it was ensured that the injected otic vesicle was always at the bottom (as it was an inverted microscope). Throughout the screening experiments, a consistent embryo orientation was maintained, and preparing a single imaging plate typically took 20-30 minutes.

7.2.5.2. Image acquisition workflow

After positioning the embryos in a 96 well plate, the imaging plate was sealed with a gas-permeable adhesive seal (4titude Cat: 4ti-0517/ST) to prevent media evaporation. The imaging machine's temperature was set to 28^0C, and the imaging plate was inserted for imaging. In the initial prescreening, a single z-slice per well was acquired using a 2x 0.06 objective in a bright-field and 470nm (GFP) channel (see Table 15). The acquired prescreen data was visualized using Plateviewer (provided by ACQUIFER), and the microinjected otic vesicle of *Tg(mpx:GFP)* was marked using the click tool for higher magnified time-lapse acquisition. The optimal focal plane in the Z-axis was set manually for each well. The coordinates of the selected region and the optimal focal plane were saved within the acquisition script, and the time-lapse acquisition was initiated, involving the acquisition of 44 z-slices with a ΔZ of 3µm per well. Images were acquired every hour for 7 hours (See Table 15)

The plate was divided into Group A (first four rows) and Group B (remaining rows) to synchronize the timeline across all samples during the time-lapse acquisition. Since the embryos were manually microinjected (see Section 7.2.5.3), resulting in slight time differences between injections, a 30–40 minute delay was introduced between the acquisitions of the two groups. Group A was imaged first, followed by Group B

after the delay, ensuring synchronized data acquisition across the time-lapse. The entire imaging process was controlled using imaging machine scripts to manage various aspects of the experiments

Table 15: Imaging parameters for 2x prescreen acquisition for otic vesicle immune response screen.

Channel	Power	Exposure Time
Bright-Field (BF)	30%	20 ms
470nm (GFP)	50%	50 ms

Table 16: Imaging parameters for time-lapse acquisitions for otic vesicle immune response screen.

Channel	Power	Exposure Time	ΔZ	No. Z Slices
Bright-Field (BF)	30%	20 ms	3 µm	44
470nm (GFP)	50%	50 ms	3 µm	44

7.2.5.3. Microinjecting substrate in zebrafish otic vesicle

2 dpf *Tg(mpx*:GFP) embryos were dechorionated and positioned in a V-shaped 3% agarose-based injection mold filled with working E3 media and tricaine (80-100 mg/ml). Glass microinjection needles were pulled using a puller instrument with the following parameters: heating = 600, voltage = 80, velocity = 80, time = 200, and pressure = 90-200. The pulled needles were loaded with a few µl of the substrate mixed with 10% red phenol to facilitate the visualization of the injected substrate. Each embryo was microinjected at the otic vesicle and then transferred to a 25 ml petri dish containing working E3 media.

7.2.5.4. Image analysis workflow pipelines and scripts

The analysis pipeline primarily comprised an image processing segment and a segment dedicated to data visualization and analysis. The analysis pipeline was designed to be user-friendly and tailored to users in an open-source environment. The entire pipeline is available on GitHub and can be accessed using this link (https://github.com/sankeert1999/NeutrophilsPopulationAnalyser).

Image processing

After acquiring time-lapse data, the acquired data was converted to a hyperstack using the HyperStackMaker plugin in Fiji. The hyperstacks were then processed using a custom Fiji macro, “Neutrophil_Population_Estimator.ijm.”

The script started by splitting the hyper stack into individual channels. A maximum intensity projection was created for the green (GFP) channel, while the central slice was extracted for the bright-field channel. These resulting images were merged across time to generate a new hyper stack.

For further processing, the user was prompted to manually select the otic vesicle region from the newly generated hyperstack, which was cropped accordingly. A second prompt allowed the user to annotate the otic vesicle across time, and these annotations were recorded in Fiji’s ROI manager and subsequently saved.

The cropped hyperstack was split into two channels; the GFP channel was segmented to identify neutrophils using the StarDist plugin, with parameters adjusted for different experiments. Segmentation masks were generated and further analyzed using Fiji's "Analyze Particles" function to extract neutrophil ROIs. The previously recorded user-annotated ROIs were applied using the PTBioP Fiji plugin to limit the analysis to the selected otic vesicle region.

Finally, the neutrophil masks within the user-annotated region, including area and other attributes, were exported as CSV files. The area of the user-annotated region across different time points was also saved. The cropped hyperstack (with split channels), segmentation masks, and ROI data were saved for future reference.

The script was designed to handle images in batches by taking a folder of hyperstacks as input. The entire image processing workflow was automated, requiring user input only for marking and annotating the otic vesicle region and otic vesicle across time.

Data analysis and visualization

The result exported after image processing was further analyzed to assess neutrophil recruitment over time using a custom KNIME workflow named "Neutrophil_Recruitment_Analyzer.knwf." This workflow took two input folders: one containing files with the detected neutrophil area and the other with the area of user-annotated regions of interest. For each timepoint across all samples, the total detected neutrophil area was calculated and divided by the corresponding user-annotated region's area. This resulted in a table of each timepoint and the

corresponding ratio of detected neutrophil area to annotated region area. The resulting table was then exported as a CSV file and saved to the respective folder.The entire workflow was fully automated, requiring the user only to specify the input folders.

Publications

Satheesan, S., Gehrig, J., & Thomas, L. S. V. (2024). Virtual Orientation Tools (VOTj): Fiji plugins for object centering and alignment. *microPublication Biology*, *2024*. https://doi.org/10.17912/micropub.biology.001221

Declaration

Hereby, I declare that I conducted the PhD thesis “Design and implementation of workflow tools for multiplexed time-lapse imaging experiments in zebrafish screening” on my own and with no other sources and aids than quoted.

Heidelberg, 2025

Acknowledgments

The acknowledgments are not necessarily listed in order of importance, as I deeply appreciate every person and organization that supported me throughout this PhD journey.

First and foremost, I would like to express my sincere gratitude to my daily supervisors, Jochen Gehrig and Laurent Thomas, from Acquifer Luxendo. Their guidance, expertise, patience, and encouragement have been invaluable at every research stage. Beyond their insightful feedback, they dedicated countless hours to reviewing manuscripts, refining this thesis, and rigorously testing the software tools developed in this work. I am also thankful to ACQUIFER Luxendo for giving me an ideal work atmosphere and integrating me into their team.

I am grateful to my faculty supervisor, Jochen Wittbrodt, for his valuable feedback, constructive criticism, and guidance throughout this PhD process. I am thankful to Jochen for his continuous support, for integrating me into the 5th-floor lab community, and for facilitating access to essential research infrastructure, including faculty rooms and microscopy facilities.

A special thanks goes to the fish room team for their invaluable help in raising and maintaining zebrafish over the years. I am especially grateful to Beate Wittbrodt and Eric for always assisting me, even with the smallest doubts and queries. I would also like to thank Tanja Kellner for her technical support in the BioQuant lab and her assistance with ordering and organization. I am grateful to all 5th-floor members for creating a collaborative and supportive work environment. In particular, I want to thank Rashi, Bettina, Phillip, and Encarni for their organizational help and assistance whenever needed. Additionally, I sincerely appreciate Eva Hasel de Carvalho and Frederike Seibold for taking care of essential paperwork, advising me on administrative matters, and accommodating last-minute requests to schedule meetings. I want to thank my lab colleagues, Anthi, Kristaps, and Fariha, for making life in BioQuant vibrant and creating a great working atmosphere. I also want to thank Leon, who is currently taking this study to the next level, for his help and support during the protocol building.

I deeply appreciate Venera Weinhardt and Thomas Dickmeis for accepting my request to be my thesis examiners, supporting me throughout the scheduling process, and being part of this crucial milestone in my academic journey.

I also want to sincerely thank Steve Renshaw (my reviewer) for his critical insights and invaluable input throughout my PhD journey. I particularly appreciate his generosity in hosting me in his lab for collaborative projects with Nils, providing a warm and welcoming atmosphere that allowed me to apply my skills in a different domain beyond my main research project. I also extend my gratitude to the members of the Renshaw lab for their support during my time there.

I am thankful to Laure Yatime, Liz Hernández, and the members of the LPHI for welcoming me during my secondment project in LPHI, France. Their generosity in hosting me allowed me to expand my research beyond my primary project and apply my skills in a new context. I also extend my gratitude to INFLANET, the program that funded me throughout my PhD, and Veronica and Arianna for their administrative support, especially for assisting with travel and accommodation arrangements—even at the last minute. I am also grateful to Reusl, Liz, Nils, Hannah, and Mayra from the INFLANET consortium for their mutual support throughout our PhD journeys.

I also thank the open-source software community, particularly the ImageSC forum, for fostering such a supportive environment and assisting users with their queries. I would also like to thank the AI writing tools (Grammarly, ChatGPT, and Grok) that assisted with paraphrasing my writing in this thesis.

Beyond academia, I want to thank my friends in Heidelberg—Felix, Adarsh, Dhrisya, Rejith, and Parvathi—for enriching my life outside work. I also want to thank my close friends Theja, Mridhul, Akshay, Athil, Anandu, and Sudeep for their unwavering support throughout this journey.

Finally, I sincerely thank my parents and brother for their unconditional love and encouragement. Last but certainly not least, I am profoundly thankful to my partner, Abhi, for her unwavering support, patience, and resilience through all the ups and downs of this PhD journey—and to myself for persevering through the challenges and staying committed to this path.

List of Figures

List of Supplementary Figures

List of Tables

List of Supplementary Tables